UNIVERSITY OF SOUTHAMPTON

Faculty of Environmental and Life Sciences
School of Ocean and Earth Science

Shelf-Ocean Exchange in the Polar Regions

by

Ryan Matthew Scott
MSci
ORCiD: 0000-0002-2141-7978

A thesis for the degree of
Doctor of Philosophy

August 2021

UNIVERSITY OF SOUTHAMPTON

ABSTRACT

FACULTY OF ENVIRONMENTAL AND LIFE SCIENCES
School of Ocean and Earth Science

Doctor of Philosophy

Shelf-Ocean Exchange in the Polar Regions

by Ryan Matthew Scott

The polar oceans are of paramount importance to Earth's climate system. The unprecedented changes that these regions are now experiencing have the potential to impact everyone on our planet, via sea level rise, extreme weather events and by threatening food security. The complex exchange processes that occur between the deep ocean and the polar continental shelves move climatically-important quantities such as heat, salt, and nutrients, and are thus essential to the functioning of the polar oceans within the climate system. This thesis uses oceanographic observations from both polar regions to further our understanding of two components of this shelf-ocean exchange: (i) vertical mixing on the West Antarctica Peninsula (WAP) and (ii) eddies in the Arctic Ocean.

In 2016, an ocean glider deployed in Ryder Bay, WAP, collected hydrographic and microstructure data, obtaining some of the first direct measurements of turbulent kinetic energy dissipation off West Antarctica. These data reveal significant spatio-temporal variability in hydrographic and dissipation conditions, with elevated dissipation and heat fluxes observed above a topographic ridge at the bay's entrance, suggesting that the ridge is important in driving upward mixing of warm Circumpolar Deep Water. Mooring-based current and nearby meteorological data are used to attribute thermocline shoaling (deepening) to Ekman upwelling (downwelling) at Ryder Bay's southern boundary, driven by $\sim$ 3-day-long south-westward (north-westward) wind events. Anticyclonic winds generated near-inertial shear in the bay's upper layers, causing elevated bay-wide shear and dissipation $\sim$ 1.7 days later. High dissipation and heat fluxes over the ridge appear to be controlled hydraulically, being co-located (and moving) with steeply sloping isopycnals. The ridge thus provides sustained heat to the base of the thermocline, which can be released into overlying waters during the bay-wide, thermocline-focused dissipation events. This highlights the role of underwater ridges, which are widespread across the WAP, in the regional ocean heat budget.

A rapid, high-resolution hydrographic and current shipboard survey provides a unique three-dimensional view of an anti-cyclonic, cold-core eddy in the Arctic Ocean. The eddy was situated 50-km seaward of the Chukchi Sea shelfbreak, embedded in the offshore side of the Chukchi Slope Current. The eddy core (at 150-m depth) consisted of saline, newly ventilated Pacific winter water, which is important for ventilating the cold Arctic halcoline. Subtracting out the slope current signal, the eddy's velocity field was symmetrical and approximately in geostrophic balance, with a peak azimuthal velocity of $\sim$ 10 cm s^{-1}. The eddy's age is estimated to be on the order of months, and different scenarios are discussed regarding how the eddy became embedded in the slope current, the eddy's life-span, and the ramifications for halocline ventilation.

Contents

List of Figures

List of Tables

Declaration of Authorship

I declare that this thesis and the work presented in it is my own and has been generated by me as the result of my own original research.

I confirm that:

1. This work was done wholly or mainly while in candidature for a research degree at this University;
2. Where any part of this thesis has previously been submitted for a degree or any other qualification at this University or any other institution, this has been clearly stated;
3. Where I have consulted the published work of others, this is always clearly attributed;
4. Where I have quoted from the work of others, the source is always given. With the exception of such quotations, this thesis is entirely my own work;
5. I have acknowledged all main sources of help;
6. Where the thesis is based on work done by myself jointly with others, I have made clear exactly what was done by others and what I have contributed myself;
7. Parts of this work have been published as:
   Scott, R. M., J. A. Brearley, A. C. Naveira Garabato, H. J. Venables, and M. P. Meredith, 2021b: Rates and mechanisms of turbulent mixing in a coastal embayment of the west antarctic peninsula. *Journal of Geophysical Research: Oceans*, **126**, e2020JC016 861

   Scott, R. M., R. S. Pickart, P. Lin, A. Münchow, M. Li, D. A. Stockwell, and J. A. Brearley, 2019: Three-dimensional structure of a cold-core arctic eddy interacting with the chukchi slope current. *Journal of Geophysical Research: Oceans*, **124 (11)**, 8375–8391

Signed:... Date:..................

Acknowledgements

The research in this thesis has been funded by the Natural Environmental Research Council (grant NE/N012070/1) as part of the Next Generation Unmanned Systems Science (NEXUSS) Centre for Doctoral Training.

First and foremost, I would like to thank my supervisors: Alex Brearley, Alberto Naveira Garabato, Hugh Venables and Mike Meredith, without whom I would not have been able to conduct this research. In particular, Alex and Alberto have been there to explain numerous concepts, answer questions however simple or complicated, and have simply supported me in every way throughout. I have to thank Alex especially for reading everything in this thesis several times over. I would also like to thank Alex and Bob Pickart for making my research trip to Woods Hole Oceanographic Institution possible. Bob was so welcoming and inspiring, and the trip there was a fantastic way to broaden my oceanographic knowledge. The work I conducted at WHOI formed my first published paper, and I have friends and memories from that visit that will last a lifetime.

Next, I would like to thank the people who have provided me with data or have helped me during different stages of my PhD. These include those who were involved in deployment and recovery of the glider and mooring data in Ryder Bay, the Marine Assistants who collect data for the Rothera Time Series, and the crews of the RRS James Clark Ross and USCGC Healy. I also thank Laura Gerrish from the MAGIC department at the British Antarctic Survey, for their help creating Figure 1.11. I thank Dr. Lucas Merckelbach for their help with setting up the hydrodynamic flight model in Python, a fundamental stage in the processing of the glider microstructure data. I thank Prof. Mark Inall, whose advice on basin-scale wave modes and Coastal-Trapped Waves was invaluable for both Chapter 4 and ensuring a quick response to reviewers for my second paper. I would also to thank the following co-authors for their valuable contributions to my Arctic paper: Peigen Lin, Andreas Münchow, Min Li and Dean Stockwell.

I thank all of my friends who have made undertaking this PhD so enjoyable and unforgettable. From Woods Hole, I have great memories of going for late night dips and staring at the stars with my friends from Oyster Pond Road. On each of my three research cruises, I had an unbelievable experience of staying out on deck and looking for wildlife and sea ice with my crew mates. I have had some amazing laughs with my NEXUSS cohort, from the boat party in our first week, to our writing retreat in the Cairngorms. Thank you to all of the BAS students past and present who made the day-to-day life at BAS enjoyable. A special mention must go to my house mates Jake, David and Matt, who made living in Cambridge such a blast! Thank you for the endless memories, I look forward to long-lasting friendships with you all.

During my PhD I was fortunate enough to meet my girlfriend Holly. I'd like to thank her for all of her support and perseverance when I've been unavailable, particularly over the last few months. Without your help we wouldn't have a home to move into!

Lastly, I would like to thank my family. They have always believed in me and shown an interest in everything that I have been fortunate to do during my PhD. They have been patient and understanding when I have not been available during these final write-up months, have picked me up when I have been down, and continue to advise and support me throughout life. Most recently this has meant providing me with free meals and somewhere to live whilst finishing this thing!

Nomenclature

AABW	Antarctic Bottom Water
AASW	Antarctic Surface Water
ACC	Antarctic Circumpolar Current
ADCP	Acoustic Doppler Current Profiler
AOA	Angle of Attack
APCC	Antarctic Peninsula Coastal Current
ASC	Antarctic Slope Current
ASF	Antarctic Slope Front
AUV	Autonomous Underwater Vehicle
AW	Atlantic Water
CCW	Counter-Clockwise
CDW	Circumpolar Deep Water
CPD	Cycles Per Day
CTD	Conductivity-Temperature-Depth
CTW	Coastal-Trapped Wave
CW	Clockwise
ENSO	El Niño-Southern Oscillation
GMSL	Global Mean Sea Levels
GPS	Global Positioning System
HAB	Height Above Bottom
ITP	Ice-Tethered Profiler
LTER	Long Term Ecological Research
MLD	Mixed Layer Depth
MOC	Meridional Overturning Circulation
NADW	North Atlantic Deep Water
NEXUSS	Next Generation Unmanned Systems Science
NVWW	Newly Ventilated Winter Water
PSD	Power Spectral Density
PSU	Practical Salinity Unit
QAA	Quality Assessment Algorithm
RaTS	Rothera Time Series
RCP	Representative Concentration Pathway

RMSE	Root Mean Square Error
RSI	Rockland Scientific Incorporated
RWW	Remnant Winter Water
SAM	Southern Annular Mode
SSH	Sea Surface Height
SSS	Sea Surface Salinity
SST	Sea Surface Temperature
TKE	Turbulent Kinetic Energy
TWR	Teledyne Webb Research
VMADCP	Vessel Mounted Acoustic Doppler Current Profiler
VMP	Vertical Microstructure Profiler
WAP	West Antarctic Peninsula
WW	Winter Water
XCTD	Expendable Conductivity-Temperature-Depth
XBT	Expendable-BathyThermograph

Chapter 1

Introduction

The polar regions are of paramount importance to Earth's ocean and climate system. These regions are experiencing unprecedented changes, with the potential to affect everyone on the planet, via sea level rise, extreme weather events and by threatening food security. Developing our understanding of these processes is therefore fundamental for adapting to the changing environment, minimising our impact and sustaining life on Earth. The exchange processes between the deep ocean and the polar continental shelves are an essential component of the climate system, moving important quantities such as heat, salt, carbon and nutrients. However, these processes are complex and our understanding has been limited by the difficulty of observing these remote environments. This thesis uses oceanographic observations from both polar regions to further our understanding of two essential components of this shelf-ocean exchange: (i) vertical mixing on the West Antarctica Peninsula (WAP), where warm, saline water intrudes onto the continental shelf, towards Antarctica's glaciers and ice shelves; and (ii) eddies in the Arctic Ocean, which export cold, dense water off of the shelf and into the deep basin of the Arctic Ocean, preventing heat from rising and melting the sea ice.

This chapter introduces the reader to the polar regions and their importance, including their major circulation patterns and water masses, and the relevant shelf-ocean exchange mechanisms. The chapter also provides a brief background on mixing, a primary focus of this thesis (as highlighted above). The chapter finishes by outlining the aims and structure of the thesis.

1.1 Geography and Bathymetry of the Polar Regions

The Arctic and Antarctic may both be polar regions, but they are geographically very different. Centred over the North Pole is the Arctic Ocean, a semi-enclosed deep basin that is surrounded by Alaska, Canada, Greenland, Iceland, Scandinavia and Russia

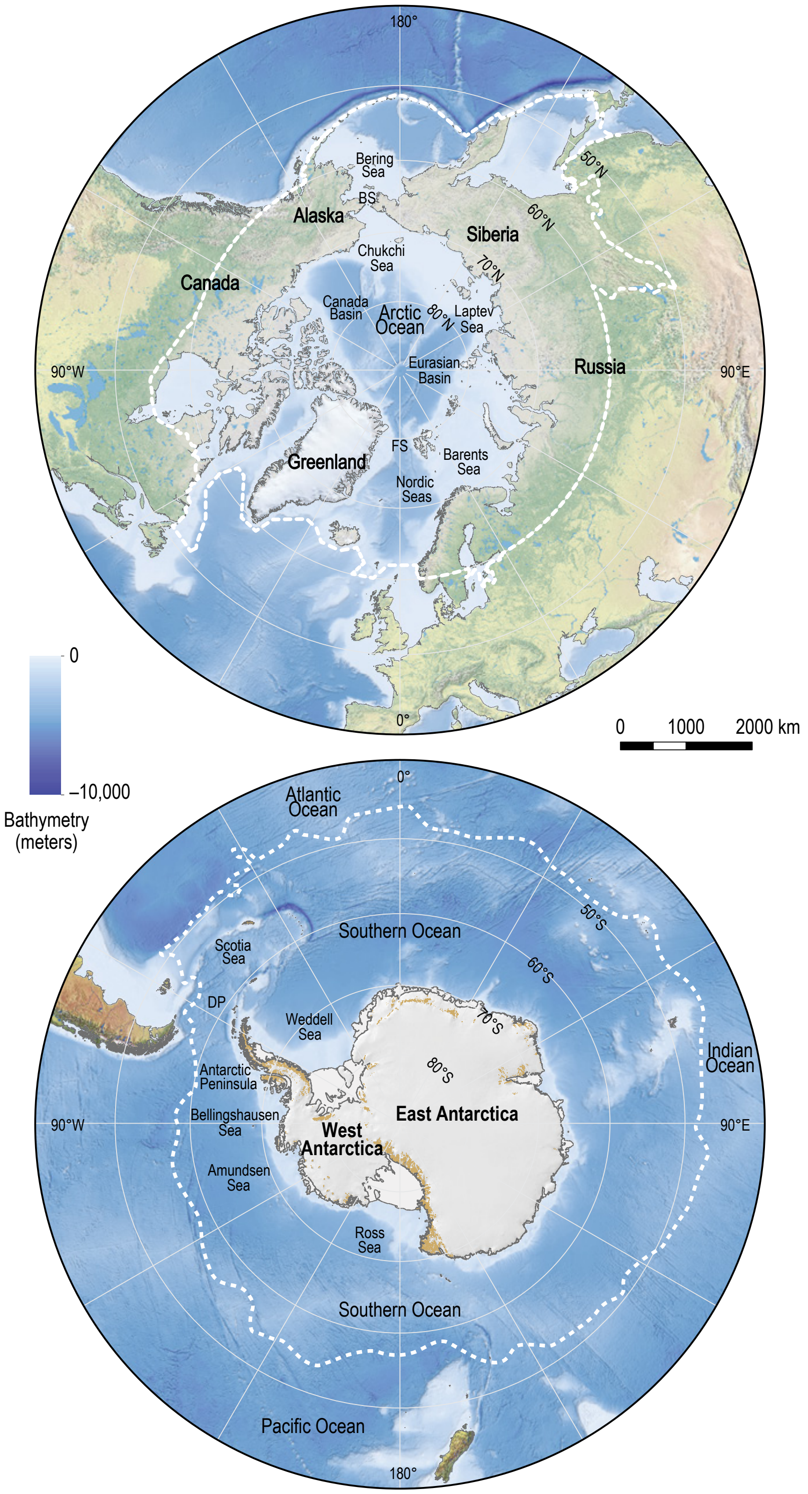

FIGURE 1.1: The Arctic (top) and Antarctic (bottom) polar regions (from Meredith et al., 2019). Various place names referred to in the text are indicated, including the Bering Strait (BS), Fram Strait (FS) and Drake Passage (DP). Dashed lines represent the approximate boundary of the polar regions, using a flexible definition encompassing different ocean and cryosphere definitions; these include (but are not limited to) ocean fronts, conservation areas and the permafrost zone (see Meredith et al., 2019, for more detail).

(Figure 1.1, top). By contrast, Antarctica is centered at the South Pole and is itself a landmass, surrounded by the Southern Ocean (Figure 1.1, bottom).

In the Arctic, the $\sim$ 4000-m deep central basin is divided into the Canada and Eurasian Basins, separated by the Lomonosov Ridge, with a mean depth of 1500 m (Cochran et al., 2006). The Canada Basin can be further divided into the Canada and Makarov Basins, separated by the Alpha and Mendeleev Ridges; and the Eurasian Basin into the (southern) Nansen and (northern) Amundsen Basins, separated by the Gakkel Ridge (Rudels, 2015). Surrounding these basins are shallow ($\sim$ 100 m) continental shelf-sea regions, which constitute 53% of the total Arctic area (9.7×10^6 km^2; Jakobsson et al., 2004). Clockwise from the northeast coast of Alaska, these are the Chukchi Sea, East Siberia Sea, Laptev Sea, Kara Sea, and Barents Sea.

The semi-enclosed nature of the Arctic means that there are only four major gateways for the Arctic Ocean to exchange water with its surrounding oceans (Figure 1.1, top). The only connection of the Arctic Ocean to the Pacific Ocean is through the Bering Strait, the 85 km wide and 50 m deep passageway between Alaska and Russia (Rudels, 2015). The Atlantic Ocean is connected to the Arctic Ocean through the Fram Strait, which is the Arctic's deepest connection to the world's oceans at 2600 m, the $200 - 300$ m deep Barents Sea Opening, and the convoluted $125 - 230$ m deep and narrow Canadian Arctic Archipelago (Rudels, 2015).

Antarctica contains multiple shelf-seas, however, these are typically deeper ($300 - 400$ m) than those in the Arctic. In West Antarctica, the major seas include the Weddell Sea (though much of the Weddell Sea is deep ocean rather than continental shelf), Bellingshausen Sea, Amundsen Sea and the Ross Sea (Figure 1.1, bottom). Unlike the Arctic, the continental shelf-sea regions constitute a smaller percentage of the Southern Ocean's total area, which is largely composed of $\sim 4000 - 5000$ m deep abyssal plains. The abyssal plains are well connected, with the narrowest oceanic gateway (850 km) found between the tip of the WAP and South America, known as Drake Passage (Bohoyo et al., 2019). The open boundary to the north enables easy communication between the Pacific, Atlantic, and Indian Oceans. Despite the large abyssal plains, the Southern Ocean also contains regions of complex bathymetry. Lying centrally across Drake Passage is the Shackleton Fracture Zone ($100 - 1000$ m above the surrounding seafloor; Bohoyo et al., 2019), which bounds the western part of the Scotia Arc. To the north and south, the Scotia Arc is bounded by the North and South Scotia Ridges, and to the east by the South Sandwich Trench. Multiple seamounts are found in the Southern Ocean, including Discovery Bank at the eastern end of the South Scotia Ridge and Maud Rise at 65° S 3° E (3000 m above the surrounding seafloor; Brandt et al., 2011). Other major bathymetric features found in the Southern Ocean include the Pacific Antarctic Ridge ($\sim$ 2500 m depths) found north of the Ross Sea, and the Kerguelen Plateau (which rises $>$ 2000 m above the surrounding seafloor; Bénard et al., 2010).

Such ridges interact with the overlying Antarctic Circumpolar Current (ACC; see Section 1.4.1) and are important locations of intense turbulent mixing (e.g., Naveira Garabato et al., 2004, see Section 1.3.2).

1.2 Importance of the Polar Regions

1.2.1 Contribution to Sea Level Rise

The polar regions contain $\sim$ 99% of the world's freshwater ice, the majority of which is stored in the Antarctic and Greenland Ice Sheets; these contain 26.5×10^6 km^3 and 2.9×10^6 km^3 of freshwater ice, respectively (Fretwell et al., 2013; Morlighem et al., 2017). For comparison, all of the world's glaciers and ice caps contain 158×10^3 km^3 of freshwater ice (Farinotti et al., 2019); the remaining small percentage of freshwater ice is stored in permafrost, frozen lakes and rivers and snow. Complete melting of the Antarctic and Greenland Ice Sheets would raise global mean sea levels (GMSL) by 58.3 m and 7.4 m, respectively (Fretwell et al., 2013; Morlighem et al., 2017). This compares with a potential 0.3 m rise of GMSL from all of the glaciers and ice caps (Farinotti et al., 2019). Consequently, whilst complete synchronous melting of the ice sheets is perhaps unlikely (de Boer et al., 2017), the polar regions are disproportionately important for future GMSL rise. GMSL is rising and accelerating, from rates of 1.4 mm yr^{-1} between $1901 - 1990$, to 3.6 mm yr^{-1} between $2005 - 2015$ (Oppenheimer et al., 2019). Rates of GMSL rise are predicted to increase to $\sim$ 15 mm yr^{-1} by 2100 (with a total rise of 0.84 m rise relative to the $1986 - 2005$ mean) under Representative Concentration Pathway (RCP)8.5 (Oppenheimer et al., 2019). The Greenland Ice Sheet currently provides the largest land-based ice contribution to GMSL (37%), compared to 34% from the world's glaciers and ice caps and 29% from the Antarctic Ice Sheet (Bamber et al., 2018). However, $\sim$ 90% of the Antarctic Ice Sheet's contribution already comes from its western constituent: the West Antarctic Ice Sheet (Bamber et al., 2018), and, with West Antarctica being one of the fastest warming environments on our planet, the region could become the dominant contributor to future sea level rise (as discussed below).

West Antarctica is experiencing significant loss of freshwater ice (e.g., Pritchard et al., 2012). Marine-terminating glaciers on the WAP are accelerating (Cook et al., 2016), with the potential to raise global sea levels by 69 ± 5 mm (if all the ice were to melt; Huss and Farinotti, 2014). This is of similar magnitude to the potential contribution from Arctic Canada, and much greater than that from Alaska and Arctic Russia (Huss and Farinotti, 2012). Furthermore, the imbalance between upstream ice gain and downstream ice mass loss (through basal melting and iceberg calving) is causing thinning of the ice shelves (Rignot et al., 2013). Although melting of ice shelves does not directly contribute to sea level rise, thinning reduces their ability to buttress grounded glaciers (Dupont and Alley, 2005), causing these glaciers to accelerate and contribute to sea

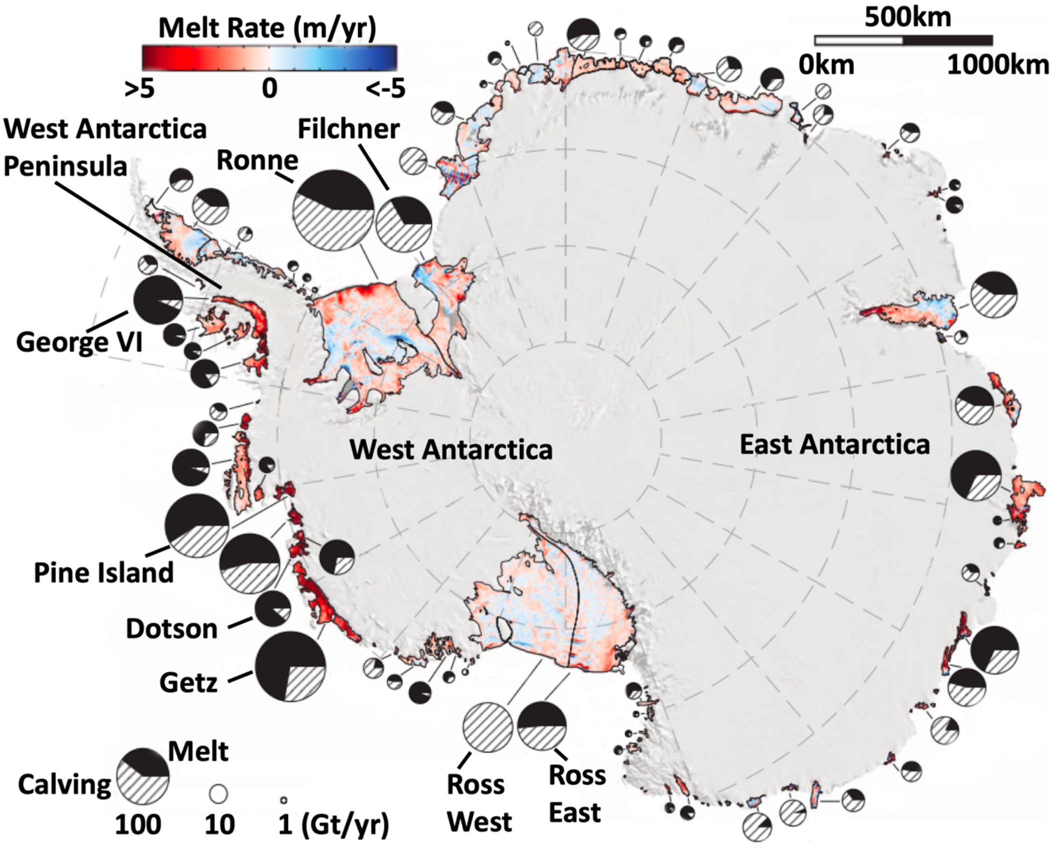

FIGURE 1.2: Basal ice shelf melt rates across Antarctica (after Rignot et al., 2013). Red and blue values are area-averaged melting and freezing rates respectively. Each circle is proportional to the ice mass loss (Gt yr^{-1}), and is divided into the contributions from iceberg calving (hatch fill) and basal melting (solid fill). Ice shelves mentioned in this article are labelled. Ice loss and basal melt rates were calculated by comparing the volume flux divergence, surface accumulations and thinning from model and satellite data.

level rise (Rott et al., 2002). This is particularly important in West Antarctica because these glaciers drain the West Antarctic Ice Sheet, which is grounded below sea-level, with the bedrock sloping downwards towards Antarctica's interior (e.g., Thomas, 1979; Fretwell et al., 2013). Consequently, the West Antarctic Ice Sheet is especially vulnerable to ocean-driven mass loss (Fretwell et al., 2013), and the melting of ice shelves in West Antarctica could lead to marine ice sheet instability; the rapid, irreversible migration of the grounding line towards the interior (e.g., Weertman, 1974). A collapse of the West Antarctic Ice Sheet through this mechanism has the potential to raise global sea levels by over 3 m (Bamber et al., 2009; Fretwell et al., 2013). Model simulations from the Thwaites Basin suggest this may have already begun (Joughin et al., 2014), leading to a complete disintegration on a millennial timescale (Feldmann and Levermann, 2015). Larour et al. (2017) suggest that such mass loss will change Earth's gravitational field, causing a local decrease in sea level, and enhancing global sea level rise elsewhere.

Across Antarctica, the thinning and retreat of ice shelves is strongly regional (Figure 1.2; Rignot et al., 2013). Ice shelves in the West Antarctic Sector, from the northern part of the George VI Ice Shelf to the western part of the Getz Ice Shelf in the southeast Pacific sector, experience melt rates of $\sim$ 5 m yr^{-1}. This region also has the largest amount of ice mass loss, with a large proportion being attributed to basal melting of the ice shelves (Figure 1.2; Rignot et al., 2013). The Pine Island Glacier Ice Shelf experiences the largest observable basal melt rates of $\sim$ 40 m yr^{-1} close to the grounding line (Rignot and Jacobs, 2002). With the Getz Ice Shelf producing $\sim$ 10% of Antarctica's meltwater alone (the largest source between 2003 $-$ 2008), the southeast Pacific sector accounts for 48% of Antarctica's total meltwater over only 8% of the total area (Rignot et al., 2013). These rates are very different to those found in East Antarctica, which generally experiences much lower melt rates, with average values close to zero, and in places, freezing of up to 5 m yr^{-1} (Rignot et al., 2013). The melt rates in the southeast Pacific sector also greatly contrast to those of the four largest ice shelves (Ross East, Ross West, Filchner and Ronne), which constitute 61% of the total ice shelf area in Antarctica but only produce 15% of the total meltwater (Rignot et al., 2013). The correlation between high ice mass loss and increased basal melt rates suggests that basal melting from the ocean is a significant driver of ice loss in West Antarctica (Depoorter et al., 2013). The shelf-ocean exchange and vertical mixing mechanisms controlling these high basal melt rates are explored in Section 1.4.2.

1.2.2 Sea Ice and its Role in Global Climate

Sea ice is a fundamental component of the polar regions. The formation of sea ice causes brine rejection, leads to an increase in salinity and can start convection. Conversely, the melting of sea ice leads to freshwater input, lowers salinity and increases stratification, thereby inhibiting vertical mixing. In the Arctic, winter sea ice expansion is limited by land, whilst in Antarctica, expansion is limited by the ACC (see Section 1.4.1). Sea ice can be categorised into thin (0.3 $-$ 2 m) first-year ice, which is typically flat, and does not survive the melt season, and thicker (2 $-$ 4 m) multi-year ice, which has topography and has survived at least one summer. Multi-year ice circulates in the central Arctic basin. Seasonal atmospheric heating causes dramatic variation in sea ice extent, with 2019 Arctic winter and summer extents of $\sim 15 \times 10^6$ km^2 and $\sim 4 \times 10^6$ km^2 (Perovich et al., 2020), and $\sim 20 \times 10^6$ km^2 and $\sim 3 \times 10^6$ km^2 in Antarctica (Reid et al., 2020). The future of Antarctic sea ice extent is uncertain, with positive trends observed until 2015 (Comiso et al., 2017) and a consistent drop below-average since 2016 (Turner et al., 2017). However, Arctic sea ice extent has decreased dramatically, reducing in all months of the year, with the largest reductions in September in the Chukchi Sea (Figure 1.3). The overall September monthly mean trend between 1979 $-$ 2018 was -12.8 ± 2.3% per decade (relative to the 1981 $-$ 2010 mean; Meredith et al., 2019).

The sea ice extent and its seasonal variation is important for global climate because it has a high albedo that efficiently reflects the incoming shortwave solar radiation, and it

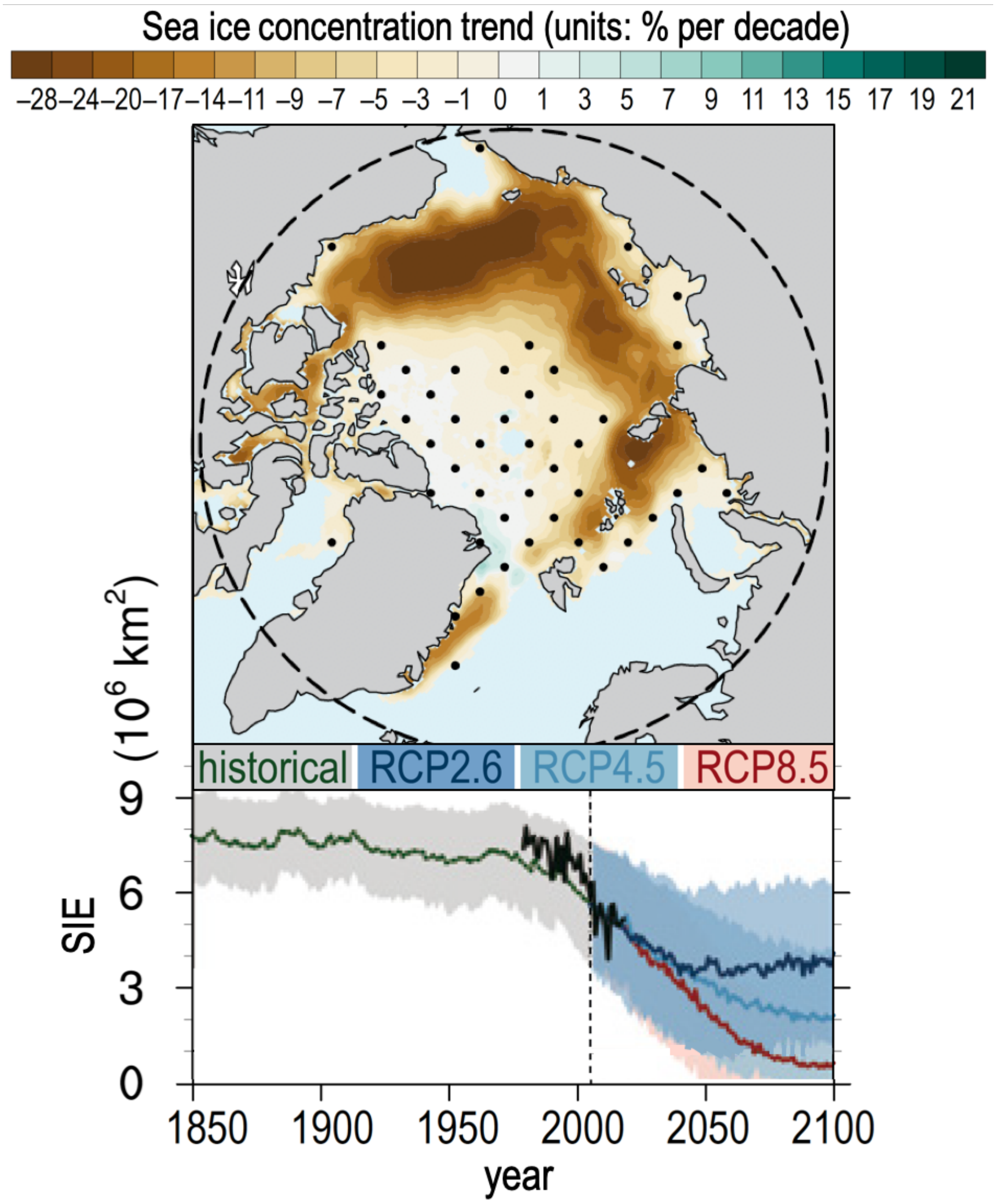

FIGURE 1.3: Decline in Arctic sea ice (after Meredith et al., 2019). (Top) Map showing linear sea ice trend for September, the month of minimum sea ice extent (SIE), between 1982 − 2017. Dotted regions indicate insignificant trends, dashed circle shows the Arctic Circle. (Bottom) Time series of September Arctic SIE. Black, green, blue, orange, and red curves indicate observations, Coupled Model Intercomparison Project Phase 5 historical simulation, Representative Concentration Pathway (RCP)2.6, RCP4.5, and RCP8.5 projections, respectively. Shaded regions are ± standard deviation of the multi-models.

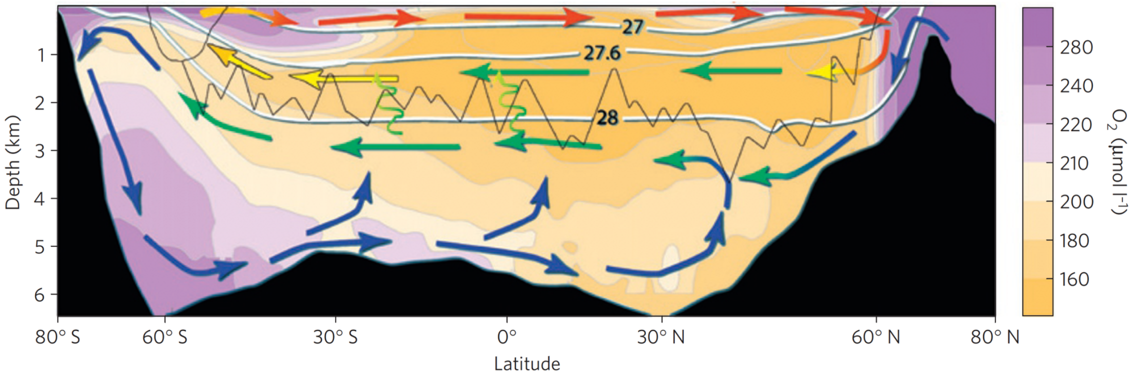

FIGURE 1.4: Schematic showing the upper and lower cells of the global Meridional Overturning Circulation (MOC; from Marshall and Speer, 2012). Arrow colours show approximate density of the different water masses: lighter mode and thermocline waters (red), upper deep waters (yellow), deep waters (green, including North Atlantic Deep Water) and bottom waters (blue, including Antarctic Bottom Water). Background colour represent zonally averaged oxygen distribution; purple (yellow) indicates high (low) oxygen, and are indicative of recently ventilated (old) waters. White lines are neutral density surfaces; 27.6 kg m^{-3} is the approximate divide between the upper and lower cells. Black line shows the rough depth of the Mid-Atlantic and Scotia Ridges, and the green squiggly lines represent vertical mixing associated with bathymetry. Note that this is a very simplified schematic; a more complete, three-dimensional version can be found in Marshall and Speer (2012), Box 1.

forms a physical barrier that modulates the amount of heat and momentum exchanged between the ocean and the atmosphere (Bourassa et al., 2013). Significant warming has been observed in the Arctic Ocean, and this has largely been attributed to a dramatic loss of sea ice in the shelf sea regions (Timmermans et al., 2020). Sea ice is therefore critical in controlling the heat budget of the polar oceans, disrupting the equator-to-pole temperature gradient, and altering global oceanic and atmospheric circulation (e.g., Ferrari et al., 2014; Deser et al., 2015). In Antarctica, sea ice is also believed to be important for protecting ice shelf calving fronts from strong ocean swells that might otherwise increase their rate of disintegration (Massom et al., 2018). In the Arctic, variations in sea ice extent are particularly important for local indigenous communities and ecosystems. For example, the recent dramatic decline in Arctic sea ice extent (e.g., Perovich et al., 2019) has lead to a reduction in food security (e.g, by impacting infrastructure such as ice roads) and protection against coastal erosion and the loss of permafrost (e.g., from sea ice; Cochran et al., 2013). Enhanced sea ice loss has also lead to increased spatial overlap between polar bears and ringed seals, which has significant implications for the predator-prey relationship and wider ecosystem dynamics (Hamilton et al., 2017).

1.2.3 The Meridional Overturning Circulation

The polar oceans are also important for Earth's ocean and climate system through the pivotal role they play in the global meridional overturning circulation (MOC; Marshall and Speer, 2012), which transports heat, freshwater, carbon and nutrients around the world's oceans. A simple model of the MOC has an upper and lower cell (Figure 1.4), and the connectivity of the Southern Ocean means the region has a central role in driving both of these. In particular, both vertical and horizontal mixing within the Southern Ocean is important for facilitating exchange between the MOC's upper and lower cells (Naveira Garabato et al., 2007). The lower cell is driven by formation of Antarctic Bottom Water (AABW) in the Southern Ocean's Weddell and Ross seas (Orsi et al., 2002). AABW is cold, dense water that forms through brine rejection during sea ice formation, and is subducted and transported northwards along the seafloor towards the north Atlantic. The upper cell is driven both by deep upwelling of this bottom water and downwelling North Atlantic Deep Water (NADW), which forms through cooling-induced buoyancy loss (Marshall and Speer, 2012). These waters move southward at depth, with significant forcing by strong westerly winds in the Southern Ocean. These winds cause Ekman upwelling of the deep waters, where they freshen and are advected northward through residual-mean transport; the residual between the northward wind-driven transport and the poleward eddy transport, where eddies form through baroclinic instability (see Section 1.3.2). The mixing processes in the Southern Ocean make the region disproportionately important in Earth's heat and carbon budgets, accounting for $\sim$ 75% of the global ocean heat uptake and $\sim$ 43% of anthropogenic carbon sequestration (Frölicher et al., 2015). Increased CO_2 uptake is leading to ocean acidification in both polar regions, causing corrosive conditions for organisms that form calcium carbonate shells, with implications for wider ecosystems (Sasse et al., 2015).

1.3 A Brief Background on Mixing

1.3.1 Introduction to Mixing

The previous section highlighted the important role Southern Ocean mixing has for Earth's ocean and climate system. Such mixing is a primary focus of this thesis, so it is therefore necessary to provide a brief background here.

Turbulent mixing is ultimately the mechanism through which the kinetic energy of a fluid is dissipated and converted to heat at the very smallest scales. In the ocean, vertical mixing of water occurs across density surfaces (diapycnal), acting to weaken density gradients (stratification). However, mixing can also occur horizontally along density surfaces (isopycnal), reducing horizontal pressure gradients. Turbulent mixing thereby weakens gradients in temperature and salinity, as well as tracers such as greenhouse gases, nutrients and carbon. A turbulent fluid is composed of many rotating parcels called eddies, which have a range of different sizes and velocities. Under the assumptions of stationary, homogeneous and isotropic turbulence (statistically unchanging in time and uniform in all directions), the velocity of an eddy (and therefore

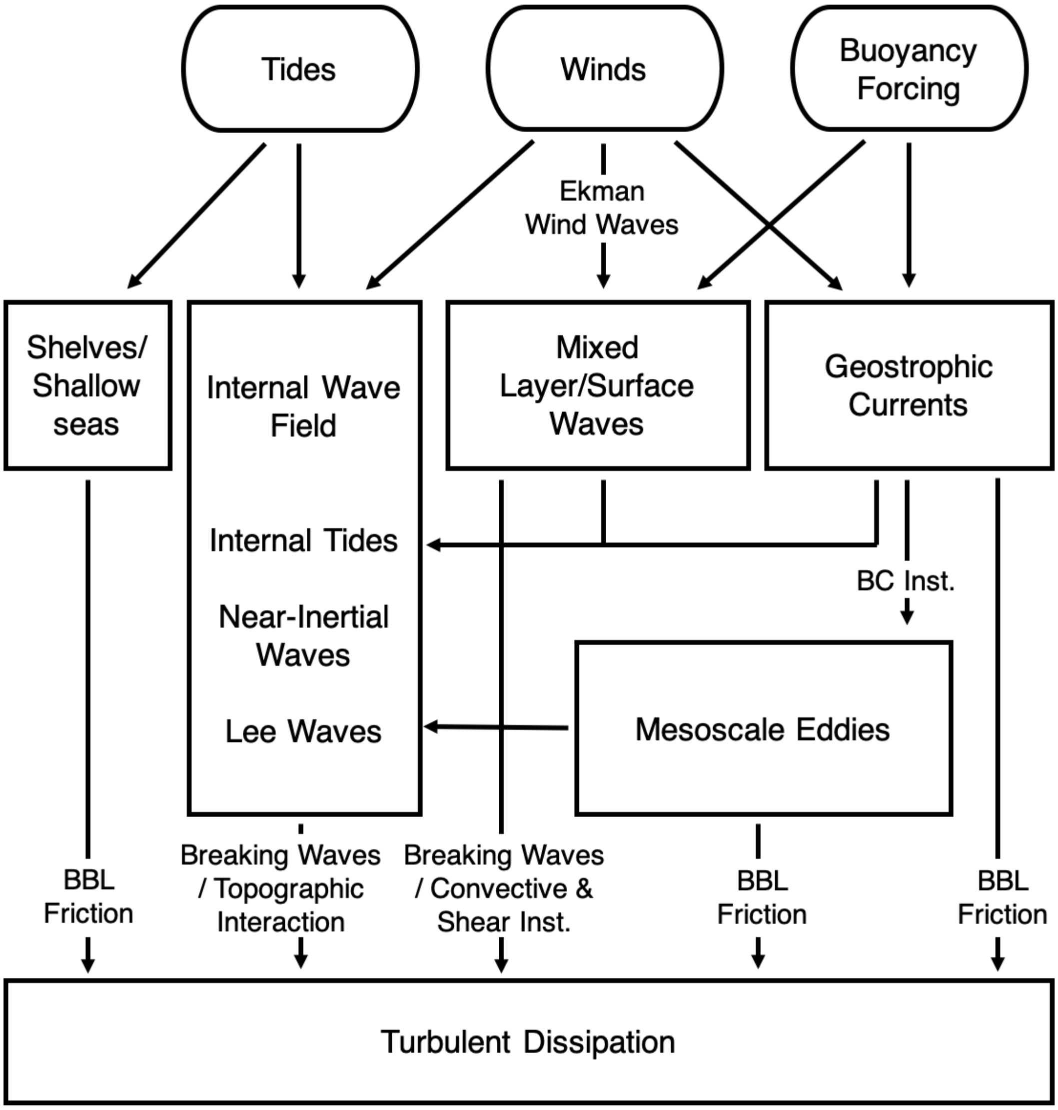

FIGURE 1.5: Schematic showing various energy transfer routes from sources to turbulent dissipation (adapted from Ferrari and Wunsch, 2009). Please note that this schematic does not contain all energy sources, reservoirs, pathways and sinks. Several processes are labelled, including Bottom Boundary Layer (BBL) friction and Baroclinic Instabilities (BC Inst.). The box sizes are not representative of a scale. For a more complete energy budget see Ferrari and Wunsch (2009) Figure S1.

its kinetic energy) is a function of its size. In the ocean, energy is provided to the largest eddies by surface buoyancy fluxes (e.g., surface cooling), winds and tides and geostrophic currents (where there is a balance between the horizontal pressure gradients and the Coriolis force). The large eddies provide energy to eddies of smaller and smaller scales, until reaching the scale at which viscosity becomes important and the energy is dissipated; this is known as the turbulent energy cascade. The scale at which dissipation occurs (typically lengths of mm to cms) is termed the Kolmogorov length scale, $l_K = (\nu^3/\epsilon)^{1/4}$, where ν is the fluid's kinematic viscosity (in seawater $\nu = 1 \times 10^{-6}$ m^2 s^{-1}) and ϵ is the rate of dissipation of turbulent kinetic energy (TKE), with units W kg^{-1} (e.g., Thorpe, 2005). The range of eddy length scales between l_K and the much larger energy-containing eddies is called the inertial subrange; the energy at these scales decreases rapidly, with a constant slope of $k^{-5/3}$ as wavenumber, k, increases (where $k = 2\pi/(\text{eddy diameter})$; Thorpe, 2005). Consequently, small-scale turbulent mixing provides a mechanism for closing the global ocean energy budget (e.g., Wunsch and Ferrari, 2004). Figure 1.5 is a very simplified schematic showing the major energy pathways of global ocean energy budget, from source to turbulent dissipation.

1.3.2 Processes of Turbulent Dissipation

Turbulent mixing arises from instability; the property of a steady state such that disturbances or perturbations grow to amplitudes larger than the initial perturbation. Instabilities occur across a wide range of scales, and there are many different processes that are important for their formation. Baroclinic instability is a type of mesoscale ($O(10-100)$ km) instability that is relevant to this thesis (and was mentioned in Section 1.2.3). Baroclinic instability is a mechanism that converts the potential energy of a geostrophic current into kinetic energy (Figure 1.5); such flows contain potential energy due to their sloping lateral density gradients. Unlike convective instabilities, which occur to individual particles instantaneously (see below), baroclinic instabilities require particles to act together and gradually manifest over time (Cushman-Roisin and Beckers, 2011). In order for baroclinic instabilities to develop, a number of conditions must be satisfied (Cushman-Roisin and Beckers, 2011), one of which is that the perturbation of the mean flow must be of the same scale as the internal Rossby Radius of deformation, r_r (the scale at which rotation becomes important):

$$r_r = \frac{NH}{f}\,, \tag{1.1}$$

where N is the buoyancy frequency, H is the water depth, and f is the Coriolis parameter. Perturbations on these scales can cause a slumping of the density gradients, and can generate large eddies. These eddies can then provide energy for the internal wave field (discussed below) and cause turbulent mixing through bottom boundary layer friction (e.g., Polzin, 2010). Baroclinic instabilities are actually an end member of mixed barotropic-baroclinic instability; baroclinic instabilities have no shear in the horizontal, whilst barotropic instabilities have no shear in the vertical (Cushman-Roisin and Beckers, 2011). Both baroclinic and barotropic instabilities are thought to be important in the polar oceans where strong boundary currents exist (e.g., Spall et al., 2008; Langlais et al., 2015; Brearley et al., 2019).

At the ocean's surface, turbulent dissipation is enhanced within a surface mixed layer of approximately uniform density. The global average mixed layer depth (MLD) is ~ 50

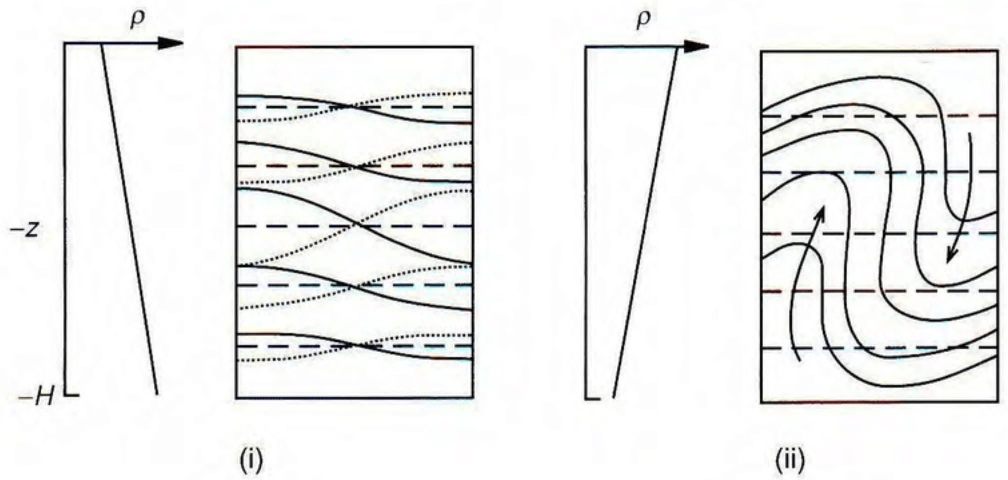

FIGURE 1.6: Statically stable (i) and statically unstable (ii) stratification (from Thorpe, 2005). Density increases and decreases linearly with depth in (i) and (ii) respectively. Dashed horizontal lines represent undisturbed isopycnals. Periodic disturbances in (i) are shown by solid and dotted lines, whilst solid lines and arrows in (ii) indicates a growing convective instability.

m, but MLDs can vary in density and depth, diurnally, seasonally and with latitude (Thorpe, 2005). The mixed layer is predominantly forced externally by surface buoyancy fluxes and wind stress (Figure 1.5). Surface cooling or salinification (for example through sea ice formation; see Section 1.2.2) can cause denser fluid to overly lighter fluid, resulting in convective instabilities where the buoyancy force acts to restore stable stratification, leading to turbulent mixing (Figure 1.6). Wind stress, τ_w, causes breaking waves on the ocean surface, with turbulence below (in the upper mixed layer) following the 'law of the wall'; ϵ having a log-normal distribution from the surface, scaling with depth and the friction velocity, $u_* = (\tau_w/\rho)^{1/2}$ (where ρ is the mixed layer density; Oakey, 1985; Thorpe, 2005). Within the mixed layer, the energy for turbulence comes from shear-instabilities, and at the base, by shear and breaking internal waves (see below).

In the ocean interior, internal waves are the primary cause of turbulent mixing (see Whalen et al., 2020, for a comprehensive review on internal wave-driven mixing), extracting their energy from winds, tides and geostrophic currents (Figure 1.5; e.g., D'Asaro, 1985; Klymak and Gregg, 2004; Fer et al., 2010). Both shear and convective instabilities can form from internal waves (Thorpe, 2018), extracting kinetic and potential energy from the wave respectively. Shear instabilities form between layers of different densities, where acceleration of the overlying layers of fluid produces a velocity difference with the underlying layers. The Kelvin-Helmholtz instability is an example of a shear-driven instability, where a pressure decrease causes the underlying layer to lift up and become entrained by the flow of the overlying layer. Kelvin-Helmholtz instabilities are found in a wide range of oceanic conditions and are thought to be an important mechanism for mixing, playing a key role in the development of breaking internal waves and the start of the downscale energy cascade (Smyth and Moum, 2012). Internal waves can interact with other internal waves (e.g., Olbers, 1976), topography (e.g., Legg and Adcroft, 2003) and currents (e.g., Kelly et al., 2016) to transfer energy to smaller scales. Close to the seafloor, internal wave-topographic interactions are the main driver of turbulent mixing. Across much of the world, turbulent mixing close to the seafloor is tidally-driven, where tides that flow over rough topography form breaking internal waves (termed internal tides) through the transfer of energy from barotropic to baroclinic motions (Stigebrandt, 1999). However, in the Southern Ocean, the ACC is so strong and deep-reaching that the dominant mechanism for turbulent mixing near the seafloor is through the breaking of internal lee waves that form when geostrophic currents flow over rough topography (e.g., Nikurashin and Ferrari, 2013; Sheen et al., 2013).

A mechanism that commonly causes small-scale convective instabilities in low-shear environments is double-diffusion, which occur because salinity has a lower rate of diffusion than temperature (Huppert and Turner, 1981). Two types of fluid displacement occur depending on which parameter is stably stratified; this is determined using the Turner Angle, Tu:

$$Tu = \tan^{-1}\left(\frac{\alpha\partial_z T + \beta\partial_z S}{\alpha\partial_z T - \beta\partial_z S}\right) \tag{1.2}$$

where α and β are the thermal expansion and haline contraction coefficients, and $\partial_z T$ and $\partial_z S$ are the vertical temperature and salinity gradients respectively (Ruddick, 1983). Double-diffusive convection occurs when the ocean is salinity-stratified and is destabilised by a vertical temperature gradient ($-90^\circ < Tu < -45^\circ$); this is typical of the polar regions where, cold, fresh melt water overlies warm, saline water. Thermohaline staircases, well mixed layers separated by sharp interfaces, are indicative of double-diffusive convection and are strongest when Tu is close to -90°. Thermohaline staircases are commonly observed in both the Arctic (Timmermans et al., 2008) and the Weddell Sea (Muench et al., 1990). When a temperature-stratified water column (warm, saline water overlying cold, fresh water) is destabilised by a salinity gradient ($45^\circ < Tu < 90^\circ$), the warm, saline water loses heat because it is surrounded by the cold, fresh water. Heat diffuses more quickly than salt, causing (cold) salt fingers to form downwards; this is typically found in tropical oceans.

1.3.3 Mixing Measurements

The purpose of this section is not to provide the equations used for calculating the dissipation of TKE (which are described in Section 2.1.4.4), but rather to give a background on the methods used to observe mixing. There are three main types of mixing observations: microstructure (mm to cm scales) measurements and tracer experiments provide

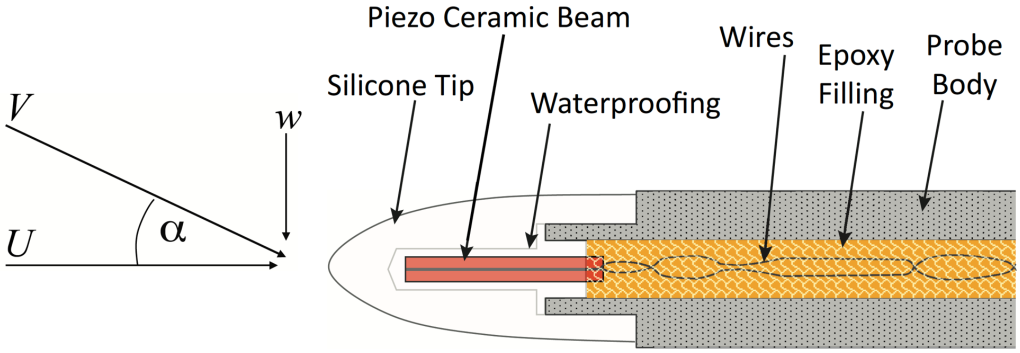

FIGURE 1.7: Schematic of an air-foil shear probe in a horizontal orientation (from Lueck, 2013). Here, V is the instantaneous speed, w is the cross-stream velocity fluctuation, U is the along-axis velocity, and α is the instantaneous angle of attack. The cross-stream velocity fluctuation is converted into a electric charge that is proportional to the net force exerted by the cross-stream flow.

direct (not-inferred) estimates of turbulent mixing, whilst finestructure (scales on the order of metres) measurements are used to obtain inferred estimates.

Given the small-scales over which turbulent dissipation occurs, recording direct estimates is not trivial. However, the invention of the air-foil shear probe (Figure 1.7) by Osborn (1974) enables microstructure measurements to be recorded in many environments, including those with low dissipation and strong temperature gradients (where previous methods could not). A shear probe contains a piezo-ceramic beam that detects velocity fluctuations perpendicular to the direction of travel. By sensing the net force exerted by the cross-stream flow, an electric charge is produced, which is later converted into shear data using the probe's velocity and calibration coefficients (Lueck and Picklo, 1990). Data from the shear probe is used to produce shear spectra, which are then fitted to an empirically derived Nasmyth spectrum that shows the expected shear variance as a function of wavenumber down to l_K (Nasmyth, 1970; Oakey, 1982). This is necessary because the size of the probe means that variance on scales as small as l_K cannot be resolved. The shear spectra are then integrated to obtain direct estimates of ϵ (see Chapter 2 for more details).

Traditionally, vertical microstructure profilers (VMPs) were the primary instruments used to obtain microstructure measurements; these are free-falling and generally fitted with two shear probes and two thermistor probes (the latter can be used as an independent, but inferred estimate of dissipation). However, data acquisition using VMPs can only take place one profile at a time. This mode of operation thus requires a ship, cannot be completed in bad weather, and is both time consuming and expensive. Recently, microstructure-equipped autonomous underwater vehicles (AUVs) have been developed, increasing the number of available measurements by an order of magnitude. Perhaps the most well-known vehicle is Autosub Long Range (popularly known

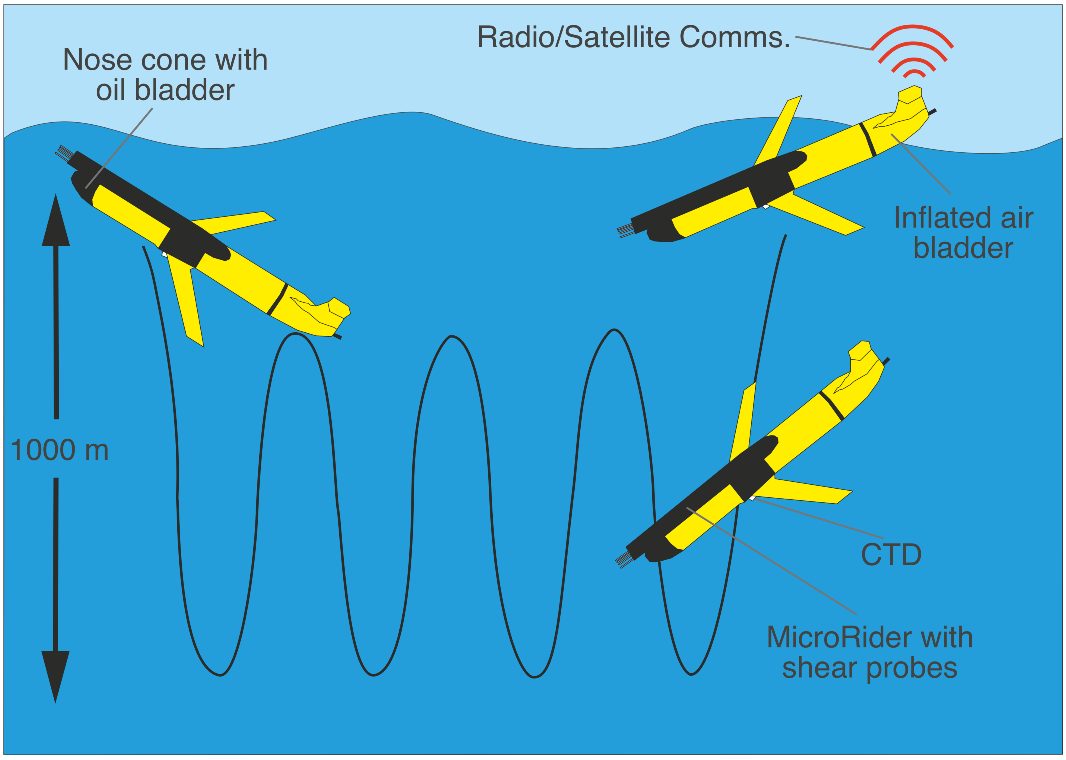

FIGURE 1.8: Schematic of a Teledyne Webb Research Slocum glider equipped with an Rockland Scientific Inc. MicroRider (microstructure package). All gliders are fitted with a conductivity-temperature-depth (CTD) sensor. Gliders typically have a maximum depth of 1000 m and travel in a saw-tooth pattern by pumping oil into and out of an oil bladder. At the surface the glider inflates an air bladder and communicates with the user using either radio or satellite communication.

as Boaty McBoatFace), which is propeller driven and can be deployed as deep as 6000 m for up to $\sim$ 20 days. The vehicles most relevant to this thesis are underwater gliders (Figure 1.8). These are buoyancy-driven vehicles that have a fixed mass but change their volume (and therefore buoyancy) by pumping oil into and out of a bladder that is half contained within the glider, but also occupies space external to the vehicle, within the glider's flooded nose cone. When oil is contained in the internal (external) portion of the bladder, the glider sinks (floats). The glider has a battery pack that moves forwards and backwards to shift the centre of gravity with respect to the centre of buoyancy, thereby pointing the nose down (up) during a dive (climb). This, together with the glider's wings, provides a horizontal component to the vertical buoyancy force, allowing the glider to move forwards. Consequently, the glider moves through the water column in a saw-tooth pattern. This mechanism of propulsion is very efficient, only using power to move when pumping oil at inflections, enabling the glider to conduction missions with durations on the order of months (depending on the sensors installed). Gliders either have a rudder or can rotate their batteries to steer, and typically have a depth rating of 1000 m, though 6000 m gliders are now being developed. At the surface gliders raise their tails out of the water (some models have an air bladder to do help facilitate this), enabling either radio or satellite communication. Gliders can send packets of data and also receive new mission coordinates and objectives.

Tracer experiments involve measuring the concentration of substances that are conserved during advection and mixing, enabling the history of the fluid to be tracked from a known source. Tracers can be naturally occurring, such as ^{3}Helium, which is released from hydrothermal vents (e.g., Naveira Garabato et al., 2007), however, typically radioactive substances (^{14}C) or chemical tracers (e.g., CF_3SF_5) are purposefully released at specific density surfaces. Crucially, the substances need to be detectable even in low concentrations and have a lifespan that is longer than the process being studied. By measuring the vertical and horizontal extents of the tracer distribution as it evolves, spatially and temporally averaged direct vertical and horizontal mixing rates can be obtained. Whilst the averaging means it is hard to study smaller scale mixing processes, tracer experiments provide a more statistically-robust estimate than instantaneous microstructure measurements. They are particularly useful for budget calculations, and have been used to identify regions of enhanced diapycnal and isopycnal mixing (Ledwell et al., 1993; Mackay et al., 2018).

Finestructure measurements from both conductivity-temperature-depth (CTD) and acoustic Doppler current profiler (ADCP; measures water velocity) sensors provide multiple methods for obtaining inferred estimates of the dissipation of TKE. One method involves reordering density profile inversions so that density monotonically increases downwards. The root mean square of the vertical displacements required to produce a stable profile gives the Thorpe Scale, which is used in conjunction with the buoyancy frequency to estimate ϵ. This requires deploying the CTD slowly with little change in vertical acceleration. Another method is a parameterisation based on wave-wave interaction theory (Gregg et al., 2003). ADCP and CTD data can be used to generate shear and strain spectra respectively (e.g., Kunze et al., 2006). Individually these can be used to estimate vertical mixing, but together, through the calculation of a shear/strain ratio, estimates of ϵ can be slightly improved. ϵ estimates derived using these methods assume that all of the energy at finestructure scales cascades down to dissipative scales, which is not always the case, particularly around ocean boundaries (i.e., continental slopes and shelves). Consequently, whilst finestructure measurements are useful because CTD and ADCP data are widely available, ϵ estimates are not as accurate as those obtained from microstructure data.

1.4 The Southern Ocean

1.4.1 Large-Scale Circulation

The ACC dominates Southern Ocean circulation and is the largest current in the world (Figure 1.9). Continuous around the pole, the ACC connects all of the major oceans and is fundamental to the MOC (described in Section 1.2). Facilitated by this connectivity, in the mid-layers of the ACC forms the Southern Ocean's most voluminous water mass: warm, saline Circumpolar Deep Water (CDW). CDW is created through heavy mixing of North Atlantic Deep Water with water masses from the other oceans (e.g., Santoso et al., 2006). CDW has Upper (UCDW) and Lower (LCDW) constituents, which are distinguished by temperature (UCDW) and salinity (LCDW) maximum, respectively (Gordon, 1971). The ACC's southern boundary is defined as the southernmost extent of the UCDW (Orsi et al., 1995). For future reference, note the close proximity of the ACC's southern boundary to the continental shelfbreak along the WAP. Three deep fronts account for most of the ACC's transport and can be traced, unbroken around Antarctica: the Subantarctic Front, the Polar Front, and the Southern ACC Front (Orsi et al., 1995). The ACC is primarily forced by strong westerly winds, which are characteristic of the Southern Ocean (Nowlin Jr. and Klinck, 1986). Original estimates of the total volume transport across Drake Passage were $\sim$ 134 Sv (Whitworth III and Peterson, 1985, where 1 Sv $= 1 \times 10^6$ m^3 s^{-1}), however, more recent estimates of the full depth ($\sim$ 3500 m) transport are 30% larger at 173 Sv (Donohue et al., 2016).

Additional large-scale circulation features in the Southern Ocean include the Weddell and Ross Gyres (orange and yellow lines, respectively; Figure 1.9). These gyres are regions of deep, coherent cyclonic rotation south of the ACC. Both gyres are steered by bathymetry and are primarily driven by wind forcing (e.g., Armitage et al., 2018; Dotto et al., 2018). These gyres have important roles for sea ice formation and thickness, AABW formation and variability, global ocean circulation, the vertical exchange of heat and carbon between the ocean and atmosphere, and the fate of the Antarctic Ice Sheet (e.g., Bebieva and Speer, 2019; Jullion et al., 2010; Vernet et al., 2019).

Figure 1.9 also shows the Antarctic Slope Current (ASC; red line), which circulates westward along the continental shelfbreak, regulating the flow towards the coast (Jacobs, 1991). The ASC surrounds the majority of the Antarctic continent and is driven by strong, persistent easterly winds in large portions of East Antarctica and in the western Amundsen / eastern Ross seas, and by the export of dense shelf water downstream of its formation region (Thompson et al., 2018). The easterlies cause Ekman downwelling, which deepens isopycnals and helps to establish the Antarctic Slope Front (ASF), the barrier between warm, saline CDW and cold, fresh shelf water (Jacobs, 1991). The current therefore responds to changes in both local wind stresses (Stewart and Thompson, 2015) and large scale climatic variability (Spence et al., 2014). The ASC is not circumpolar, diminishing on the WAP and in the Bellingshausen and Amundsen Seas. This is attributed to the close proximity of the shelfbreak with the ACC (which strongly flows north-eastward - the opposite direction to the ASC), the Amundsen Sea and Bellingshausen Sea lows (low pressure centres that impart weaker and more variable wind forcing; Turner et al., 2013), and the lack of dense shelf water formation (Thompson et al., 2018).

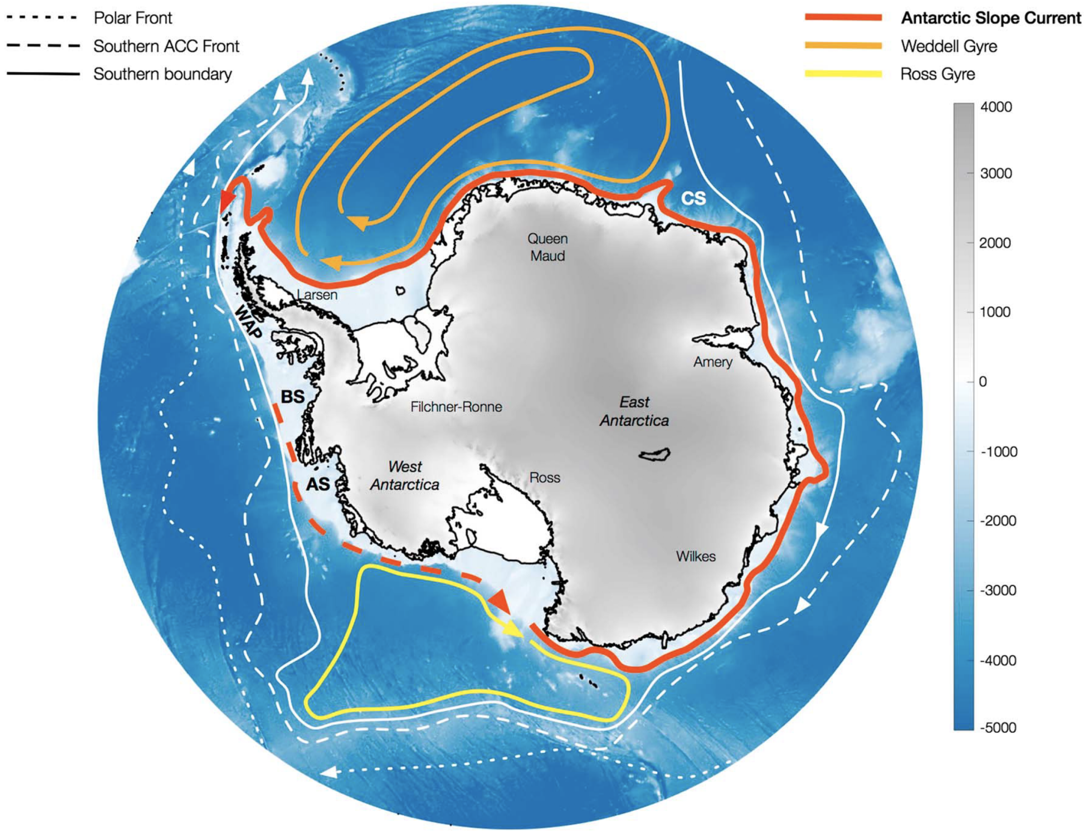

FIGURE 1.9: A schematic of Southern Ocean circulation around Antarctica (from Thompson et al., 2018). The Antarctic Circumpolar Current (ACC) fronts and southern boundary are indicated using dashed and solid white lines, respectively (from Orsi et al., 1995). The cyclonic Weddell (orange line) and Ross (yellow line) gyres (from Armitage et al., 2018), and Antarctic Slope Current (ASC; red line; along 1000-m isobath) are also shown. Red dashed line in Bellingshausen and Amundsen Seas (BS, AS) represents uncertainty in ASC initiation. Colour shows topography; depth for ocean and elevation for ice shelves and ice sheets (from Schaffer et al., 2016).

The close proximity of the ACC's southern boundary (and therefore CDW) to the continental shelfbreak on the WAP and in the Bellingshausen and northern Amundsen seas, is the fundamental reason why Antarctica's southeast Pacific sector has experienced the highest ice shelf mass loss and basal melt rates (discussed in Section 1.2). CTD profiles taken in Pine Island Bay in 1994, 2000, 2007 and 2009 (Jacobs et al., 2011), show a southwards intrusion of warm CDW above the seafloor, extending onto the continental shelf and beneath the Pine Island Glacier Ice Shelf. The thermocline warmed ~ 0.45 °C between $2007 - 2009$, and has shoaled everywhere since 1994, indicating an increase in CDW temperature and volume (Jacobs et al., 2011). These changes alone are probably inadequate for the extremely high observed basal melt rates, however, local geometry under the ice shelf could enhance the melting by creating a positive feedback: warm CDW flowing over a sub-shelf ridge (Figure 1.10) could produce cold, buoyant meltwater that exits over the ridge. This could lead to upwelling of CDW, increasing sub-shelf circulation, resulting in more melting (Jacobs et al., 2011).

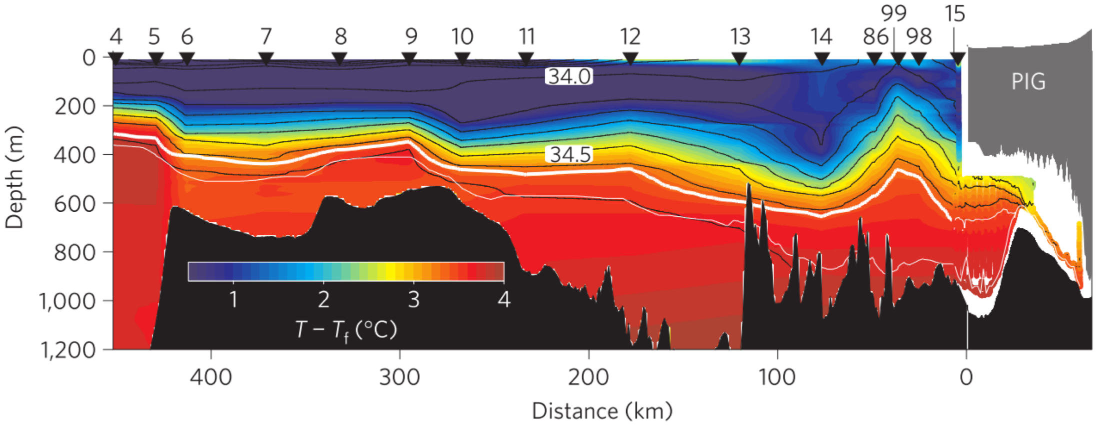

FIGURE 1.10: Intrusion of CDW at Pine Island Glacier Ice Shelf in 2009 (from Jacobs et al., 2011). Black lines represent salinity contours. Thick and thin white lines show the potential temperature maximum, and the 27.75 kg m^{-3} surface referenced potential density isopycnal, respectively. Colours represent temperature of the water relative to the in situ freezing temperature.

The intrusion of CDW onto the continental shelf is observed elsewhere in West Antarctica (Arneborg et al., 2012; Pritchard et al., 2012). For example, hydrographic and ADCP velocity measurements have been used to examine the inflow of warm CDW through a channel leading to the Getz and Dotson Ice Shelves (Wåhlin et al., 2010). These are regions where the ACC closely follows the continental shelfbreak, promoting the exchange of CDW onto and across the continental shelf, and providing a source of heat to the base of the ice shelves. By contrast, CTD data in regions like the Weddell Sea (Nicholls et al., 2009) reveal cold shelf waters with little sign of CDW, and the majority of the water close to the ice front being close to the in situ freezing point. The spatial coverage of CDW therefore correlates well with the ACC's spatial distribution (Figure 1.9). In the Weddell and Ross seas, where the ACC is the furthest from the shelfbreak, and in much of East Antarctica, where the ACC is generally $>$ 250 km from the shelfbreak, it is more difficult for CDW to access and cross the continental shelves. This suggests that CDW is the primary cause of basal melting in Antarctica, but what are the shelf-ocean exchange and mixing mechanisms that are transporting CDW onto and across the shelf?

1.4.2 Shelf-Ocean Exchange: Poleward Flux of Circumpolar Deep Water

1.4.2.1 Advection Through Troughs

One way CDW can reach the base of the ice shelves is advection through glacially-carved troughs that cut across the continental shelf (e.g., Klinck et al., 2004; Moffat et al., 2009; Wåhlin et al., 2010; Arneborg et al., 2012). UCDW and LCDW on the WAP have temperatures and salinities between approximately 1.7 – 2.0 °C and 1.0 – 1.5 °C, and

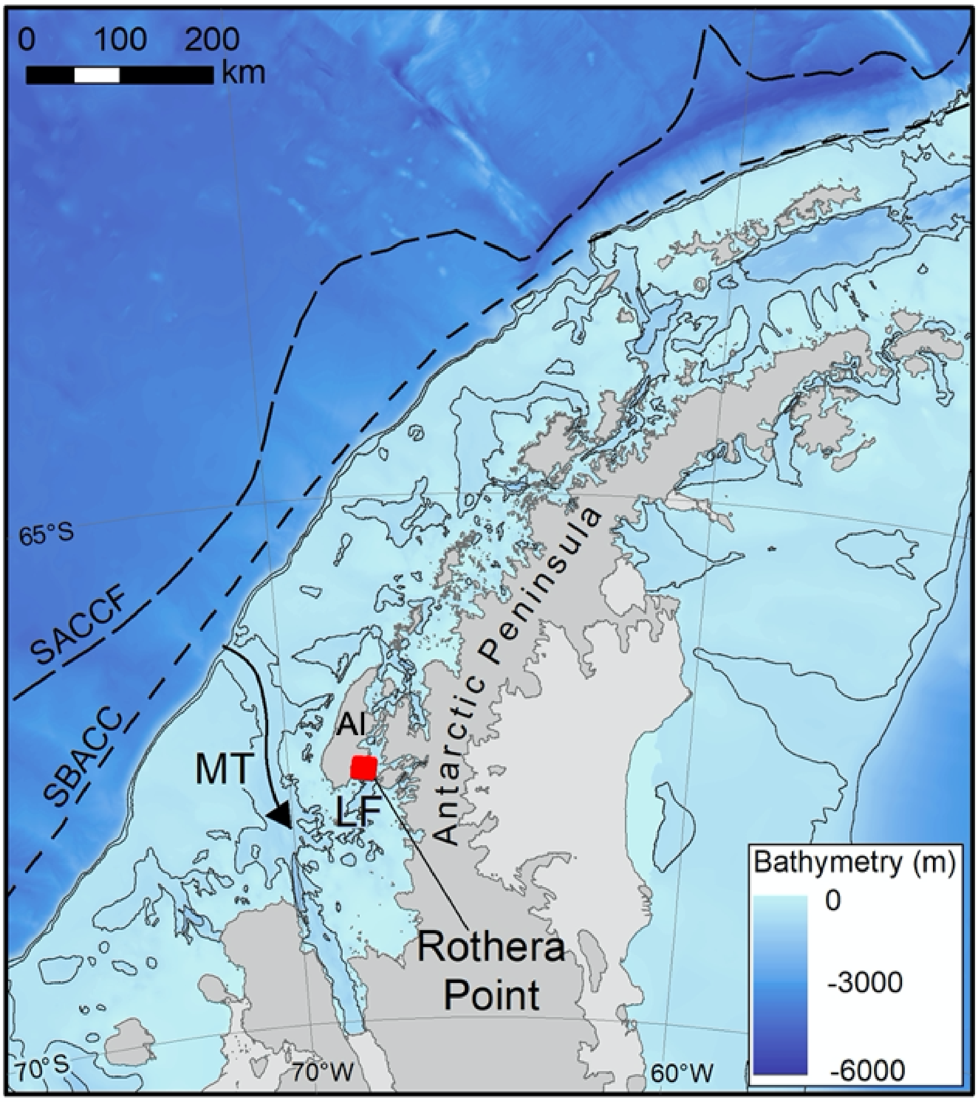

FIGURE 1.11: Bathymetry of the West Antarctic Peninsula (WAP; Gerrish, L. J., personal comms., August, 2020). Schematic black arrow in Marguerite Trough (MT) represents advection of circumpolar deep water. Location of Rothera Point on the WAP. Rothera Point is the location of Rothera Research Station, and is adjacent to Ryder Bay. Adelaide Island (AI) and Laubeuf Fjord (LF) are also indicated. 500 m and 1000 m isobaths from the International Bathymetric Chart of the Southern Ocean (IBCSO) are shown. Dashed black lines indicate the Southern Antarctic Circumpolar Current Front (SACCF) and Southern Boundary of the ACC (SBACC) from Orsi et al. (1995).

34.55 − 34.72 and 34.70 − 34.74 PSU respectively (Klinck et al., 2004). Whilst UCDW is relatively light and can be fluxed onto the shelf via multiple processes (see following sections), LCDW is typically too dense to be fluxed onto the shelf. However, numerous deep troughs (typically $>$ 300 m) were formed by ice streams that extended to the shelfbreak during the Last Glacial Maximum when sea level was lower (Livingstone et al., 2012). These troughs therefore provide a pathway for LCDW to be transported towards the coast. Marguerite Trough is one example of such a glacially-carved feature on the WAP, extending from the shelfbreak to the George VI Ice Shelf, with a maximum depth of 1440 m (Livingstone et al., 2013). Marguerite Trough therefore provides an access route for LCDW to flow onto the shelf (Figure 1.11; Klinck et al., 2004; Martinson et al., 2008). LCDW is found in other deep canyons along the WAP shelfbreak (Moffat et al., 2009), and mooring data in the western Amundsen Sea trough reveals a persistent flow of LCDW towards the ice shelves during 2010 (Arneborg et al., 2012) and 2011 (Wåhlin et al., 2013). There is a strong correlation between rapid ice shelf thinning (e.g., at the Pine Island Glacier Ice Shelf) and close proximity to deep submarine canyons; the ice shelves that are not close to deep bathymetric troughs are not thinning at high rates (Pritchard et al., 2012).

Episodic diversions of the ACC by momentum advection may have an important role in transporting CDW through these canyons (Dinniman and Klinck, 2004). If the ACC's along-slope flow is strong enough, a seaward curvature in the shelfbreak may stop the flow bending with the topography and force it into the trough (Dinniman and Klinck, 2004). In order to get sufficient CDW inflow, the general shelf circulation is then required to pull the CDW across the shelf (Dinniman and Klinck, 2004). A correlation between along-shelf velocity and on-shelf heat content has been modelled for Marguerite Trough (Dinniman and Klinck, 2004; Dinniman et al., 2011; Graham et al., 2016; St-Laurent et al., 2013), and is observed (to some extent) in the mooring data (Martinson and McKee, 2012). Increases in the strength of the along-shelf current and therefore heat transport have been associated with increased north-eastward wind stress (Dinniman et al., 2011; Graham et al., 2016).

1.4.2.2 Wind-Driven Upwelling

As mentioned above, the ASF can act as a barrier to the inflow of CDW onto the shelf (Jacobs, 1991), however, along the WAP, Bellingshausen and Amundsen Seas, the ASF is not distinguishable and CDW intrudes onto the continental shelf (Stewart and Thompson, 2015). This could be explained through upwelling of CDW onto the continental shelf (Martinson et al., 2008). In order for upwelling to occur, south westerly winds are required to drive the surface waters offshore via Ekman transport, inducing a flow of CDW onshore by mass continuity (Martinson and McKee, 2012). However, the prevailing easterly coastal winds on the WAP shelf, and the shelf depth of $\sim$ 450 m, are not optimal conditions for causing the required amount of Ekman suction (Klinck and Dinniman, 2010); onshore flow of CDW on the shelf by mass continuity therefore does not typically occur.

The Palmer Long Term Ecological Research (LTER) shipboard CTD data, collected in the WAP region in January from $1993 - 2004$, shows a strong positive correlation between an increase in ocean heat content and elevated pycnoclines (which is a proxy for upwelling; Martinson and McKee, 2012). This suggests that increased upwelling could be a contributor to the increased heat content, however, a poleward shift in westerly

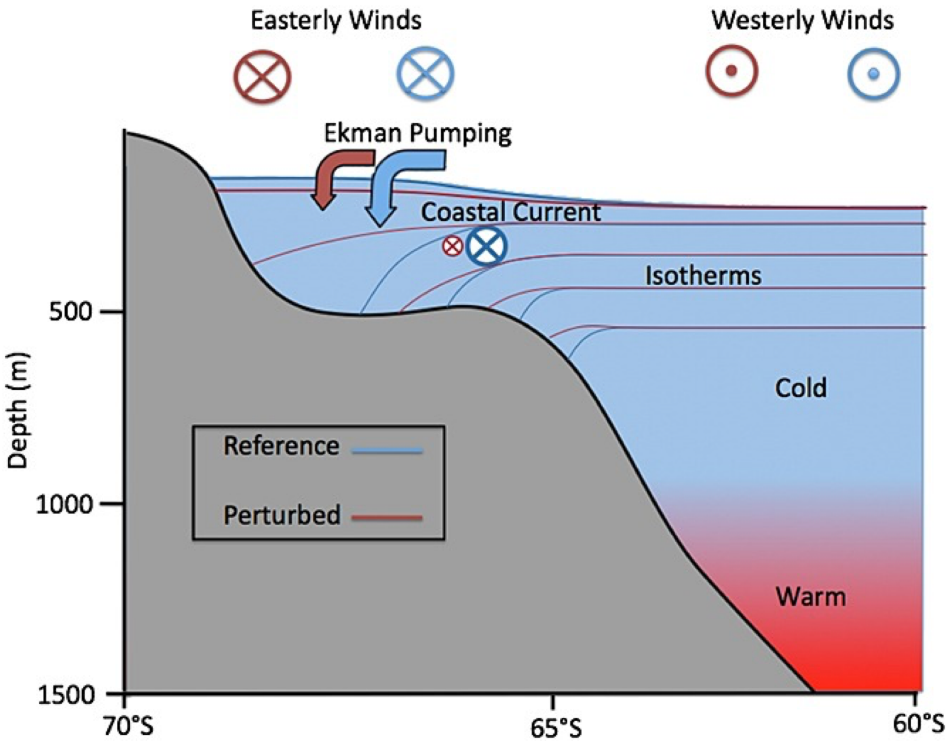

FIGURE 1.12: Schematic diagram showing upwelling of CDW due to poleward shift in westerly winds (from Spence et al., 2014). Before and after positions of the winds, Ekman pumping (arrows) and coastal currents are shown in blue and red respectively. Isopycnals are generally well aligned with isotherms.

winds would be required (Figure 1.12). This could cause a weakening of the Antarctic easterlies, decreasing the coastal Ekman downwelling and increasing the offshore Ekman transport, reducing the sea level (Nicholls et al., 2009). This flattens the isopycnals, weakens the coastal current and the ASF, and results in an influx of CDW (Nicholls et al., 2009). Additionally, rather than upwelling, the observed correlation between heat content and elevated pycnoclines could also be attributed to stretching and squeezing of the CDW layer caused by the passing of eddies (Martinson and McKee, 2012).

The 2010 – 2011 mooring data from the western Amundsen Sea trough (Arneborg et al., 2012; Wåhlin et al., 2013), shows a high correlation between horizontal fluctuations in the along trough velocity and local wind stress changes; with eastward winds producing a persistent flow of CDW towards the ice shelves. This correlation is clearly seen when assessing the change in Amundsen Sea Embayment wind stress between 1990 – 99 (Figure 1.13a) and 1980 – 89 (Figure 1.13b; Steig et al., 2012), and comparing it to the CDW layer thickness change between 1990 – 99 (Figure 1.13c) and 1980 – 89 (Figure 1.13d; Thoma et al., 2008). The maximum westerly wind stress is consistently in winter and spring and more than doubles in autumn (Figure 1.13a-b). There is a consistent lag of 1 – 3 months between the max wind stress and the max thickness of CDW on the inner shelf. A similar lag (2.5 months) is observed between the maximum

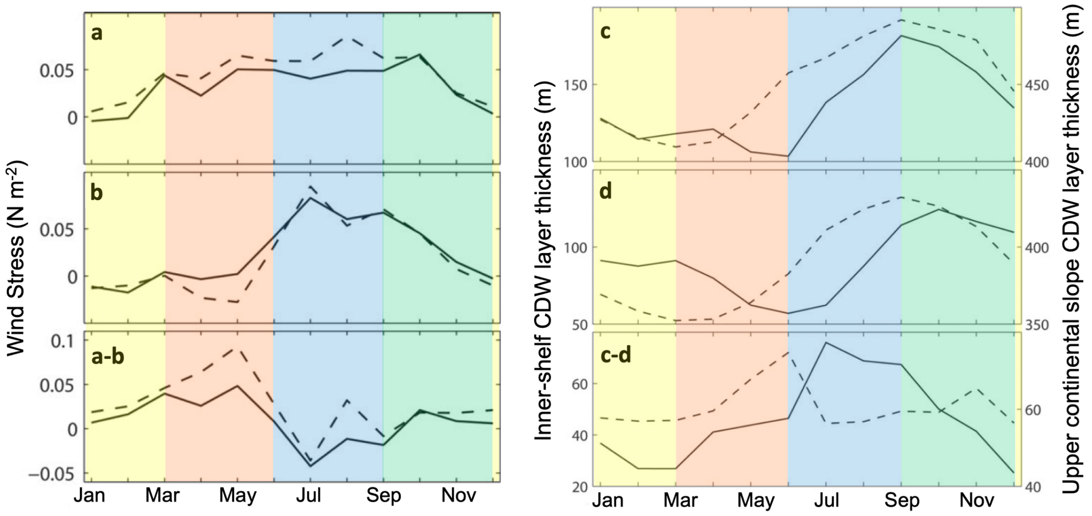

FIGURE 1.13: Relationship between westerly wind stress and CDW layer thickness (after Steig et al., 2012). NCEP2 (dashed lines) and ERA-40 (solid lines) wind stress reanalysis data, from 1990 – 99 (a), 1980 – 89 (b), and their difference (a-b). Positive values are westerly winds. Thickness of the CDW on the continental slope (dashed lines) and the inner-shelf (solid lines; from Thoma et al., 2008), from 1990 – 99 (c), 1980 – 89 (d), and their difference (c-d). The left and right hand scales correlate with the inner and outer slopes respectively. Yellow, pink, blue and green colours represent summer, autumn, winter and spring seasons respectively.

change in wind stress over the continental slope and the maximum change in inner-shelf CDW thickness (Figure 1.13c-d), suggesting that the wind stress enhances CDW inflow (Steig et al., 2012).

Large-scale atmospheric circulation can influence local and regional wind stress variability and therefore the shoreward transport of CDW to the base of the ice shelves and marine terminating glaciers. Two climate modes that are particularly important for Antarctica are the Southern Annual Mode (SAM) and El Niño-Southern Oscillation (ENSO). The SAM describes the north-south movement of a belt of westerly winds or low pressure surrounding Antarctica (Turner et al., 2005); with westerly winds strengthening and moving further south in a positive phase. ENSO is a climate driver in the tropical Pacific that fluctuates between 3 phases: La Niña (negative phase), where strong easterly trade winds cause cooling of Sea Surface Temperatures (SSTs) in the central Pacific; El Niño (positive phase), where the trade winds weaken or reverse, causing warming of tropical SSTs; and a neutral phase between the two extremes. In an El Niño phase, anomalously high SSTs in the central Pacific can force increased tropical convection, causing a poleward-propagating atmospheric Rossby wave response (meandering of high-altitude winds) towards the Amundsen Sea, increasing westerly wind stress (Steig et al., 2012). The interplay between the SAM and ENSO can influence the spatial distribution of the wind stress, with a positive ENSO and SAM potentially doubling the wind anomalies (Langlais et al., 2015). With SAM being in an increasingly positive phase over the last $\sim$ 30 years (Turner et al., 2005) and tropical SSTs potentially being enhanced by anthropogenic radiative forcing, these processes could play an important role for flow of CDW through troughs, the location of Ekman pumping, and the generation of eddies.

1.4.2.3 Eddies

Eddies originating in the ACC are another possible mechanism that could move CDW across the continental shelf and bring it into contact with the ice shelves (Moffat et al., 2009; Martinson and McKee, 2012). Hydrographic and current velocity observations from $2001 - 2003$ show that $\sim$ 4 km wide anticyclonic eddies of UCDW were present within Marguerite Trough approximately four times per month (Moffat et al., 2009). Two mooring stations, one located on the north eastern edge of Marguerite Trough close to the shelfbreak, and a second on a fork in the northern side of the trough, support this observation (Martinson and McKee, 2012). At the first of these moorings a Rossby Radius of $\sim$ 5 km was calculated, and at the second eddies with radii of $\sim 3 - 5$ km were observed (Martinson and McKee, 2012). These similarities, together with rises in heat content in the trough coinciding with mid-depth boluses, suggest that the boluses can be attributed to bathymetric steered, warm core eddies originating in the ACC (Martinson and McKee, 2012; St-Laurent et al., 2013). Gliders deployed on the WAP shelf during the austral summers of $2010 - 2013$ also support this observation, finding 33, $\sim$ 10 km wide subsurface eddies containing UCDW, with those found along the northern wall of Marguerite Trough potentially contributing to $20 - 53\%$ of the lateral onshore heat flux to the WAP (Couto et al., 2017).

A comparison of 4 km and 1.5 km resolution models of the Belgica and Marguerite Troughs illustrates the importance of eddies in transporting heat onto the shelf (Graham et al., 2016). The 1.5 km model shows larger on-shelf heat transport, which is attributed to increased eddy activity. At the Belgica Trough this is represented by a larger volume transport (i.e. more or larger eddies), whereas at the Marguerite Trough, the temperature of the water being fluxed onto the shelf is higher, possibly due to increased off-shelf eddy activity that ensures the availability of heat for transport onto the shelf via momentum advection (as described in Section 1.4.2.1; Graham et al., 2016).

The dominant eddy formation mechanisms are yet to be determined, however, the leading suggestions are through instabilities in the ACC and at the shelfbreak. For example, the number of eddies could be controlled by the ACC's state. In an eddy saturated state, where wind increases do not alter the ACC's transport but increase its eddy kinetic energy (Hogg et al., 2008), strengthened northward Ekman transport can increase the tilt of the isopyncals. This increases the potential energy, which then is converted to eddy kinetic energy through baroclinic instability (Langlais et al., 2015); the eddy activity counteracts the temporarily enhanced isopycnal tilt. Hogg et al. (2015) suggest that through this mechanism, increasing winds have led to an observed increase in eddy kinetic energy in recent decades.

The Southern ACC Front is known to be baroclinically unstable and interactions with topographic features such as ridges at the base of the continental slope (Klinck and Dinniman, 2010) and across-shelf troughs (St-Laurent et al., 2013), can perturb the flow, creating eddies at specific locations. Brearley et al. (2019) recently showed evidence of an instability-driven eddy field, finding both baroclinic and barotropic instabilities in the open ocean near the mouth of Marguerite Trough, with the latter dominating on the shelf slopes. This suggests that the presence of the slope can suppress baroclinic instabilities, supporting Reszka and Swaters (1999); they find that topography sloping in the same direction as a front tends to stabilise the water column, whilst topography in the opposite sense tends to promote baroclinic instability. Brearley et al. (2019) also highlight the importance of flow-topographic interactions, observing a quasi-stationary eddy at the mouth of Marguerite Trough, which is believed to form as the boundary current meanders around a bank; this can detach from the boundary current and propagate into the ACC, thereby facilitating shelf-ocean exchange. Additionally, Rossby waves can propagate along the shelfbreak and interact with such topographic features, generating eddies similar to those observed in Marguerite Trough (Zhang et al., 2011; St-Laurent et al., 2013).

1.4.3 On-Shelf Modification of Circumpolar Deep Water

The section above describes how direct inflow through cross-shelf troughs, shedding of eddies from the ACC, and Ekman-induced upwelling, are all thought to be important in conveying CDW onto the shelf (e.g., Arneborg et al., 2012; Moffat et al., 2009; Martinson and McKee, 2012). However, what happens to the CDW once it is on the shelf? The fate of the CDW heat is controlled by spatially and temporally varying processes (Martinson et al., 2008), such as advection, vertical and horizontal mixing, and heat exchange between the ocean and the atmosphere (Turner et al., 2013). These processes define the components of the WAP oceanic heat budget (Figure 1.14; Moffat and Meredith, 2018).

The WAP heat budget remains poorly constrained, mainly due to a lack of measurements of horizontal and vertical mixing (and corresponding heat flux) in the partially ice-covered ocean. However, several studies have produced indirect estimates of various components of the system. Howard et al. (2004) used a Richardson number-based parameterisation to infer vertical diffusivities of $< 1 \times 10^{-5}$ m^2 s^{-1} from CTD and ADCP data in Marguerite Bay, south of Adelaide Island (Figure 1.11), with an associated upward heat flux of < 2 W m^{-2}. Similarly small upward heat fluxes of ~ 1 W m^{-2} were inferred in Ryder Bay, on the southeast coast of Adelaide Island, using a finescale parameterisation applied to CTD and ADCP data (Brearley et al., 2017). However, as

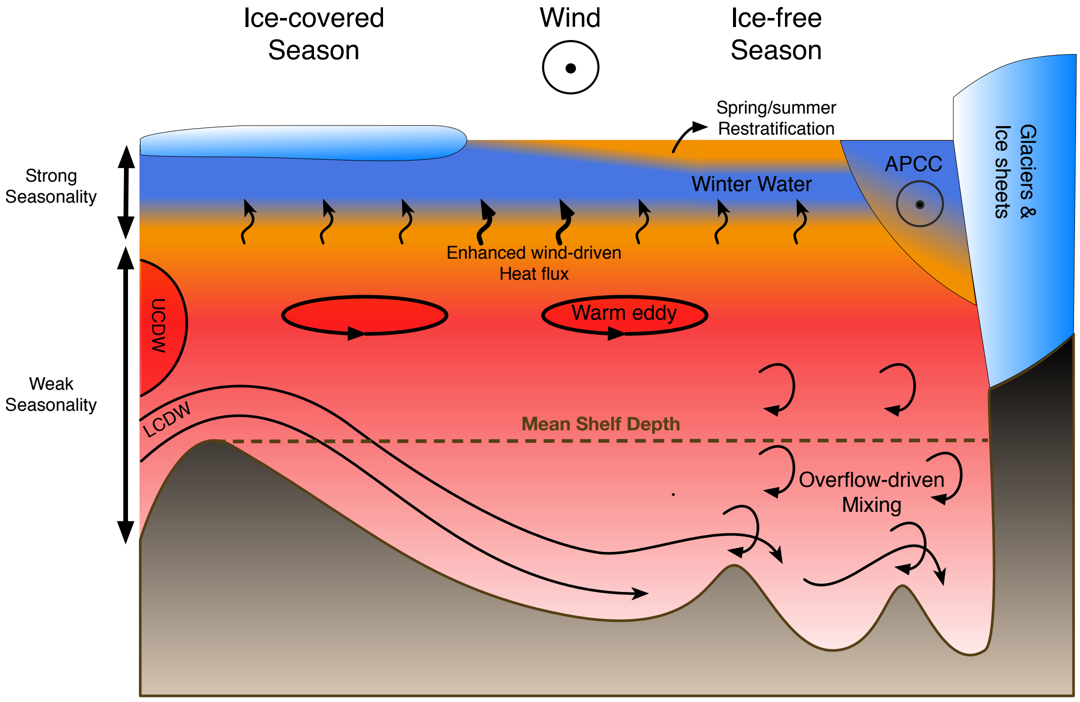

FIGURE 1.14: Schematic showing the major features of the West Antarctic Peninsula heat budget (from Moffat and Meredith, 2018). At the surface there is strong seasonal variation; wind-driven vertical mixing and heat flux between CDW and the overlying Winter Water is enhanced in the period between the break up of fast-ice and before increased stratification due to atmospheric warming. Warm UCDW is advected from the ACC across the shelf towards ice at the coast via mean flow and eddies. LCDW is advected through deep canyons, with flow interacting with topography causing vertical mixing. The Antarctic Peninsula Coastal Current (APCC) transports cold, fresh water southwards along the coast.

the authors acknowledge, the use of such parameterisations introduces a large element of uncertainty, so our understanding of the processes that cause vertical mixing on the WAP remains incomplete. This aside, the vertical heat fluxes inferred by these authors are of a comparable magnitude to the characteristic vertical heat flux associated with the interaction of CDW with ice shelves ($\sim$ 8 W m^{-2} below George VI Ice Shelf; Jenkins and Jacobs, 2008), and are therefore considered important for the WAP heat budget.

As CDW flows southward towards the coast it loses heat to the overlying surface layers and mixes with cold, fresh water to form modified CDW (mCDW; Moffat et al., 2009). The water column is salinity stratified; directly overlying the mCDW lies Winter Water (WW), which has salinities between $33.85 - 34.13$ PSU (Martinson et al., 2008). WW forms close to freezing point, and during winter constitutes the entire surface mixed layer ($\sim$ 100 m; Moffat et al., 2009). Additionally, during summer, fresh ($\sim 32.5 - 33.25$ PSU) meltwater rich Antarctic Surface Waters (AASW) simultaneously heats the WW from above (AASW can be wide range of temperatures $-0.75 - 1.5$ °C), increasing stratification and leaving a remnant WW layer (Moffat et al., 2009). The structure of these water masses on the WAP shelf may be influenced seasonally by the Antarctic

Peninsula Coastal Current (APCC). The APCC is a geostrophically balanced buoyancy current that brings freshwater southward in the summer and autumn months, from Adelaide to Alexander Island, and is forced by freshwater discharge, melting sea ice and downwelling-favourable winds (Moffat et al., 2008). Once winter sea ice forms and freshwater input declines, the APCC disappears (Moffat et al., 2008).

There are multiple vertical mixing processes that can modify the CDW as it travels across the WAP continental shelf towards the coast. As highlighted in Section 1.3.2, close to the surface, buoyancy forcing and wind-driven vertical mixing forms a surface mixed layer that facilitates exchange of heat between the ocean and the atmosphere; typical MLDs on the WAP are between $25 - 50$ m (Schofield et al., 2018). Strong wind, associated with large scale atmospheric variations, can also cause near-inertial internal waves that generate shear and vertical mixing at depths greater than the MLD (D'Asaro, 1985). Howard et al. (2004); Brearley et al. (2017) suggest such near-inertial energy is significant for mixing in the WAP's ice free season. Other types of internal wave that are typically driven by winds include coastal-trapped waves (Allen, 1975) and basin-scale wave modes (Arneborg and Liljebladh, 2001). These processes are thought to be important for mixing in Arctic fjordic systems (e.g., Inall et al., 2015; Fraser et al., 2018) and could therefore also be important in analogous embayments on the WAP (see Section 4.2 for more information). Internal waves (including internal tides) can also cause elevated mixing due to interactions with rough topography (as discussed in Section 1.3.2), and the glacially-carved features across the shelf means these processes may also be important for mixing on the WAP. Marguerite Trough is connected via several topographic constrictions to Laubeuf Fjord, a $\sim$ 800 m-deep channel that extends eastward between Adelaide Island and the WAP's coast (Figure 1.11). This passage contains multiple transverse ridges that are potential sites for vertical mixing. Underwater gliders deployed over these ridges have provided data with high spatial resolution and revealed evidence of localised vertical mixing of CDW (Venables et al., 2017). The ridges block the densest waters, and as the overflowing water descends hundreds of metres, it entrains the cooler, fresher, but seasonally-varying overlying AASW. The relative contribution of each of these potential mixing processes to the WAP heat budget is still uncertain.

Situated on the southeast coast of Adelaide Island, Ryder Bay has a $\sim$ 520-m deep basin and is separated from Laubeuf Fjord by a $\sim$ 300 m-deep ridge at its entrance (Figure 1.15). The bay is bounded to the north by Sheldon Glacier, which is a marine-terminating glacier that is retreating (Cook et al., 2005), to the west by two smaller marine-terminating glaciers, and to the south by a series of small islands that form a $\sim$ 300 m-deep shelf. The semi-enclosed nature of Ryder Bay and its close proximity to the marine-terminating glaciers means it can be considered an end point for CDW that intrudes onto the shelf through Marguerite Trough and Laubeuf Fjord (Klinck et al., 2004). Ryder Bay is also adjacent to the British Antarctic Survey's main Antarctic base:

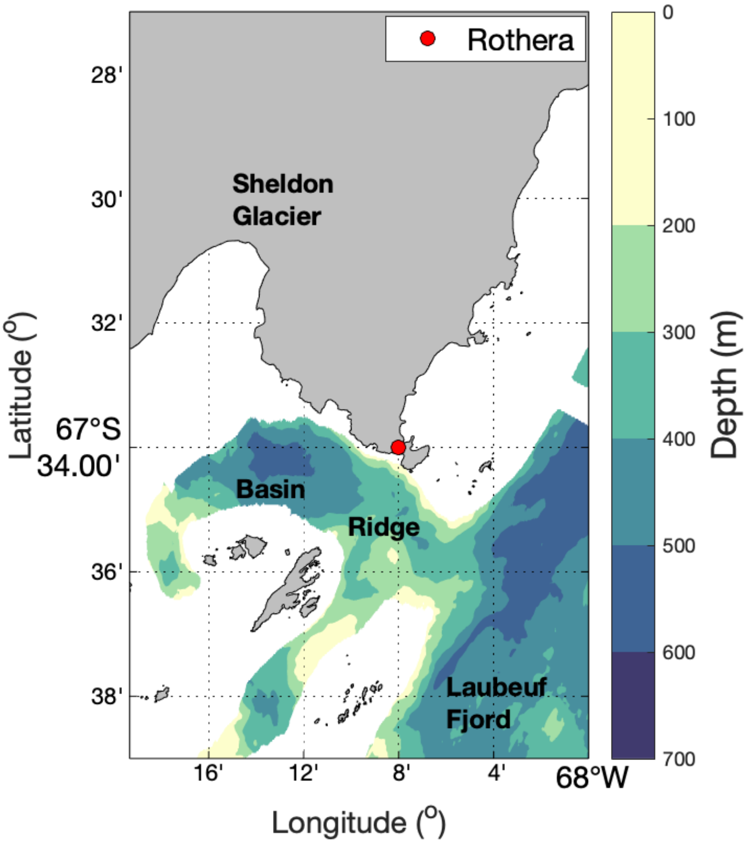

FIGURE 1.15: Map of Ryder Bay, southeast coast of Adelaide Island, on the West Antarctic Peninsula (see Figure 1.11). Areas of interest are labelled. Colours represent quality-controlled bathymetric data (Fremand, 2020), with unsurveyed areas in white.

Rothera Research Station. The relatively easy access, close proximity to glaciers, and the presence of the ridge at the bay's entrance, makes Ryder Bay a fitting locality to study vertical mixing processes and their contribution to closing the WAP heat budget.

1.5 The Arctic Ocean

1.5.1 Large-Scale Circulation

Sea ice drift can be used to identify two large-scale patterns that dominate circulation in the Arctic Ocean: the Beaufort Gyre and the Transpolar Drift Stream (Figure 1.16a). The Transpolar Drift Stream is a current that flows across the central Arctic, from the Siberian coast towards Greenland and the Fram Strait, continuing down Greenland's east coast in the East Greenland Current. This circulation feature is a major export of sea ice and cold, fresh surface water out of the Arctic Ocean and into the north Atlantic (an amount equivalent to $\sim$ 10% of the ice within the Arctic Basin; Smedsrud et al., 2017). The strength and orientation of the Transpolar Drift Stream is controlled by the relative locations and intensity of the Beaufort High and Icelandic Low (Kwok et al., 2013); semi-permanent atmospheric pressure systems. A strengthened Beaufort High leads to more widespread anticyclonic circulation, and a more direct flow path from the Laptev Sea to the Fram Strait in the Eurasian Basin (Kwok et al., 2013). A strengthened Icelandic Low leads to cyclonic circulation and a route that extends further into the Canada Basin (Kwok et al., 2013). The dominant pressure system shifts on timescales of $5 - 7$ years (Proshutinsky and Johnson, 1997), although the controlling mechanism is unclear (Proshutinsky et al., 2015). Consequently, the centre of the current varies, but can be considered approximately parallel with the Lomonosov Ridge. The Lomonosov Ridge is the approximate location of a front that exists between warm, fresh surface waters of the northern Beaufort Gyre and colder, more saline surface waters of the Transpolar Drift Stream (e.g., Steele et al., 2004). This front can form eddies and cause water mass transformation through baroclinic instability (Timmermans et al., 2008). Upper 20 m current speeds are between $6 - 10$ cm s^{-1}, suggesting the transport across the Arctic takes $\sim$ 1 year (Armitage et al., 2017; Timmermans and Marshall, 2020).

The second major circulation feature in the Arctic Ocean is the Beaufort Gyre, situated in the Canada Basin. The Beaufort Gyre is a coherent anticyclonic rotating body of water with a diameter of $\sim$ 800 km (Timmermans and Marshall, 2020). The gyre is forced by prevailing anticyclonic winds that are associated with the Beaufort High (e.g., Proshutinsky et al., 2019). Through Ekman transport (Ekman, 1905), these winds move surface waters at 90 ° to the right of wind direction (in the northern hemisphere), into the centre of the gyre (e.g., Proshutinsky et al., 2009). The anticyclonic winds and ocean surface circulation therefore ensure that, unlike the Transpolar Drift Stream, the Beaufort Gyre traps sea ice, circulating it around the Arctic Ocean (Figure 1.16a).

Figures 1.16a,b show the Arctic Ocean's sea-surface-salinity (SSS) and SST, respectively. The freshest regions are close to the Siberian and Canadian coastlines where there is significant sea ice melt and fresh water river input (e.g., from the Mackenzie River, northwest Canada Proshutinsky et al., 2019). However, persistent anticyclonic winds also export this fresh, surface water into the centre of the Beaufort Gyre through Ekman transport (e.g., Proshutinsky et al., 2009). Through a combination of these processes, together with increased freshwater transport through the Bering Strait (Woodgate, 2018), the Beaufort Gyre has experienced a 40% increase in freshwater content compared to values in the 1970s (Proshutinsky et al., 2019). Consequently, SSSs at the centre of the Beaufort Gyre ($\sim$ 27 PSU) are fresh compared to those in the Eurasian Basin ($>$ 33 PSU). Much of the Canada Basin is covered by Arctic sea ice (Figure 1.16b) even in summer, though the sea ice extent during 2018 is significantly lower than the average between $1982 - 2010$. Arctic Ocean August SSTs are typically < -1 °C (Figure 1.16b), with warmer waters ($>$ 4 °C) entering the Arctic Ocean both through the Bering Strait and in the north Atlantic, via the Fram Strait.

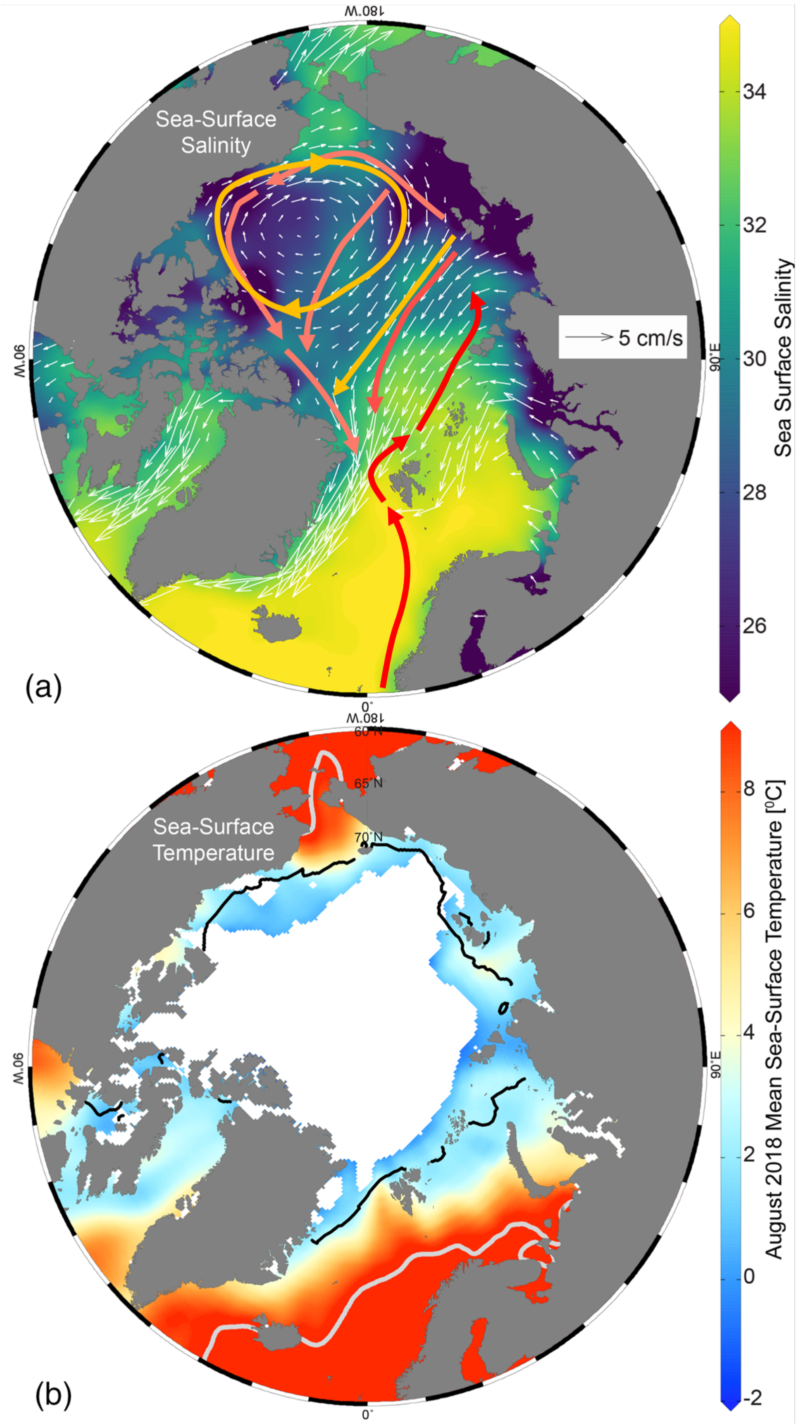

FIGURE 1.16: (a) Mean sea-surface salinity and March sea ice motion between 2005 – 2017 (from Timmermans and Marshall, 2020). Overlain is a schematic showing the major circulation pathways within the Arctic Ocean. At the surface are the Beaufort Gyre (closed orange loop) and the Transpolar Drift Stream (straight orange arrow, after Armitage et al., 2017). Red arrows represent deep circulation of Atlantic Water in the Arctic Circumpolar Boundary Current; lightening colours are indicative of cooling (after Polyakov et al., 2020b). (b) August 2018 mean sea-surface temperature (°C) and sea ice extent (white regions; from Timmermans and Marshall, 2020). Thick grey and black contours indicate the 10 °C isotherm and the median sea ice edge for August 1982 – 2010, respectively.

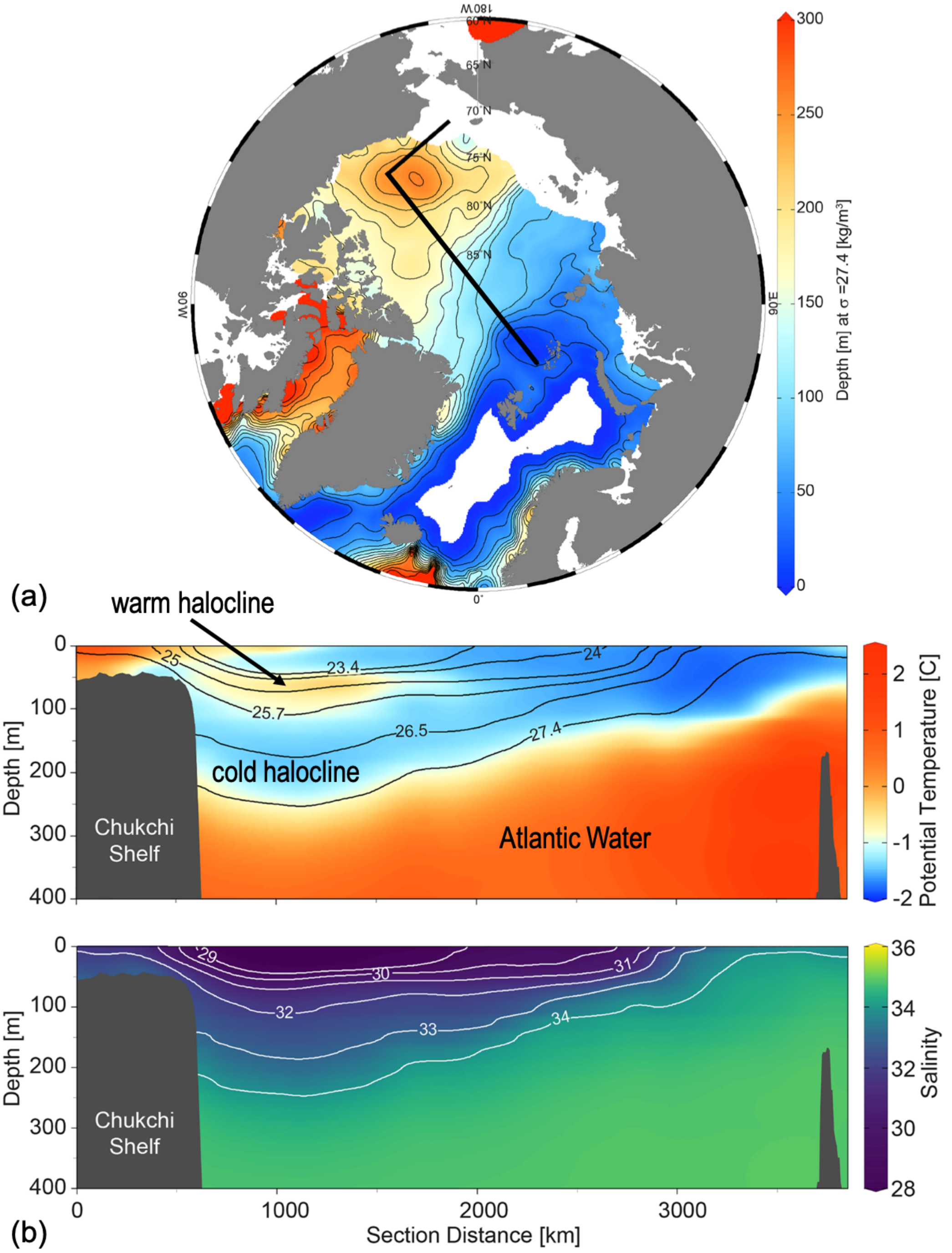

FIGURE 1.17: (a) Depth of the 27.4 kg m^{-3} surface referenced potential density isopycnal, which typically represents to the base of the Arctic halocline (from Timmermans and Marshall, 2020). Black line represents the section shown in (b). White regions are where water of 27.4 kg m^{-3} density was either not recorded or was at the surface. (b) Potential temperature (top; °C) and salinity (bottom; PSU) from the Chukchi Sea to the Eurasian Basin (from Timmermans and Marshall, 2020). Black and white lines are isopycnals (kg m^{-3}) and salinity contours, respectively. The warm and cold halocline are labelled.

Below much of the surface of the Arctic Ocean lies a strong gradient in density, the Arctic halocline. The base of the Arctic halocline is typically assumed to be the 27.4 kg m^{-3} potential density isopycnal, and is deepest in the Beaufort Gyre ($>$ 200 m; Figure 1.17a), shoaling to the surface in the Eurasian Basin. The Arctic halocline in the Beaufort Gyre and surrounding Canada Basin can be divided into the warm halocline and the cold halocline (Figure 1.17b, upper panel). The warm halocline consists of summer Pacific water, with salinities between $31 - 33$ PSU (Steele et al., 2004). Approximately 0.83 Sv of Pacific water flows northward through the Bering Strait and towards the shelfbreak (Roach et al., 1995), driven largely by far-field pressure forcing (Woodgate, 2018). The summer Pacific water forms through solar heating in the warm months of the year, and has constituent water masses originating from different regions of the Bering Sea shelf (e.g., Steele et al., 2004). The cold halocline is composed of denser Pacific waters that are formed during the cold winter months and flow through the Bering Strait (Steele et al., 2004). The cold halocline can be separated into upper and lower layers; a salinity of 33.5 PSU is the rough divide between the two layers (Pickart, 2004). Only the densest waters constitute the cold halocline's lower layer.

Figure 1.17b shows that the Arctic halocline is cold and fresh relative to the underlying Atlantic Water (AW). AW enters the Arctic Ocean through the Fram Strait in the Arctic Circumpolar Boundary Current (Aksenov et al., 2011). This current is steered by the bathymetry and takes a cyclonic pathway around the edge of the Arctic Basin; the lighter shades of red represent cooling of the AW due to mixing with the cold, fresh water above (Timmermans and Marshall, 2020, Figure 1.16a). The cyclonic flow occurs on contours of f/H (where f and H are the Coriolis parameter and water depth respectively) and is set by cyclonic wind stress curl over the Nordic Seas (Timmermans and Marshall, 2020); wind stress curl is the vertical component of the curl of the wind stress, $\vec{\tau_{curl}}$: $\frac{\partial \tau_y}{\partial x} - \frac{\partial \tau_x}{\partial y}$. The AW typically has temperatures and salinities > 1 °C and > 34 PSU, and is found at depths between $\sim 150 - 900$ m (Polyakov et al., 2020b). This layer of water contains enough heat to melt all the Arctic sea ice $3 - 4$ times over (Carmack et al., 2015). Recent studies have associated changes to sea ice extent and stratification to a northward progression of AW, a process that has been termed Atlantification (Årthun et al., 2012; Polyakov et al., 2017; Årthun et al., 2019). Were this heat to be released and Atlantification to continue (as predicted; Årthun et al., 2019), it would have major consequences for global climate, ocean circulation, and local communities and ecosystems. The mechanisms that supply the relatively fresh Pacific water to the Arctic halocline are therefore extremely important: by ventilating the halocline, they maintain the stratification required for protecting the Arctic sea ice from heat within the underlying AW. This ventilation is especially important in the Beaufort Gyre, where the stratification is greater and a large volume of sea ice is retained.

1.5.2 Shelf-Ocean Exchange: Ventilation of the Cold Arctic Halocline

The cold halocline is a particularly important part of the Arctic Ocean's water column because it has enhanced stratification compared to the overlying waters and lies immediately above the warm AW layer. The cold halocline is therefore critical for preventing the AW from mixing vertically to the sea surface and melting the pack ice. It is now well established that the cold halocline is ventilated laterally from the edges of the Arctic basin, rather than vertically from above (Aagaard et al., 1981). In the Canadian sector of the Arctic, dense winter water that is near the freezing point on the Bering, Chukchi, Beaufort, and East Siberian shelves provides source water for the cold halocline (Muench et al., 1988; Melling, 1993; Weingartner et al., 1998; Anderson et al., 2013). This water mass is referred to as Newly Ventilated Winter Water (NVWW) and forms through brine rejection induced winter convection. A significant portion of NVWW forms in the Bering Sea and flows through the Bering Strait between January and April (Woodgate et al., 2005). However, Pacini et al. (2019) have recently highlighted the importance of leads (linear cracks in sea ice caused by divergence or shear) on the Chukchi Shelf for the formation of NVWW. As the NVWW travels northwards across the shelf it transforms, slightly freshening and warming, either through solar insolation or mixing with the summer water masses (Gong and Pickart, 2016), to form Remnant Winter Water (RWW). The cold dense water is also high in nutrients, in part because during formation, regenerated nutrients from the sediments are mixed into the water column (Cooper et al., 1997; Arrigo et al., 2017). Hence the winter water also contributes to the nutricline of the Canada Basin (Jones and Anderson, 1986), impacting primary production. The processes fluxing the cold winter water off of the shelf and ventilating the cold halocline of the Canada Basin are discussed below.

1.5.2.1 Advection Through Canyons

In order to ventilate the cold halocline, the dense winter water must be fluxed from the shelves into the interior basin. Figure 1.18 presents a circulation schematic for the vicinity of the Chukchi and Western Beaufort Seas. Pacific water is known to exit the Chukchi shelf through Barrow Canyon in the east (Pickart et al., 2005; Weingartner et al., 2017) and Herald Canyon in the west (Pickart et al., 2010; Linders et al., 2017). Both of these outflows form a shelfbreak jet that flows to the east. The Chukchi shelfbreak jet transports between $0.01 - 0.10$ Sv of Pacific water (Corlett and Pickart, 2017; Li et al., 2019), while the transport of the Beaufort shelfbreak jet is in the range $0.02 - 0.13$ Sv (Nikolopoulos et al., 2009; Brugler et al., 2014). Recently it has been documented that Pacific water is advected in a westward-flowing boundary current along the continental slope of the Chukchi Sea (Corlett and Pickart, 2017; Li et al., 2019). This current has been named the Chukchi Slope Current and is believed to emanate from Barrow Canyon (Spall et al., 2018). Spall et al. (2018) show that the influence of wind forcing

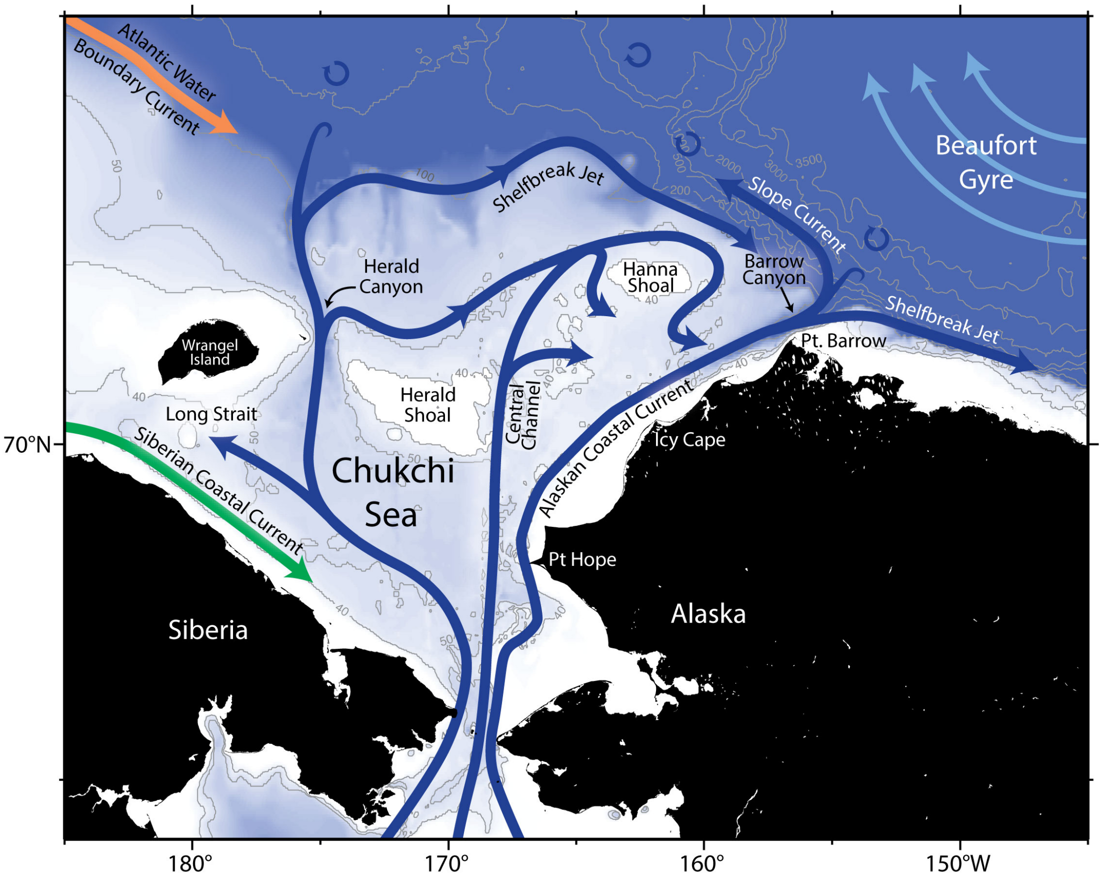

FIGURE 1.18: Schematic circulation of the Chukchi and Beaufort Seas, including place names (from Corlett and Pickart, 2017).

on formation of the Chukchi Slope Current is negligible, and that strong, nonlinear advection, caused by flow passing through the narrow Barrow Canyon, results in the Pacific water crossing the shelfbreak and exiting the shelf. Corlett and Pickart (2017) constructed a mass budget of the Chukchi shelf, in which the slope current constitutes the dominant outflow. Transport estimates of the Pacific water component of the current range from $0.50 - 0.57$ Sv (Corlett and Pickart, 2017; Li et al., 2019).

The current system at the shelfbreak in the Chukchi Sea region shows significant variability. The Chukchi Slope Current is surface-intensified in the summer and autumn, however, in winter and spring it is mid-depth intensified, weakens, and moves shoreward (Li et al., 2019). The slope current transports RWW year-round, NVWW at $50 - 170$ m between March-August, and warm, fresh waters in the upper 100 m between November-March (Li et al., 2019). There is also evidence of NVWW formation in the upper layers between December-February (Li et al., 2019). The Chukchi shelfbreak jet is less variable, always being bottom-intensified, weakening in spring and becoming westward in May/June (Li et al., 2019). The Chukchi shelfbreak jet is dominated by NVWW in May-September, and RWW during the remaining times of the year (Li et al., 2019). The different modes of the Chukchi Slope Current and shelfbreak jet are largely controlled by wind stress curl on the Chukchi shelf; positive wind stress curl causes an enhanced westward slope current and a reversed shelfbreak jet, whilst negative wind stress curl causes a strong eastward shelfbreak jet and a weak slope current (Li et al., 2019). Additionally, the Beaufort shelfbreak jet exhibits large seasonal variation; it is bottom-intensified and transports cold Pacific winter water during spring and early summer, whilst it transports warm summer Pacific waters in a surface-intensified jet from mid-summer to autumn (Nikolopoulos et al., 2009). For the remainder of the year the Beaufort shelfbreak jet transports modified summer and winter Pacific waters (Nikolopoulos et al., 2009). The jet's transport is greatest in summer (Brugler et al., 2014; Lin et al., 2016) and can be decomposed into background and wind components; prevailing easterly winds largely associated with the Beaufort High are strongest between June-October and oppose the eastward background transport (Lin et al., 2016).

The fate of the currents once they flow through Herald and Barrow canyons determine the horizontal location of the Pacific water and are therefore particularly relevant to Arctic halocline ventilation. At Barrow Canyon, the eastward flowing Chukchi Shelfbreak jet intersects and becomes entrained in the westward flowing Chukchi Slope Current (Figure 1.18). von Appen and Pickart (2012) investigate the distance over which the Beaufort shelfbreak jet spins-down. They suggest that the bottom-intensified, winter configuration likely extends beyond the first entrance to the Canadian Archipelago (towards the Fram Strait), whilst the surface-intensified, summer configuration likely does not extend beyond the Alaskan Beaufort Sea. Lin et al. (2020) have recently supported this suggestion, observing no summer Pacific water in the vicinity of the Mackenzie Canyon, and a reduction in transport of the shelfbreak jet from 0.08 ± 0.02 Sv to 0.03 ± 0.02 Sv. The fate of the Chukchi Slope Current is perhaps the most important, given it transports the greatest volume of Pacific water (Corlett and Pickart, 2017). Recently, Boury et al. (2020) deployed Lagrangian floats within the Chukchi Slope Current, revealing that flow sharply turns northwards in the vicinity of Hanna Canyon and likely becomes entrained in the Beaufort Gyre. They suggest that this may occur when the slope current is situated over isobaths deeper than 200 m (which turn northwards), whilst when residing over the upper continental slope ($<$ 200 m), the slope current may follow the isobaths westward, towards the East Siberian Sea. Wind-driven stresses and eddy-slope current interactions can influence the slope current. For example, an anticyclonic eddy is believed to have temporarily slowed down the slope current, permanently expelling water and ejecting a float from the current's path (Boury et al., 2020). These processes are key to understanding the fate of the Pacific water and uncovering the major ventilation region of the Arctic halocline.

1.5.2.2 Ekman Processes

There are various mechanisms by which the Pacific water carried by the system of boundary currents stemming from the Chukchi shelf could be fluxed seaward into the basin. This can occur via wind-forced upwelling and downwelling at the shelfbreak. The former process has been studied extensively in the Beaufort Sea and occurs throughout the year during all ice conditions (e.g., Pickart et al., 2009, 2011, 2013; Lin et al., 2016). The offshore Ekman transport during these events carries Pacific water from the surface layer on the shelf into the basin (Ekman depth approximately 45 m, Schulze and Pickart, 2012), and is strongest when there is partial sea ice cover (Schulze and Pickart, 2012). Although this water can be as cold as Pacific winter water during much of the year, it is typically too fresh (and light) to ventilate the cold halocline. Upwelling has also been observed on the Chukchi slope, although there is less evidence of an offshore surface Ekman circulation (Li et al., 2019). Timmermans et al. (2014) suggest that the upwelling is coincident with Ekman subduction of surface Pacific waters further offshore, where outcropping warm halocline isopycnals occur. This has been suggested as a primary ventilation mechanism for the warm and cold haloclines in summer and winter, respectively (Timmermans et al., 2017). However, this hypothesis does not account for the boundary current system at the shelfbreak, and Corlett and Pickart (2017) note that any volume flux would likely get entrained in either the Chukchi shelfbreak jet or the Chukchi Slope Current. Spall et al. (2018) also show that the majority of the Pacific water exiting the Chukchi Shelf leaves through Barrow Canyon in the Chukchi Slope Current. Downwelling, on the other hand, does transport Pacific winter water offshore in the density range of the upper halocline. This has been demonstrated in the Canadian Beaufort Sea (Dmitrenko et al., 2016) and in the Alaskan Beaufort Sea (Foukal et al., 2019).

1.5.2.3 Eddies

Another mechanism for transporting Pacific winter water offshore is via eddies. Halocline eddies are a ubiquitous feature of the Canada Basin, and are commonly observed by a variety of measurement platforms (e.g. Manley and Hunkins, 1985; Plueddemann et al., 1999; Muench et al., 2000; Mathis et al., 2007; Kawaguchi et al., 2012; Zhao and Timmermans, 2015; Fine et al., 2018). Zhao et al. (2016) used ice-tethered profilers (ITPs) to find 243 eddies in the Canada Basin between $2005 - 2015$ (Figure 1.19a). The vast majority of these eddies are cold-core anticyclones with lateral scales on the order of the Rossby deformation radius (Equation 1.1), which is between $10 - 15$ km in this region (Zhao et al., 2014); 98% of the eddies were anticyclonic, with 70% having anomalously cold-cores (Zhao et al., 2016). The southern and western regions of the Canada Basin have the highest eddy density (Figure 1.19b), and Zhao et al. (2016) suggest that these regions exhibit more cold (lower in Figure 1.19c) halocline eddies than the northern

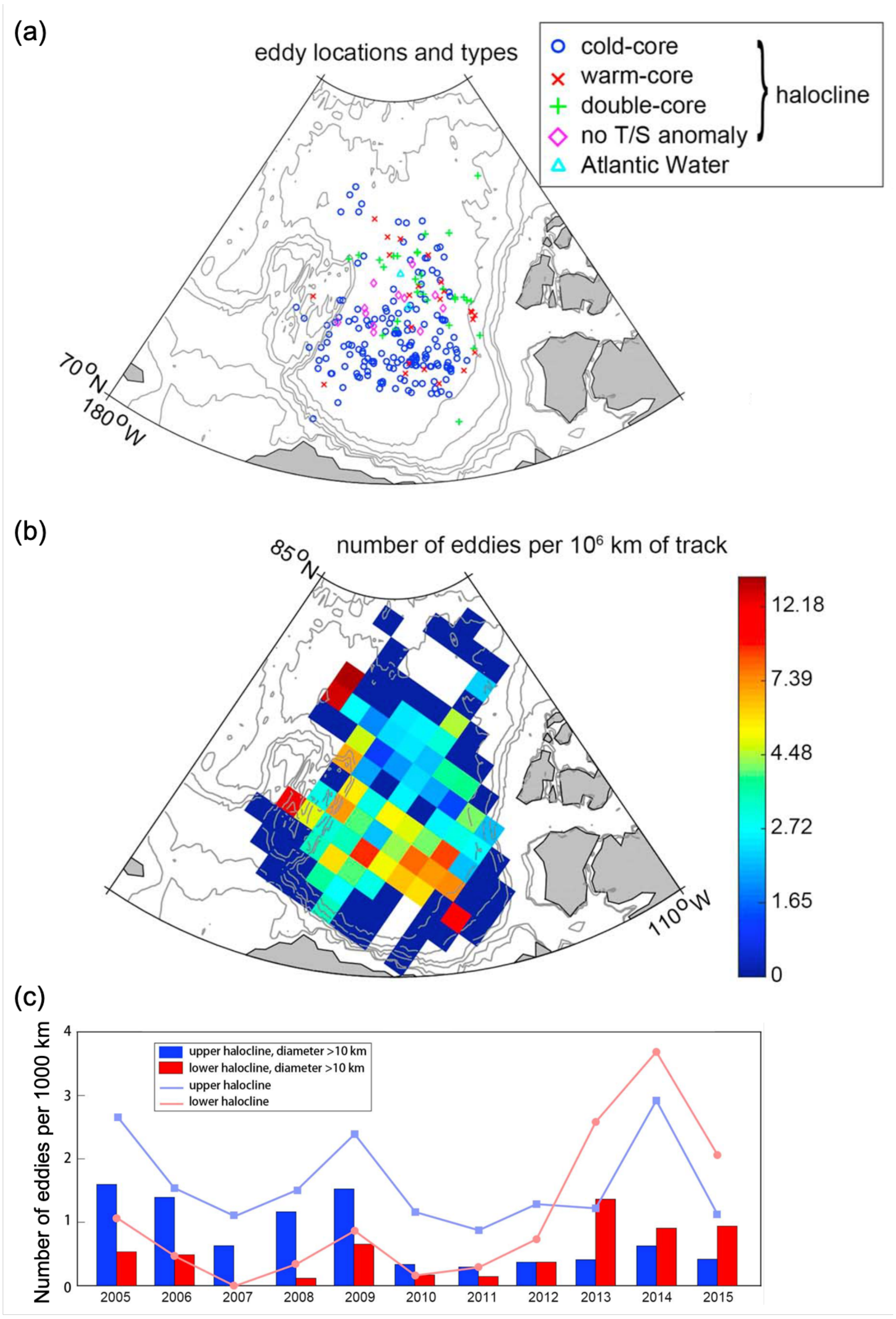

FIGURE 1.19: a) Eddy types and locations sampled between $2005 - 2015$ using Ice-Tethered Profilers (ITPs; from Zhao et al., 2016). (b) Number of eddies per 10^6 km of ITP drift track for each 100 km × 100 km grid cell (from Zhao et al., 2016). (c) Time series of upper (blue, core salinity < 32 PSU) and lower (red, core salinity > 32 PSU) halocline eddies per 1000 drift track (note the upper and lower halocline terms used in (c) approximately correspond to the warm and cold halocline definitions used elsewhere in this thesis). The bars only include eddies with a diameter > 10 km, whilst the lines include all eddies recorded from temperature and salinity measurements (from Zhao et al., 2016).

and eastern regions. The eddies that reside in the northern part of the Canada Basin are generally shallow (centred above 80 m) and are believed to be spawned via baroclinic instability of the hydrographic front that divides Canadian Arctic waters from Eurasian Arctic waters (Timmermans et al., 2008). By contrast, the cold-core anticyclones observed in the southern portion of the Canada Basin are deeper (centred below 80 m), saltier, and denser. These features are believed to last up to a year before spinning down, and their population has increased, particularly between $2013 - 2014$ (Figure 1.19c; Zhao et al., 2016).

The deeper cold-core eddies found in the southern Canada Basin are thought to emanate from the two canyons on the outer Chukchi shelf or from the boundary currents that emerge from these canyons. Numerical, laboratory, theoretical, and observational studies have argued that the dense water flowing down Barrow Canyon should form anticyclonic eddies, either through sidewall friction (D'Asaro, 1988), flow-topography interactions (Cenedese and Whitehead, 2000; Chao and Shaw, 2003), or baroclinic instability (Pickart et al., 2005). Pickart and Stossmeister (2008) present MODIS satellite ice images showing a train of anticyclones being generated from the canyon outflow, which provides observational support for these mechanisms. Presumably the same argument applies to the Herald Canyon outflow. Indeed, Pisareva et al. (2015) observed a cold-core anticyclone of Pacific winter water situated directly offshore of the mouth of that canyon.

It is also believed that Pacific winter water anticyclones are spawned from the shelfbreak jet of the Chukchi and Beaufort Seas via baroclinic instability. This process was investigated by Spall et al. (2008) who used mooring observations to assess the stability characteristics of the Beaufort shelfbreak jet and to calculate the mean-to-eddy energy fluxes. This implied that baroclinic instability was active, and the numerical model they employed showed how the unstable boundary current readily formed eddies with the same characteristics of those observed in the basin. The Chukchi shelfbreak jet should be similarly unstable, and Pickart et al. (2005) presented evidence of a cold-core anticyclone being spawned from the current. It remains to be determined if the Chukchi Slope Current can form Pacific water eddies. Corlett and Pickart (2017) showed that the potential vorticity structure of the current satisfies the necessary condition for baroclinic instability, and the current undergoes meanders which are suggestive of an unstable current. The eddies spawned from the canyon outflows and boundary currents are represented schematically in Figure 1.18. Pickart et al. (2005) argued that, in order for the locus of these eddies to be the dominant ventilation source of the Canada Basin's upper cold halocline, $100 - 200$ eddies must be formed each year. This does not seem unreasonable in light of the large numbers of cold-core anticyclones observed in the basin (e.g., Zhao et al., 2014, 2016).

1.6 Thesis Aims and Structure

This introduction has shown the important role the polar regions have for Earth's ocean and climate system. Major components of this system are the shelf-ocean exchange processes that bring heat towards Antarctica, causing melting of the marine-terminating glaciers and ice shelves; and that ventilate the cold halocline in the Arctic, thereby protecting the sea ice. The overarching aim of this thesis is to contribute to our understanding of these exchange processes using observational oceanographic datasets. More specifically, this thesis aim can be further divided into two main objectives: (i) to use autonomous underwater gliders to quantify the rates and mechanisms of turbulent mixing within Ryder Bay, and (ii) to use hydrographic data to analyse a cold-core anticyclonic eddy observed at the Chukchi Sea shelfbreak.

Chapter 2 first introduces the datasets analysed in this thesis and the methodology used for processing. The chapter is split into Antarctic and Arctic sections, with subsections for each dataset. The majority of this chapter is comprised of a newly developed method for automatically processing glider microstruture data. This was created because the microstructure processing software was originally developed for VMPs, which collect a much smaller volume of data than a glider. Chapters 3 and 4 then focus on objective one in the Southern Ocean, whilst Chapter 5 addresses objective two in the Arctic Ocean.

Chapter 3 describes the mean hydrographic and dissipation patterns observed within Ryder Bay, and documents their temporal variability. These data are some of the first direct estimates of dissipation off the WAP collected using an autonomous Slocum glider equipped with a microstructure (MicroRider) package. The corresponding vertical mixing rates and heat fluxes are also described. Chapter 4 then uses ancillary CTD, ADCP and wind data to investigate the spatio-temporal controls on vertical mixing both within Ryder Bay's basin and over the ridge at its entrance. The chapter finishes by using the corresponding heat fluxes to explore the relative importance of these mixing mechanisms.

Chapter 5 then switches focus to a first-of-its-kind three dimensional hydrographic survey of an eddy in the Chukchi Sea. The eddy's hydrographic characteristics are first explored, revealing the eddy's anomalously cold-core. ADCP data is then used to study the eddy's kinematics and dynamics. This reveals that the anticyclonic eddy is embedded on the seaward side of the Chukchi Slope Current. The current signature is removed, enabling calculation of the cyclogeostrophic velocity. The eddy's spin-down time and fate are then considered.

Lastly, Chapter 6 presents a summary of the key findings from this thesis. The chapter finishes by exploring how the studied mechanisms could change in the future and what the implications may be for the polar regions.

Chapter 2

Data and Methodology

This chapter introduces the various datasets that are used in this thesis. Section 2.1 details the collection and processing of the West Antarctic data that are used in chapters 3 and 4. Section 2.2 describes the collection and processing of the Arctic data that are used in Chapter 5.

2.1 Antarctic Data

The work in this section contributed to the following published paper:
Scott, R. M., J. A. Brearley, A. C. Naveira Garabato, H. J. Venables, and M. P. Meredith, 2021b: Rates and mechanisms of turbulent mixing in a coastal embayment of the west antarctic peninsula. *Journal of Geophysical Research: Oceans*, **126**, e2020JC016 861.

2.1.1 Glider and Rothera Time Series Hydrographic Data

CTD data were acquired using a 1000 m-rated Teledyne Webb Research (TWR) Slocum glider equipped with a pumped Seabird SBE-41 sensor. The glider was deployed / recovered multiple times in Ryder Bay between 11th January 2016 and 1st March 2016, using a rigid inflatable boat that operates out of the British Antarctic Survey's Rothera Research Station. The glider recorded data in both the bay's deep region (maximum depth of 520 m) and over the topographic ridge ($\sim$ 320 m) that separates the bay from the upstream Laubeuf Fjord (Figure 2.1).

A TWR Slocum glider records glider flight and science data in DBD and EBD binary file formats respectively. After downloading the data from the glider's memory card, the files need to be renamed and converted into ascii format using the Linux $rename\_dbd\_files$ and $dbd2asc$ functions provided by TWR. The scripts must be executable and in the

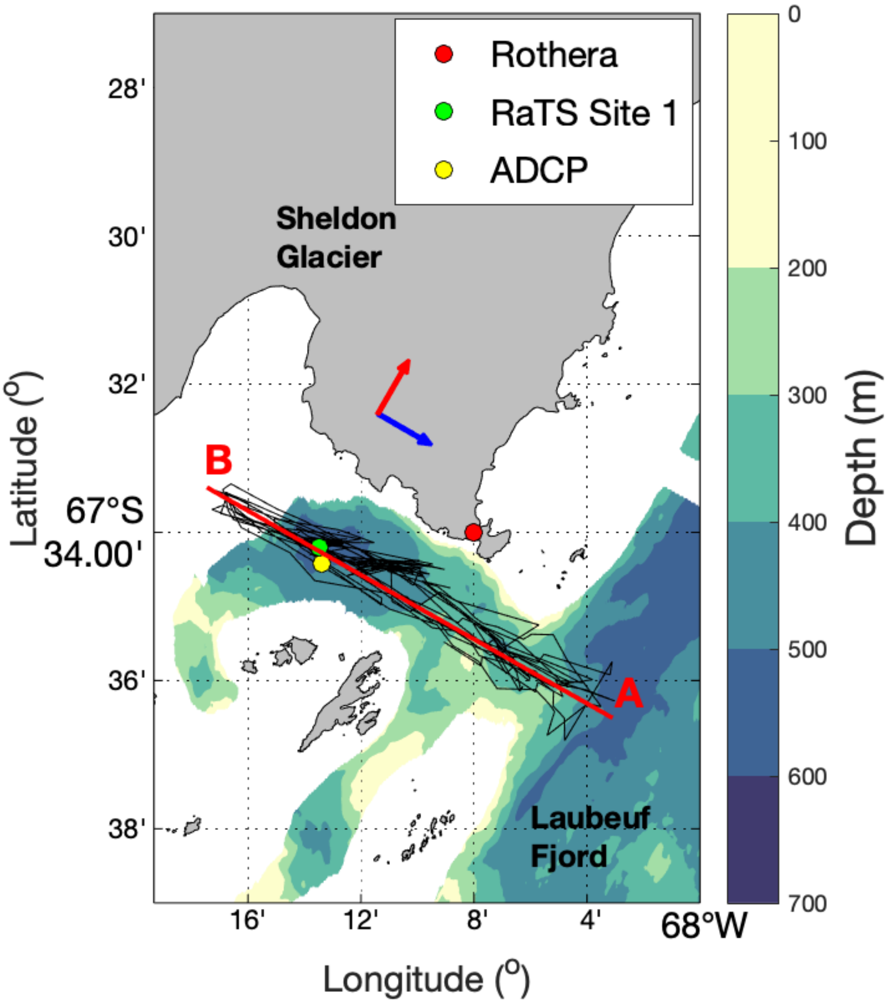

FIGURE 2.1: Map of Ryder Bay, showing the location of Rothera (red) in relation to the glider tracks. For legibility, only glider data with quality-controlled dissipation estimates are shown. Colours represent quality-controlled bathymetric data (Fremand, 2020), with unsurveyed areas in white. The locations of the Rothera Time Series (RaTS) Site 1 (green) and the ADCP mooring (yellow) are indicated. Glider data are collapsed onto the A-B transect (red line). Blue (alongshore) and red (cross-shore) arrows show the orientation of the rotated reference frame used in Chapter 4.

same directory as the data files. Example commands using the *dbd2asc* script are found below:

$$dir\ *.dbd\ |\ ./dbd2asc\ -s > dbdtemp.dba$$

$$dir\ *.ebd\ |\ ./dbd2asc\ -s > ebdtemp.dba$$

The full ascii header information is found within cache files contained within the first mission files, and are required for the conversion process. If a file missing error occurs their locations can be specified.

The SOCIB Glider Toolbox (Troupin et al., 2015) can be used to load the ascii file into MATLAB and create a data structure using the *loadSlocumData* function. The functions

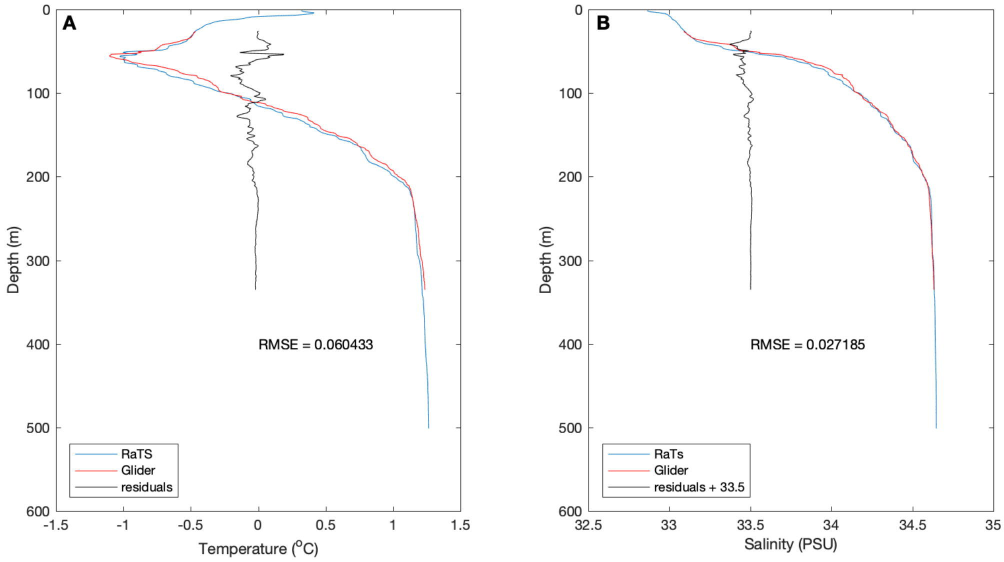

FIGURE 2.2: An example comparison between a glider and a near-concurrent calibrated RaTS temperature (a) and salinity (b) depth profile. These profiles were recorded approximately 32 days into the glider deployment.

preprocessGliderData and *processGliderData* are used to process the glider dataset. This involves interpolation of glider Global Positioning System (GPS) positions for periods when the glider is underwater, attitude information and depths, as well as a thermal lag correction (Garau et al., 2011). The thermal lag correction is required due to the spatial and temporal mismatch between temperature and conductivity sensors, which worsens in the presence of sharp temperature gradients (Lueck and Picklo, 1990). If left uncorrected then calculated values for salinity and density could be incorrect, however, the glider used for the Ryder Bay dataset has a pumped CTD, ensuring that a constant flow speed through the sensor is maintained and the required thermal lag corrections were small. The error magnitude and error time constant parameters were $\alpha = 0.0192$ and $\tau = 11.1432$ respectively, and there were no observable differences with the uncorrected data. Spikes in the data are also removed and can form due to faulty sensors or, for the salinity data in particular, through collisions with organic material that alter the recorded conductivity.

The $\sim$ 20 year Rothera Time Series (RaTS) aims to sample oceanographic and biological data twice weekly in summer (weekly in winter) using a hand-winched SBE-19 pumped CTD package at Site 1 (Figure 2.1). This includes calibrated temperature and salinity data collected in 2016, which is compared to the glider's CTD data to ensure that there are no temperature and salinity offsets and no CTD sensor drift. Estimates for the accuracy of the RaTS temperature and salinity data are 0.002 °C and 0.005 PSU, respectively (Venables et al., 2013). The primary RaTS site (67.570 °S, 68.225 °W) is located at the deepest part of Ryder Bay (520 m), and there were three occasions when the glider travelled to within $\leq$ 0.5 km of this location at the same time that the RaTS

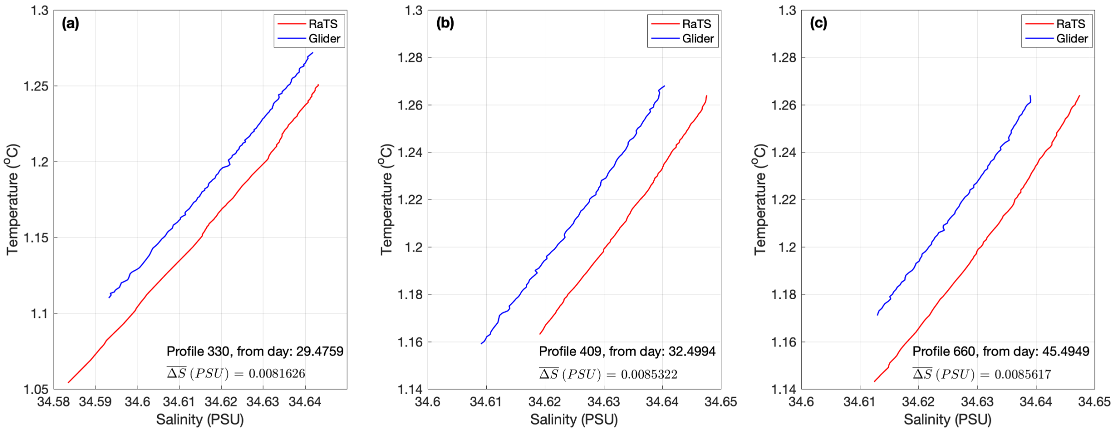

FIGURE 2.3: Salinity interpolated onto a common temperature grid for the three RaTS and glider profiles that were collected on days 29 (a), 32 (b) and 45 (c) into the glider deployment. A consistent offset is observed and the salinity data has been corrected accordingly.

data were being collected (on days 29, 32 and 45 days into the glider deployment). Individual glider profiles recorded close to this location are linearly interpolated onto the depths of the concurrent RaTS profiles and are compared (Figure 2.2). The profiles for each day have temperature and salinity Root Mean Square Error (RMSE) values of 0.082, 0.060 and 0.062 °C and 0.038, 0.027 and 0.047 PSU respectively. Whilst these values demonstrate that differences are not insignificant, they are not systematic and appear to be due to isopycnal heave, with the largest differences in the upper $\sim$ 100 m. Consequently, the discrepancies are assumed to be caused by differences in location between profiles, and no temperature offset or drift correction was applied.

Data below 250 m, where the temperature-salinity relationship is most stable, is used to better assess salinity differences between the RaTS and glider profiles. Sorting the temperature profiles from lowest to highest, and interpolating onto a common temperature grid revealed salinity offsets of 0.00816, 0.00853, and 0.00856 PSU for the profiles on days 29, 32 and 45 respectively (Figure 2.3). The mean offset is therefore 0.0084 PSU, which exceeds the accuracy of the RaTS CTD sensor, so this offset was applied as a constant to correct the glider salinity data.

It is worth also mentioning here that the glider's CTD was switched off every other yo (downcast - upcast cycle) so the influence of the pumped CTD on the glider's microstructure data could be assessed. This produced profiles with glider depth but missing CTD data. Consequently, the final glider CTD dataset contains many interpolated CTD profiles. A detailed description of this processing and analysis is found in sections 2.1.4.2 and 2.1.4.3 respectively.

2.1.2 Acoustic Doppler Velocity Data

ADCP data were obtained from a mooring deployed in Ryder Bay between 23rd January 2016 and 11th January 2017, approximately 1 km to the south-east of Site 1 at 67° 34.44′ S and 68° 13.38′ W (Figure 2.1). The RDI Workhorse Long Ranger, 75-kHz upward-looking ADCP was deployed at a depth of 476 m, 18 m above the bottom (494 m). Horizontal u and v velocities were recorded every $\sim$ 16 m and 30 minutes; starting at 451 m to remove the ADCP's blanking distance, this produces a total of 29 bins. The top depth bin contained extremely high velocities that dominated the barotropic signal, and that most likely resulted from contamination by reflections at the surface. Consequently, the top bin was discarded and velocities were interpolated onto a grid with depths of 25 m and then every 50 m between $50 - 450$ m. Data points with a percentage good of less than 50% were also removed, and an offset of $-20\ ^{\circ}$ was applied to correct for magnetic declination. ADCP velocities are projected into a -30° rotated reference frame, in order to derive the alongshore u' and cross-shore v' velocities, with positive u' and v' corresponding with flow out of the bay (east-south-east) and towards the north-north-east, respectively (see Figure 2.1).

2.1.3 Rothera Meteorological Data

Year-round, hourly wind speed and direction data are collected at Rothera Research Station, approximately 4 km to the north-east of the ADCP mooring location. 10 m wind speed and direction data are converted into eastward and northward wind components, and are used to calculate τ_x and τ_y wind stress components following Equation 2.1:

$$\vec{\tau} \ = \ \rho_a \ C_d \ \vec{U_{10}}|\vec{U_{10}}| \ , \tag{2.1}$$

where $\vec{\tau} = (\tau_x, \tau_y)$, $\rho_a \ = \ 1.2$ kg m^{-3} is the density of air, $\vec{U_{10}} = (u, v)$ is the 10 m wind stress vector velocity, and C_d is the drag coefficient. Wind speed is originally recorded in knots, so values are multiplied by 0.51444 to convert to m s^{-1}. Following Trenberth et al. (1990), the value of C_d used varies depending on wind speed; for $U_{10} \ < \ 10$ m s^{-1}, C_d decreases with increasing wind speed, whilst for $U_{10} \ > \ 10$ m s^{-1}, the value of C_d increases with wind speed. Wind stress is projected into a $-30\ ^{\circ}$ rotated reference frame, to infer alongshore $\tau_{x'}$ and cross-shore $\tau_{y'}$ wind stress components, with positive $\tau_{x'}$ and $\tau_{y'}$ oriented out of the bay (east-south-east) and towards the north-north-east, respectively. Wind direction is defined relative to the $\tau_{x'}$ axis, with positive values in the clockwise direction.

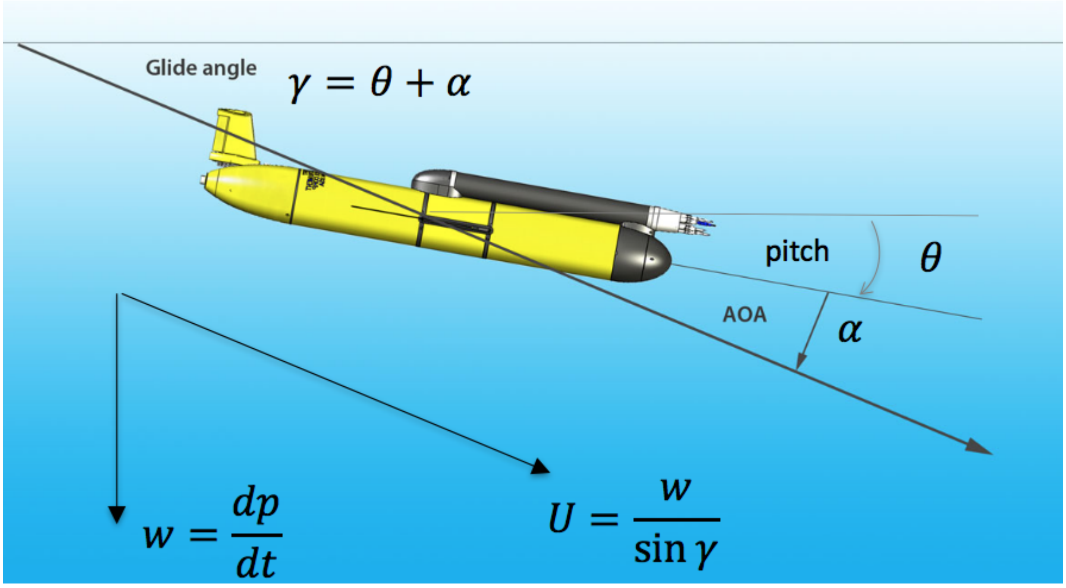

FIGURE 2.4: Glider Angle of Attack (AOA) schematic (Courtesy of Rockland Scientific Inc.). Glider along-path velocity, U, cannot simply be obtained through the rate of change in depth (w); the AOA, α; the angle between the glide angle (γ) and the pitch (θ) need to be accounted for.

2.1.4 Glider Microstructure Data

The Slocum glider deployed in Ryder Bay was also equipped with a Rockland Scientific International (RSI) MicroRider-1000, providing concurrent microstructure data. The MicroRider had four (512 Hz) microstructure probes installed - two thermistor probes and two orthogonally placed shear probes, which can provide estimates of the rate of dissipation of TKE, ϵ. The data collected in this thesis had the shear-1 and shear-2 probes orientated with their sensitive axes in the vertical plane (measuring horizontally) and horizontal plane (measuring vertically) respectively. Processing microstructure data involves multiple stages, and these are detailed in each of the sub-sections below. The final sub-section (Section 2.1.4.7) is an additional investigation into the glider's flight quality.

2.1.4.1 Glider Dynamics

Accurate dissipation rates of TKE from microstructure data require the along-path velocity (U) of the recording instrument to be estimated. U is used in the conversion of raw data into physical units in Equation 2.2, where the recorded charge, Q, is proportional to the cross-stream velocity fluctuation, u, multiplied by the along-path velocity:

$$Q = 2\sqrt{2}SUu \tag{2.2}$$

where $2\sqrt{2}$ is an artifact of the probe calibration and S is the probe sensitivity (C m^2 s^{-2}; Lueck, 2016). Buoyancy driven gliders move up and down in the water column in a saw-tooth pattern, therefore unlike for VMPs, U cannot simply be obtained through the rate of change in depth ($w = dP/dt$). Instead, Equation 2.3 is used:

$$U = -\frac{w}{sin(\gamma)}, \tag{2.3}$$

where $\gamma = \theta + \alpha$. This equation incorporates the angle of attack (AOA; α), which is the angle between the glide angle (γ) and the pitch (θ; Figure 2.4). The AOA must be accounted for to avoid a $\sim$ 10 % overestimation of the glider's speed (Merckelbach et al., 2010; Schultze et al., 2017).

Merckelbach et al. (2010) have developed a hydrodynamic glider flight model that uses the glider's in situ density, buoyancy change and pitch to produce calibration parameters and generate AOAs at each time step. The glider's oil volume is used for the buoyancy change. This was fixed during the deployment to 246 and −248 cc for upcasts and downcasts respectively, to minimise pump noise that could affect the microstructure measurements. To generate the AOAs, the model must first be run to obtain the three required calibration parameters: the glider's volume (V_g), the hull compressibility (ϵ) and the parasite drag coefficient (C_{D_0}). These are generated for each Julian Day by minimising Equation 2.4, the cost function, F:

$$F = \sum_{i}^{N}[w^2 - w_g(C_{D_0}, \epsilon, V_g)^2] \tag{2.4}$$

where w is the measured glider depth rate and w_g is the modelled vertical velocity (see Merckelbach et al., 2010, for more details). The model uses the calibration parameters and the induced drag coefficient, C_{D_1}, to generate vertical water velocities and AOAs. The AOAs are generated using Equation 2.5:

$$\alpha = \frac{C_{D_0} + \alpha^2 C_{D_1}}{\alpha \tan(\theta + \alpha).} \tag{2.5}$$

The model assumes a steady-state flight, where the buoyancy, drag and lift forces are in equilibrium, however, this assumption breaks down in stratified regions producing less accurate results. Consequently, following Schultze et al. (2017), only the modelled AOAs are used here to estimate U (using Equation 2.3, rather than using the modelled vertical water velocities). This retains the glider's dynamic response to variations in external forcing, for example when the glider crosses a strong density gradient (Schultze et al., 2017).

The hull lift coefficient (a_h) is a parameter used in the generation of model calibration parameters and the equation for AOA (Merckelbach et al., 2010, Equation 12). a_h has

FIGURE 2.5: A photograph of a MicroRider equipped Slocum glider with a probe guard installed. The glider has dummy probes installed.

previously been a large source of uncertainty (despite ultimately determining the relationship between the glider's vertical and horizontal speed), with values used ranging from 1.2 to 2.4 rad^{-1} (e.g., Merckelbach et al., 2010; Peterson and Fer, 2014; Palmer et al., 2015). Using the model's default value for a_h generated parasitic drag coefficients and modelled AOAs (Table 2.1) that were larger than the expected values of ~ 0.15 and $\sim 3\,^{\circ}$ respectively (Merckelbach et al., 2010). This suggests that the lift coefficient was underestimated and that a tuning of the model was necessary; increasing the lift coefficient would produce lower AOAs and parasitic drag coefficients. A higher value of the lift coefficient is actually more likely because the default lift coefficient was an estimate for a standard Slocum glider (rather than MicroRider-equipped). Merckelbach et al. (2019) have recently tested and calibrated the flight model using a Slocum glider equipped with a MicroRider, Doppler Velocity Log and Electromagnetic Current meter. This provided a better estimate of the hull drag coefficient, which was used here to rerun the flight model, generating AOAs closer to the expected value of $\sim 3^{\circ}$ (Table 2.1). However, the parasitic drag coefficient calibration parameters are still higher than the ~ 0.15 rad^{-2} reported by Merckelbach et al. (2019). This discrepancy could be explained by the use of a microstructure probe guard (Figure 2.5), which unlike in their study, was used in the Ryder Bay deployment to prevent damage to the probes. This is thought to significantly increase the glider's drag. An investigation into the effect of the probe guard on the glider's drag and dissipation estimates is found in Section 2.1.4.7.

Model run	**Hull lift coefficient** (rad $^{-1}$)	**Mean parasitic drag coefficient calibration parameter** (rad $^{-2}$)	**Mean modelled AOA** (°)
1	1.2	0.35	6.0
2	3.8	0.29	3.5

TABLE 2.1: Hydrodynamic glider flight model parameters and outputs

2.1.4.2 Hotel File Creation

The MicroRider instrument records and stores data separately to the integrated glider sensors, however, various glider data are needed for processing the microstructure data. Consequently, data of interest such as CTD data, the newly calculated AOAs and along-path glider velocity, and GPS coordinates are stored in a hotel mat-file. The hotel file is then ingested by the RSI ODAS MATLAB Toolbox and the data are interpolated onto the same timestamp as the microstructure data.

To prepare the 2016 glider data for a hotel file, several steps are taken to format the data structure created using *loadSlocumData*. The glider's CTD pressure record is multiplied by 10 to convert the data from bar to dbar, whilst the first 94 rows from the CTD data are removed as they contain values collected whilst the glider was out of the water. Additionally, parameters generated by the flight model are reshaped into column vectors, and the pitch and AOAs are converted from radians to degrees.

The 2016 glider deployment has profiles with missing CTD data (Figure 2.6). The empty profiles were produced because the CTD sensor was switched off every other yo so that the influence of the pumped CTD sensor on the microstructure data could be assessed (the outcome is discussed in Section 2.1.4.3). The empty profiles are exemplified by the glider's pressure (thin blue lines, bottom panel), indicating that the glider dived deeper than the CTD pressure record. CTD values across these empty profiles have been incorrectly linearly interpolated as straight lines in depth (as highlighted using the red circle). This is problematic because the CTD temperature data is not only used in the processing of the microstructure data, but also in the hydrodynamic flight model. The model uses the raw glider science files in the AOA calculation, and so the empty profiles also lead to erroneous modelled AOAs and subsequent along-path velocities (Equation 2.3). This is illustrated by the higher-than expected velocities that span across the empty yos (e.g., as highlighted by a red circle, top panel). Consequently, both the erroneous CTD data and AOAs generated for these empty profiles need to be addressed.

The empty profiles were filled in using a multi-stage process. Firstly, all NaNs were removed and the CTD data were interpolated onto the same timestamp as the glider data. The CTD pressure time series could then be subtracted from the original glider pressure time series, leaving a time series containing only the empty profiles. For ease, from here onwards this time series will be referred to as the empty time series, whilst the original

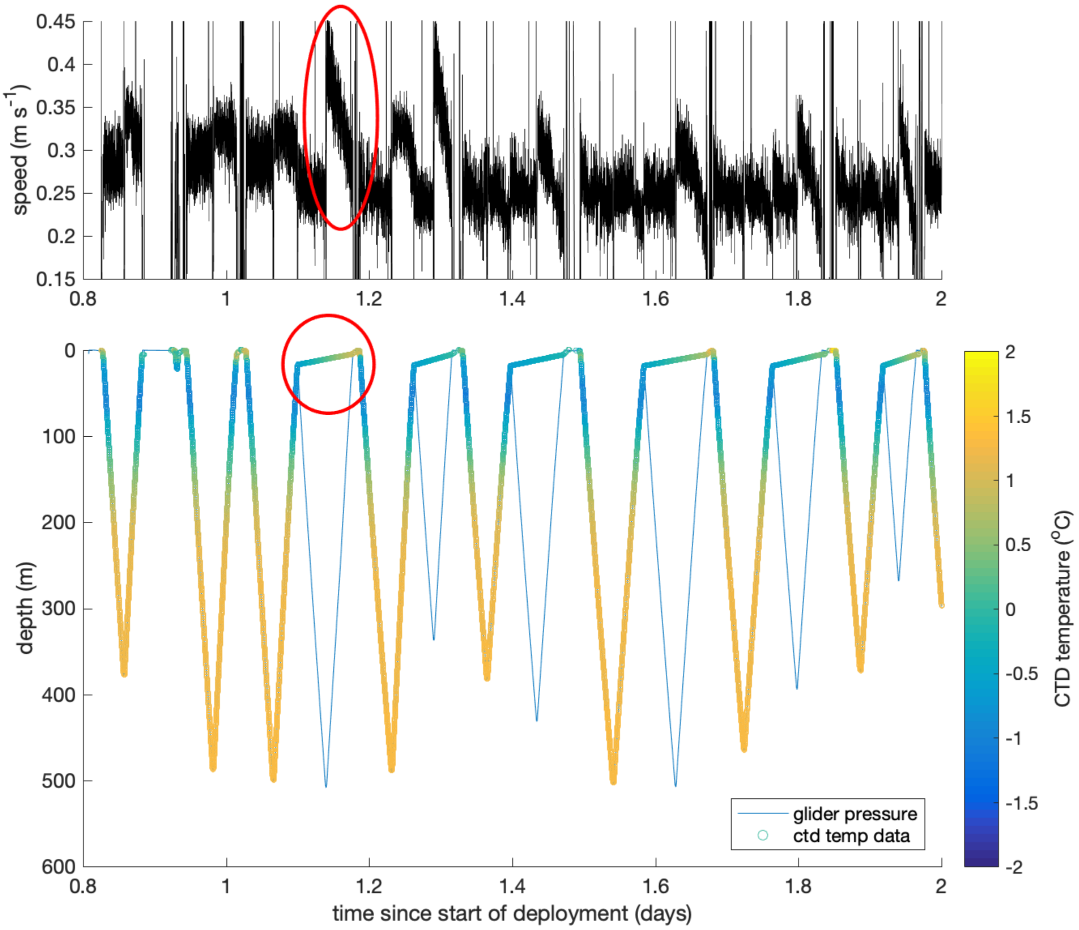

FIGURE 2.6: Empty CTD profiles from the start of the glider deployment. After an initial period, the glider's CTD data was only recorded every other yo, to test whether the pumped CTD sensor had any influence of the dissipation data, leading to 'empty' CTD profiles (bottom panel, red ellipse shows incorrect interpolation). The empty profiles were used in the flight model, causing inaccurate model output that needed to be addressed (e.g., erroneous model speeds - red circle, top panel).

glider time series will be shortened to the original time series. The profiles in the empty and original time series were assigned profile numbers using the $findProfiles$ function from the SOCIB Toolbox. This identifies profiles based on several different user definable parameters that account for small inversions and the glider stalling. The parameters used here were stall = 1.5 m (maximum depth range of a stalled segment), inversion = 1.5 m (maximum allowed depth inversion), length = 40 m (minimum length of a profile), period = 100 s (minimum duration of a profile) and interrupt = 1000 s (maximum time separation between profile segments; see Troupin et al., 2015, for more details).

Following the assignment of profile numbers, an algorithm was designed to iteratively find and match the empty time series profiles with those in the original time series. The two adjacent profiles containing real data are subsequently identified, duplicate

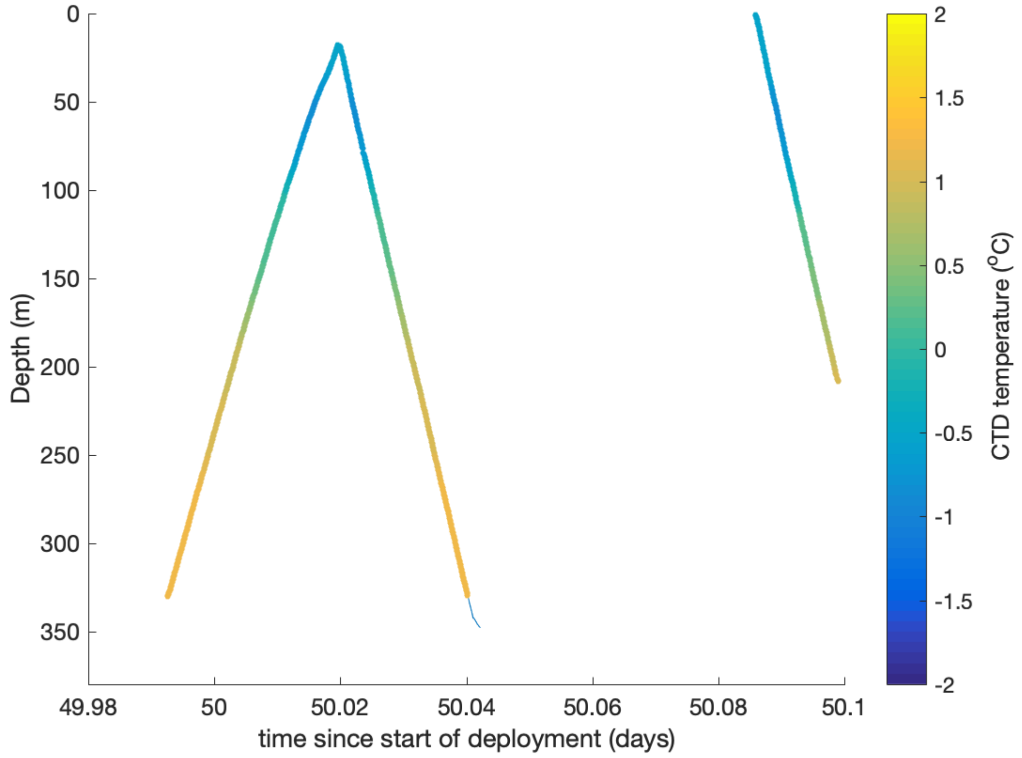

FIGURE 2.7: Incomplete filling of a profile of interest. After searching the adjacent profiles, the profile of interest (centre) may be incomplete. Indicated by the thin blue line.

depths are removed, and then the CTD data are linearly interpolated onto the depths of the empty profile of interest. A mean of the two interpolated profiles is taken and the empty profile is filled in. This process is then repeated for the next profile of interest. If only one of the adjacent profiles contains real data spanning the full depth of the profile of interest (e.g., for the missing upcast at $\sim$ 1.45 days, only the downcast to the right contains data deeper than 430 m; Figure 2.6), then the data from that real profile is used to complete the remainder of the profile. CTD data from the adjacent profiles closest to the profile of interest are the most appropriate to use, to avoid discontinuities in the interpolated profiles. However, for the modelled AOAs, adjacent downcasts (upcasts), were used if the profile of interest was a downcast (upcast). This is because AOAs are opposite in sign between upcasts and downcasts, and also the magnitude of speed, pitch and AOAs flight parameters can vary between the two directions.

After an empty profile is filled in with the first two adjacent profiles, the profile is assessed to see whether there are any NaNs remaining in the profile. For the majority of the empty profiles, no NaNs were found and the algorithm could move onto the next empty profile. However, there are some cases where neither of the two adjacent profiles extend as deep as the profile of interest (Figure 2.7), leaving the profile incomplete. For the CTD data, the algorithm tackles this by searching up to 4 adjacent profiles before

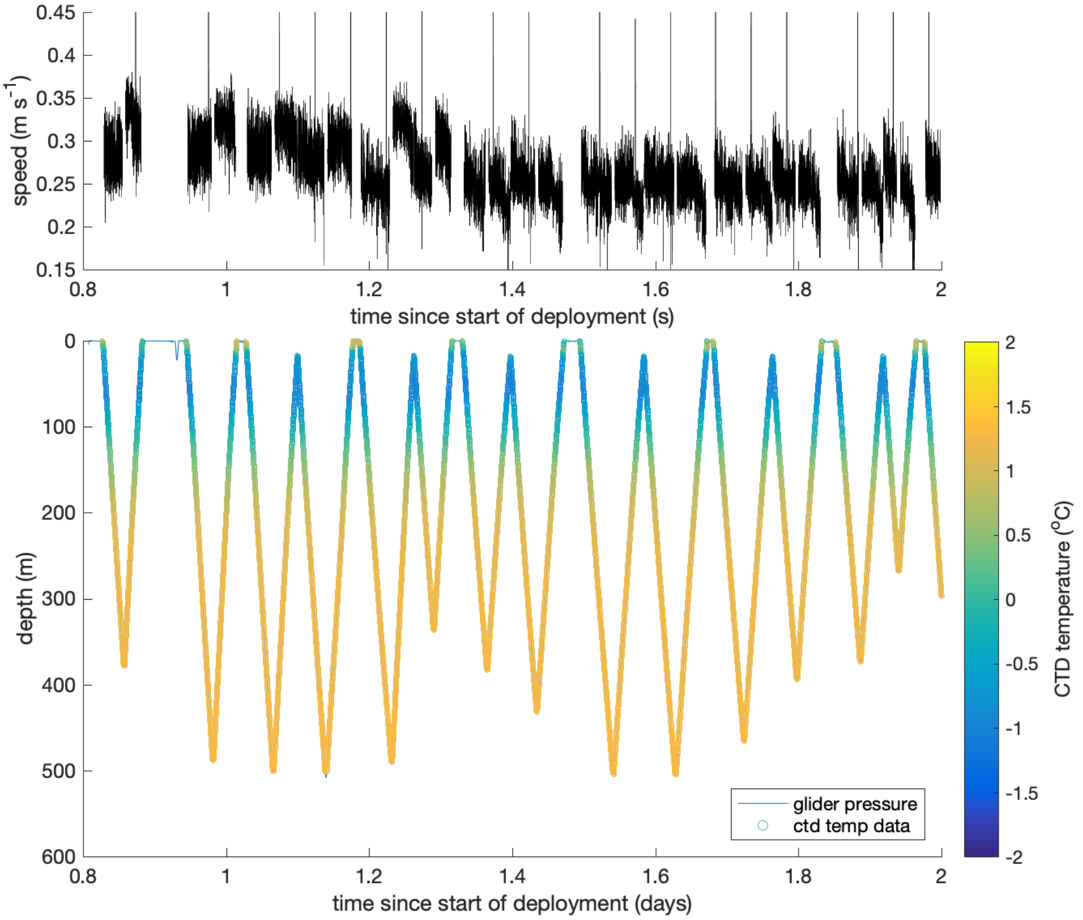

FIGURE 2.8: Interpolated glider speed (top) and temperature (bottom) profiles, for the same period as in Figure 2.6. The interpolation process is complete and the 'empty' profiles have been filled. Note that the remaining gaps in top panel are periods containing no profiles.

and after the profile of interest. For the modelled AOAs, the algorithm moves to the next two down/upcasts, and repeats the process, searching up to 7 profiles. A larger number can be used here because the modelled AOAs are less likely to change in time than the CTD data (upcast/downcast mean and standard errors for the real profiles AOAs are $3.68/-2.78 \pm 0.04/0.04$ °). If filling of the CTD and AOA profiles is not completed after searching the additional profiles, then the bottom part of that profile is deemed lost. Once the AOAs have been interpolated, AOAs calculated < 20 m from either end of the profiles are removed because erroneous values are generated when the glider turns. The AOAs are then used in conjunction with glider's pitch and depth rate to recalculate the along-path velocity of the glider (Equation 2.3). All of the filled profiles are saved into a new variable, along with the original profiles containing real data. The interpolated temperature (bottom panel) and speed (top panel) is show in Figure 2.8, for comparison with Figure 2.6. The empty profiles have been filled with interpolated values.

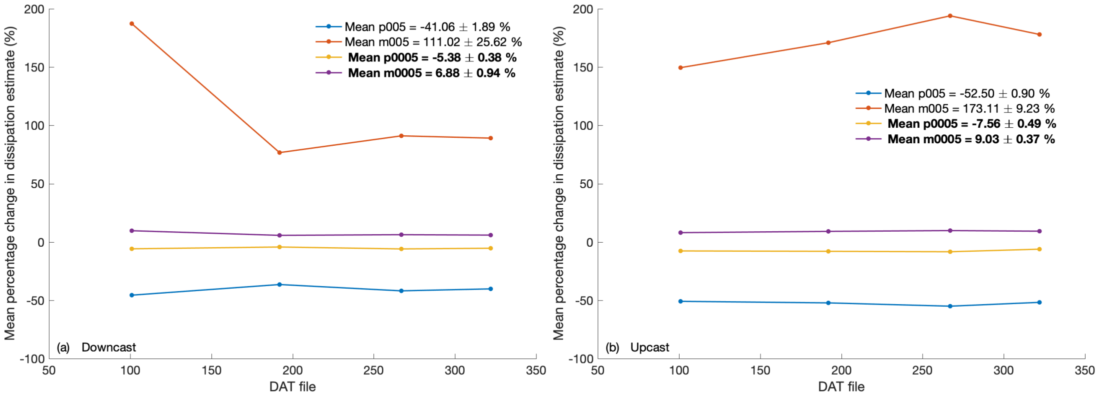

FIGURE 2.9: Investigation into how different along-path glider velocities change the calculated dissipation estimates, using 4 DAT-files that span the glider deployment. (a) Downcast mean percentage changes. (b) Upcast mean percentage changes. The legend shows overall mean percentage change when adding (p) and subtracting (m) velocities from the original value, with a standard error calculated using 1 standard deviation. The bold values in the legend highlight the percentage changes for the cases when the velocities were altered by the same value as the overall RMSE between real and reconstructed velocity profiles.

As a check to ensure that the interpolation algorithm is reliable, profiles from 6 real yos that were also adjacent to real profiles were withheld (these profiles were from the start / end of the main deployment periods, when the glider's CTD was not programmed to turn off every other yo). This enabled a comparison between the original profiles and the reconstructed profiles that were generated by the interpolation method. This was completed separately for the modelled AOAs and the CTD data, using the same interpolation process as outlined above. For the AOAs, values within 50 m from either end of the profile were used in the comparison (as additional precaution to avoid erroneous AOA values at turns). The deployment mean RMSE between the original and reconstructed profiles of modelled AOAs was $\sim 0.5\,^\circ$. Adding $0.5\,^\circ$ to the AOAs of all real upcasts and downcasts values yields a mean change in speed of 0.003 m s^{-1} and -0.005 m s^{-1} respectively.

A pair of upcasts and downcasts from 4 DAT-files, chosen because they span the duration of the glider deployment, were used to test how changing the speed would affect the calculated dissipation rates. 0.005 m s^{-1} and 0.05 m s^{-1} were added and subtracted from the original along-path velocities, and the mean percentage change in dissipation estimates were calculated (Figure 2.9). Decreasing the glider's along-path velocity increases the calculated dissipation rates in both upcasts and downcasts, with the largest percentage changes of up to 194 % occurring when subtracting 0.05 m s^{-1} from the original upcast velocities (Figure 2.9b). When altering the glider's speed by 0.005 m s^{-1}, an order of magnitude lower (and the same as the mean change in speed calculated above), the differences in dissipation estimates are much smaller (between absolute values of

$\sim 5-9$ %) and more consistent between DAT-files. Differences of these sizes are acceptable given that dissipation estimates vary by orders of magnitude, and the AOA interpolation method is therefore deemed viable.

The same 12 real profiles withheld above (those with adjacent real profiles) are also used here to assess the performance of the interpolation method for the CTD profiles. Three example temperature profiles from early (Figure 2.10a), mid (Figure 2.10b), and later in the glider deployment (Figure 2.10c) show that the reconstructed profiles closely resemble their corresponding real profiles, with individual RMSE values of $\sim$ 0.03 °C, $\sim$ 0.04 °C and $\sim$ 0.04 °C respectively. The largest discrepancies typically occur in the upper 200 m, particularly close to the surface (e.g., in the upper 10 m). This is perhaps expected; the temperature variation at these depths is greater than below $\sim$ 200 m, where the reconstructed profiles closely match the real profiles. The low variation in temperature at depth is what makes the search of up to 4 adjacent profiles feasible (to fill in the deepest portions of empty profiles, as described above). The RMSE analysis was conducted for the whole dataset, producing a mean RMSE value of 0.04 °C. Whilst this value is not insignificant, it is acceptable for this study, which predominantly uses the microstructure data. This is because a temperature difference of 0.05 °C causes a $<$ 1 % difference in the calculation of kinematic viscosity and the dissipation estimates of turbulent kinetic energy (which uses the viscosity, see Equation 2.6).

How the empty profile interpolation process performs in temperature-salinity space is also considered. The reconstructed and original CTD data for the withheld real profiles were used to calculate conservative temperature and absolute salinity (Figure 2.11). The largest offsets occur in the AASW. This water mass is closest to the surface (Figure 2.10) and is likely to experience the most variation due to surface fluxes. Despite this, the reconstructed WW and CDW match well with the original data, and the RMSE errors are similar to those reported above. The interpolation method is therefore also deemed viable for the CTD data.

The last parameter to add to the hotel file was the GPS data. The GPS data found in the data structure created by the SOCIB *loadSlocumData* function is only in a raw format, which means that there are data only when the glider is at the surface. The *processGliderData* function was therefore used to linearly interpolate between these GPS positions. This ensures that the dissipation estimates from a single profile are not all located at the same position. Once this step was completed, all of the variables were arranged in structures containing a data field and a corresponding time field; this is called the hotel file. The hotel file makes the data compatible with the RSI ODAS software.

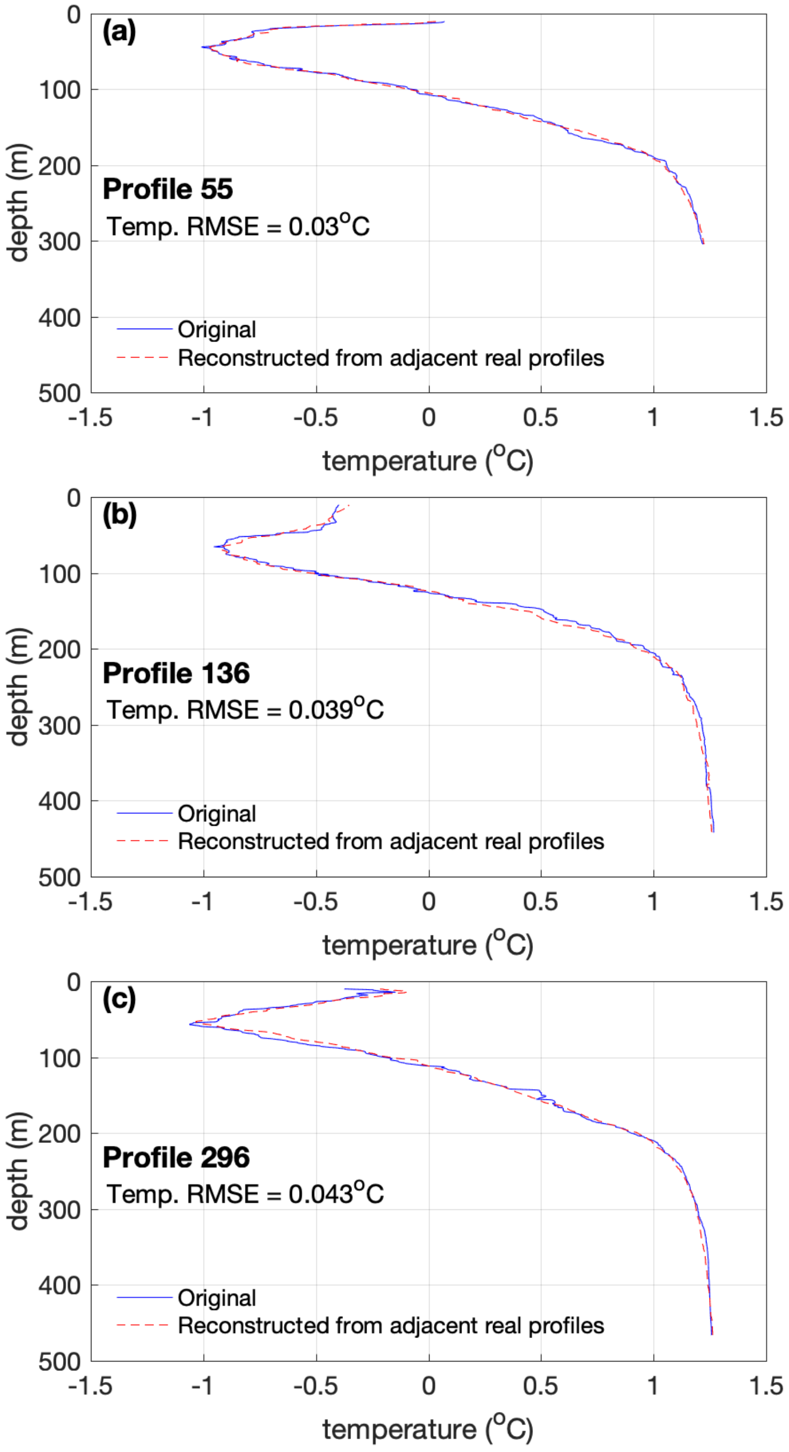

FIGURE 2.10: Reconstructed temperature-depth profiles. Real CTD profiles were withheld and reconstructed using the interpolation method. These reconstructed profiles are compared with the original profiles, with a mean RMSE of 0.04 °C. Profiles 55 (a) 126 (b) and 296 (c) are shown here as examples. These were collected on days 3, 27 and 38 respectively. Note: residuals < 10 m below the surface are expected to be large and were therefore excluded from the RMSE calculations. This avoided skewing the RMSE values high, which would have suggested that the interpolation method was less effective than it actually was for the rest of the water column.

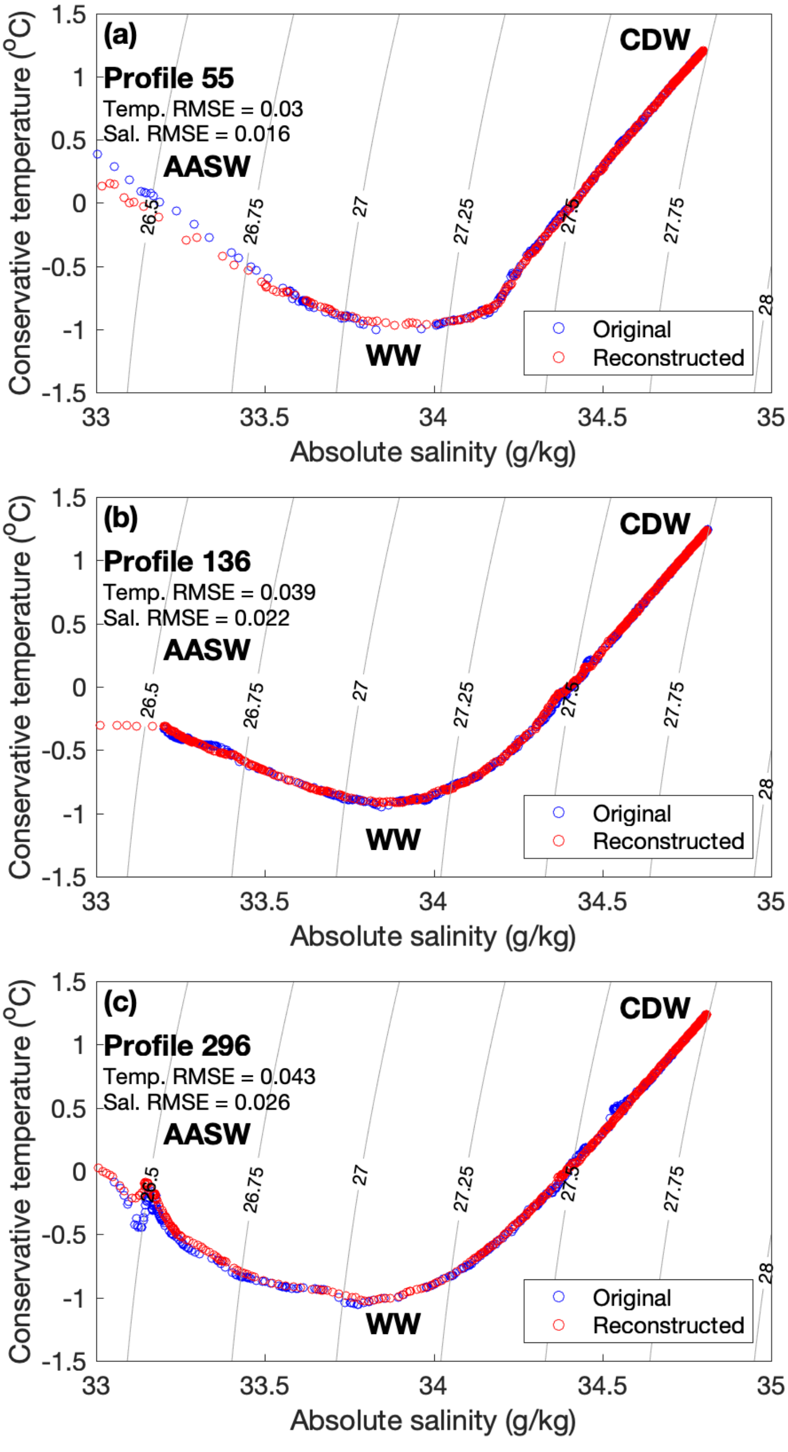

FIGURE 2.11: Comparison of reconstructed CTD data in temperature-salinity space. Antarctic Surface Water (AASW), Winter Water (WW) and Circumpolar Deep Water (CDW) are labelled. Conservative temperature-absolute salinity diagram for profiles 55 (a) 126 (b) and 296 (c), collected on days 3, 27 and 38 respectively. Note: residuals < 10 m below the surface are expected to be large and were therefore excluded from the RMSE calculations. This avoided skewing the RMSE values high, which would have suggested that the interpolation method was less effective than it actually was for the rest of the water column.

2.1.4.3 Preliminary Microstructure Processing

The microstructure dataset comprises DAT-files which are processed using the RSI ODAS MATLAB Toolbox. The main function is *quick_look*, which calls on a multitude of other ODAS functions to provide a quick insight into a DAT-file of interest. A first run of the function produces a mat-file containing all of the data within the DAT-file, presents the data in several figures, and generates dissipation estimates in a structure called *diss*. To use *quick_look* the following syntax is used:

$$diss = quick\_look(fname, P\_start, P\_end, ql\_info)$$

where, $fname$ is the name of the DAT-file, P_start and P_end are the minimum and maximum pressure used for spectral estimates, and ql_info is a structure that provides *quick_look* with a set of tuneable processing parameters (for more information see Murowinski and Lueck, 2012).

Despite its name, *quick_look* calls various functions that can be used to fully process a microstructure dataset, providing that the processing parameters in ql_info are correctly chosen. The default parameters are for VMP data and need to be changed in order to process microstructure data collected using a glider (particularly *vehicle*, $profile\_min\_w$ and $profile\_min\_duration$). The values, descriptions and reasons for the parameters whose default values were changed are found in Table 2.2. Not included are the time offsets (which changes with each DAT-file) and the name of the hotel file. The *diss_length*, fft_length, and *overlap* were chosen to ensure a significant number of degrees of freedom were kept whilst still obtaining a high spatial resolution (this is discussed in more detail at the start of Section 2.1.4.4).

The same 4 DAT-files used to test the dissipation rate sensitivity to changing speeds (Section 2.1.4.2) were also used in a sensitivity analysis assessing the effect of the parameter choices in Table 2.2 on the final dissipation rates. Three *diss_length* (64 s, 32 s, 16 s) and corresponding *overlap* (32 s, 16 s, 8 s) values were used in conjunction with 2 fft_length values (6 s, 2 s) to process each DAT-file (please check Table 2.2 for definitions). Figure 2.12 shows the results for the upcast in DAT-file 267, which is a representative profile. Although little difference can be seen between profiles created at the same *diss_length* but different fft_length values, a smaller fft_length produced fewer (or no) accepted final dissipation estimates (black circles Figure 2.12) after passing through the Quality Assessment Algorithm (see sections 2.1.4.5 and 2.1.4.6). Additionally, having a fft_length value of 2 produced interpolation errors when processing a number of DAT-files. The longer the *diss_length* value, the less high frequency variability in dissipation estimate you obtain, and the overall structure of the profile is clearer, making it is easier to pick out regions of elevated and low dissipation. The HP_cut value was lowered from 0.4 to 0.2 (which is more suitable for a glider), leading

Tuneable parameter	**Value**	**Description**	**Reason**
vehicle	*'slocum_glider'*	Defines the type of vehicle	A glider was used to collect the microstructure data
profile_min_w	0.01	The minimum vertical speed (dbar s^{-1})	Slower than default to look at all of the available data, unwanted data can be removed at a later stage
profile_min_duration	100	The minimum duration in which the pressure and speed must be satisfied (s)	Longer than default to capture full glider profiles, unwanted data can be removed at a later stage
diss_length	64	The time span over which to make each estimate of the rate of dissipation (s)	Long, to increase the signal to noise ratio and the number of degrees of freedom
fft_length	6	The length of the fft-segments that will be ensemble-averaged into a spectrum (s)	Long. Chosen so that ~ 20 spectra are are averaged into each dissipation estimate
overlap	32	The overlap of each dissipation estimate (s)	Half of *diss_length*, giving a 50 % overlap
HP_cut	0.2	The cut-off frequency of the high pass filter applied to the shear-probe signal (Hz)	Lower than default, increases the percentage of accepted spectra (see text)
despike_A	$[Inf, 0, 0]$	The threshold, cut-off frequency and number of points triplet of parameters for the *despike* function applied to the accelerometer signals	These switch off despiking for the accelerometer data
despike_sh	$[8, 0.1, 0.04]$	The threshold, cut-off frequency and number of points triplet of parameters for the *despike* function applied to the shear probe signals	These were chosen through an iterative process (see text)

TABLE 2.2: Values used in *ql_info*. Descriptions are from Murowinski and Lueck (2012), where more information can be found.

to an $\sim$ 4 % increase in the percentage of accepted spectra (after passing the Quality Assessment Algorithm; see Section 2.1.4.5).

The quality of the shear spectra can be strongly affected by noise contamination. This is predominantly caused by vibrations within the glider, and vibrations of the glider's tail fin assembly are known to cause peaks in the frequency spectra at approximately 28, 60, and 80 Hz (Wolk et al., 2009). However, there are also other potential noise sources, such as flow over the glider, plankton striking the shear probes, vibrations associated with additional sensors and electrical noise. Noise can be removed from the shear data using two features of the ODAS Toolbox: the Goodman coherent noise reduction algorithm (Goodman et al., 2006) and the ODAS *despike* function. Vibrations recorded in the accelerometer data are used in the Goodman algorithm to remove coherent signals in the shear data. The coherence estimation in the Goodman algorithm has greater statistical reliability when there are a high number of degrees of freedom (Lueck, 2013). This is achieved when the $diss\_length$ is multiple times the fft_length (Lueck, 2013), so the values used in this thesis were chosen accordingly (see Table 2.2). One risk of using the Goodman technique is that it can potentially underestimate the dissipation rates by removing some non-coherent noise in the process (Fer et al., 2014). Indeed Schultze et al. (2017) observed a decrease by a factor of $0.6 - 0.8$ when using the Goodman technique, however, this is acceptable considering that the dissipation estimates vary by several orders of magnitudes.

One sensor that causes additional vibrations is a pumped CTD. The spike associated with CTD pumped induced vibrations is found in wavenumber spectra at $\sim$ 100 cpm. Where this spike lies relative to the shoulder of the shear spectra (the real environmental peak) depends on the level of dissipation being recorded; more of the wavenumber domain is typically resolved at higher dissipation estimates (Lueck, 2013). Many subsequent microstructure gliders are equipped with an unpumped CTD sensor to avoid any issues, despite the compromise in CTD data quality. The background levels of dissipation within Ryder Bay were relatively unknown, and so the affect this spike would have on the shear microstructure data was also unknown. The portion of the data that is recorded by the vibration-coherent parts of the accelerometer spectra are removed by the Goodman et al. (2006) method, however, there was uncertainty as to how well this would perform. Consequently, as mentioned in Section 2.1.4.2, the glider in this study was equipped with a pumped CTD that was programmed to turn off every other yo. The dissipation estimates generated from real CTD profiles (when the sensor was switched on) and interpolated CTD profiles (when the sensor was switched off) show no systematic differences (Figure 2.13); the 90% bootstrapped errors overlap (see below). Figure 2.13 shows that Ryder Bay dissipation rates were typically lower than 1×10^{-8} W kg^{-1}, and so the CTD spike in the shear spectra was located at wavenumbers higher than the range used to generate dissipation estimates (e.g., Figure 2.14d). Additionally, although the CTD spike was observed in the shear spectra, the Goodman

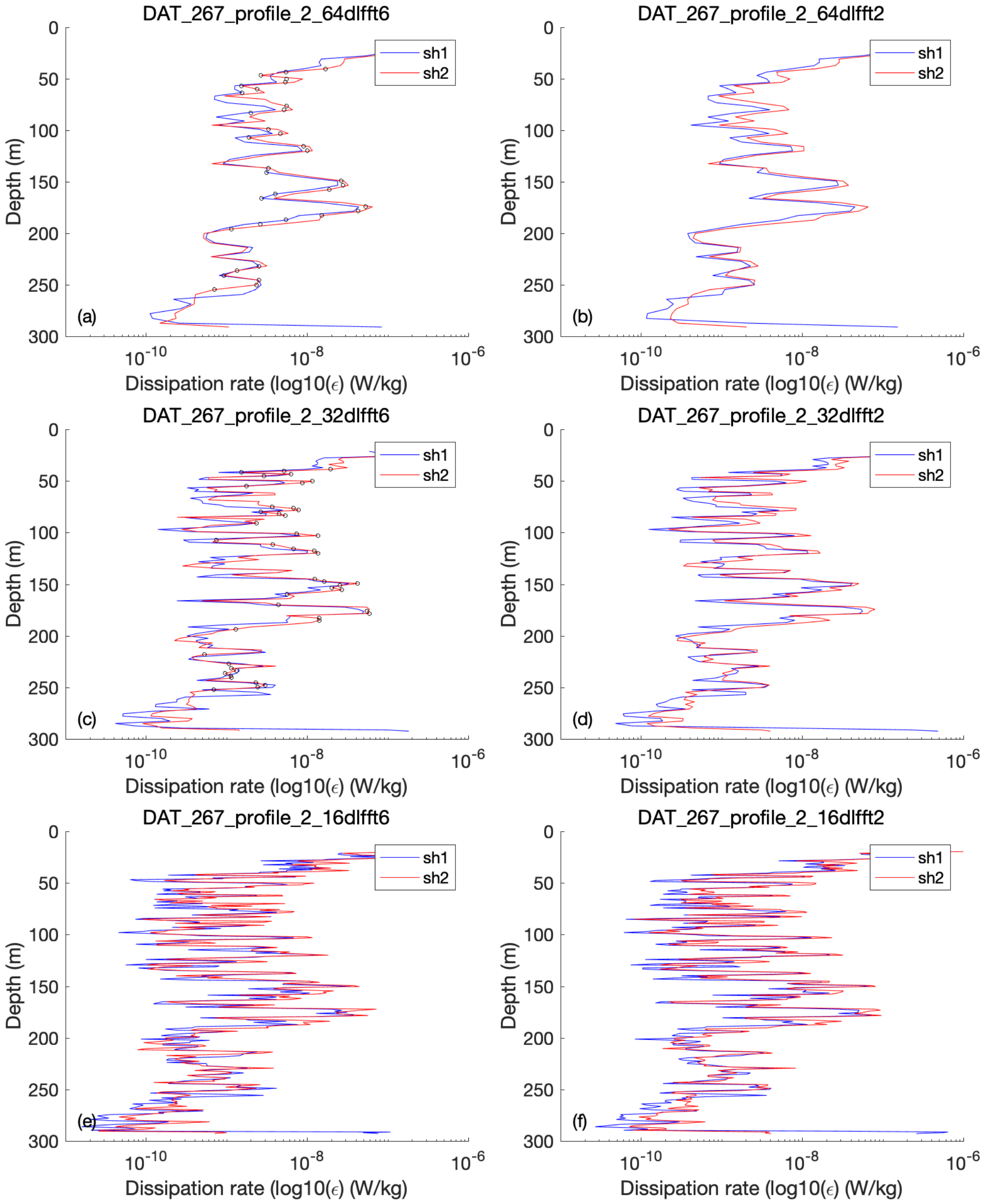

FIGURE 2.12: Comparison of different configurations of *diss_length*, *overlap* and *fft_length* for the DAT-file 267 upcast. Configurations are shown at the end of the subplot title - 64dlfft6, means a *diss_length* of 64 and an *fft_length* of 6. Black circles are final dissipation estimates after going through the Quality Assessment Algorithm (see sections 2.1.4.5 and 2.1.4.6). Note that panels b, d, e and f do not have any accepted dissipation estimates (there are no black circles).

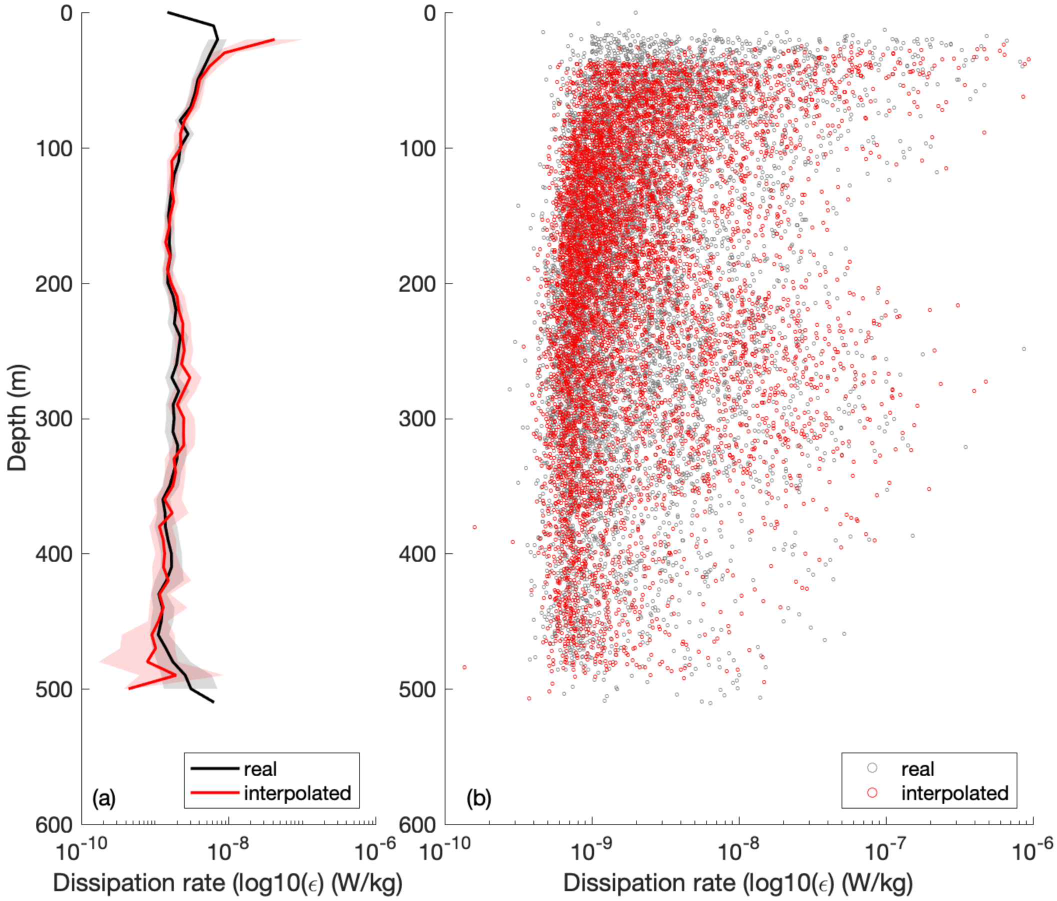

FIGURE 2.13: Comparison of dissipation estimates from real and interpolated CTD profiles (see Section 2.1.4.2). (a) Mean profiles of dissipation on a 10 m depth grid. Shaded regions indicate 90% bootstrapped errors, using 1000 bootstrap datasets (see text for details). (b) All accepted dissipation estimates after passing through the Quality Assessment Algorithm (see Section 2.1.4.5), used to create (a).

et al. (2006) technique was able to effectively remove the peak from the spectra. This suggests that a pumped CTD sensor can be used on a microstructure equipped glider, and therefore all of the available microstructure profiles are initially used in this study.

The bootstrapped error bars in Figure 2.13a and others throughout this thesis were calculated using the *bootstrp* MATLAB function. The function generates a defined number of bootstrap datasets using randomly selected values from the input data and by sampling with replacement (the same values can be selected on multiple occasions). The size of a bootstrap dataset matches the sample size of the input data, and the *bootstrp* function is typically used iteratively for gridded data. For Figure 2.13a the *bootstrp* function was used for each depth grid cell, so the sample size is therefore the number of dissipation estimates within each depth grid cell (i.e. the value is not a defined constant). The number of bootstrap datasets used throughout this thesis is set to 1000, chosen as it is typically much larger than the sample size of the input data, though the error bars show no obvious differences when using larger values (e.g., using 10000 bootstrap datasets). A statistical function is computed on each bootstrap dataset (throughout this thesis the mean is used). The bootstrap means are then sorted from lowest to highest, so the 90th percentiles can be selected.

The ODAS *despike* function was created to remove the plankton strikes, but it can also be used for removing other spikes (see Murowinski and Lueck, 2012, for information on the despiking method). RSI typically suggest turning off despiking for the glider data so that the Goodman technique is more effective, however, when processing the microstructure data without any despiking, a number of shear spectra were significantly contaminated by noise that was not removed by the Goodman method. Figure 2.14 shows a set of example shear spectra with extremely uncharacteristic shapes at frequencies greater than $\sim$ 1.5 Hz (a) or 5 cpm (b). However, when despiking is turned on, the shape of the spectra after using the Goodman method are similar to what is expected (they better match the empirically derived Nasmyth spectra (Nasmyth, 1970); Figures 2.14c,d). Consequently, whilst the despiking of the accelerometer data was turned off, despiking of the shear data was switched on. This removed the largest spikes in the shear data, but still allowed effective use of the Goodman noise removal technique on the majority of profiles (i.e the spikes in the accelerometer data can be used to remove any remaining coherent spikes in the shear data). The despiking function uses threshold, cut-off frequency and number of points parameters, and the values used here are shown in Table 2.2. These were chosen through an iterative process where the despike function was run multiple times using different sets of parameters. The chosen parameters were those that best removed the majority of the shear spikes but did not remove the too much of the real signal; this configuration removed approximately 1 % of the data.

Once ql_info has been configured for a glider, there are 3 additional preliminary processing stages that were automated. Running iteratively through each DAT-file, progress is recorded at each stage, and if the script fails then the DAT-file, profile and stage numbers are recorded for later investigation. Stage 1 is a first look at the DAT-file pressure record, assessing how many profiles the file contains; for the Ryder Bay 2016 dataset there are typically 4 profiles in each DAT-file. A set of processing parameters are recorded for each DAT-file, including the number of profiles, whether the profile is an upcast or a downcast, and a minimum and maximum pressure that can be used for generating average spectra (defined here as the minimum/maximum pressure minus 20 m, to avoid glider turning effects).

Stage 2 is working out the time offset between the glider data within the hotel file and the microstructure data. This is required because there can be discrepancies between the two, likely due to an erroneously configured MicroRider clock or clock drift. For each DAT-file, the time offset is found by calculating the difference in time between the first inflection points in both the glider CTD data and the microstructure pressure

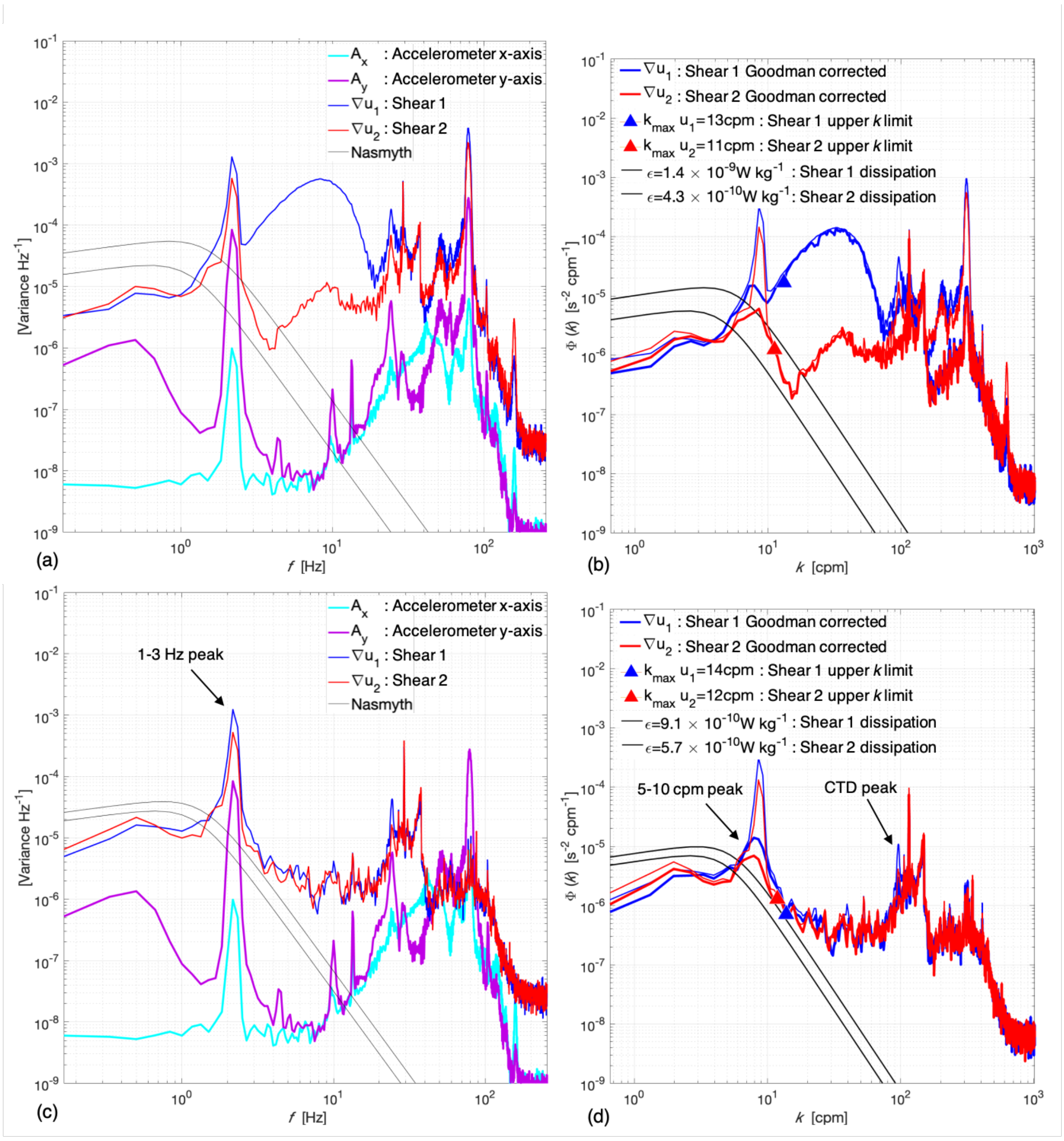

FIGURE 2.14: Despiking the shear data. Example shear spectra without despiking in the frequency (a) and wavenumber (b) domains. Thin red and blue lines indicate the uncorrected shear-1 and shear-2 spectra respectively, whilst the thick lines indicate the corresponding Goodman corrected spectra. The Goodman corrected spectra in b do not have characteristic shapes similar to the Nasmyth spectra. Shear spectra after despiking (using the parameters in Table 2.2) have shapes that more closely resemble the expected Nasmyth spectra in both the frequency (c) and wavenumber (d) domains. Also note the large accelerometer (A_x,A_y) peaks between $1-3$ Hz, which can cause corresponding peaks in the Goodman corrected shear spectra between $5-10$ cpm (as is the case in d). These peaks are discussed in more detail in Section 2.1.4.5. Note that the sharp drop-off in the shear spectra at $\sim$ 38 Hz is due to the low pass cut-off frequency filter that is used for plotting purposes. The spike associated with the pumped CTD is also observed at $\sim$ 100 cpm in (d).

record (Figure 2.15). The microstructure pressure was consistently later than the CTD pressure, so time synchronisation is achieved by multiplying the calculated time offset by -1 and inserting the value into ql_info. $quick\_look$ then adds this offset to the microstructure record. Stage 3 involves running $quick\_look$ for each DAT_file using the

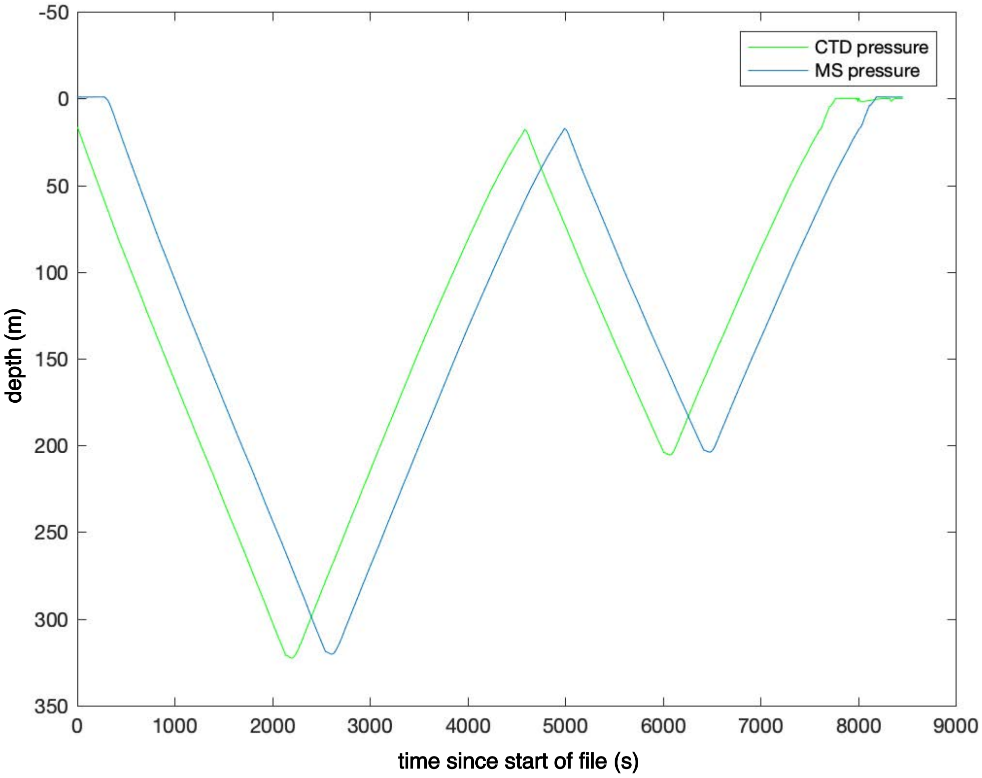

FIGURE 2.15: Time offset. A time offset between the microstructure pressure (MS) and the glider's CTD pressure is calculated for each DAT-file.

newly calculated time offsets. This is to check that no errors are produced when running *quick_look* and that the correct data is used in the calculation of the dissipation of turbulent kinetic energy.

2.1.4.4 Calculation of TKE Dissipation Rates

Once the shear data are converted into physical units using Equation 2.2 and the glider's along-path velocity, spectral analysis is performed to produce shear spectra in the wavenumber domain, $\Phi(k)$. The conversion of the shear spectra from the frequency domain, $\Phi(f)$, to the wavenumber domain uses $\Phi(k) = \Phi(f)U$ and $k = f/U$, and is facilitated by adoption of Taylor's frozen turbulence hypothesis, which assumes that the temporal rate of change is less significant than spatial variability. Dissipation estimates are calculated by integrating $\Phi(k)$ using Equation 2.6:

$$\epsilon = \frac{15\nu}{2} \int_{k_{min}}^{k_{max}} \Phi(k)\, dk\,, \tag{2.6}$$

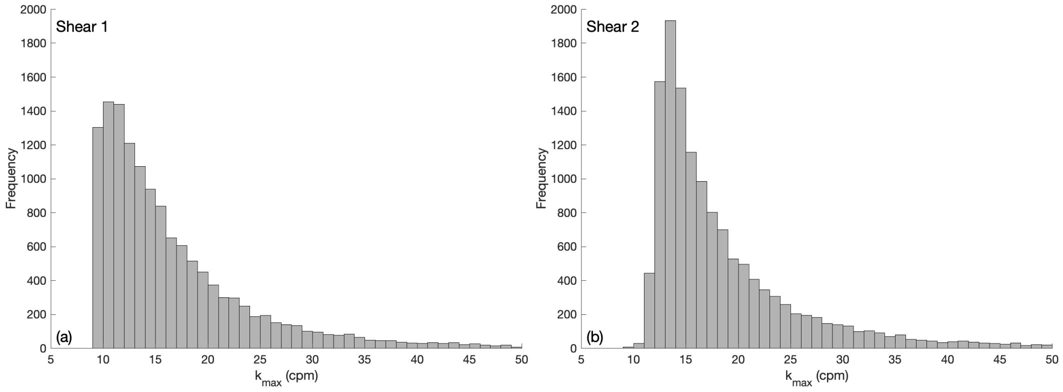

FIGURE 2.16: Histograms of shear-1 (a) and shear-2 (b) final k_{max} values used in the calculation of the dissipation of turbulent kinetic energy estimates (using spectra that passed the Quality Assessment Algorithm - see Section 2.1.4.5). Bins are in increments of 1, and the x-axis upper limit has been truncated for plotting purposes (the maximum values for shear-1 and 2 are $\sim$ 120 cpm).

where $\frac{15}{2}$ is a scale factor accounting for the assumption of isotropic turbulence, ν is the kinematic viscosity of seawater (typically $\sim 1.8 \times 10^{-6}$ m^2 s^{-1} in this dataset, calculated using the fast temperature data), and k_{min} and k_{max} are the minimum and maximum limits of integration, respectively (Lueck et al., 2002; Wolk et al., 2002). k_{min} is the lowest possible wavenumber, and k_{max} is refined through an iterative process (see below), such that the shear spectra best fit empirically-derived Nasmyth spectra (Nasmyth, 1970); these describe the expected shear spectral shape for a given dissipation rate (Wolk et al., 2002; Lueck, 2013). This approach is useful to eliminate the parts of the shear spectrum contaminated with instrumental noise. Each shear probe record is divided into 64 s segments that have a 50% overlap, leading to dissipation estimates being calculated every $\sim$ 7 m horizontally and $\sim$ 5 m vertically (choices are discussed in Section 2.1.4.3). Fast Fourier transform lengths of 6 s are used, with each transform segment also having a 50% overlap using a cosine tapered window. This incorporates 20 dissipation estimates into each ensemble average estimate, providing 40 degrees of freedom (see Lueck, 2013, for more detail). This process is repeated for each shear probe.

Dissipation rates are generated via an iterative process that refines the spectral limits (Lueck, 2013). Initially, a preliminary estimate of ϵ is computed using the lowest wavenumber and k_{max} = 10 cpm, a value that, for the majority of dissipation rates, eliminates contamination from noise at higher frequencies. This initial dissipation estimate is then used to refine the value of k_{max}. If there are enough data points, the value of k_{max} is found by fitting a low-order polynomial to the shear spectrum and finding the spectral minimum. However, if there are not enough points or no minimum is found above 10 cpm, then k_{max} is set to the wavenumber corresponding to 95% of the expected variance under the non-dimensional Nasmyth spectrum (Lueck, 2013). The dissipation estimate calculated using this new value of k_{max} is then used by Lueck (2013)'s model

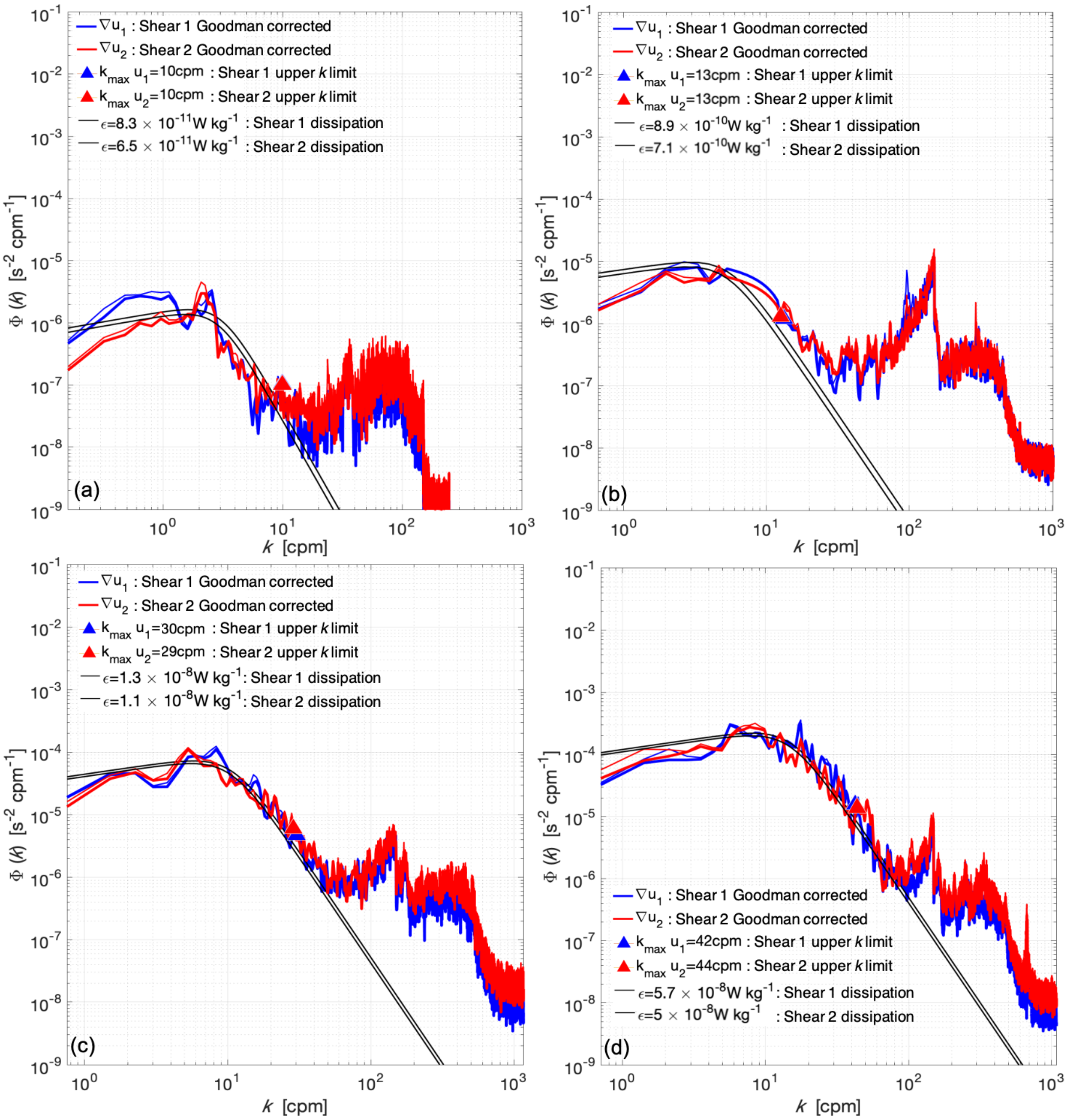

FIGURE 2.17: Example spectra for a range of k_{max} values, showing that higher quality spectra typically have higher k_{max} values. Spectra with final k_{max} values close to 10 (a), 13 (b), 30 (c) and 40 cpm (d). These are spectra that passed the Quality Assessment Algorithm - see Section 2.1.4.5; both shear spectra in b have had a peak removed). It's worth noting that high k_{max} values do not automatically mean the spectra is accepted.

of the integral of the Nasmyth spectrum, which compares the shear spectrum to the Nasmyth spectrum by assessing the fraction of variance resolved using the integration limits. If necessary, the integration limits are then further adjusted to account for the missing variance: if the shear spectrum is above (below) the expected Nasmyth Spectrum then k_{max} is increased (decreased); the aim is to resolve as much of the spectrum as possible for a better dissipation estimate. The range of final k_{max} values used for shear-1 (a) and shear-2 (b) are found in Figure 2.16. Although higher quality spectra typically have k_{max} values close to the wavenumber at which the spectrum drops off due to noise (Figure 2.17 and Schultze et al., 2017), it is worth noting that this is not exclusively the case and the spectra have to be assessed further.

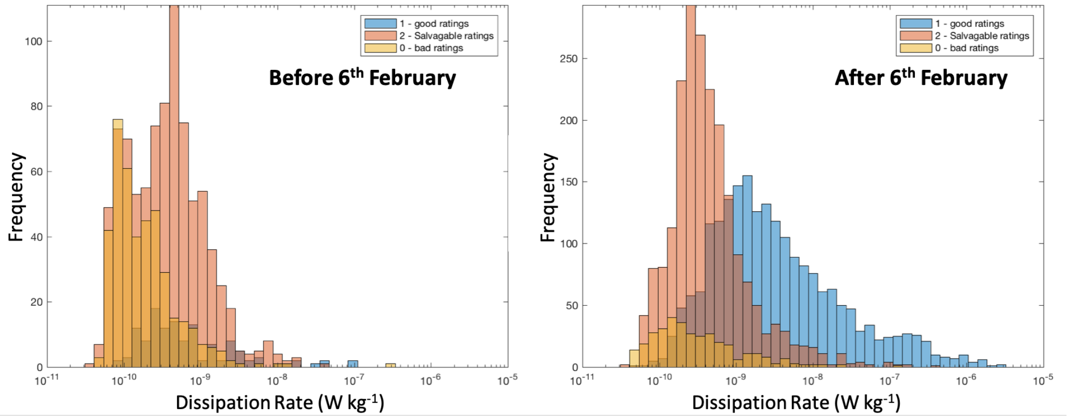

FIGURE 2.18: Peak investigation. A comparison between shear spectra ratings and dissipation rates collected early in the in 2016 deployment (a), and later in the deployment (b). The 6th February is used because the glider was re-ballasted on this date.

2.1.4.5 Assessing Data Quality

An initial assessment of a subset of the dataset revealed that, despite despiking and use of the Goodman coherent noise reduction algorithm (Goodman et al., 2006), shear and accelerometer spectra sometimes contained unrealistic peaks between $1-3$ Hz or $5-10$ cpm (Figure 2.14c,d). Consequently, spectra in this subset were manually assessed and given a rating: 1 for good - even when a $1-3$ Hz peak is present in the accelerometer data there was no clear evidence of the peak in the shear spectra (they resembled the Nasmyth spectra); 0 for bad - the spike was so wide that the shear spectra bared no resemblance to the Nasmyth spectra; and 2 for salvageable - a peak is present, but otherwise the spectra generally fits the Nasmyth spectra at lower and higher frequencies/wavenumbers.

Peaks were found in both upcasts and downcasts with no preference in depth, and were more prevalent at lower dissipation rates (Figure 2.18). A higher proportion of good spectra are observed after 6th February ($\sim 45\,\%$ of the spectra are good and only $\sim 7\,\%$ are bad; Figure 2.18b), compared to before ($\sim 30\,\%$ of spectra are bad; Figure 2.18a). Although many more (31) DAT-files before 6th February were analysed compared to afterwards (9), the peak is most prevalent in spectra associated with lower dissipation rates. This is because the size of the $1-3$ Hz peak is masked by the background spectral level at higher dissipation rates. Part-way through the deployment the glider was re-ballasted in an attempt to increase the glider's H-moment; the distance between the glider's center of buoyancy and center of gravity, which is a measure of the glider's dynamic stability. If the H-moment is too small (large) then the glider is too unstable (stiff). The H-moment for a MicroRider-equipped glider is typically low because of the presence of the MicroRider on top of the vehicle. The spurious peak is therefore believed to be related to the glider's motion, and the resultant spectra thus required careful quality control before being used to estimate dissipation rates. Further investigation into the cause of the peak is found in Section 2.1.4.7.

A multi-stage Quality Assessment Algorithm (QAA) was created by adapting the existing RSI ODAS MATLAB Toolbox to iteratively assess each shear spectrum. Stage 1 of the algorithm involves calculating the sum of the squared normalised residuals, S, between the observed shear spectrum (y_{obs}) and the Nasmyth spectrum (y_{nas}), from the lowest possible wavenumber, k_{min}, up to a wavenumber of $k = 40$ cpm, avoiding the noise drop-off at higher wavenumbers:

$$S = \sum_{k_{min}}^{k=40} \left(\frac{(y_{obs} - y_{nas})k}{\epsilon} \right)^2 . \tag{2.7}$$

The residuals at each point along the spectrum are normalised by dividing by the dissipation estimate corresponding to the fitted Nasmyth Spectrum (ϵ). This allows for a single set of rules to work with spectra that span several orders of magnitude of dissipation. Additionally, each normalised residual is multiplied by the wavenumber at which it is calculated (k). This makes the calculation variance preserving, which means that, upon integration, the variance is equal to the area under the curve. This ensures that appropriate weight is given to each point of the spectrum, rather than erroneously over-weighting residuals at lower frequencies compared to those at higher frequencies; this is important for Stage 2 of the QAA.

In Stage 2, the sum of the squared normalised residuals in the peak region, S_p, are compared with S (Figure 2.19). The peak region, $5 - 12$ cpm (Figure 2.19a), was chosen after observing the peak most commonly in this wavenumber range during the initial dataset assessment. The ratio of the residuals in the peak region with those in the whole spectrum, $R_p = \frac{S_p}{S}$, is calculated using variance preserving spectra and is used to decide whether the spectrum contains a peak that needs removing (Figure 2.19b). If R_p is greater than 0.7 then a peak is identified and removed (0.7 was iteratively chosen by assessing the performance of the threshold based on multiple spectra that span the duration of the glider deployment). The shear spectrum is then linearly interpolated across the peak region (Figure 2.19c), a technique chosen for its simplicity due to a lack of any other available information. This process is the same for both shear-1 and shear-2 spectra, and when a peak is removed it is logged with a peak removal flag (Y/N). The dissipation estimates are then recalculated, ready for the next stage of the QAA.

The same upcasts and downcasts from the 4 DAT-files used in previous sensitivity tests (Sections 2.1.4.2 and 2.1.4.3) were also used here to assess the effect of removing the peak on the dissipation estimates. 631 pairs of shear-1 (Figure 2.20a) and shear-2 (Figure 2.20b) dissipation estimates were calculated before and after peak removal. Overall, 18 and 16 % of shear-1 and shear-2 spectra had a peak removed, and 91 and 95 % of these

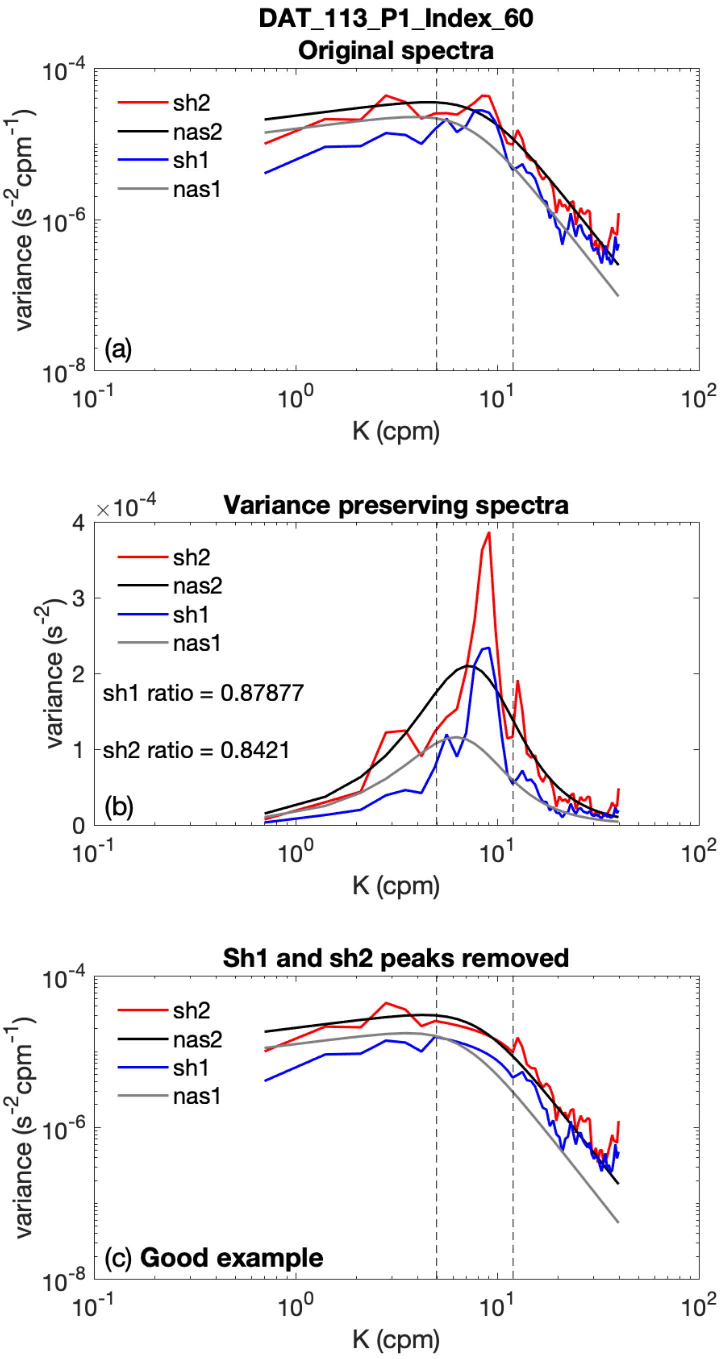

FIGURE 2.19: Peak assessment example. (a) The original spectra. (b) The variance preserving spectra used for assessing R_p, the ratio of the normalised residuals in the peak region with the rest of the spectrum. (c) A peak has been removed in both the shear-1 and shear-2 spectra. Vertical dashed lines signify the peak region, defined as between $5 - 12$ cpm.

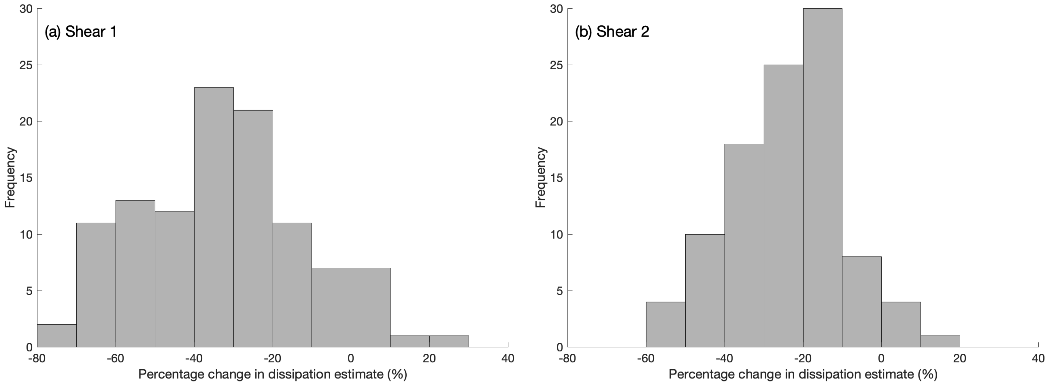

FIGURE 2.20: Peak removal sensitivity analysis. Histograms of percentage change for shear-1 (a) and shear-2 (b), using 10% bins. 110 and 100 peaks were removed for shear-1 and shear-2 respectively. A subset of the whole dataset was used, 631 spectra were used in total).

caused a reduction in the calculated dissipation estimate. 40 and 55 % of the removed peaks caused a percentage change in the range of -40 to -20 % and -30 to -10 % for shear-1 and shear-2 respectively. Whilst the dissipation estimates' order of magnitude do not change, these differences are significant, suggesting that peak removal is a valuable stage in the QAA. After processing the full microstructure dataset, the algorithm removed a peak in $\sim$ 20 % of both shear-1 and shear-2 spectra.

Once the dissipation estimates for the full deployment are produced in Stage 2, they can be assessed as a whole to see if there are any systematic differences that need to be addressed. Figures 2.21a and b show no systematic differences between upcasts and downcasts; the 90% bootstrapped error bars on the mean dissipation depth profiles overlap between $\sim 10-300$ m. Small differences between the upcast and downcast mean profiles are observed at depths $<$ 10 m and $>$ 300 m (Figure 2.21a), however, these are water column depths with a lower number of dissipation estimates (e.g., due the glider flying multiple yos before surfacing and the presence of the ridge), so the mean is likely more sensitive to anomalous values. The region below 300 m exhibits the largest differences, with downcast dissipation estimates being greater than upcast values. The cause of the differences below 300 m is not entirely clear, though it could be related to differences in the glider's along-path velocity. The MicroRider performs best when the glider's along-path velocity is $\sim$ 0.40 m s^{-1} (Wolk et al., 2009), with a tolerable range between $0.2-1.0$ m s^{-1} (Goldberg, J. (RSI), personal comms., February, 2021); the spectral shapes will be clearer at faster along-path velocities. The average along-path velocities for upcasts and downcasts were 0.25 m s^{-1} and 0.34 m s^{-1}, respectively, suggesting that the MicroRider likely performed better on the downcasts (producing better spectral shapes). Dissipation estimates at depths $>$ 300 m would predominantly originate from the deep basin within Ryder Bay, where dissipation rates are typically

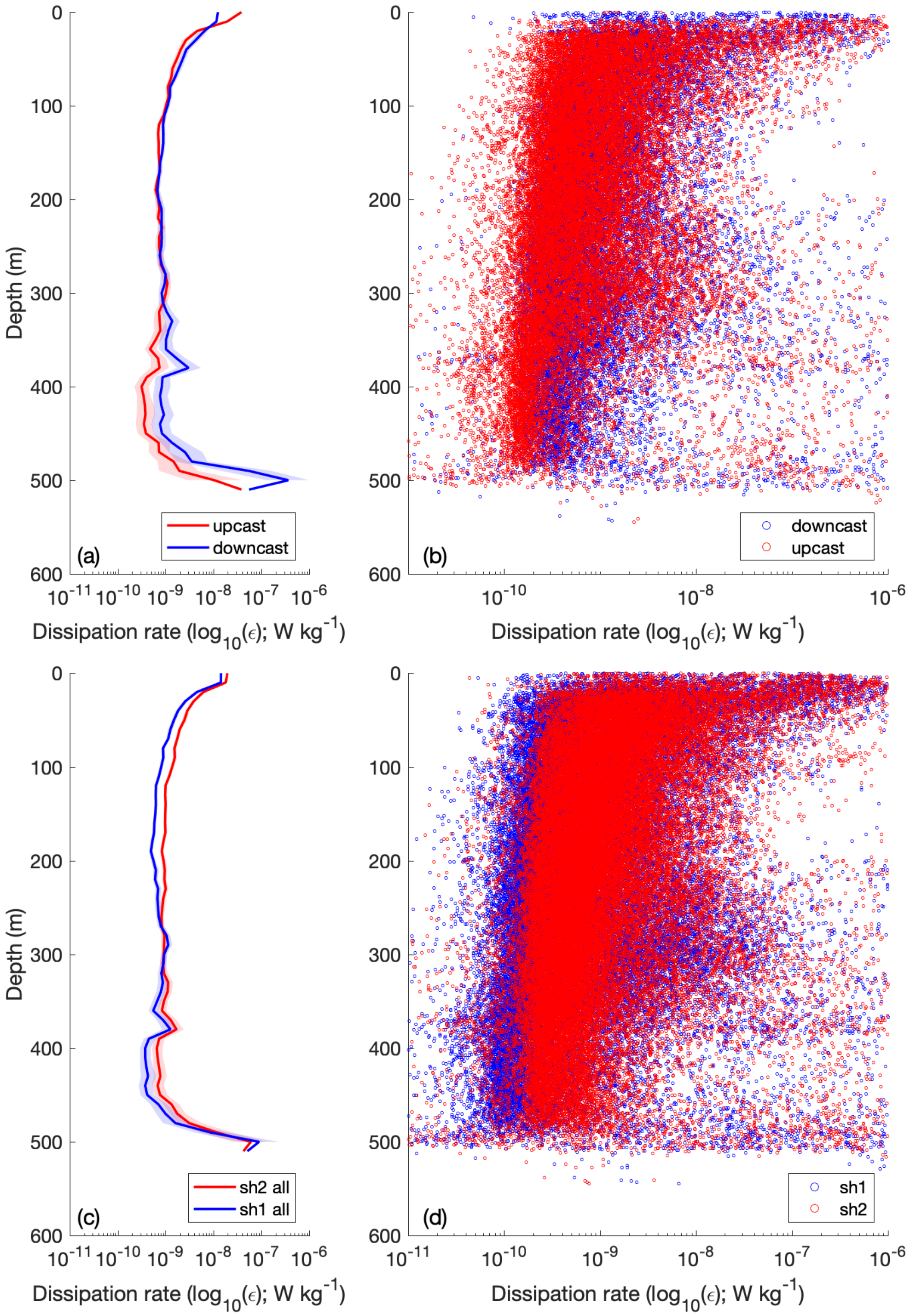

FIGURE 2.21: Assessment of the full dissipation dataset after peak removal in Stage 2. Comparison of dissipation estimates from upcasts and downcasts (top). Comparison of dissipation estimates from shear-1 and shear-2 (bottom). (a) Mean upcast and downcast depth profiles of dissipation on a 10 m depth grid. (b) Individual dissipation estimates from upcasts and downcasts from the full dataset, used to create (a). (c) Mean shear-1 and shear-2 depth profiles of dissipation on a 10 m depth grid. (d) Individual shear-1 and shear-2 dissipation estimates from the full dataset, used to create (c). Shaded regions in (a) and (c) represent 90% bootstrapped errors, using 1000 bootstrap datasets.

lower than in the upper water column, closer to the surface (see Chapter 3). Consequently, whilst the MicroRider may have been able to capture the higher dissipation estimates close to the surface at upcast speeds, it may have struggled to accurately capture the spectral shape of the shear spectra at depth, where there were lower rates of dissipation.

Figures 2.21c and d compares the dissipation estimates from the shear-1 probe with those generated from the shear-2 probe. The mean depth profile of shear-2 dissipation appears slightly higher than the shear-1 dissipation estimates, particularly between $20 - 220$ m. However, the median shear-1/shear-2 ratio is only 0.65 and is therefore deemed acceptable, since it is align with (and in fact smaller than) the accepted factor of 4 used by Schultze et al. (2017). Furthermore, because the shear probes are orthogonally placed in the MicroRider (as previously mentioned, the shear-2 probe in this study was configured to measure vertical shear), it is common for one shear probe to have a higher noise floor than the other, since the glider typically vibrates more in one orientation than another. Consequently, upcast and downcast dissipation estimates from both shear-1 and shear-2 probes can be used in Stage 3 of the QAA.

To assess whether the individual dissipation estimates produced in Stage 2 are reliable, Stage 3 of the QAA compares the shapes of normalised, variance preserving shear spectra with their associated Nasmyth spectra. This is completed by fitting second order polynomials of the form:

$$P_{s,n}(k) = C_1 k^2 + C_2 k + C_3$$

to the shoulder of the shear, P_s, and Nasmyth spectra, P_n (Figure 2.22), where C_1, C_2 and C_3 are the polynomial coefficients and k is the wavenumber. The shoulder is used here because it is the region that is used to generate the dissipation estimates.

The shoulder region is specified as a number of indices either side of the maximum value of the Nasmyth spectrum (Nasmyth, 1970), which is an index of N_{max}. N_{max} varies depending on the dissipation rate because the shoulder of spectra move to higher wavenumbers with increasing dissipation (Lueck, 2013). This alters the number of available points in the spectra, with larger dissipation rates having a greater number of points either side of N_{max}, so different index ranges (N_r) are used for different dissipation estimates:

$$\text{If } \epsilon < 1 \times 10^{-8} WKg^{-1}, N_{range} = N_{max} - 3 : N_{max} + 25.$$

$$\text{If } \epsilon > 1 \times 10^{-8} WKg^{-1}, N_{range} = N_{max} - 7 : N_{max} + 50.$$

The ranges were chosen by assessing the indices required to capture the shoulder for multiple spectra across the duration of the deployment. Some spectra at low dissipation estimates had fewer than 3 data points at wavenumbers less than N_{max}, so in these

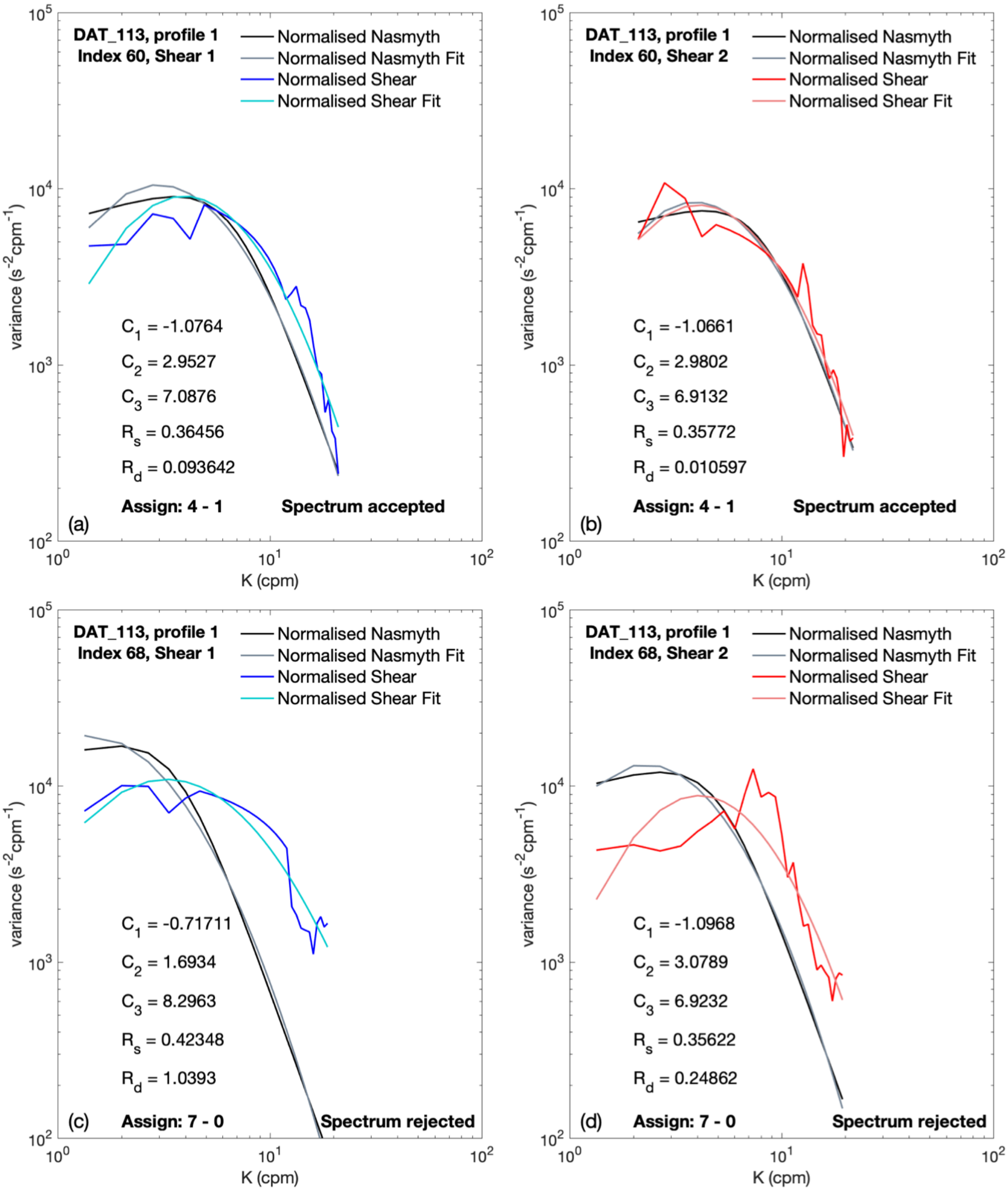

FIGURE 2.22: Example polynomial comparisons. 2^{nd} order polynomials are fitted to the shear-1 (a,c) and shear-2 (b,d) spectra and their corresponding Nasmyth spectra. Coefficients and ratios are compared to conditions to assess whether the spectra should be accepted (number - outcome; see Table 2.3 for more information). Example from accepted (a,b) and rejected spectra (c,d) are shown.

Number	**Condition**	**Outcome** (1 = accepted, 0 = rejected)
1	$C_1 \geq -0.95$	$Y = 1; N = 0$
2	$-0.95 < C_1 \leq -0.80; C_2 < 2$	$Y = 1$
3	$-0.95 < C_1 \leq -0.80; R_{diff} < 0.08$	$Y = 1$
4	$0.25 < R_s < 0.4; C_1 < -0.75$	$Y = 1$
5	$0.25 < R_s < 0.4; C_1 < -0.70; R_{diff} < 0.1$	$Y = 1$
6	$0.25 < R_s < 0.45; C_1 < -0.60; R_{diff} < 0.07$	$Y = 1$
7	$R_{diff} > 0.2$	$Y = 0$
8	$C_1 > 0$	$Y = 0$

TABLE 2.3: The 8 conditions used to assess the quality of shear spectra. Shear spectra are compared to Nasmyth by fitting second order polynomials and comparing the coefficients. Thresholds were chosen by assessing the performance of the conditions based on multiple spectra that span the duration of the glider deployment.

cases the minimum for the index range was set to 3.

The polynomial coefficients are recorded and the $R = C_1/C_2$ ratio is calculated for both the shear and Nasmyth spectra (R_s and R_n respectively). The difference between these ratios $R_{diff} = |R_s - R_n|$ provides an additional metric that is used to assess each spectrum against 8 conditions (Table 2.3). These conditions are used to decide whether or not a spectrum is accepted; later conditions overwrite previous. A rating of 1 is given if the spectrum is accepted (Figures 2.22a,b) and a rating of 0 is assigned if it is rejected (Figures 2.22c,d). The results along with the final condition met are recorded for each shear spectrum. After processing the full microstructure dataset, the algorithm accepted 19% of the shear-1 spectra and 32% of the shear-2 spectra. This discrepancy is not explained by malfunctioning shear probes: both shear probes continued to work sufficiently throughout the deployment. However, the discrepancy stems from a greater number of low shear-2 dissipation estimates being accepted by the QAA compared with those from shear-1 spectra (Figure 2.23a). This is likely linked to the number of similarly low shear-2 dissipation estimates that were accepted in the downcasts (Figure 2.23b; 66%, compared to 34% from upcasts - before calculation of the final dissipation estimates; see Section 2.1.4.6). More low dissipation estimates were accepted in downcasts due to differences in the along-path velocity of the glider, with average along-path velocities of 0.25 m s^{-1} on the upcasts and 0.34 m s^{-1} on the downcasts. As previously mentioned, the MicroRider performs best when glider along-path velocities are $\sim$ 0.40 m s^{-1} (Wolk et al., 2009), with a tolerable range between $0.2 - 1.0$ m s^{-1} (Goldberg, J. (RSI), personal comms., February, 2021), and the shear probes are orthogonally placed. The higher number of accepted spectra from the shear-2 probe in the downcasts therefore could reflect a preference in probe orientation when travelling in the this direction. This is supported by the slightly higher number of accepted dissipation estimates from the shear-1 probe when travelling in the upcast direction (Figure 2.23c).

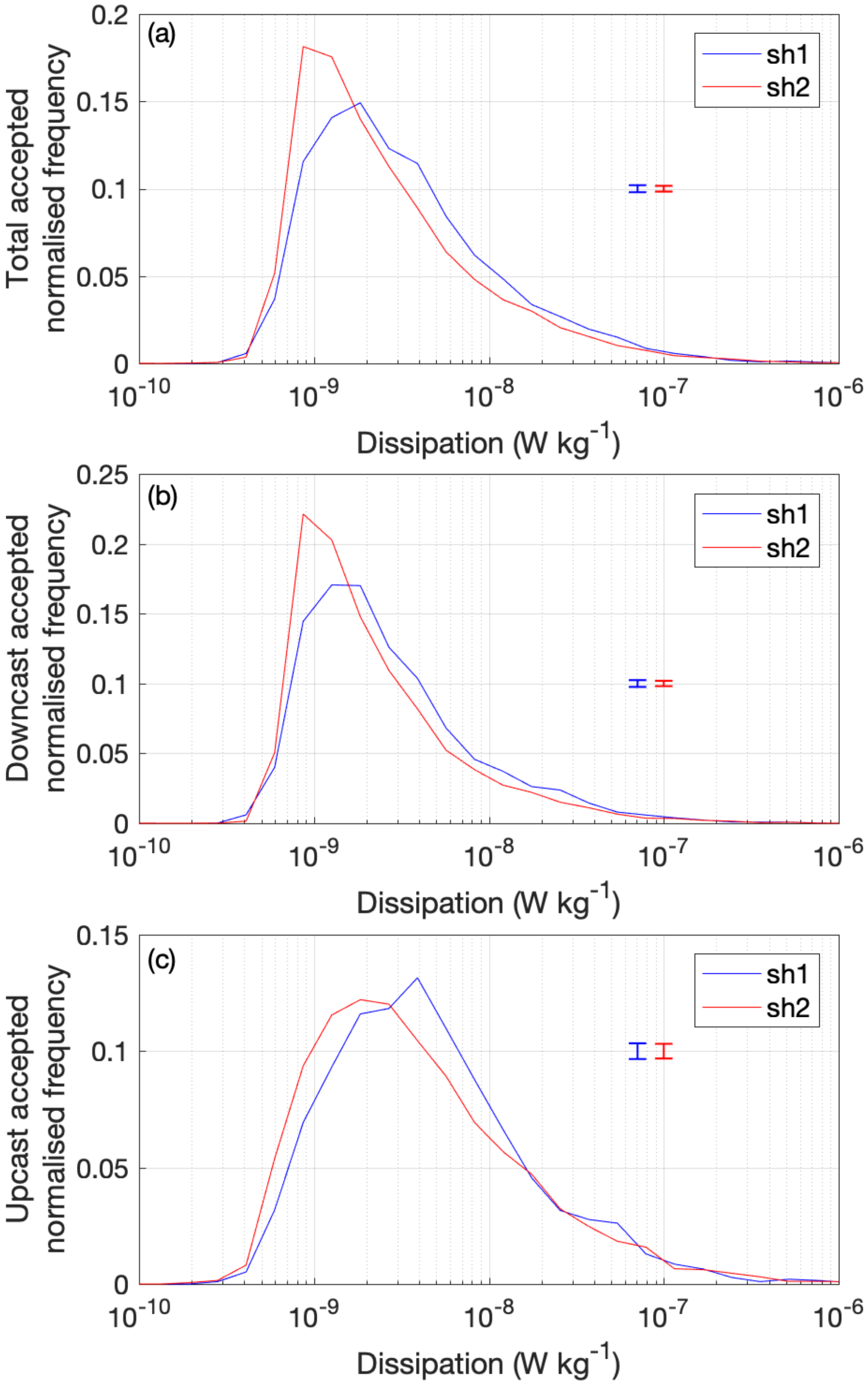

FIGURE 2.23: Comparison of the shear-1 and shear-2 accepted dissipation estimate distributions. Total (a), downcast (b) and upcast (c) distributions are shown. Note the peak at low dissipation estimates in a and b, and the slight preference for shear-1 in c. The numbers in these panels correspond to dissipation estimates that passed the QAA, but are before the final dissipation estimates are calculated (see Section 2.1.4.6). Mean 90% bootstrapped error bars, using 1000 bootstrap datasets, are shown in each panel for shear-1 (blue) and shear-2 (red), respectively (averaged across dissipation rate).

2.1.4.6 Calculating Final Dissipation Estimates

Once a profile's spectra have past through the Quality Assessment Algorithm, additional measures are taken to ensure that only data of the highest quality is used in analysis. Spectra generated less than 20 m from inflection points are discarded (not only could the recorded shear data be affected by turns, the modelled AOAs have been removed from these parts of the profiles, and so the glider's speed will be incorrect). Similarly, although there appears to be little contamination of the microstructure spectra, to be safe the gradient of the battery position is used to remove spectra collected during periods of battery movement.

Final dissipation estimates within a profile depend on the percentage of accepted shear-1 and shear-2 spectra within that profile. If either shear-1 or shear-2 contains less than 30% of accepted spectra, then data from that probe are ignored for that profile. For profiles that have over 30% accepted spectra from both shear probes, a mean log_{10} of the two dissipation estimates was calculated. Taking the mean log_{10} of dissipation estimates is typically necessary to avoid mean values being dominated by high values in a log normal distribution. Ultimately this method has a negligible impact on the final dissipation estimates in this study because the shear-1 and shear-2 estimates are close together (see the shear-1/shear-2 ratios below). However, the method was used here to ensure consistency with mean values reported elsewhere in this study. Dissipation estimates from both probes were always used where possible, unlike Schultze et al. (2017), who used the estimate from one probe if the shear-1/shear-2 ratio was greater than 4. This was not deemed necessary here, since the median shear-1/shear-2 ratios from the pre- and post-quality controlled datasets were only 0.65 (shown above) and 0.7 (not shown), respectively. Profiles containing less than 30% of accepted spectra in both shear-1 or shear-2 were not used. Despite taking this extra precaution, a comparison of the overall mean vertical profiles of dissipation using no threshold for removing the profile altogether and 30% and 50% thresholds, suggests that the difference is relatively small (all of the 90% bootstrapped error bars overlapped; Figure 2.24).

Using these somewhat conservative criteria, 26% of the dissipation estimates were of good quality, and are considered in this study. $\sim$ 52 % of the estimates used shear-1 data and $\sim$ 95 % used shear-2 data. The glider performed better in the downcasts than the upcasts, with $\sim$ 81 % of the accepted dissipation estimates coming from the downcasts and only $\sim$ 19 % from the upcasts. As mentioned above, these discrepancies likely reflect the different upcast and downcast velocities, with downcasts having a higher velocity closer to the optimum glider speed for performance of the MicroRider. The differences are also likely exaggerated due to the exclusion of whole profiles of shear-1 or shear-2 that occur under the 30% threshold of accepted spectra; this final step in the algorithm rejected 10% and 7% of the overall shear-1 and shear-2 spectra respectively. The high percentage of rejected spectra primarily stems from Ryder Bay being typically

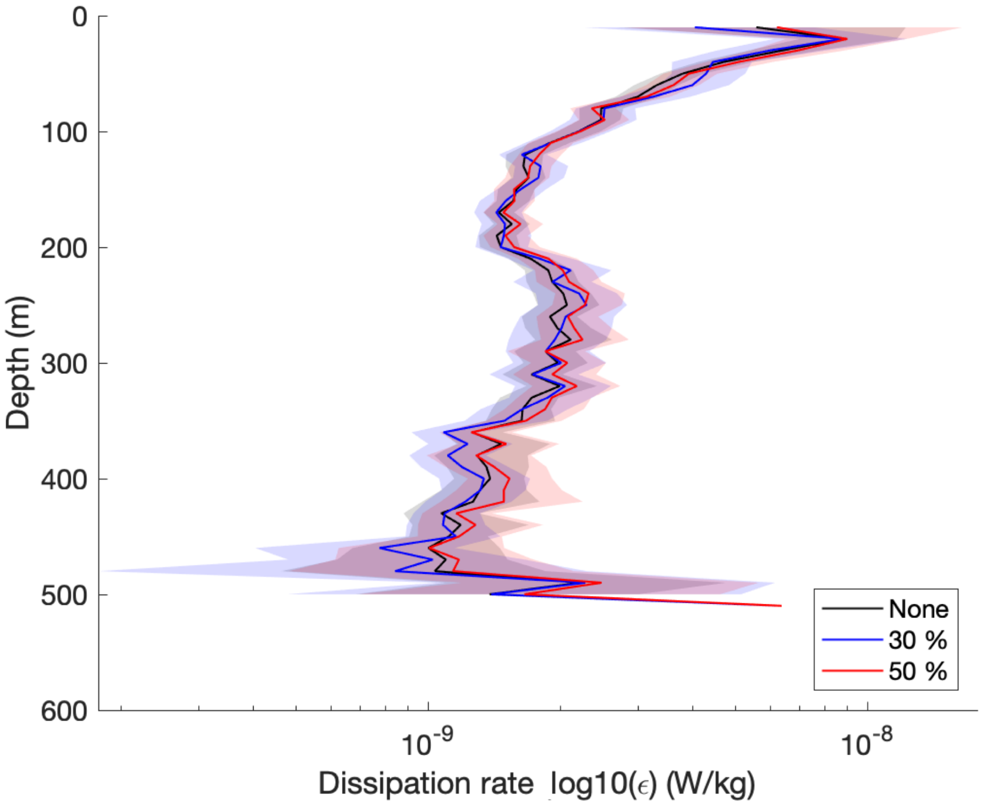

FIGURE 2.24: A comparison of deployment mean dissipation profiles, using all good spectra (black), after excluding profiles with less than 30 % (red) and 50 % (blue) good spectra. A 10 m depth grid is used. The total number of dissipation estimates used in each case were 18632, 13538, and 8871 respectively. Filled regions represent 90 % bootstrapped errors, using 1000 bootstrap datasets (colors match the mean profiles).

a low-dissipation environment, with dissipation rates close to the noise floor of the instrument, leading to flat spectra that did not clearly agree with the Nasmyth spectra. Additionally, 11% of the overall shear-1 and shear-2 fell within $<$ 20 m from either end of profiles, and were rejected to remove noise contamination associated with glider turning.

The final dissipation estimates are saved into a matrix called $information\_extract\_all\_saved.mat$. This contains: time, CTD, GPS, battery position and oil volume data, whether or not the dissipation estimate was produced from an empty CTD profile (see Section 2.1.4.3). Also included are the along-path velocity model outputs (see Section 2.1.4.1), and the QAA outcome. This is the methodology product that is used in chapters 3 and 4. The final processed glider dissipation data, together with the glider hydrographic data from thesis, have been published (Scott et al., 2021a), and can be found at `DOI:10/fx2f`.

2.1.4.7 Peak/Probe Guard Investigation

The higher than expected parasitic drag coefficients obtained during the Ryder Bay deployment (Table 2.1), and the $1-3$ Hz peak found in a large proportion of the shear spectra (see Section 2.1.4.5), prompted further investigation into the glider's flight quality and the possible influence of the installed probe guard. A MicroRider equipped Slocum glider was deployed in Loch Linnhe, off of the coast of Oban, Scotland, over a period of $\sim$ 3 days between 20th - 23rd November 2018. The glider was first deployed without a probe guard, before being recovered, fitted with a probe guard, re-ballasted on deck using wing rail weights, and then deployed for a further day. During the second day of the deployment, the glider converged on an oil volume and battery position that produced efficient flying (i.e. not pumping full oil each yo) and the best possible symmetry between upcasts and downcasts (notice the reduction in pumped oil volume and roll/pitch variability; Figure 2.25). This test was conducted with the hypothesis that the probe guard would significantly alter the glider's flight quality, leading to the observed $1-3$ Hz shear spectra peak.

AOAs, parasitic drag coefficients and along path glider velocities were all generated throughout the deployment using Merckelbach et al. (2010)'s hydrodynamic flight model (Figure 2.26). 0.5 days before and after the installation of the probe guard is the period that provides the best data for comparison, as it is then that the glider has finished converging on an optimum battery position and oil volume (and were subsequently fixed), and the pitch and roll are relatively unchanged.

To assess the influence of the probe guard on the glider's flight quality, the profile-means for each of the recorded flight variables were calculated and split into upcasts and downcasts (Figure 2.27). This was necessary because the glider's flight quality is often different between the two directions, and splitting up the profiles in this way enables comparison between pre- and post-probe guard installation values. A two-sample t-test was used to statistically compare the mean upcast and downcast flight variables before and after the probe guard installation. The null hypothesis was that the mean flight variables pre- and post-probe guard will be equal. The null hypothesis for the mean values of oil volume, pitch and battery positions, could not be rejected for both upcasts and downcasts at the 95 % significance level, suggesting that the probe guard has no effect on these variables. Although there is only a small decrease in the glider's roll (0.3 °), the difference is statistically significant for both upcasts (both $p = 1.7 \times 10^{-9}$) and downcasts ($p = 1.6 \times 10^{-5}$).

Figure 2.28 shows the profile average model output for upcasts and downcasts. Ignoring the AOAs at the start of the detailed analysis period (before 22/11; Figure 2.28), there is no significant difference between the AOAs before and after the probe guard installation ($p = 0.21$ and $p = 0.46$ at the 5 % significance level, for upcasts and downcasts respectively). The values at the start are ignored because they are smaller ($<\sim$ 2.5

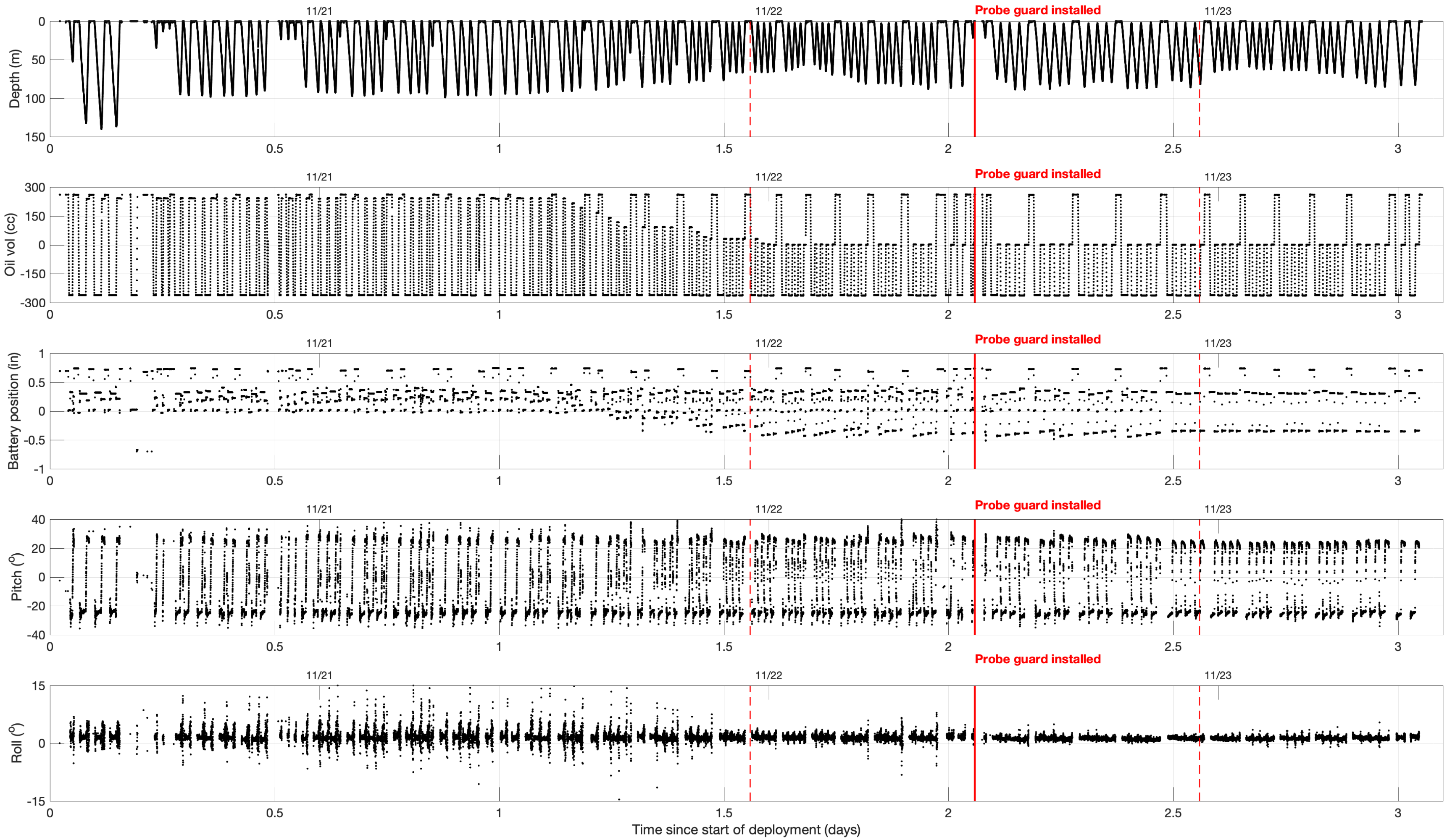

FIGURE 2.25: The glider flight variables for the deployment in Oban, Scotland. The glider was first deployed without a probe guard, before being re-ballasted and redeployed with a probe guard. The red dashed vertical lines represent the period over which the detailed analysis was conducted.

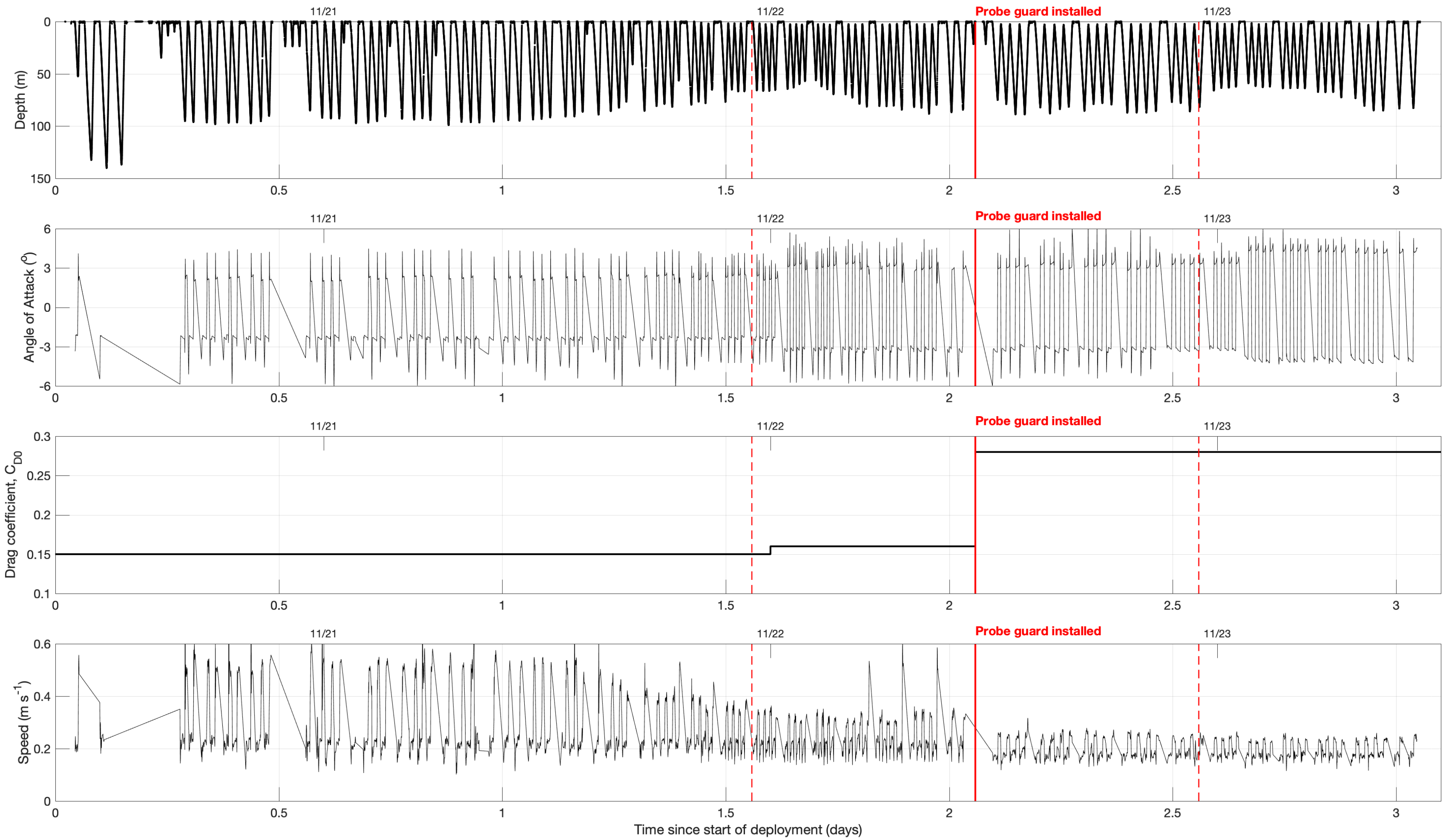

FIGURE 2.26: The modelled flight variables for the deployment in Oban, Scotland, using Merckelbach et al. (2010)'s hydrodynamic flight model. The glider was first deployed without a probe guard, before being re-ballasted and redeployed with a probe guard. The red dashed vertical lines represent the period over which the detailed analysis was conducted.

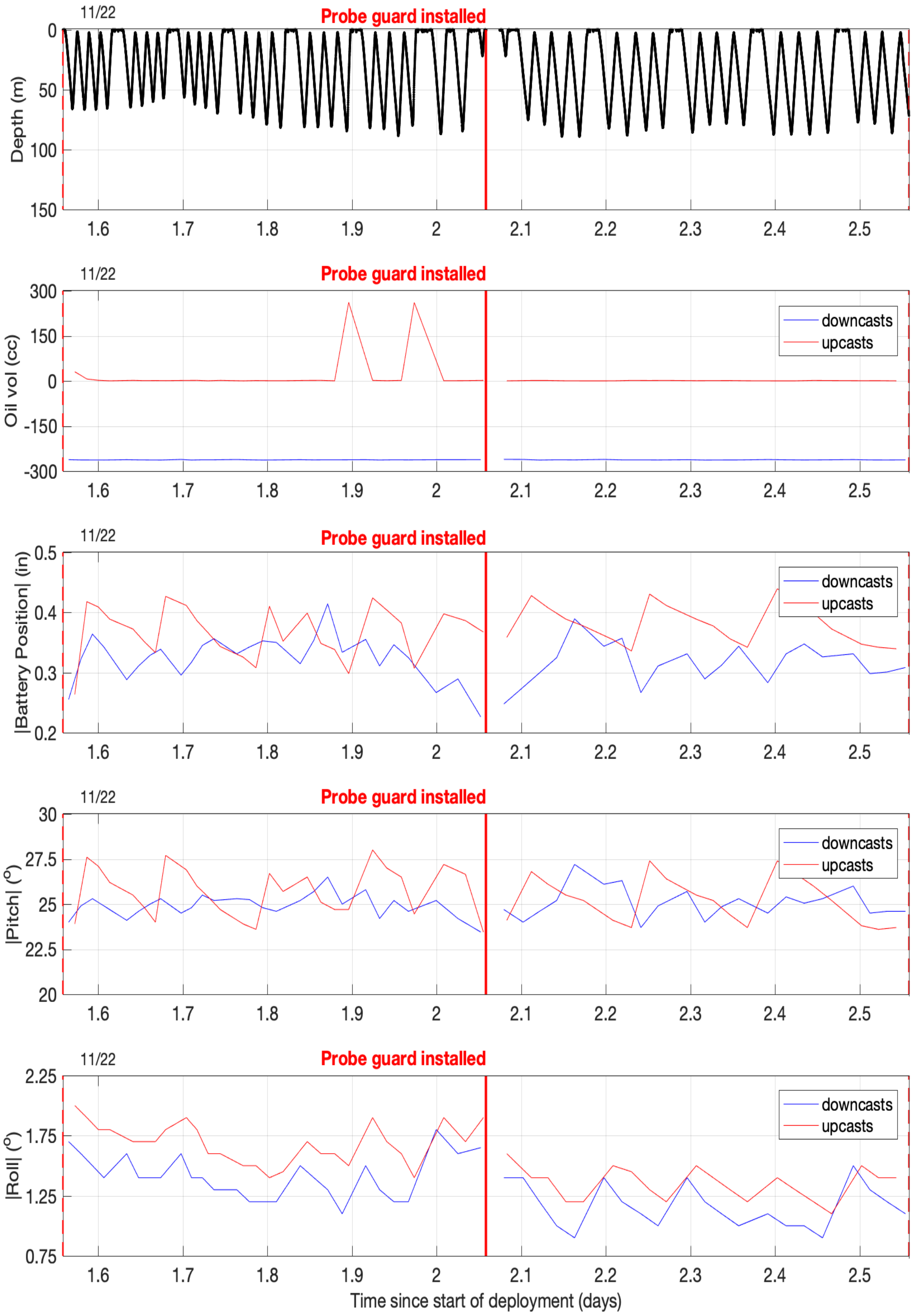

FIGURE 2.27: Profile average glider flight variables before and after the probe guard was installed. The variables have been split into upcast and downcast components, for better comparison. The two spikes in oil volume during the pre-installation upcasts were due to the glider aborting.

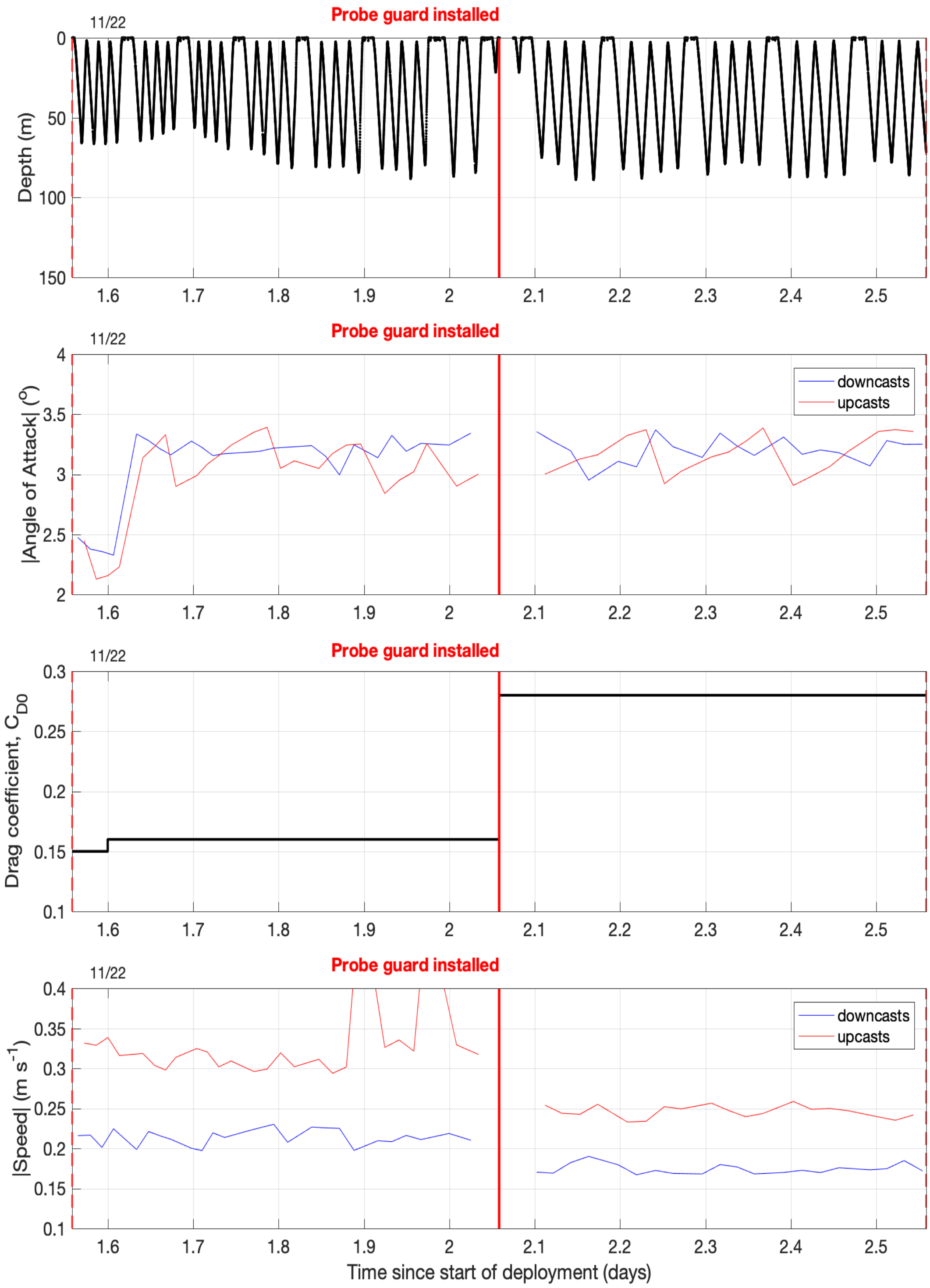

FIGURE 2.28: The modelled flight variables for the deployment in Oban, Scotland, using Merckelbach et al. (2010)'s hydrodynamic flight model. The glider was first deployed without a probe guard, before being re-ballasted and redeployed with a probe guard. The red dashed vertical lines represent the period over which the detailed analysis was conducted. The two spikes in speed during the pre-installation upcasts were due to the glider aborting.

°) than for the rest of the analysis period ($\geq\sim 3$), likely reflecting a change in the model calibration parameters between 21/11 and 22/11. Note the smaller drag coefficient - the parameters are generated for each Julian Day and earlier values will differ because the glider was still optimising battery position and oil volume (see Section 2.1.4.1 for more details).

The modelled parasitic drag coefficient and along path velocity of the glider both change significantly when the probe guard is installed (Figure 2.28). The drag coefficient almost doubles from 0.15 pre- to 0.28 post-probe guard installation. This suggests that the probe guard is a large source of elevated drag, compared with values of 0.15 that are typical of gliders flown without a probe guard (Merckelbach et al., 2010, 2019). The increased drag is reflected in the modelled mean along path glider velocity, with speeds decreasing between pre- and post-probe guard installation by 0.08 m s^{-1} for upcasts (from 0.33 m s^{-1} to 0.25 m s^{-1}), and 0.04 m s^{-1} for downcasts (from 0.21 m s^{-1} to 0.17 m s^{-1}). These differences are statistically significant ($p \ll 0.01$ for both) at the 95 % significance level. The increased drag could also explain the observed decrease in the glider's roll after probe guard installation.

The reduction in the glider's along path velocity might be expected to affect the quality of the microstructure data recorded by the MicroRider, which requires flow speeds between $0.2 - 1.0$ m s^{-1} (Goldberg, J. (RSI), personal comms., February, 2021). However, the shear spectra across the three days of the deployment are very good, predominantly having shapes similar to the Nasmyth spectra, both before and after probe guard installation. Only 28 (32) peaks are removed from either shear-1 or shear-2 spectra before (after) the probe guard installation, out of 3055 (1972) spectra. This could be because the background levels of dissipation in Oban are higher than those in Antarctica: only 49 % of accepted spectra had a dissipation estimate that was $\leq 1 \times 10^{-8}$ W kg^{-1}, compared to 88 % in the Ryder Bay dataset. However, spectra at dissipation levels below this threshold were often well resolved in the Oban dataset, both before an after the probe guard installation (Figure 2.29).

The lack of a clear difference between pre- and post-probe guard installation shear spectra prompted a closer look at the accelerometer (A_x, A_y) spectra, which would not be masked by background dissipation levels and still contain large $1 - 3$ Hz peaks throughout the deployment. Consequently, each accelerometer spectrum was integrated between $1 <= f <= 3.5$ Hz, gaining an insight into how the size of the peak changes with the installation of the probe guard (Figure 2.30). Overall there was a small increase in the size of the A_x and A_y peaks after probe guard installation (1.9 and 1.2 times larger, respectively), however, the largest changes occurred when decomposing into upcasts and downcasts. For the upcasts, the A_x and A_y peaks were 5 and 6 times larger after the probe guard was installed. For the downcasts, the A_x and A_y peaks increased and decreased by 10 and 50% respectively.

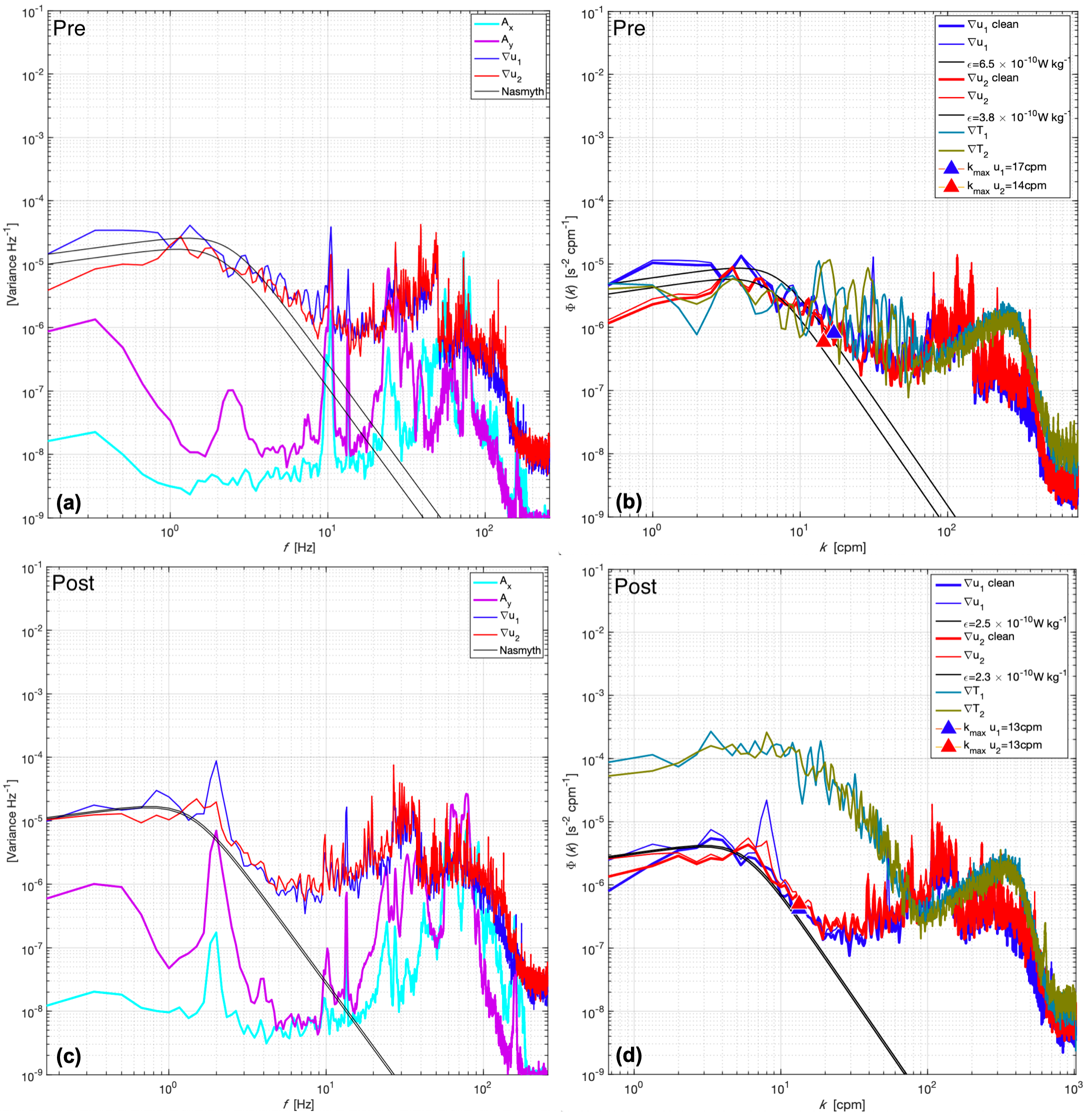

FIGURE 2.29: Low-dissipation shear spectra recorded during the probe guard investigation in Oban, Scotland. Pre- and post-probe guard installation spectra in the frequency (a,c) and wavenumber (b,d) domains fit the Nasmyth spectra. A $1-3$ Hz peak is observed in the accelerometer spectra (A_x, A_y) and is larger after probe guard installation. The dissipation estimates corresponding to the shear-1 and shear-2 Nasmyth spectra in the wavenumber domain are shown.

The size of the accelerometer peak changes by different amounts and signs for upcasts and downcasts (e.g., the A_y peak size is actually reduced with the addition of the probe guard in the downcasts). The simplest explanation for this would be that the size of the peak is influenced by the glider's flight quality. This is supported by the fact that the upcasts experienced both the largest change in peak size and the along path velocity: the increases to A_x and A_y peak sizes are stated above; the upcast along path velocity decreased from > 0.3 m s^{-1} to 0.25 m s^{-1} after probe guard installation (as seen in Figure 2.28). Additionally, the suggestion that the size of the peak is influenced by the glider's flight quality is supported by extending the accelerometer peak analysis to

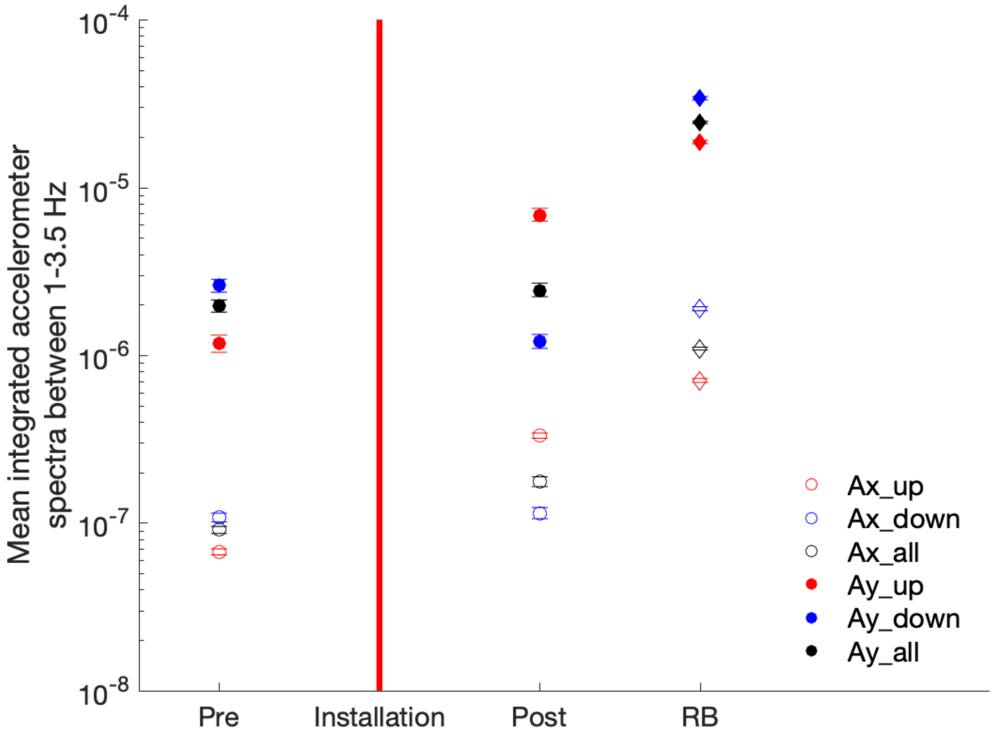

FIGURE 2.30: Accelerometer peak analysis. A comparison of mean integrated accelerometer spectra between $1-3.5$ Hz, for upcasts (red) and downcasts (blue) for periods pre- and post-probe guard installation. Also shown are overall means (black). Diamonds are corresponding values from the whole Ryder Bay (RB) deployment. Horizontal lines are 90 % bootstrapped error bars, using 1000 bootstrap datasets.

the Ryder Bay dataset. Comparing the mean peak sizes for the Ryder Bay and post-installation Oban datasets reveals opposite upcast and downcast relationships (e.g., the A_y peak is largest in the downcasts and upcasts respectively; Figure 2.30), despite both having the probe guard installed. The most plausible explanation for this are ballasting differences, and these are reflected by the change in fastest profile direction; upcast/downcast values for the Ryder Bay and Oban datasets were 0.25/0.34 m s^{-1} and 0.25/0.17 m s^{-1} respectively. (Peak sizes are an order of magnitude higher in the Ryder Bay dataset than in the Oban dataset, however, these differences could be due to the use of different uncalibrated sensors).

If a MicroRider-equipped glider is not ballasted sufficiently, then it is likely that its H-moment is too low, which would mean the glider is comparatively unstable (see Section 2.1.4.5). This makes the glider twitchy and susceptible to small oscillations in density caused by small-scale water motions. If the $1-3$ Hz peak is caused by a ballasting problem, you would also expect to see oscillations of similar frequencies reflected in the MicroRider's fast pressure record. Figure 2.31 shows dP_dt, Ax and Ay power spectra from a portion of DAT-file 86 profile 3. This profile was collected pre-probe guard

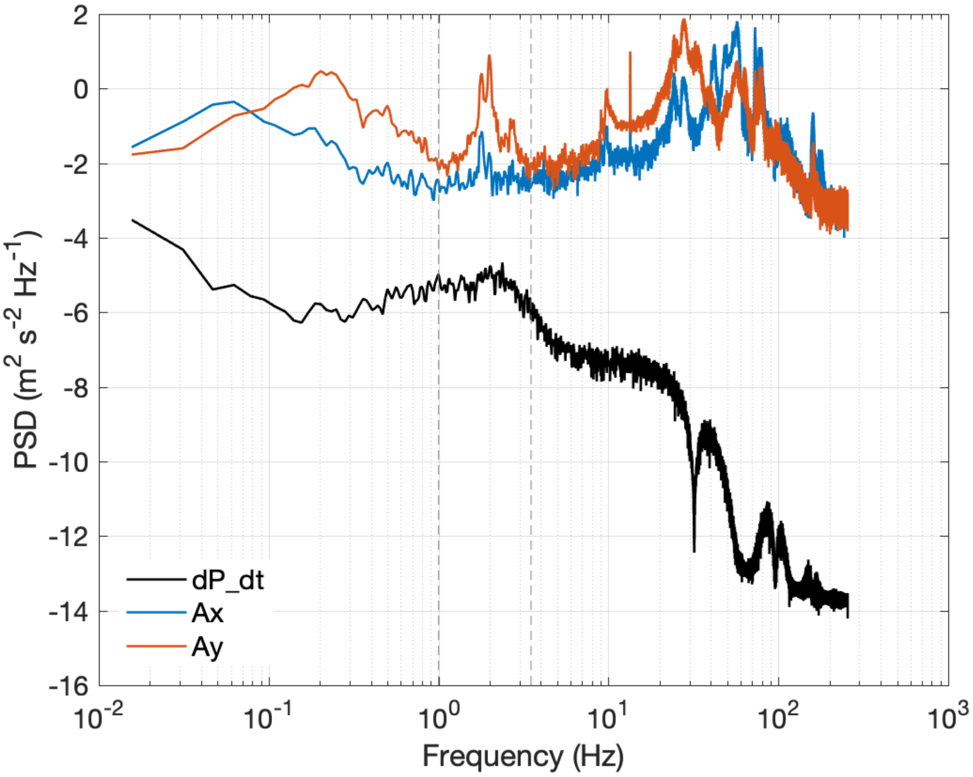

FIGURE 2.31: Power spectral density comparison, using a portion of DAT-file 86 profile 3. Vertical dashed lines at 1 and 3.5 Hz define the region used for the integration of the accelerometer spectra. High power is observed in all spectra within this region.

installation, however, the spectra have elevated power between $1 - 3.5$ Hz (the integration range used above). This suggests that the observed $1 - 3$ Hz peak is caused by real body oscillations (as seen in dP_dt) that can occur whether the probe guard is installed or not. Additionally, lower frequency changes in the glider's depth rate (dP_dt) are also reflected in both the glider's pitch and roll; notice the quiescent period between 3200 and 3400 s compared with the higher amplitude oscillations between 3500 and 3700 s in Figure 2.32.

Another potential source of noise in the accelerometer and shear spectra are vibrations caused by digifin (rudder) movements. Comparison of the change in digifin angle in time with the raw accelerometer counts shows that the digifin is a source of considerable noise, causing large spikes in the accelerometer data (Figure 2.32, second from bottom panel), however, these spikes are of too lower frequency to cause the observed $1 - 3$ Hz peak. Additionally, there appears to be no correlation between changes in the digifin angle and the size of the accelerometer peak within the $1 - 3.5$ Hz integration region (Figure 2.32, bottom panel).

This investigation has demonstrated that the source of the $1 - 3$ Hz peak is likely caused by real body oscillations of the glider. The addition of the probe guard increases the drag by a factor of 2, and although this marginally increases the overall size of the

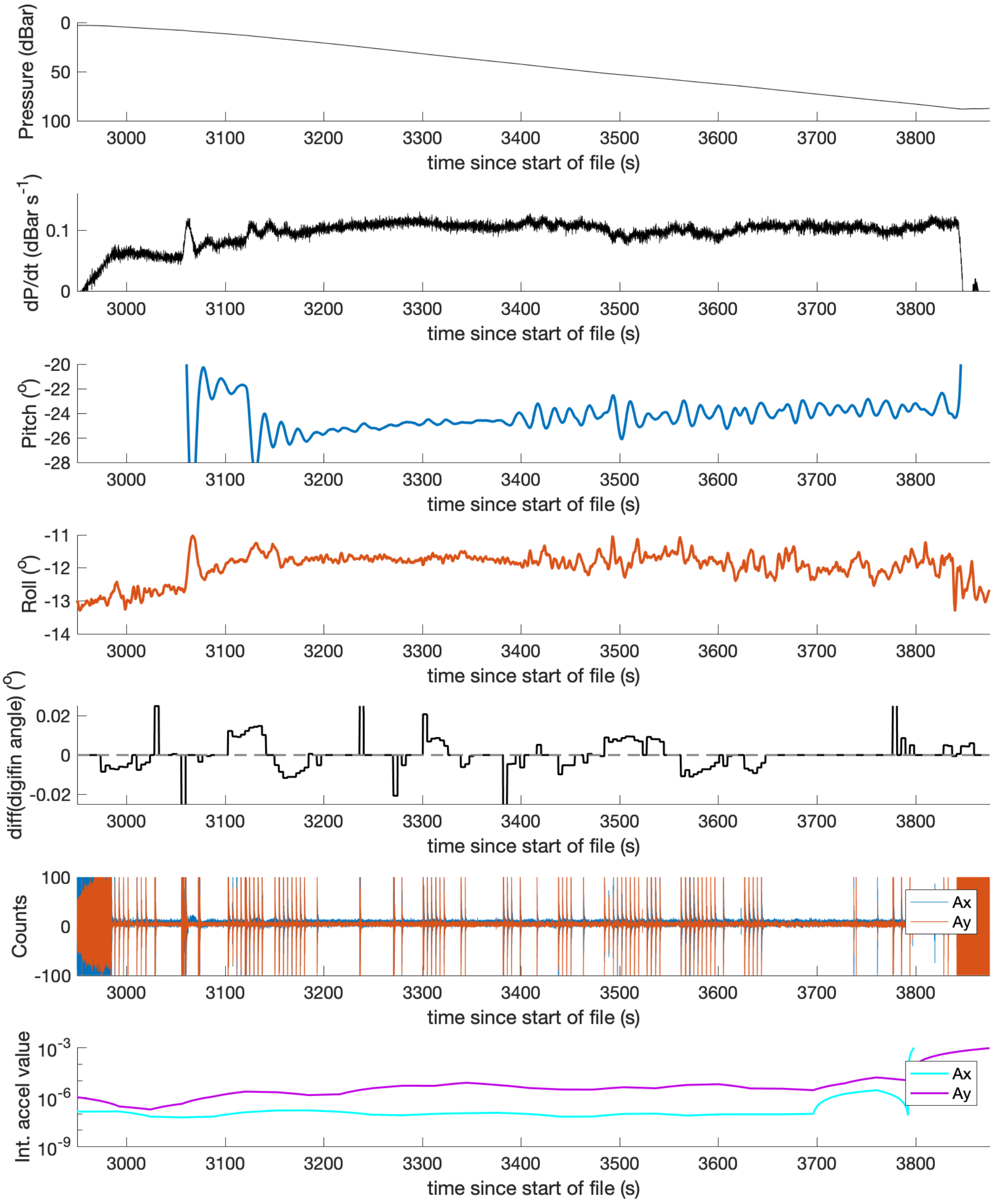

FIGURE 2.32: Comparison of DAT-file 86 profile 3's flight parameters. From top to bottom are the glider depth profile, the depth rate (dP_dt), pitch, roll, change in digifin (rudder) angle, raw (A_x, A_y) accelerometer record, and the integrated accelerometer value between $1 - 3.5$ Hz. All of the variables shown here, bar the digifin angle, were measured using the MicroRider. The MicroRider precisely measures small-scale changes but it is not so necessary to be accurate. The MicroRider's roll was not calibrated, explaining the difference in magnitude compared with the true values as measured by the glider's compass (Figure 2.27, bottom panel).

peak, changes are up to 6 times greater when comparing pre- and post-installation upcasts and downcasts. Differences between upcasts and downcasts are likely due to how well the glider is ballasted, which becomes harder when using the probe guard. For future deployments, if the glider was going to be deployed in a low energy environment like Ryder Bay, it could be beneficial to deploy the glider without a probe guard because it is easier to ballast/obtain a higher glider H-moment. This would increase the likelihood of a cleaner dataset, however, this benefit must still be weighed against the risk of damaging the probe and losing data. If the glider was going to be deployed in a higher energy environment like Oban, the probe guard does not overly effect the data, providing the utmost care is taken when ballasting (as was the case for the Oban deployment).

2.2 Arctic Data

The work in this section contributed to the following published paper:
Scott, R. M., R. S. Pickart, P. Lin, A. Münchow, M. Li, D. A. Stockwell, and J. A. Brearley, 2019: Three-dimensional structure of a cold-core arctic eddy interacting with the chukchi slope current. *Journal of Geophysical Research: Oceans*, **124 (11)**, 8375–8391.

2.2.1 Hydrographic Data

The in situ data used in Chapter 5 were collected on the USCGC *Healy*, as part of the Western Arctic Shelf Basin Interactions program. The Shelf Basin Interactions program aim was to investigate the impact of global change on the physical, biological and geochemical exchanges processes between the Chukchi and Beaufort Seas and the Canada Basin. As highlighted in Chapter 1, this is a region of significant shelf-ocean exchange, with the Chukchi shelfbreak jet, Beaufort Shelfbreak jet and the Chukchi Slope Current all forming from Herald and Barrow canyons, with the potential to form eddies (e.g., D'Asaro, 1988; Pickart et al., 2005; Corlett and Pickart, 2017; Spall et al., 2018). The program was comprised of three research cruises sampling both the Chukchi and Alaskan Beaufort Seas, and multiple eddies were observed in the first two cruises in 2002 and 2003. Consequently, on the third cruise of the program, in September 2004, the ship set out to conduct a more detailed survey of one of these eddies. This study presents the first full three-dimensional structure of a cold-core halocline eddy, which was found on the Chukchi continental slope to the south of the Northwind Ridge (Figure 2.33). Different aspects of the eddy have been previously reported, addressing the off-shelf flux of carbon (Mathis et al., 2007), the age of the eddy determined by radium dating (Kadko et al., 2008), and the different zooplankton species contained within the feature (Llinás et al., 2009). The focus in Chapter 5 is predominantly on the physical attributes of the eddy.

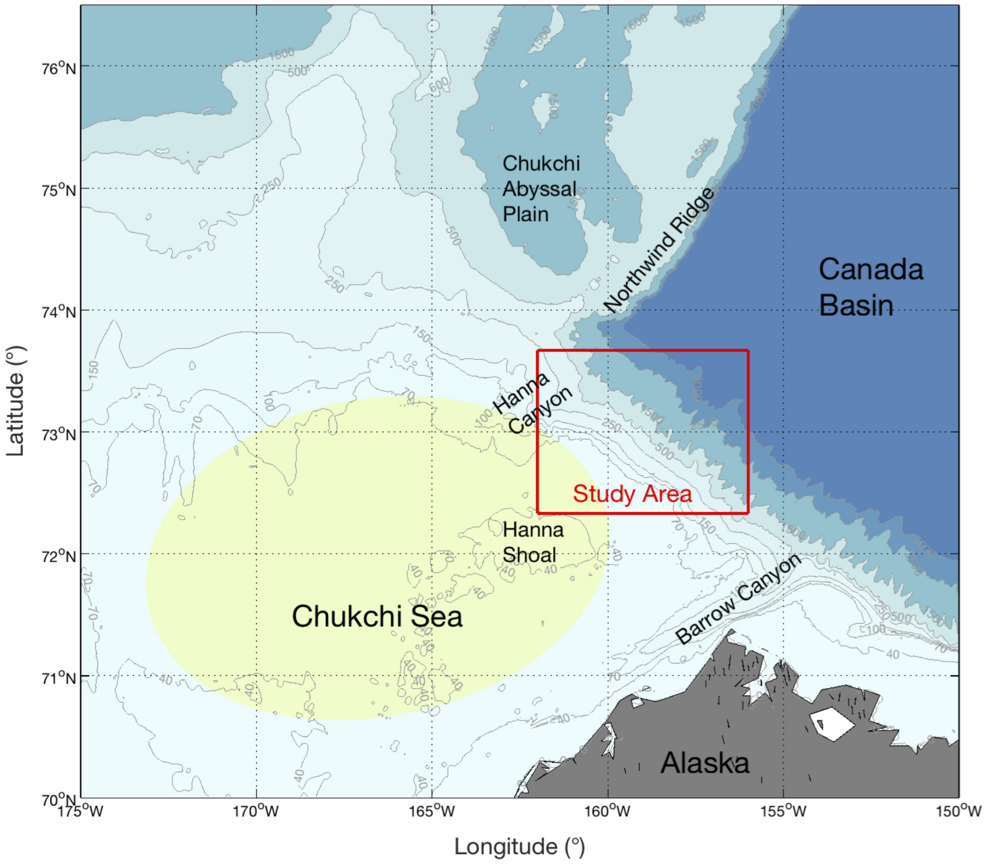

FIGURE 2.33: Study domain and place names (Lin, P., personal comms., July, 2019). The bathymetry is from IBCAO v3 (Jakobsson et al., 2012). The area outlined in red is shown in Figure 2.34. The yellow shaded area on the Chukchi shelf is where the wind stress curl was averaged to construct the time series of Figure 5.16 and is the same region as used by Li et al. (2019).

The eddy was initially revealed by occupying a series of expendable-bathythermograph (XBT) sections across the Chukchi continental slope (sections x1-x5; Figure 2.34). Only the western-most line (x1, which was occupied first) showed any evidence of an eddy. After completing section x5, the ship steamed back to section x2 and did a back-and-forth XBT line (x6), in order to pinpoint the location of the eddy core and determine its along slope length scale. Using this information, a high-resolution grid was laid out to be occupied as quickly as possible using expendable conductivity-temperature-depth (XCTD) probes (Figure 2.35). Due to inventory constraints, *Healy*'s CTD package was used to complete Transect 1 and extend XCTD Transect 2 (green squares). The CTD casts were taken to 300 m, and no water sampling was done in order to save time.

The average station spacing of the eddy grid was 5 km, and it took approximately

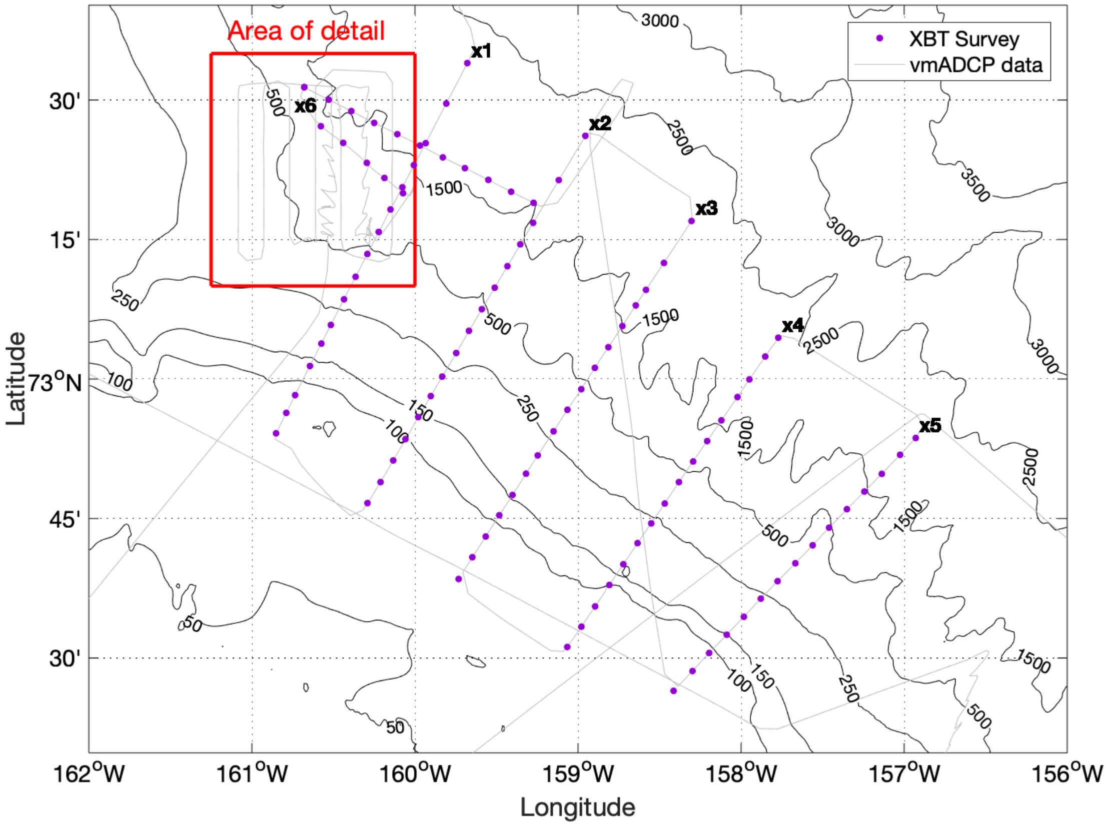

FIGURE 2.34: Expendable-bathythermograph (XBT) transects occupied in order to locate the eddy (the XBT drops are denoted by the purple dots). The ship track is indicated by the gray lines. The area of detail outlined in red is shown in Figure 2.35. The black lines are the bathymetry contours from IBCAO v3 (Jakobsson et al., 2012).

24 hr to complete. This resulted in a synoptic snapshot encompassing the eddy with uniform spatial coverage. This is the only known survey that resolves the complete three-dimensional structure of an Arctic eddy. Approximately 4 hr after the XCTD survey was completed, a CTD section was occupied across the centre of the eddy. This took 25 hr to complete and included water sampling for dissolved oxygen, total CO2, nutrients, total alkalinity, chlorophyll, dissolved and particulate organic matter, and salinity. At six of the stations a multi-net cast was done to sample for zooplankton. Many of the biochemical aspects of the eddy are reported elsewhere (Mathis et al., 2007; Kadko et al., 2008; Llinás et al., 2009).

The CTD used on the *Healy* was a Sea-Bird 911+ with dual temperature and conductivity sensors mounted on a 24-place rosette with 12-L Niskin bottles. Laboratory calibrations were done on the temperature sensors, and the conductivity data were calibrated using the bottle salinity data (using additional CTD casts; as mentioned above, no samples were taken in the survey in Figure 2.35). The accuracies were deemed to be 0.001 °C and 0.007 PSU for temperature and salinity, respectively. Additional CTD variables included transmissivity and fluorescence, although these were not calibrated. The final CTD data were used to create 1-db averaged downcast files. Kadko et al. (2008) describe

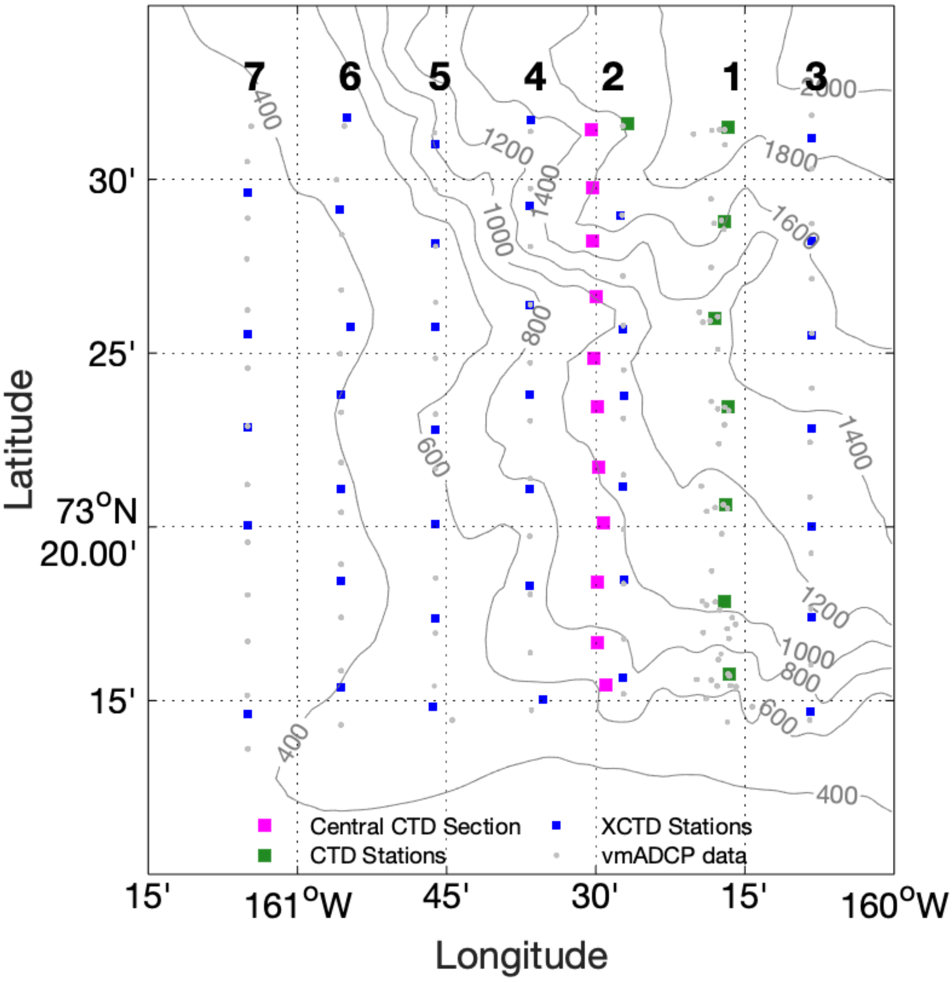

FIGURE 2.35: The eddy survey consisting of expendable conductivity-temperature-depth (XCTD) stations (blue squares), CTD stations (magenta and green squares), and vessel-mounted ADCP profiles (grey dots). The transect numbers of the grid are indicated along the top (the central CTD section [magenta square] is not considered part of the synoptic grid). The bathymetry is from the ship's multi-beam system.

the processing and calibration of the XCTD data. The XCTD temperature, salinity, and depth are deemed accurate to within 0.02 °C, 0.04 PSU, and 1 m, respectively. The final XCTD data were used to construct 2-m averaged profiles of temperature and salinity. Both the CTD and XCTD data were used to calibrate *Healy*'s multi-beam system, which produced the bathymetry used in the "area of detail" figures (Figures 2.35, 5.4, 5.8 and 5.12).

Vertical sections of various properties in the Arctic hydrographic dataset were constructed using Laplacian-Spline interpolation, a widely accepted and commonly used interpolation method that sufficiently handles discontinuities (Emery and Thomson, 2004). A vertical grid spacing of 5 m and horizontal grid spacing of 1 km were used, where the meridional distance is relative to the latitude of 73.24 °N (which is just south of the XCTD survey minimum latitude; Figure 2.35). Lateral plots were constructed using the same interpolator, with a grid spacing of 0.01 ° in latitude and 0.02 ° in longitude. The lateral maps do not include the hydrographic or velocity data from central CTD section because, as noted above, it took approximately 25 hr to occupy the section after the eddy survey was completed.

2.2.2 Velocity Data

Vessel-mounted ADCP (VMADCP) data were obtained from *Healy*'s 75-kHz phased-array Ocean Surveyor instrument. Attitude information (heading, pitch, and roll) was provided by an Ashtech ADU2 − 3DGPS receiver, and the ship's position was determined by a Trimble Centurion p-code DGPS system. Processing and merging of these data streams resulted in calibrated, earth-referenced profiles of horizontal currents from about 20 m below the surface to a maximum depth of 400 m depth every 2 min in 15 m vertical bins. The reader is referred to Münchow et al. (2006, 2015) for details about the system and its overall performance. The velocity data set was quality controlled using standard *Healy* protocol, sorting the data within each 2 min ensemble and discarding extreme values from the record. This forced the data towards a normal distribution for which the standard deviation decreases as $N^{-1/2}$, where N is the number of independent estimates (pings). With a single ping error of about 14 cm s^{-1} and $N = 50$ pings within each 2-min ensemble, the estimated absolute random errors are about 2 cm s^{-1}. For analysis, 10-min averages (calculating using the mean) of the ensembles were created.

Based on mooring data from the Chukchi continental slope, tidal velocities in this region are small ($<$ 2.2 cm s^{-1}; Li et al., 2019). Nonetheless, the major barotropic tidal signals (M_2, S_2, K_1, O_1) were removed from the VMADCP profiles using the Oregon State University Arctic tidal model, which has a resolution of 5 km and predicted similarly small tides ($<$ 2 cm s^{-1}; Padman and Erofeeva, 2004; Llinás et al., 2009). The detided VMADCP data were interpolated onto the same grid as the CTD sections (vertical and horizontal grid spacings of 5 m and 1 km respectively) and together these data were used to calculate sections of absolute geostrophic velocity (V_{agv}). This first involved calculating sections of relative geostrophic velocity (V_{rgv}) from the dynamic height relative to the sea surface using the gridded CTD data and the following equation:

$$V_{rgv} = V_p - V_0 = \frac{g}{f}\frac{(\Delta D_B - \Delta D_A)}{x} \tag{2.8}$$

where $V_{p,0}$ are the geostrophic velocities at pressure p and at the sea surface, g is the acceleration due to gravity, f is the Coriolis parameter, and $\frac{\Delta D_B - \Delta D_A}{x}$ is the gradient in the dynamic height anomaly, ΔD, between two consecutive grid points along the section (A and B, separated by a distance of x, which in this case is 1 km). ΔD was calculated using the *gsw_geo_strf_dyn_height* function from the Gibbs-SeaWater Oceanographic

Toolbox (McDougall and Barker, 2011). The relative geostrophic velocities were then made absolute by referencing them to the detided, 10-min averaged VMADCP velocities (Equation 2.9). In particular, for each grid point along a section, the vertically averaged relative geostrophic velocity ($V_{rgv_{av}}$) was matched to the vertically averaged cross-track VMADCP velocity ($V_{VMADCP_{av}}$) over their common depth range (typically, $0 - 250$ m):

$$V_{agv} = V_{rgv} + V_{ref}, \tag{2.9}$$

$$\text{where } V_{ref} = V_{VMADCP_{av}} - V_{rgv_{av}}.$$

This produced vertical sections of absolute geostrophic velocity along each transect.

2.2.3 Biochemical Data

Chlorophyll a and phaeopigments were determined fluorometrically (Holm-Hansen et al., 1965) by filtration through 25 mm Whatman GF/F filters as outlined in Evans et al. (1987). Samples were collected from the CTD casts and immediately filtered. The filters were placed in vials on ice, sonicated in 90 % acetone, and extracted for 24 hr. Extracted fluorescence was measured before and after acidification (10 % HCL), with a Turner Designs model AU-10 fluorometer calibrated with commercially purified Chlorophyll a (Turner Designs).

Sample methods for nutrients have already been described in detail elsewhere (see Codispoti et al., 2005). In brief, nutrient analyses (phosphate, silicate, nitrate + nitrite, urea, ammonium, and nitrite) were performed on an ODF-modified 6-channel Technicon AutoAnalyzer II. The samples collected from CTD casts were generally analyzed within a few hours after sample collection. Methodologies and modification for the individual nutrient species are also described in detail in Codispoti et al. (2005).

2.2.4 Wind and Surface Geostrophic Velocity Data

Time series of wind stress curl over the Chukchi shelf were constructed using 10 m wind fields from the ERA-Interim reanalysis provided by the European Center for Medium-Range Weather Forecasts (Berrisford et al., 2009). The data have a temporal and spatial resolution of 6 hr and 0.75 °, respectively. The surface geostrophic velocity during the time period of the eddy survey was provided by Copernicus Marine and Environment Monitoring Service (`http://marine.copernicus.eu/`). This product consists of daily gridded fields with a resolution of 0.25 ° in latitude and longitude, based on data from multiple satellite altimeter missions.

Chapter 3

Rates of Turbulent Mixing in a Coastal Embayment of the West Antarctic Peninsula

The work in this chapter contributed to the following published paper:
Scott, R. M., J. A. Brearley, A. C. Naveira Garabato, H. J. Venables, and M. P. Meredith, 2021b: Rates and mechanisms of turbulent mixing in a coastal embayment of the west antarctic peninsula. *Journal of Geophysical Research: Oceans*, **126**, e2020JC016 861.

3.1 Introduction

As mentioned in Chapter 1, Ryder Bay is a coastal embayment situated on the south-east coast Adelaide Island on the WAP (Figure 1.11). The bay is semi-enclosed, being bounded to the north by Sheldon Glacier, which is a marine-terminating glacier that is retreating (Cook et al., 2005), to the west by two smaller marine-terminating glaciers, and to the south by a series of small islands that are surrounded by a $\sim 200 - 300$ m deep shelf (Figure 3.1). The unsurveyed regions are believed to have depths typical of the surrounding shelf (shoaling towards the coast), as suggested by the lower resolution bathymetry data in Venables et al. (2013). The bay can therefore be considered an end-point for CDW that intrudes onto the shelf. The deepest part of the bay is $\sim$ 520 m, and its entrance is marked by a $\sim$ 300 m deep ridge separating the bay from Laubeuf Fjord, which is connected to the south by Marguerite Trough via several topographic constrictions that also contain similar transverse ridges. Venables et al. (2017) deployed Slocum gliders over these ridges, finding clear evidence of overflows. As CDW flows through Marguerite Trough, the densest waters are blocked by the ridges, whilst the overlying waters descend hundreds of meters, entraining the overlying cooler water

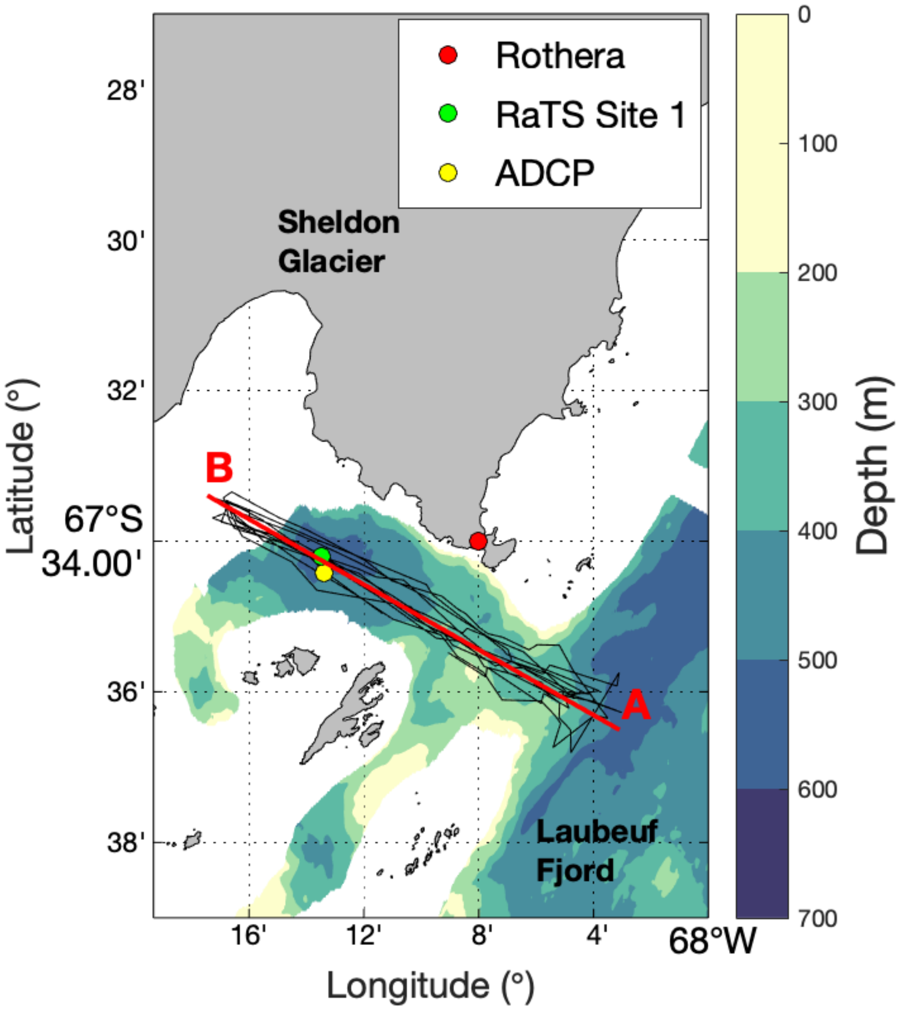

FIGURE 3.1: Map of Ryder Bay, showing the location of Rothera (red) in relation to the 13 quality-controlled glider transects that are the focus of this chapter. Colours represent quality-controlled bathymetric data (Fremand, 2020), with unsurveyed areas in white. The locations of the Rothera Time Series (RaTS) Site 1 (green) and the ADCP mooring (yellow) are indicated. Glider data are collapsed onto the A-B transect (red line).

in localised mixing events. Consequently, these ridges could have a major role in the WAP heat budget.

This chapter uses some of the first direct estimates of dissipation off the WAP collected using an autonomous Slocum glider, equipped with a microstructure (MicroRider) package. The 2016 Ryder Bay glider deployment, for which the processing is described in Chapter 2, is used in a detailed description of the mixing that occurs within Ryder Bay, with a particular focus on observations over the ridge at the bay's entrance. This chapter first contextualises the whole 2016 glider dataset using data from the RaTS (Section 3.2). The spatial distribution of hydrographic, dissipation and heat fluxes are then described in Section 3.3, with comparison between mean values over the ridge compared to those in the deep basin (using data from the whole glider deployment;

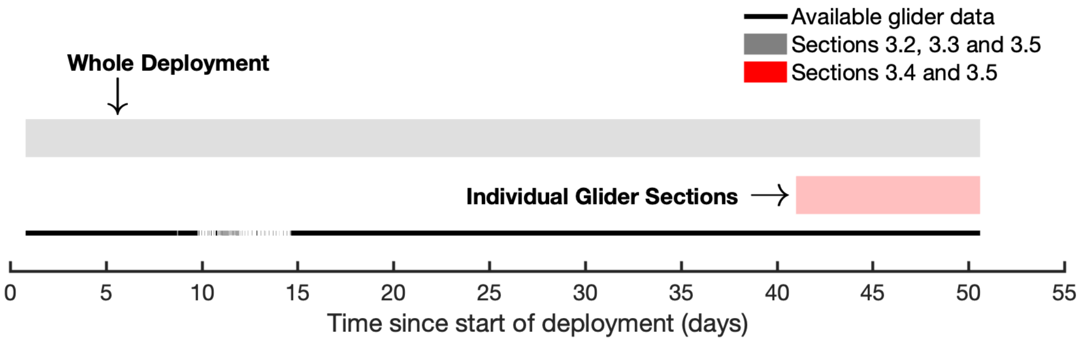

FIGURE 3.2: Schematic showing which periods of glider data are used in each of the remaining sections in Chapter 3. Section 3.4 focuses especially on the individual glider transects that were recorded at the end of the deployment.

Figure 3.2). Individual glider transects (Figure 3.1) are then used in Section 3.4 to show the temporal variability in hydrographic, dissipation and heat flux patterns within Ryder Bay (Figure 3.2). The chapter finishes with a summary and discussion (Section 3.5), and uses surface heat fluxes to explain some of the observed surface water temporal variability.

3.2 Contextualising the Ryder Bay Glider Deployment

The RaTS is the longest year-round hydrographic time series in Antarctica, providing quasi-weekly, hand-winched CTD data and bottle samples (for chlorophyll) within Ryder Bay (predominantly at Site 1; Figure 3.1). RaTS data from 2013 – 2017 are used in conjunction with concurrent Rothera Meteorological Station surface air temperature data provide supporting data for the 2016 glider deployment (Figure 3.3). The air temperatures (Figure 3.3a) show strong seasonal variability, commonly dropping below -20 °C during winter (July-September) and rising above 0 °C in the summer (December-March). This atmospheric forcing drives similar variability in waters above the permanent thermocline, which, with cold, fresh water overlying warm and saline water, exists in Ryder Bay throughout the year (Figures 3.3b,c). The permanent thermocline typically has a depth around 130 m (dashed black line), and is defined here using the 0.25 °C isotherm, following the representative isotherm method (Fiedler, 2010). The coldest waters are defined by a temperature minimum (< -1 °C), lie above the thermocline, and are WW; forming due to winter atmospheric cooling of the ocean's surface. Below the thermocline is warm ($1 - 1.5$ °C), saline (> 34.7 g kg^{-1}) CDW. The CDW originates in the ACC and intrudes onto the continental shelf where, through vertical mixing processes, the heat reaches the required depths to melt ice shelves and marine-terminating glaciers (e.g., Arneborg et al., 2012; Moffat et al., 2009; Martinson and McKee, 2012; Cook et al., 2016). During winter, a combination of atmospheric cooling, strong wind events and brine rejection through sea ice formation drive vertical mixing, thereby reducing stratification (e.g., July 2014; Figure 3.3d). This deepens both the mixed layer and the thermocline (e.g., July 2014; Figure 3.3e). In the summer, warm atmospheric temperatures melt both sea and glacial ice, causing a large input of fresh (< 33.5 g kg^{-1}) AASW (e.g., April 2017; Figure 3.3c). This increases the stratification close to the surface (e.g., the deepening of the 27 kg m^{-3} isopycnal; Figure 3.3c), causing subduction of the WW, forming a remnant layer. Continued warming of the surface layers due to insolation can form a seasonal thermocline (also defined here using the 0.25 °C isotherm), which is shallower than the permanent one and can erode the remnant WW layer from above. This is particularly evident between January to April 2017.

Strong inter-annual variability is also observed within Ryder Bay. Mean summer (January-March) surface air temperatures for $2013 - 2017$ were 1.0, -0.7, -0.1, -0.2 and 1.1 °C respectively, and the impact this had on the development of the seasonal thermocline in each year is clear. During the warm years of 2013 and 2017, the depth of the seasonal thermocline (~ 50 m and ~ 100 m, respectively) were greater than in the colder years; at the start of the glider deployment in 2016 the seasonal thermocline was $\sim 5 - 10$ m, but this almost completely disappeared half way through the deployment. Sea ice also has a large role in controlling the inter-annual variability, and can act as a barrier to mechanical mixing processes. Low sea ice winters show evidence of increased wind-driven vertical mixing (Venables and Meredith, 2014); for example, 2013 had a short fast ice season (78 days, followed by 2 day period of fast-ice 20 days later), compared to a total of 125 days of fast-ice in 2015, enabling the formation of a 100 m deep mixed layer and a decrease in 200 m temperature (Figure 3.3e). Additionally, the longevity of sea ice appears important. Although the 2014 fast-ice season spanned ~ 170 days overall (12th June to 29th November), there was a 28 day period of intermittent fast-ice at the start of July, coinciding with a period of intense wind stress (not shown) and variable air temperatures (Figure 3.3a). This enabled enhanced mixing and the formation of the largest MLD of 154 m, 143 m deeper than the RaTS average during 2016 glider deployment (11 m). The 200 m temperature during the 2014 deep mixing winter got as low as -1.12 °C, 2.07 °C lower than the RaTS mean during the 2016 glider deployment (0.95 °C). The low stratification caused by a deep mixing winter can persist into the following summer, therefore allowing heat caused by insolation to penetrate deeper into the water column through mechanical mixing (Venables and Meredith, 2014). This mechanism could explain the difference between the more pronounced seasonal thermocline in 2015 compared with 2016, despite similar mean air temperatures. Unlike the summer of 2015 (which followed the 2014 deep mixing winter), the summer of 2016 followed a low mixing winter that had a higher stratification and a shallower MLD, making it harder for heat to penetrate into the water column. Additionally, the CDW has significant variability on inter-annual timescales, with the isopycnals heaving up and down by $100 - 150$ m (e.g., the 27.74 kg m^{-3} isopycnal). This suggests that there is

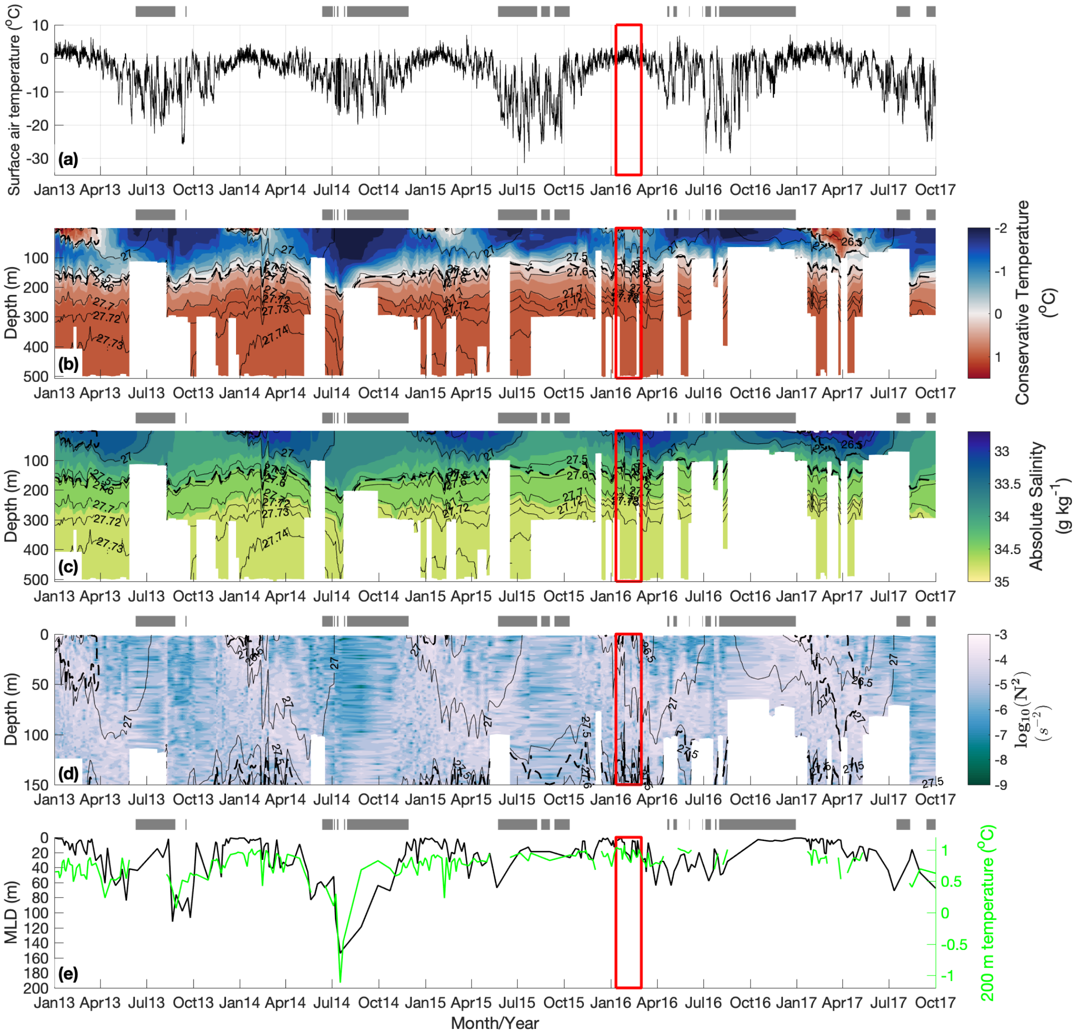

FIGURE 3.3: Contextualising the 2016 glider deployment using 2013 – 2017 data from the Rothera Meteorological Station (a, surface air temperature) and the RaTS. Sections of conservative temperature (b), absolute salinity (c) and buoyancy frequency (N^2; d) are overlain by potential density contours between 25 – 28 kg m^{-3}. The seasonal and main thermoclines are defined using the 0.25 °C isotherm (following Fiedler, 2010) and are indicated horizontal dashed black lines. Also shown is the RaTS MLD overlain by the 200 m temperature (e). The RaTS MLD is defined using a density difference of 0.05 kg m^{-3} relative to the surface (Venables et al., 2013). The red box indicates the glider deployment, and the grey bars along the top of the panels represent periods of 100% fast-ice, made by human observation.

variation in the amount of heat available to be mixed upwards into the water column over topographic ridges.

A conservative temperature-absolute salinity (TS) plot using CTD data from the entire 2016 glider deployment confirms the presence of the three water masses observed in the RaTS data, and illustrates how they are distributed in depth (Figure 3.4a) and time (Figure 3.4b). Coloured by depth, the TS plot shows fresh ($\sim < 33.25$ g kg^{-1}) AASW at the surface (< 50 m), with a wide range of temperatures (approximately $-0.75 - 2.25$ °C). At depths of $\sim$ 50 m lies WW, with low temperatures typically between ~ -1 to -1.44 °C (near-freezing point). The highest salinity (> 34.7 g kg^{-1}) and temperature ($1 - 1.5$ °C) water is CDW. Located below < 200 m, CDW has been strongly cooled and freshened relative to its unmodified form in the open Southern Ocean (Venables et al., 2017). Coloured by time since the start of the deployment, the TS plot shows that the WW becomes warmer and more saline further into the deployment, with the temperature and salinity increasing from -1.45 °C and 33.6 g kg^{-1} to -0.85 °C and 33.8 g kg^{-1}. The AASW cools with time, likely reflecting both atmospheric cooling and the erosion of the coldest WW layer below. This is supported by the depth of maximum stratification being shallower ($\sim$ 20 m) than the average (60 m) during the first $\sim$ 15 days of the deployment (not shown).

3.3 Spatial Variability

Mean hydrographic transects are constructed using data from the whole glider deployment (Figure 3.2) and Laplacian-Spline interpolation with a vertical grid spacing of 5 m and horizontal grid spacings of 0.75 km. The mean section requires a large horizontal grid spacing to smooth the section (compared with 0.25 km used for the individual transects, see Section 3.4), which is otherwise noisy due to the high number of observations within each grid cell. The horizontal distance is relative to location A along the transect from A to B (Figure 3.1). Location A is an arbitrarily chosen point beyond the ridge at Ryder Bay's entrance. Glider data were collapsed onto this line, which was composed of 100 points with a 0.12 km spacing, by finding the closest point to the location of the data.

3.3.1 Hydrography

Mean temperature (Figure 3.5), salinity (Figure 3.6) and buoyancy frequency squared (Figure 3.7a) sections for the entire glider deployment shows the spatial distribution of the AASW, WW and CDW water masses. A $\sim$ 50 m thick layer of cold AASW lies close to and freshens towards the surface, reaching salinities of < 33 g kg^{-1}, with low-densities of < 26.75 kg m^{-3}. Below the AASW lies a thin ($20 - 30$ m), very cold

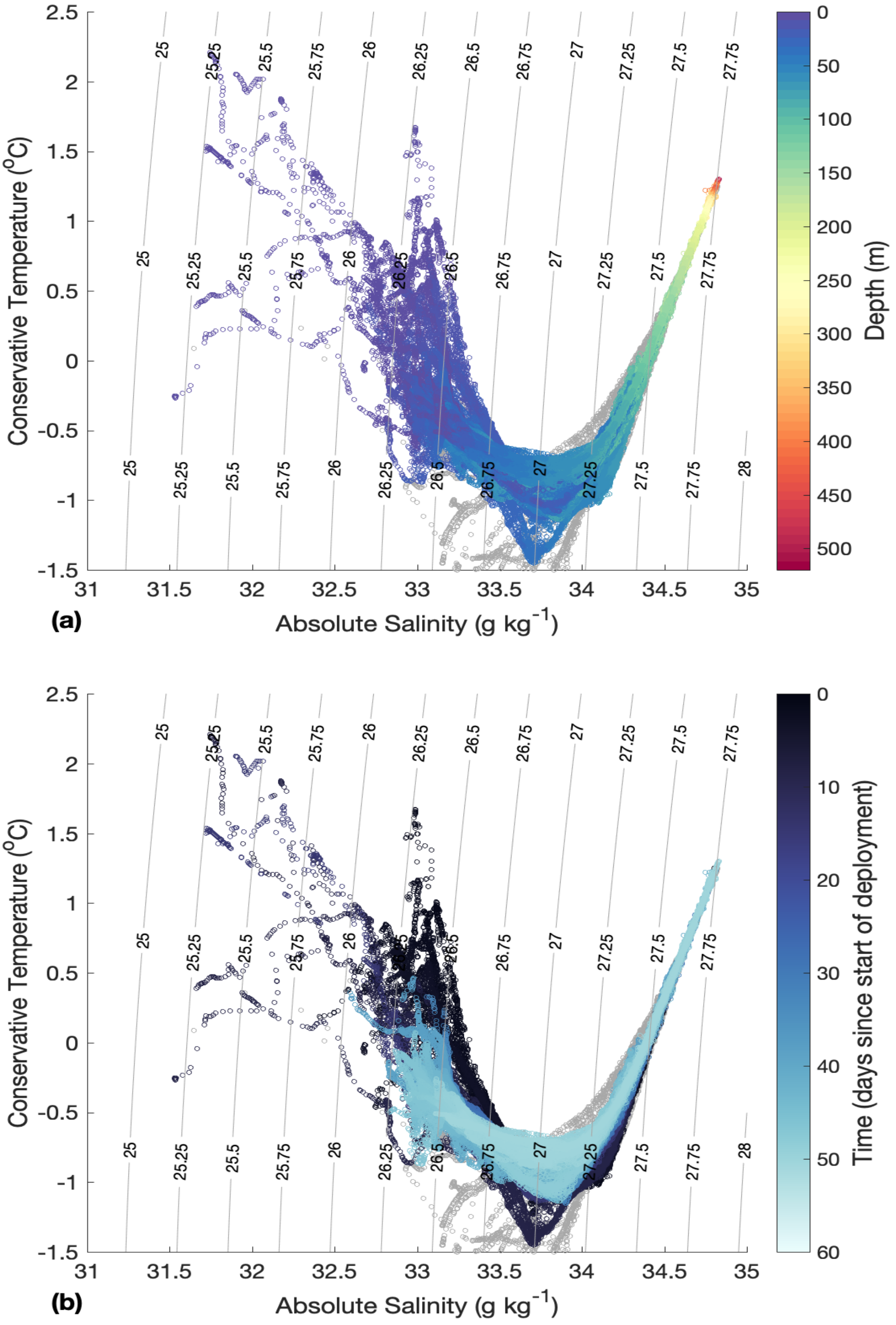

FIGURE 3.4: Conservative temperature-absolute salinity diagrams, using data from the whole glider deployment and coloured by depth (a) and time (b). Potential density contours between 25 − 28 kg m^{-3} are shown. Grey circles are from the 2016 RaTS data for context.

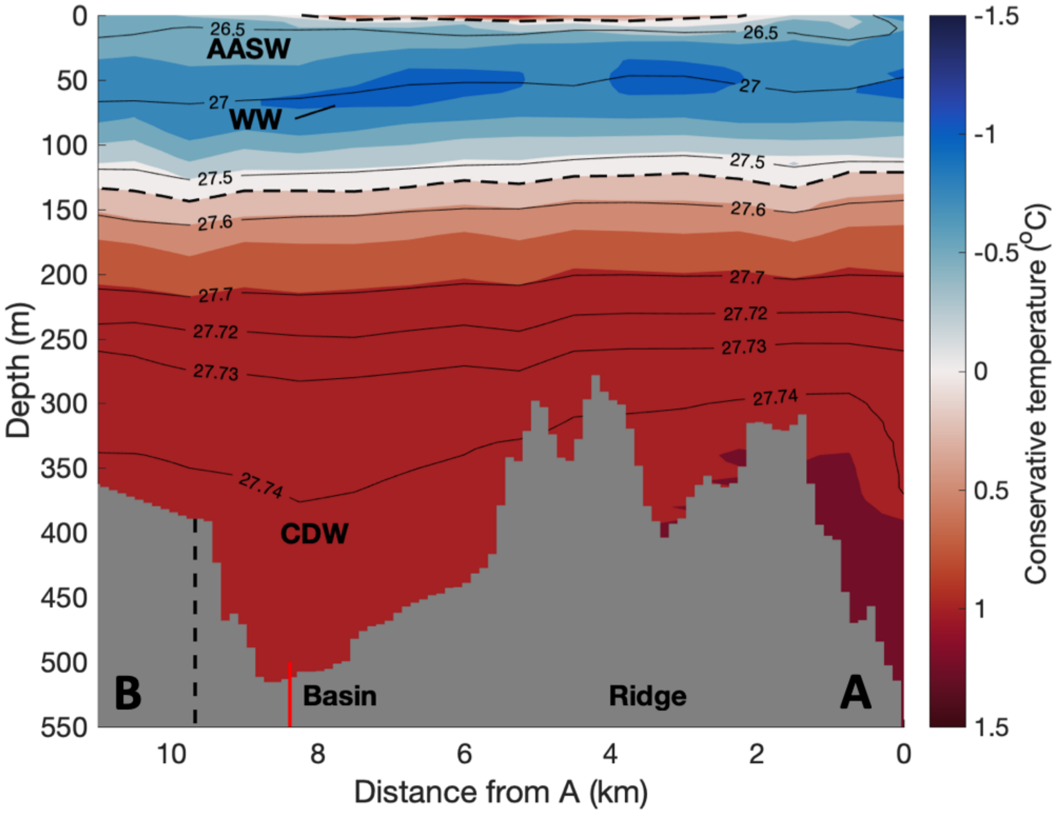

FIGURE 3.5: Mean vertical section of conservative temperature (°C). The seasonal and main thermoclines are defined using the 0.25 °C isotherm (following Fiedler, 2010) and are indicated horizontal dashed black lines. Contours are in 0.25 °C increments from -1.25 to 1.5 °C. The ADCP mooring location (vertical red line overlaying the grey bathymetry) and 26.5 – 27.74 kg m^{-3} surface-referenced potential density isopycnals (black contours) are also shown. Bathymetry is from Fremand (2020) up until $\sim$ 9.7 km (dashed vertical line), after which, no real data exists. Therefore, the bathymetry is linearly interpolated up to a depth of 350 m at 12 km along the section, in line with the glider data.

(< -1 °C) WW layer with salinities of $\sim$ 33.75 g kg^{-1}. This approximately coincides with the depth of maximum stratification (60 m; Figure 3.7b). Together these water masses lie above the main thermocline. The main thermocline has a mean depth of 130 m (again using the 0.25 °C isotherm), however, a seasonal thermocline with temperatures > 0.5 °C is also observed between $2 - 8$ km, reaching a maximum of $\sim$ 5 m depth. The seasonal thermocline is much shallower than in other years (Figure 3.3), likely reflecting the cooler summer mean air temperatures in 2016, but potentially also the preconditioned higher stratification caused by the 2015 low mixing winter. The individual glider sections described in Section 3.4 show that this seasonal thermocline has eroded away by day 40 of the deployment.

Beneath the main thermocline, warm (> 1 °C), saline (> 34.7 g kg^{-1}), dense (> 27.7 kg m^{-3}) CDW extends to the seafloor. The warmest 1.5 °C CDW is blocked by the $\sim$ 150 m tall topographic ridge that separates Ryder Bay's basin ($\sim$ 520 m) from Laubeuf Fjord.

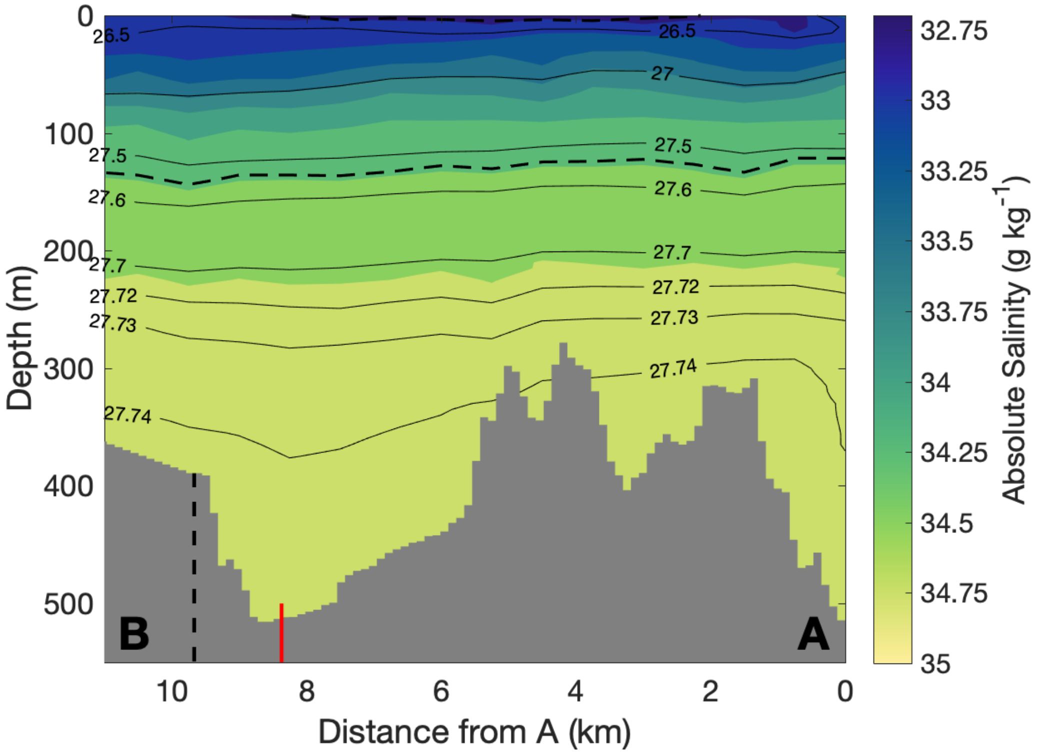

FIGURE 3.6: Mean vertical section of absolute salinity (g kg^{-1}). The seasonal and main thermoclines are defined using the 0.25 °C isotherm (following Fiedler, 2010) and are indicated horizontal dashed black lines. Contours are in 0.25 g kg^{-1} increments from 32.75 to 35 g kg^{-1}. The ADCP mooring location (vertical red line overlaying the grey bathymetry) and 26.5 – 27.74 kg m^{-3} surface-referenced potential density isopycnals (black contours) are also shown. Bathymetry is from Fremand (2020) up until $\sim$ 9.7 km (dashed vertical line), after which, no real data exists. Therefore, the bathymetry is linearly interpolated up to a depth of 350 m at 12 km along the section, in line with the glider data.

Above the thermocline, the mean isopycnals are predominantly flat and more heavily stratified than those below, where changes in density are smaller. The densest 27.74 kg m^{-3} isopycnal deepens between $\sim 2 - 8$ km along the transect, before shoaling again on the inner part of the bay approaching Sheldon Glacier, at distances > 8 km from A. The 27.74 kg m^{-3} isopycnal also deepens between $0 - 0.4$ km from A, however, this is an artefact caused by a lack of data at this end of the section and it is not representative of the hydrography in Ryder Bay; only one profile was recorded below between $0 -$ 0.4 km and below 300 m, and this occurred on day 49, after significant hydrographic changes occurred within Ryder Bay (as described in Section 3.4). The presence of the warm CDW means that there is a reservoir of heat available at depth that can be mixed upwards into the overlying cooler waters. The fact that the warmest waters are blocked by the ridge suggests that such ridges could be important for the WAP heat budget.

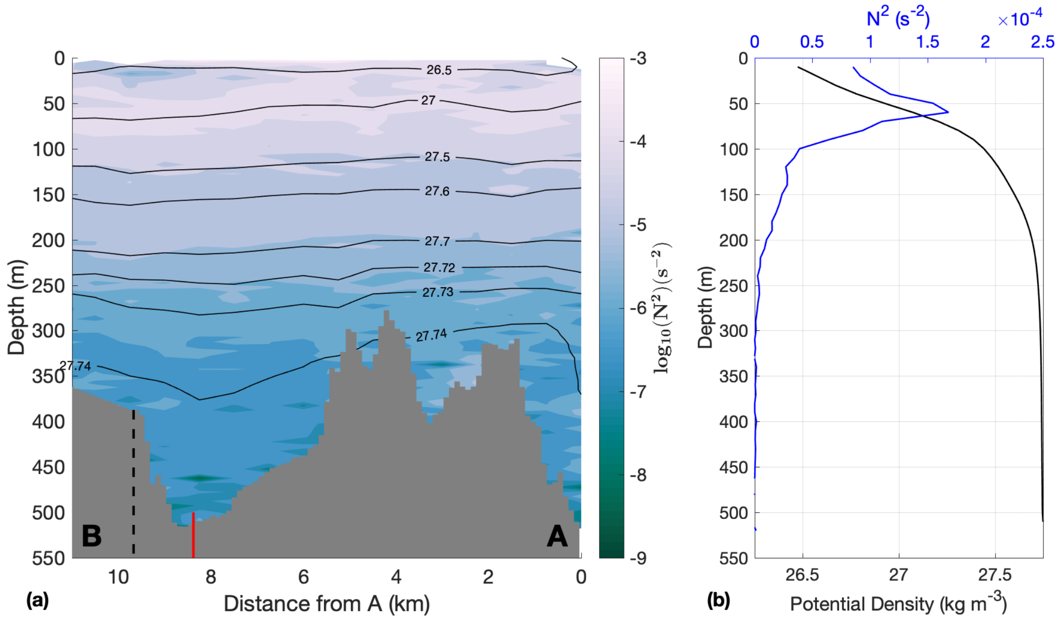

FIGURE 3.7: (a) Mean vertical section of buoyancy frequency squared (s^{-2}). Contours are in $log_{10}(0.5)$ increments from $log_{10}(-10)$ to $log_{10}(-3)$ s^{-2}. The ADCP mooring location (vertical red line overlaying the grey bathymetry) and $26.5-27.74$ kg m^{-3} surface-referenced potential density isopycnals (black contours) are also shown. Bathymetry is from Fremand (2020) up until $\sim$ 9.7 km (dashed vertical line), after which, no real data exists. Therefore, the bathymetry is linearly interpolated up to a depth of 350 m at 12 km along the section, in line with the glider data. (b) Mean depth profile of buoyancy frequency squared with potential density (-1000 kg m^{-3}).

3.3.2 Dissipation

The direct estimates of the dissipation of TKE from the glider enables the direct estimation of vertical mixing within Ryder Bay. The methodology product containing the dissipation estimates, $information\_extract\_all\_saved.mat$, is used to produce a mean section of dissipation rates along the A-B transect. The accepted dissipation estimates are gridded into 1 km distance and 10 m depth cells. This is a lower resolution than the grid used for the hydrographic data due to the smaller volume of accepted dissipation data, as determined by the conservative QAA. The QAA discards spectra that were rejected, causing temporal and spatial heterogeneity in the number of dissipation rates. The larger grid spacing is therefore necessary to ensure that there are sufficient points within each grid cell.

A plot of the mean dissipation rate within each grid cell and the number of dissipation estimates that went into each is overlain (Figure 3.8). White grid cells have zero dissipation estimates. The mean number of dissipation estimates is 25, and the highest is found between $50-200$ m depth and $8-9$ km along the section (70+). This is because the glider was initially deployed to survey the basin before being programmed to complete transects into and out of the bay. The grid cells with the lowest number of estimates are close to the seafloor. This is because dissipation estimates near glider

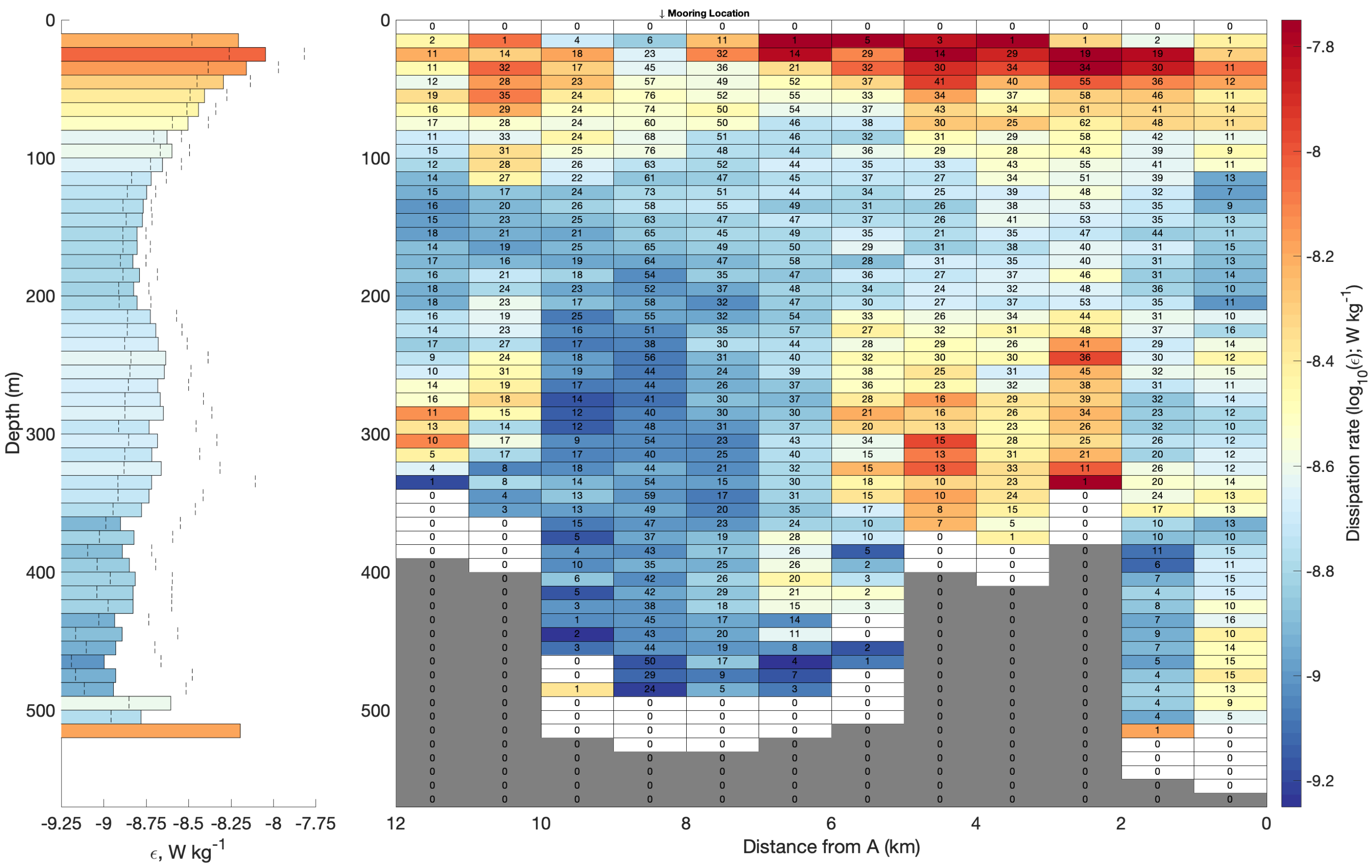

FIGURE 3.8: Plot showing the mean dissipation rates with the number of estimates overlain. Left panel is a mean depth profile of dissipation rates, weighted by the number of estimates within each grid cell (colours also represent dissipation rate). Dashed black lines represent the 90% bootstrapped errors for each depth cell, using 1000 bootstrap datasets.

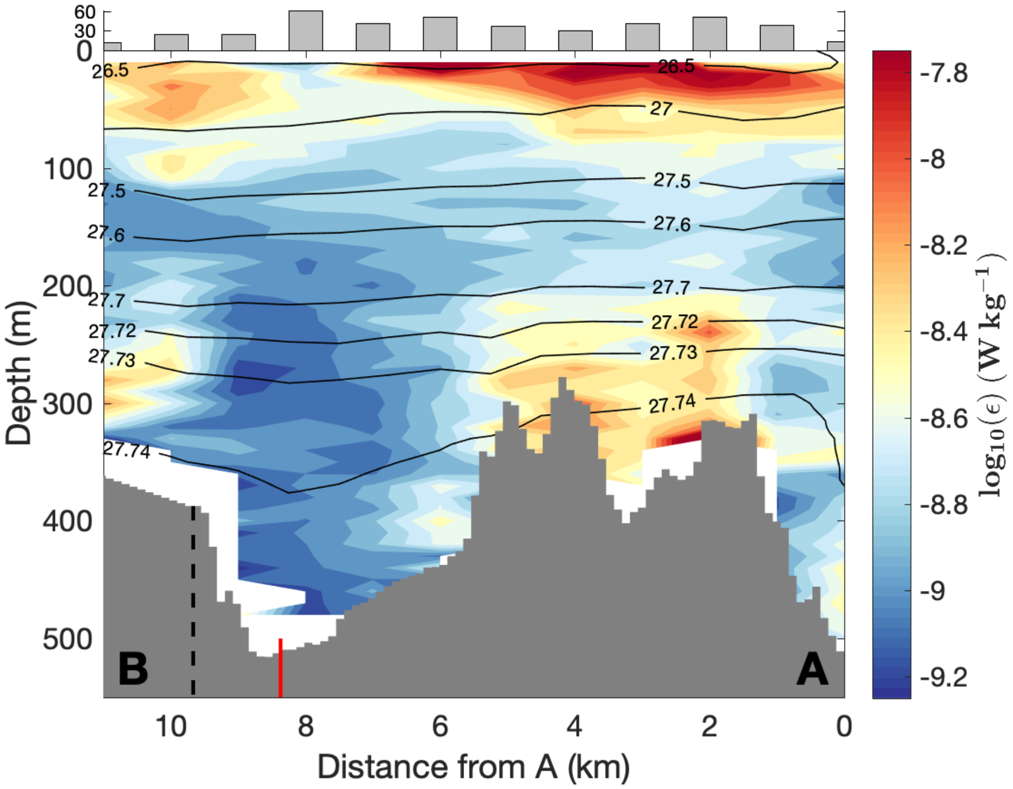

FIGURE 3.9: Mean vertical section of the dissipation of turbulent kinetic energy, ϵ. Contours are in $log_{10}(0.1)$ increments from $log_{10}(-9.5)$ to $log_{10}(-7.5)$ W kg^{-1}. Prior to plotting, dissipation data were gridded into 10 m depth and 1 km distance cells to ensure a sufficient number of data points went into each mean. To provide insight into data coverage, the number of different profiles used in each distance grid cell are shown in the bar chart above the main panel. The ADCP mooring location (vertical red line overlaying the grey bathymetry) and $26.5 - 27.74$ kg m^{-3} surface-referenced potential density isopycnals (black contours) are also shown. Bathymetry is from Fremand (2020) up until $\sim$ 9.7 km (dashed vertical line), after which, no real data exists. Therefore, the bathymetry is linearly interpolated up to a depth of 350 m at 12 km along the section, in line with the glider data.

turns are rejected (see Section 2.1.4.6), but it is also likely due to differences between the true water depth and the gridded maximum depth for the mean section.

A weighted mean depth profile of dissipation estimates (Figure 3.8, left-hand panel) highlights high dissipation close to the surface (upper $50 - 100$ m), moderate dissipation above the ridge (at $200 - 350$ m depth), and an increase in dissipation close to the bottom (at depths > 500 m). 90% bootstrapped error bars are also displayed (calculated as explained in Section 2.1.4.3). 90% error bars are small at depths shallower than the ridge, where there are more estimates and less variation in dissipation estimates across the section. The errors increase below 250 m, reflecting the strong spatial differences between the ridge and basin and the smaller number of available estimates. No error bars are shown for the bottom-most grid cell because only one dissipation estimate was observed at this depth (between $1 - 2$ km) so no bootstrapped errors could be calculated.

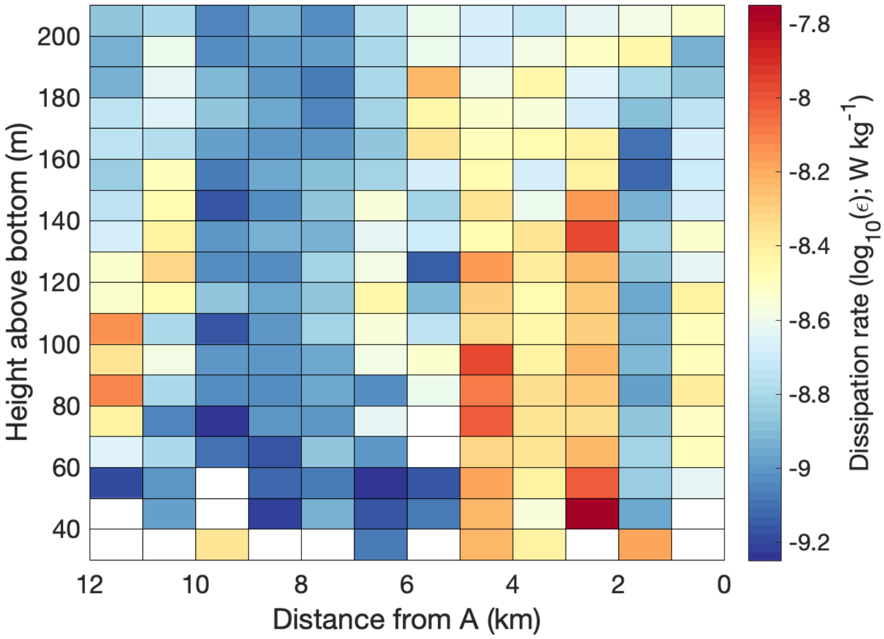

FIGURE 3.10: Height Above Bottom plot, showing mean dissipation rates 200 m from the seafloor. Colours are the dissipation estimates, white indicates no dissipation estimate.

Figure 3.8 shows the mean dissipation rate for each of the grid cells in the mean section, however, spatial patterns are perhaps more clearly seen in a filled contour plot (Figure 3.9). The section of mean dissipation of TKE reveals strong spatial patterns within Ryder Bay. Although the top 20 m are ignored due to pitch motor noise from the glider turning, elevated dissipation rates $O(10^{-8})$ W kg^{-1} are found in the top 50 m (elevated here refers to dissipation greater than the overall deployment mean of 1.6×10^{-9} W kg^{-1}). This is expected due to the wind's energy input into the water column. Dissipation rates in the basin are very low below 100 m depth, $O(10^{-10})$ W kg^{-1}. Above the ridge, in particular below $\sim$ 200 m, are higher dissipation estimates with rates $O(10^{-8})$ W kg^{-1}. The highest dissipation rates at depth are closest to the ridge, implying that the observed spatial pattern is attributable to ridge-flow interaction. The top axis is a histogram showing the number of individual profiles that went into each 1 km distance grid cell. A profile was included if it contributed 1 or more dissipation estimates. Over 20 profiles were used in all but the first and last distance grid cells, with up to 61 profiles close to the mooring.

A Height Above Bottom (HAB) plot enables a better comparison of dissipation rates close to the seafloor (Figure 3.10). Dissipation rates above the topographic ridge, between $\sim 2 - 5$ km, are clearly elevated and are $O(1 \times 10^{-8})$ W kg^{-1}. This is a large contrast to mean dissipation rates in the basin, between $\sim 5 - 10$ km, which are $O(1 \times 10^{-10})$ W kg^{-1}. This appears true for up to $\sim$ 200 m HAB, suggesting that the ridge is a significant spatial control on dissipation. This is quantified using Figure 3.11, which,

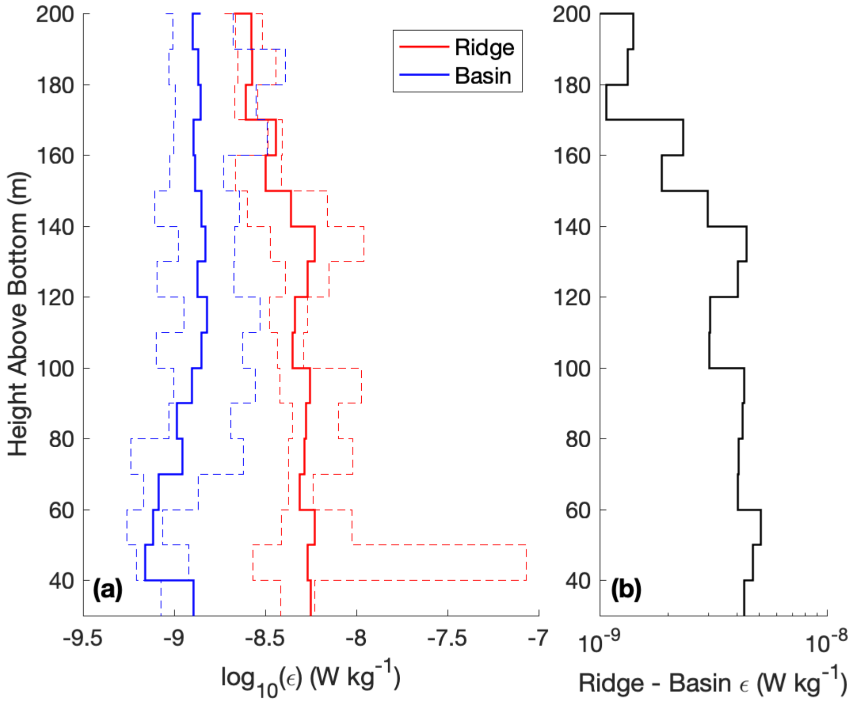

FIGURE 3.11: Comparison of mean ridge and basin dissipation rates. (a) Stairs plot comparing the mean dissipation rates within the respective regions. Dashed black lines represent the 90% bootstrapped errors for each depth cell, using 1000 bootstrap datasets. (b) Stairs plot showing the difference between ridge and basin dissipation rates at each depth.

for each depth grid cell, compares the mean dissipation within the ridge and basin regions, defined above. Although the error bars for dissipation rates between $160 - 200$ m overlap (Figure 3.11a), at each HAB grid cell the mean ridge dissipation rates are higher than in the basin. For HAB distances $<$ 160 m the 90% bootstrapped error bars also do not overlap, suggesting that the dissipation estimates above the ridge are significantly different to the those recorded in the basin.

3.3.3 Heat Fluxes

Dissipation rates can be used to quantify the diapycnal diffusivity, κ_ρ, using the Osborn relation, Equation 3.1:

$$\kappa_\rho = \Gamma \frac{\epsilon}{N^2} \tag{3.1}$$

where Γ is the mixing efficiency, taken here to be the typical value of 0.2 (Osborn, 1980), and N is the buoyancy frequency, a measure of the stratification. Glider hydrographic data from the full deployment (Figure 3.2) is used in the calculation, and the data is gridded onto a 1 km distance and 10 m depth grid (i.e. onto the same grid as the dissipation estimates). These sections are then used in conjunction with Equation 3.1 to calculate a section of diapycnal diffusivity. However, raw temperature and salinity

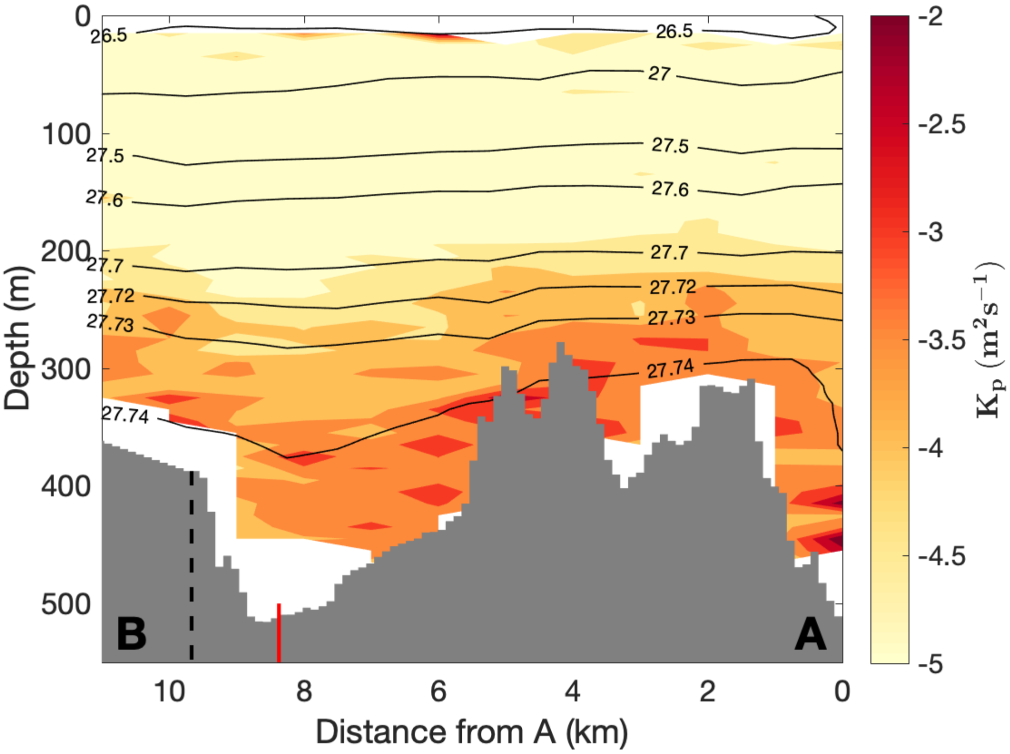

FIGURE 3.12: Mean vertical section of the diapycnal diffusivity, κ_ρ. Contours are in $log_{10}(0.5)$ increments from $log_{10}(-7)$ to $log_{10}(-2)$ m^2 s^{-1}. The ADCP mooring location (vertical red line overlaying the grey bathymetry) and $26.5 - 27.74$ kg m^{-3} surface-referenced potential density isopycnals (black contours) are shown. Bathymetry is from Fremand (2020) up until $\sim$ 9.7 km (dashed vertical line), after which, no real data exists. Therefore, the bathymetry is linearly interpolated up to a depth of 350 m at 12 km along the section, in line with the glider data.

inversions cause negative density gradients and produce imaginary κ_ρ values. Consequently, here the inversions are smoothed over by removing negative N^2 values and linearly interpolating across each depth gap.

A mean diapycnal diffusivity section (Figure 3.12) shows low diapycnal diffusivities $O(10^{-6}) - O(10^{-5})$ m^2 s^{-1} in the upper 200 m, where the stratification is higher (Figure 3.7). Below 200 m, κ_ρ values $O(10^{-4}) - O(10^{-3})$ m^2 s^{-1} are observed. The relatively high diapycnal diffusivity in this region can likely be attributed to the low stratification at these depths. Diapycnal diffusivities are highest above the ridge. This demonstrates that, in the presence of a negative upward temperature gradient, the ridge could cause a significant flux of heat from the CDW, across the thermocline and into the WW layer. At these depths the heat can be more easily mixed with surface waters through additional mixing processes.

κ_ρ can be used to quantify the transfer of different properties of interest. A relevant

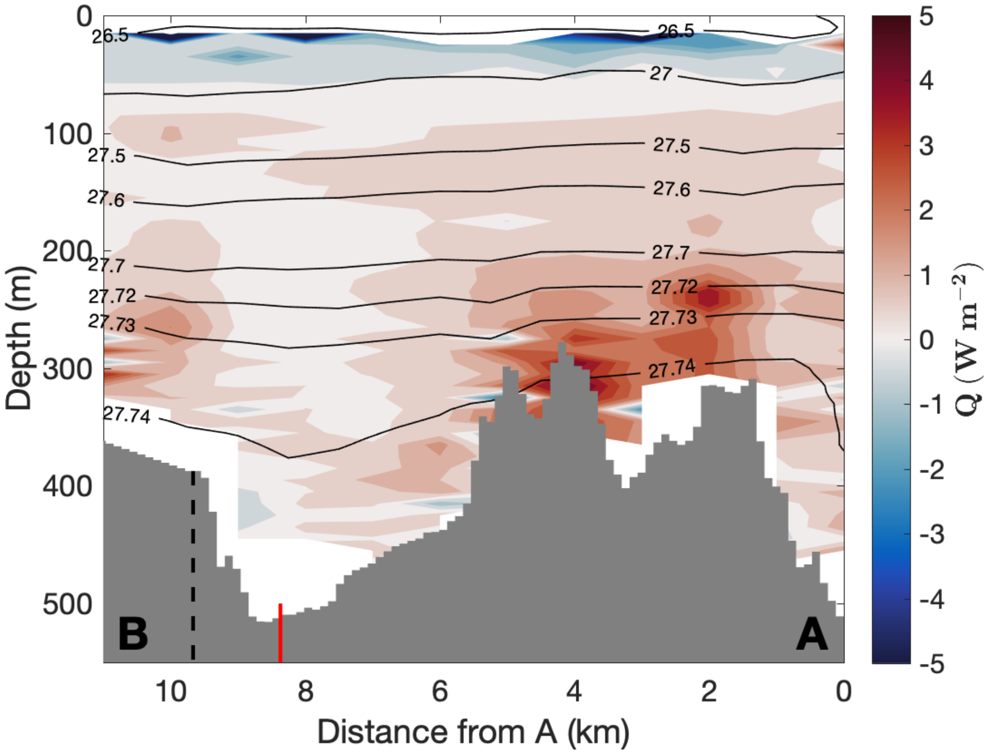

FIGURE 3.13: Mean vertical section of the upward heat flux, Q. Contours are in 0.5 W m^{-2} increments from -10 to 10 W m^{-2}. The ADCP mooring location (vertical red line overlaying the grey bathymetry) and $26.5-27.74$ kg m^{-3} surface-referenced potential density isopycnals (black contours) are shown. Bathymetry is from Fremand (2020) up until $\sim$ 9.7 km (dashed vertical line), after which, no real data exists. Therefore, the bathymetry is linearly interpolated up to a depth of 350 m at 12 km along the section, in line with the glider data.

quantity here is the upward heat flux, Q, which is calculated using the following equation:

$$Q = \rho_0 C_p \kappa_p \frac{\partial \theta}{\partial z} \tag{3.2}$$

where positive Q is upwards, ρ_0 is the reference density (1.025×10^3 kg m^{-3}), and C_p is the specific heat capacity at constant pressure (4000 J kg^{-1} °C^{-1}). The smoothed diapycnal diffusivities from Figure 3.12 were used to calculate a section of mean upward heat fluxes (Figure 3.13). Heat fluxes up to $\sim$ 5 W m^{-2} are found between $100-150$ m above the ridge, with the strongest values found closer to the seafloor. The heat fluxes over the ridge are up to $\sim$ 10 times larger than those at similar depths within the basin ($\sim 0.3-0.5$ W m^{-2}). In contrast, negative heat fluxes are observed in the upper $\sim$ 50 m, reaching less than -10 W m^{-2} close to the surface. Between $100-200$ m depth over the ridge, heat fluxes are commonly in the range of $0.7-0.9$ W m^{-2}, suggesting that they are also elevated with respect to those of similar depths above the basin. Heat fluxes of these magnitudes span $\sim 0-8$ km along the section at $\sim$ 130 m depth, suggesting that heat fluxes vertically but then spreads laterally at the base of the thermocline.

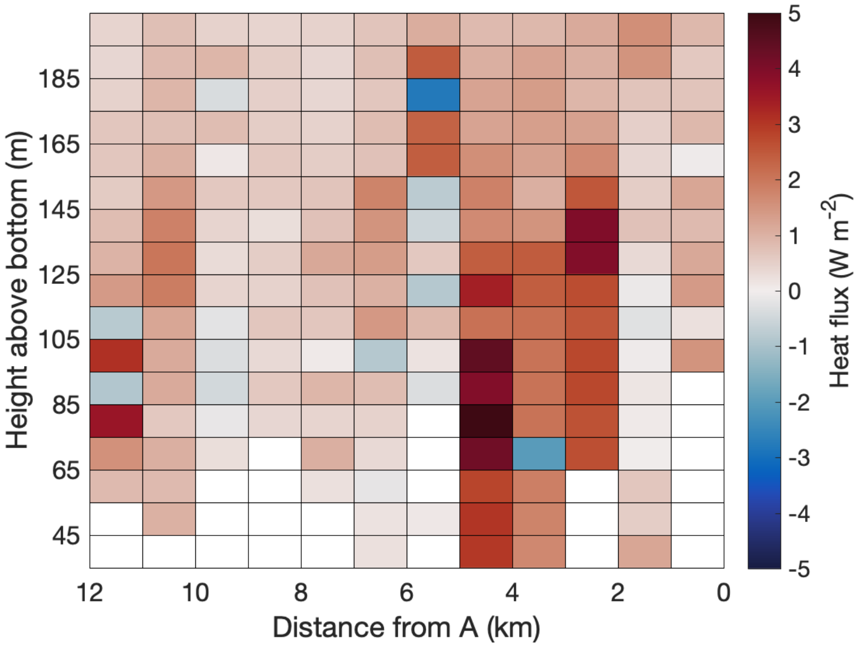

FIGURE 3.14: Height Above Bottom plot, showing mean heat fluxes 200 m from the seafloor. Colours are heat fluxes, white indicates no heat flux estimate.

Similar to Figure 3.10 above, it is instructive to use a HAB plot when looking at spatial controls related to bathymetry to better compare heat fluxes close to the seafloor (Figure 3.14). Heat fluxes in the 200 m above the bottom are predominantly positive across the length of the section, with the highest heat fluxes located over the ridge, between $2-5$ km. The majority of the observed negative heat fluxes are found in the basin, particularly between $5-6$ km and $9-10$ km along the section, however, two strong negative heat fluxes of -2 and -3 W m^{-2} are observed close to the ridge, between $3-4$ km and $5-6$ km respectively. The negative heat fluxes are caused by small temperature inversions, which occur below 250 m in 36% of glider profiles.

Differences between heat fluxes over the ridge and in the basin may not be as pronounced as in the dissipation estimates, however, they are are still significant (Figure 3.15a). The smaller differences are likely due to the relatively high diapycnal diffusivity at depth in the basin which, as mentioned above, is attributed to low stratification (Figure 3.12). At depths greater than 150 m from the bottom, and for all but the $65-75$ m depth cell, 90% ridge and basin error bars do not overlap, suggesting that heat fluxes are elevated over the ridge. The large negative error bar between $65-75$ m is caused by the presence of the negative heat flux between $3-4$ km, highlighted above. This negative heat flux also lowers the mean value at this depth, explaining the low difference in dissipation estimates between the ridge and the basin (Figure 3.15b). Excluding this depth cell, the mean heat flux over the ridge for HAB distances < 140 m is 2.5 W m^{-2}, compared to 0.4 W m^{-2} in the basin. Error bars for the heat fluxes at HAB distances greater than 150 m overlap and therefore are not significantly different between

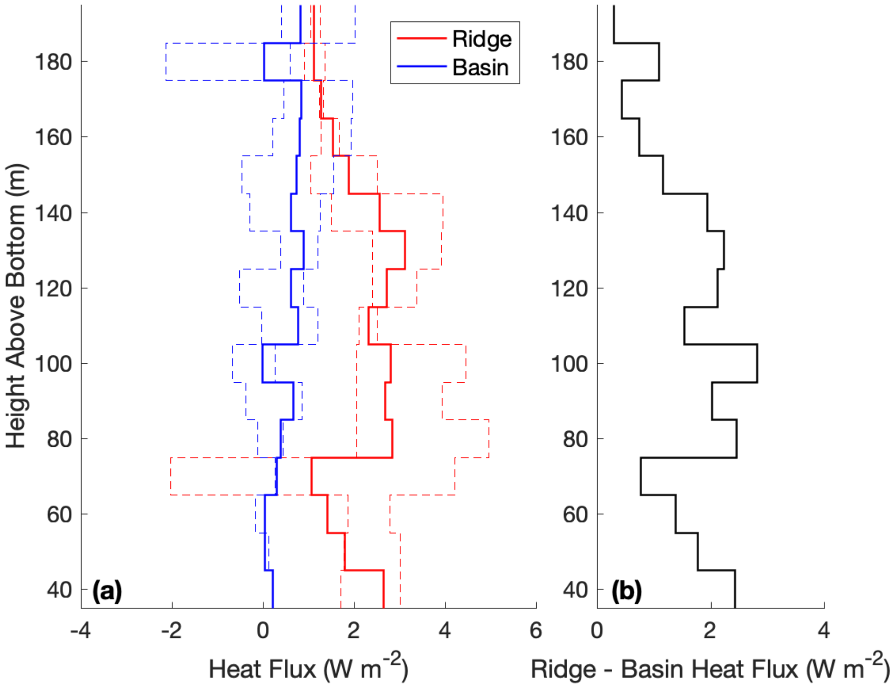

FIGURE 3.15: Comparison of mean ridge and basin heat flux estimates. (a) Stairs plot comparing the mean heat fluxes within the respective regions. Dashed black lines represent the 90% bootstrapped errors for each depth cell, using 1000 bootstrap datasets. (b) Stairs plot showing the difference between ridge and basin heat fluxes at each depth.

the ridge and the basin. This suggests that processes associated with the seafloor, in particular the ridge, have a role in controlling the heat that is transferred upwards into overlying waters.

3.4 Temporal Variability

Towards the end of the deployment the glider surveyed the A-B transect thirteen times between days 41 – 50 (since the start of the deployment), spanning the topographic ridge and the deep basin (Figures 3.1, 3.2). These transects are the focus of this section, and they reveal significant temporal variability in Ryder Bay's hydrography, dissipation, and heat fluxes. Individual hydrographic transects are constructed using Laplacian-Spline interpolation with a vertical grid spacing of 5 m and a horizontal grid spacing of 0.25 km. The horizontal grid spacing used for the individual transects is smaller than the horizontal distance covered by the glider during a profile ($\sim$ 1 km), ensuring that detail is not lost. Using a smaller grid spacing than that used for the mean sections is possible here because there is less variation in the hydrographic data from a single glider transect.

3.4.1 Hydrography

Figure 3.16 shows conservative temperature glider Transects $2-7$, which were collected between 21th-24th February 2016 (days $41-45$ since the start of the deployment). Note that Transect 1 was incomplete and is not discussed here. In the upper $50-60$ m of Transect 2, lies an AASW layer with temperatures consistently between -0.25 and -0.5 °C along the section, excluding two small regions of warmer water > -0.25 °C centred at 1.75 and 6.25 km. The permanent thermocline is predominantly flat, with a mean depth of 150 m. Above the thermocline, at a depth of $\sim$ 80 m, lies a $20-30$ m thick layer of remnant WW with temperatures ≤ -0.75 °C that extends across the full length of the section. The WW layer has approximately constant thickness, with the 27 kg m^{-3} isopycnal located at its centre. Whilst the ispycnals close to the thermocline are uniformly flat along the section, the $27.72-27.74$ kg m^{-3} isopycnals have significant changes in depth, with the largest variation occurring closest to the ridge. The isopycnals steeply shoal and pinch together over the ridge, between $3-6$ km, and are steeply sloping in the ridge's lee, the layers thickening downstream. The distance between the 27.735 and 27.74 kg m^{-3} isopycnals changes from 10 m at 3.75 km to 120 m at 6.75 km. The white gap between $\sim 0-1$ km and below $\sim$ 200 m is due to a lack of glider data.

The hydrography above the thermocline in Transect 3 remains largely unchanged compared to Transect 2. The thermocline has a constant depth of $\sim$ 150 m, and there are only small changes in the WW layer above; a temperature inversion exists $\sim 3-4.5$ km, with cooler WW rising to a depth of $55-60$ m and overlying warmer AASW. Below the thermocline, $\sim$ 200 m temperatures have increased, particularly above the ridge, where the 1 °C contour has risen from a depth of 230 m to 200 m between Transects 2 to 3. The isopyncals around the ridge have also changed significantly, with more variation in density, including inversions occurring at 2.75 and 4.75 km along the section. The location of the steeply sloping 27.735 and 27.74 kg m^{-3} isopycnals has moved to between the two ridge crests. Unlike in Transect 2, the glider surveyed the full depth between $0-1$ km along the section, revealing the warmest CDW with temperatures > 1.2 °C around 440 m.

The thermocline in Transect 4 is still relatively flat, but has shoaled to a mean depth of 143 m. Above the thermocline there is little change in the WW layer, however, in the AASW layer there is a more prominent pool of warmer (> -0.25 °C) water extending to $\sim$ 15 m depth between $\sim 5-8.5$ km. Isopyncals below the thermocline again pinch together above the ridge at 5 km along the section. The isopycnals are steeply sloping in the lee of the ridge, with the densest isopycnals having the greatest slope at distance and depth of 5.5 km and 340 m respectively. These densest layers thicken downstream in the basin. The warmest CDW ($\sim$ 1.27 °C) at the entrance to the bay has risen from 440 m to $\sim$ 350 m, and although it does not appear to breach the first ridge crest, a small volume of this water is observed close to the ridge's second crest at 4.5 km.

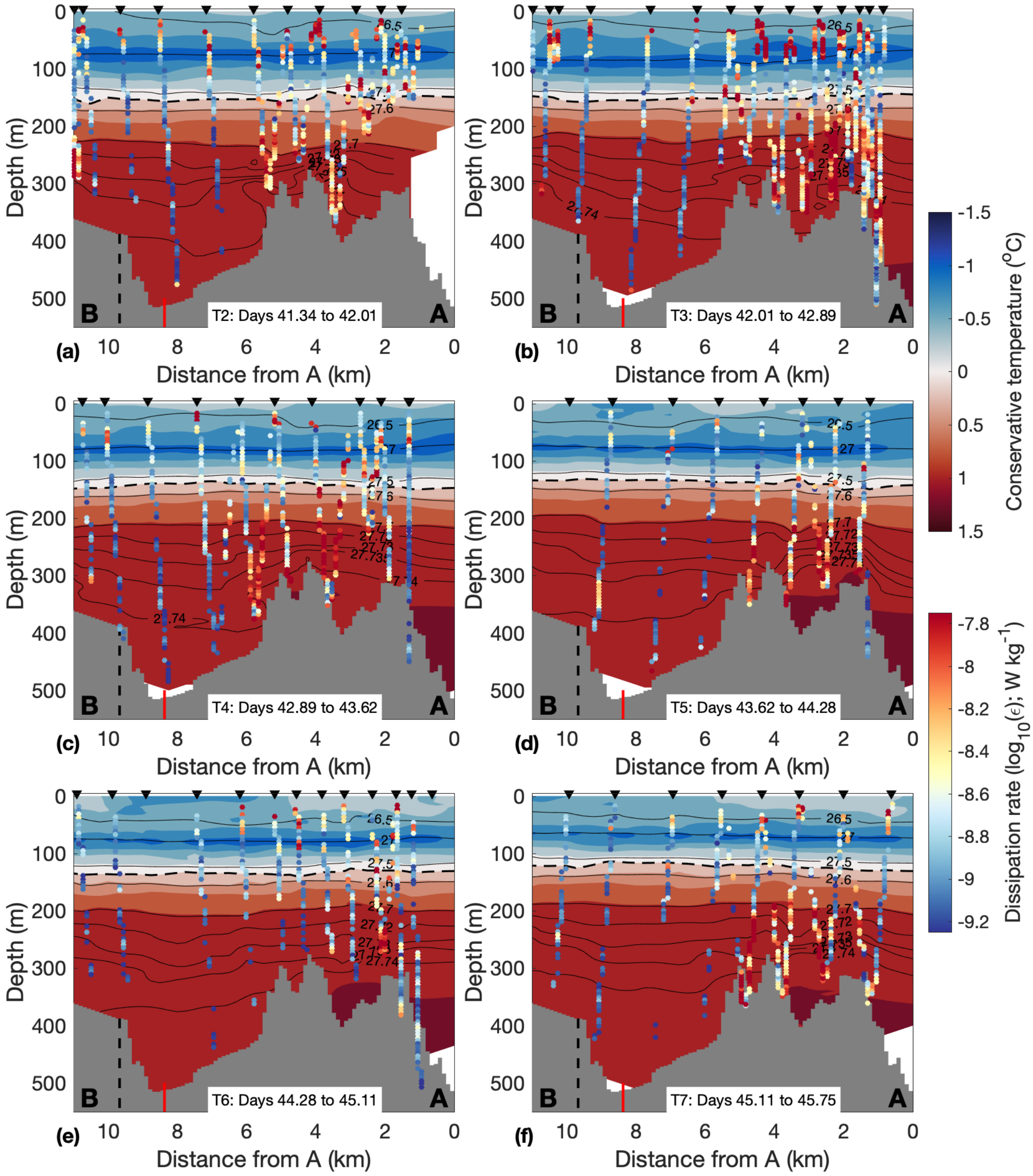

FIGURE 3.16: Vertical sections of conservative temperature for Transects $2-7$, with individual dissipation estimates overlain. Temperature contours are in 0.25 °C increments from -1.25 to 1.5 °C. Dissipation contours are in $log_{10}(0.1)$ increments from $log_{10}(-9.5)$ to $log_{10}(-7.5)$ W kg^{-1}. The black arrows indicate the start of each downcast. Dashed black lines denote the thermocline (defined using the 0.25 °C isotherm). Black contours indicate the $26.5-27.74$ kg m^{-3} surface-referenced potential density isopycnals. The ADCP mooring location is shown using the vertical red line overlaying the grey bathymetry. Bathymetry is from Fremand (2020) up until $\sim$ 9.7 km (dashed vertical line), after which, no real data exists. Therefore, the bathymetry is linearly interpolated up to a depth of 350 m at 12 km along the section, in line with the glider data.

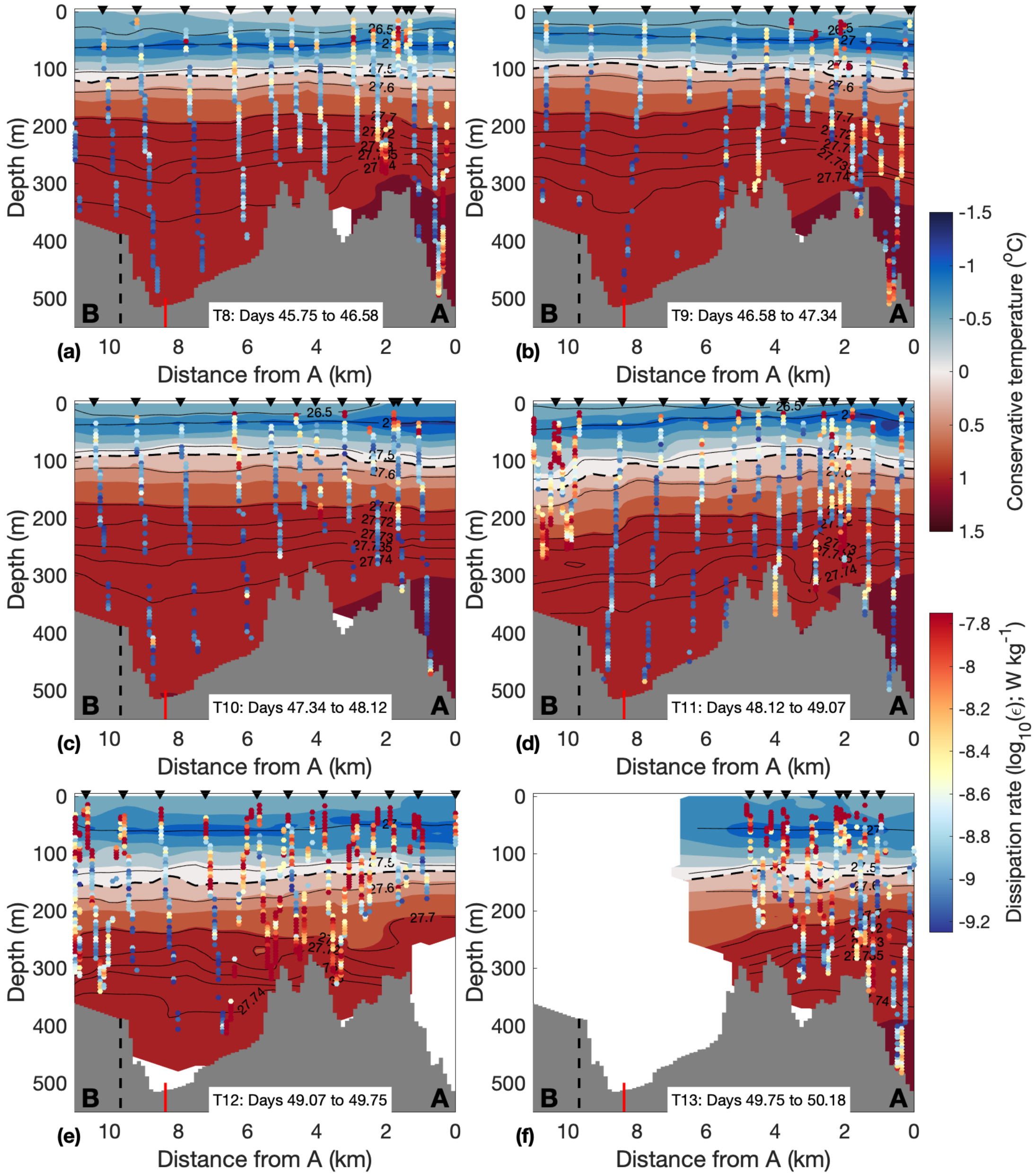

FIGURE 3.17: Vertical sections of conservative temperature for Transects 8 − 13, with individual dissipation estimates overlain. Temperature contours are in 0.25 °C increments from −1.25 to 1.5 °C. Dissipation contours are in $log_{10}(0.1)$ increments from $log_{10}(-9.5)$ to $log_{10}(-7.5)$ W kg^{-1}. The black arrows indicate the start of each downcast. Dashed black lines denote the thermocline (defined using the 0.25 °C isotherm). Black contours indicate the 26.5 − 27.74 kg m^{-3} surface-referenced potential density isopycnals. The ADCP mooring location is shown using the vertical red line overlaying the grey bathymetry. Bathymetry is from Fremand (2020) up until ∼ 9.7 km (dashed vertical line), after which, no real data exists. Therefore, the bathymetry is linearly interpolated up to a depth of 350 m at 12 km along the section, in line with the glider data.

The AASW layer in Transect 5 has more variation than in previous sections, with cool (< -0.5 °C) surface waters observed at $\sim$ 9 km along the section and a deeper warmer (> -0.25 °C) pool of surface water to $\sim$ 30 m at $5-6$ km. The WW layer shows signs of erosion and is no longer continuous along the length of the section (e.g, at 7.5 and 9.25 km). The thermocline continues to shoal, with a mean depth of 138 m. The strong pinching of the isopycnals below the thermocline persists into Transect 5, however, the pinch point has moved further out of the bay, to 2 km along the section. The warmest CDW ($\sim$ 1.27 °C) now clearly breaches the first ridge crest, and is shallowest (295 m) at 1.75 km.

In Transect 6, the variation in the AASW layer increases; the upper 15 m cool waters spreading between $5.75-9.5$ km, and the warmer waters extend to 25 m between $0-4.75$ km. The break up of the WW layer continues, with the gaps widening to $\sim$ 0.75 km between the coldest waters (≤ -0.75 °C) above the basin. The thermocline is flat and has shoaled, with a mean depth of 134 m. Below the thermocline, pinching of isopycnals over the ridge is less pronounced, and although the 27.74 kg m^{-3} isopycnal still deepens in the lee of the ridge, lighter isopycnals up to the 27.72 kg m^{-3} are much flatter than in any of the previous transects. The $\sim$ 1.27 °C CDW is still past the first ridge crest and has a shallowest depth of 330 m.

The AASW and WW layers continue to warm in Transect 7, with the disappearance of the cooler water between $5.75-9.5$ km and the further disintegration of the WW layer over the basin. Overall the thermocline has shoaled and is sloped, with a mean depth of 121 m and deepening from 115 m at 11 km to 130 m at the bay's entrance. Isopycnals immediately below the thermocline are flat, however, the $27.72-27.74$ kg m^{-3} isopycnals pinch together at 2 km, and a deepen downstream into the basin. The warmest CDW is extends close to the second ridge crest and has a depth of 340 m.

Figure 3.17 illustrates how the hydrography changes between glider Transects $8-13$, which were collected between 24th February - 1th March 2016 (days $45-50$ since the start of the deployment). In Transect 8, the warm AASW has spread along the section, now spanning from $0-9.5$ km. Below this, the WW layer continues to thin, with a gap between the coldest ≤ -0.75 °C water forming at 2 km. The mean thermocline is flat and shoals to a depth of 113 m. The $27.72-27.74$ kg m^{-3} isopycnals pinch together over the first ridge crest from 1 km to 2.75 km, and the 27.74 kg m^{-3} isopycnal is steeply sloping at 3.5 km, deepening towards the second ridge crest. The warmest CDW water has a similar shape to the 27.74 kg m^{-3} isopycnal, rising over the first crest to a depth of 285 m and deepening to $\sim$ 345 m at 2.75 km.

A 30 m thick layer of AASW with a uniform temperature of > 0.5 °C is observed in Transect 9. Much of the WW ≤ -0.75 °C over the basin has disappeared, however, the transect reveals the presence of a small layer of cold (≤ -1 °C) WW at around 55 m depth at the bay's entrance. The thermocline has shoaled significantly, with a mean depth of 101 m. The isopycnals below are much flatter than in previous sections. The $\sim$ 1.27 °C warm CDW is shallowest at 1 km and 305 m depth and has a structure similar to that in Transect 8, with perhaps more of the water spilling over the first ridge crest.

The AASW and WW layers in Transect 10 are largely unchanged compared to in Transect 9. The small ≤ -1 °C WW layer extends further into the bay and has shoaled to 35 m depth, corresponding with a cooling of the surrounding AASW between $0 - 2$ km. The thermocline shoals inshore towards B, moving from 90 m between $3 - 10$ km to $\sim$ 110 m between $0 - 3$ km; with a mean depth of 94 m. Isopycnals below the thermocline are flat, with only the 27.74 kg m^{-3} isopycnal gently deepening into the basin. The warmest CDW layer again has a similar shape to the previous two transects, but has retreated out of the bay slightly, with the same minimum depth of 305 m occurring at 0.75 km along the section.

Transect 11 shows the largest change in the structure of the water column so far. The thermocline has domed significantly, shoaling from 115 m at 1 km to 90 m at 3.75 km, then deepening down to a depth of 155 m at 11 km along the section. The doming is reciprocated by the WW layer above the thermocline, with a thin ($\sim$ 10 m) layer that extends across the full length of the section. 20 m thick parcels of ≤ -1 °C WW are observed at 0.75 and 1.5 km. The $27.6 - 27.72$ kg m^{-3} isopycnals have a shape similar to the thermocline, however, although the denser isopycnals also deepen into the bay, their structure is complicated over the ridge; e.g., the deepening and shoaling between $3 - 3.5$ km at $\sim$ 285 m depth. This variability in the thickness of the temperature and density layers suggests that the water in this region was less quiescent than in previous sections. The warmest $\sim$ 1.27 °C CDW has retreated further out of the bay, only just breaching the first ridge crest and shoaling to 300 m at 0.25 km.

The structure of the water column dramatically changes in Transect 12. The thermocline deepens from A ($\sim$ 130 m) to B ($\sim$ 160 m), with a mean depth of 144 m. The temperature of the AASW in the upper $40 - 50$ m is relatively constant, with a drop in temperature at 1.5 km along the section, likely associated with the erosion of the ≤ -1 °C WW parcels observed in Transect 11. A WW layer is observed at 55 m depth across the majority of the section, but has broken up between $3.5 - 4.5$ km and at 10 km. Unlike previous transects, where the thickness between the thermocline and the 27.7 kg m^{-3} isopycnal below is relatively constant, the thickness in Transect 12 between these layers ranges from $\sim$ 75 m at 7.50 km to 130 m at 2.75 km from A. Below $\sim$ 250 m, the density varies on smaller scales than the previous transects, with large changes in thickness and the slope of the isopycnals along the length of the section. Unfortunately, the glider did not complete the section between $\sim 0 - 2$ km and below $\sim$ 200 m depth, so the location of the warmest 1.27 °C CDW cannot be determined.

Although Transect 13 only contains data from < 5 km along the section, it still provides useful information about the hydrography within Ryder Bay. The AASW predominantly has cooler temperatures (< -0.5 °C) up to the surface, with a $20 - 30$ m thick layer of WW at a depth of ~ 60 m. The thermocline is relative flat within the observed region of the section, with a mean depth of 139 m, shoaling by 5 m compared to in Transect 12. Isopycnals below the thermocline all deepen towards the second ridge crest. Unlike in Transect 12, the glider sampled between $\sim 0 - 2$ km and below ~ 200 m depth in Transect 13, revealing that the ~ 1.27 °C CDW has retreated to a depth of 395 m, and no longer breaches the first ridge crest.

In summary, the individual glider transects reveal several features of interest. The AASW layer warms between Transects $2 - 8$, before cooling again in Transects $9 - 10$. As the AASW warms the underlying WW layer thins and shows signs of erosion. The other major feature is the gradual shoaling of the thermocline throughout the deployment between Transects $3 - 11$, followed by a dramatic ~ 50 m deepening in Transect 12.

3.4.2 Dissipation

Individual glider dissipation estimates, which overlay the conservative temperature sections described above (Figures 3.16, 3.17), vary significantly throughout the deployment. Data coverage is generally good, though it is better over the ridge where dissipation estimates are commonly high; dissipation estimates in the basin are low, often below the microstructure noise floor, in which case they are removed through the QAA (See Chapter 2). The dissipation can be divided into four regions: close to the surface in the upper $\sim 50 - 100$ m, across the base of the thermocline (between $100 - 200$ m), and below the thermocline (> 200 m), both above the ridge (defined here as between $1.3 - 5.4$ km) and in the basin ($5.4 - 10$ km).

In the upper $50 - 100$ m, patches of elevated dissipation $O(1 \times 10^{-8})$ W kg^{-1} are observed in the AASW and WW layers, down to depths of $\sim 70 - 80$ m; for example, at 4.3 km in Transect 2 and between $2 - 5.5$ km and at 10 km in Transect 3. Similarly large patches of elevated dissipation are not observed in Transects $4 - 6$, with a only a small patch of elevated dissipation around 3 km and 35 m depth in Transect 7. There is evidence of elevated dissipation between $\sim 1 - 2$ km and $25 - 75$ m depth in Transects $8 - 11$, at the interface between the AASW and WW. Transect 11 also has a large dissipation feature between $10 - 11$ km, with the full upper 100 m containing elevated dissipation $O(1 \times 10^{-8})$ W kg^{-1}. Transects 12 and 13 show similar levels of elevated dissipation across the full length of the section.

Across the base of the thermocline (between $\sim 100 - 200$ m), small regions of elevated dissipation of $O(1 \times 10^{-8})$ W kg^{-1} are observed in Transect 2 at 3.5 and 5.5 km, Transect

3 at 3.5 and 4.5 km, and in Transect 4 at 3.4 km along the section. This is in contrast to Transects $5 - 10$, where low dissipation of $O(10^{-9}) - O(10^{-10})$ W kg^{-1} is observed across the base of the thermocline. Transect 11 similarly has low dissipation between $0 - 10$ km, however, between $10 - 11$ km, the elevated dissipation in the upper 100 m extends across the thermocline down to $\sim$ 270 m depth. This elevated dissipation across the thermocline is observed across the full length of Transect 12, in a basin-wide dissipation event that is also captured by the portion of Transect 13 containing data.

As highlighted in Section 3.3.2, a major feature revealed by the glider deployment is elevated dissipation above the topographic ridge, typically $O(1 \times 10^{-8})$ W kg^{-1}. Transects $2 - 5$ have examples of this deep elevated dissipation, which is located where the $27.72 - 27.74$ kg m^{-3} isopycnals pinch together and are steeply sloping, deepening into the basin; for example at $\sim$ 5.4 km and below 270 m depth in Transect 2. Between transects, the location of the pinching isopycnals and elevated dissipation varies with respect to the ridge, moving to $\sim$ 2.4, 3.8 and 2.6 km in Transects $3 - 5$ respectively. In Transect 6, there is a small region of elevated dissipation where the isopycnals above the ridge pinch together at 2 km. However, the elevated dissipation in Transect 6 is much less widespread, which could be related to the flatter isopycnals than in previous transects, particularly the 27.74 kg m^{-3} isopycnal. Elevated dissipation spans $3 - 5.5$ km along the section in Transect 7, where the $27.72 - 27.74$ kg m^{-3} isopycnals deepen into the basin. Like Transect 6, Transect 8 has elevated dissipation confined to $\sim$ 2 km along the section, despite having a strongly sloping 27.74 kg m^{-3} isopycnal at 3.7 km; though this could be simply due to a lack of data. In Transects $9 - 11$, dissipation above the ridge is similar to that found in the deep basin $O(10^{-9}) - O(10^{-10})$ W kg^{-1}, again, likely corresponding to the flatter $27.72 - 27.74$ kg m^{-3} isopycnals. However, Transect 11 does have elevated dissipation at 2 km and 235 m, where the $27.73 - 27.735$ kg m^{-3} isopycnals deepen. Transect 12 has some of the strongest dissipation observed over the ridge, with rates up to $\sim 1 \times 10^{-7}$ W kg^{-1} occurring at 5.3 km along the section and 320 m depth, where the 27.72 kg m^{-3} isopyncal is steeply sloping and the isopycnals are pinching together. Elevated dissipation up to $\sim 1 \times 10^{-7}$ W kg^{-1} is also observed close to 6.6 km in Transect 12. In Transect 13, dissipation over the ridge is relatively low, $O(10^{-9}) - O(10^{-10})$ W kg^{-1}, and, although no data was recorded between $5 - 11$ km, the thickness of the $27.72 - 27.74$ kg m^{-3} isopycnals appear relatively constant, suggesting that they do not pinch together over the ridge. The relationship between dissipation and the slope of the $27.72 - 27.74$ kg m^{-3} isopycnals is explored further in Chapter 4.

To summarise, there are three main dissipation patterns within the individual glider transects. In the upper $50 - 100$ m, elevated dissipation is typically sporadic and patchy, primarily occurring over the ridge in Transects 2 and 3 and between Transects $8 - 11$. This is in contrast to the second dissipation feature, basin-wide elevated dissipation in Transects 12 and 13, both above 100 m and within and across the thermocline. The third feature is the persistent elevated dissipation above the topographic ridge, which moves with the location of the pinching and steeply sloping isopyncals.

3.4.3 Heat Fluxes

Section 3.3.3 showed a mean section with negative upward heat fluxes in the upper $50 - 100$ m and positive elevated heat fluxes at depth, over the topographic ridge at Ryder Bay's entrance (compared to basin values). Here, Equation 3.2 is used to generate individual heat fluxes at mid-points between the locations of the individual dissipation estimates described above. Heat fluxes overlay the glider conservative temperature sections (Figures 3.18, 3.19) and the magnitudes show similar temporal patterns as the dissipation estimates. Consequently, the regions used to describe the dissipation estimates in the section above are also used here to describe the heat fluxes. Differences with dissipation patterns predominantly arise due to variations in the vertical temperature gradient, which can alter the strength of the heat fluxes. A positive upward heat flux occurs in a region where there is a negative upward temperature gradient.

In Transects 2 and 3 heat fluxes are predominantly negative in the upper 100 m, with negative values down to $\sim 70 - 80$ m. In Transect 2, strong heat fluxes of ~ -6 W m^{-2} are observed at 4 km and $\sim$ 40 m, whilst in Transect 3, there are values up to ~ -20 W m^{-2} between $1.5 - 4.5$ km and $25 - 85$ m. Strong positive heat fluxes ($\sim$ 20 W m^{-2}) are also found in these regions, an indication of small temperature inversions that are smoothed over in the background contour plot of conservative temperature. Transects $4 - 6$ have no strong heat fluxes in the upper 100 m, with values typically between ~ -0.2 and -0.5 W m^{-2}. The small patch of dissipation around 3 km and 35 m depth in Transect 7 results in negative heat fluxes of ~ -4 W m^{-2}. Although Transects $8 - 11$ have elevated dissipation between $\sim 1 - 2$ km and $25 - 75$ m depth, they do not necessarily have strong heat fluxes; Transects 9 and 11 have heat fluxes commonly $\sim$ 2 W m^{-2} and up to $\sim \pm 5$ W m^{-2}, however, the heat fluxes in Transects 8 and 10 are predominantly $0.5 - 1$ W m^{-2}. These lower heat fluxes compare well with previous estimates by Brearley et al. (2017). The high dissipation observed in the upper 100 m of Transects $11 - 13$ caused strong heat fluxes, with negative values often exceeding -20 W m^{-2} in the upper 50 m and positive heat fluxes of $\sim 3 - 10$ W m^{-2} between $50 - 100$ m.

Individual heat fluxes across the base of the thermocline ($\sim 100 - 200$ m) vary significantly between transects. Transect 2 has strong heat fluxes of up to $\sim$ 15 W m^{-2} at 2.7 km and $\sim$ 5 W m^{-2} at 5.1 km along the section. Similarly high heat fluxes up to $\sim$ 10 W m^{-2} and $\sim$ 20 W m^{-2} are observed at 5.4 km and $2.3 - 3.2$ km in Transects 3 and 4 respectively. Heat fluxes across the base of the thermocline then decrease, with Transects $5 - 10$ having weaker heat fluxes between $\sim 0.2 - 0.5$ W m^{-2}. The elevated dissipation between $10 - 11$ km in Transect 11 and across the length of Transects 12 and

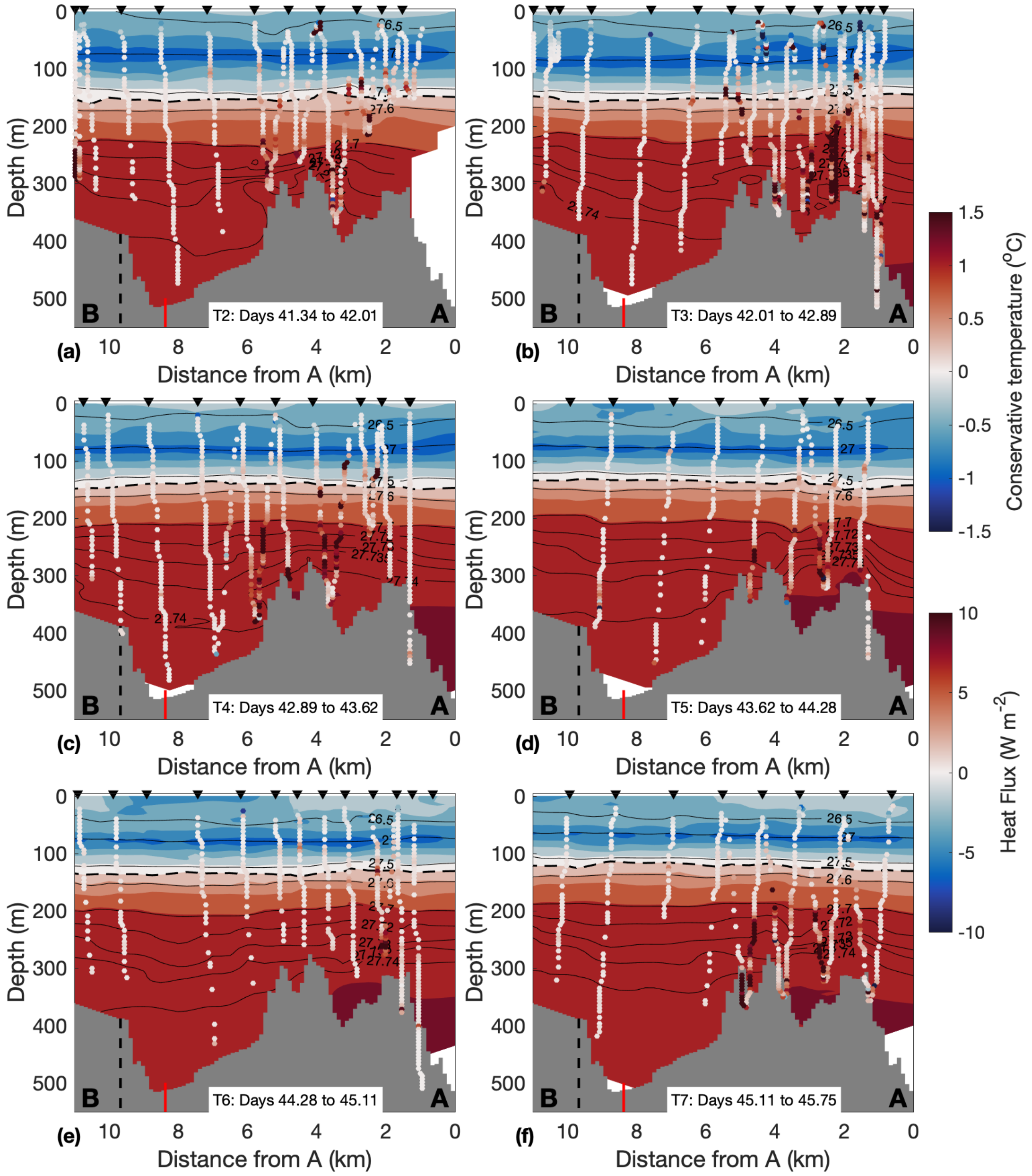

FIGURE 3.18: Vertical sections of conservative temperature for Transects 2 – 7, with individual heat fluxes overlain. Temperature contours are in 0.25 °C increments from -1.25 to 1.5 °C. Heat flux contours are in 0.5 W m^{-2} increments from -10 to 10 W m^{-2}. The black arrows indicate the start of each downcast. Dashed black lines denote the thermocline (defined using the 0.25 °C isotherm). Black contours indicate the 26.5 – 27.74 kg m^{-3} surface-referenced potential density isopycnals. The ADCP mooring location is shown using the vertical red line overlaying the grey bathymetry. Bathymetry is from Fremand (2020) up until ∼ 9.7 km (dashed vertical line), after which, no real data exists. Therefore, the bathymetry is linearly interpolated up to a depth of 350 m at 12 km along the section, in line with the glider data.

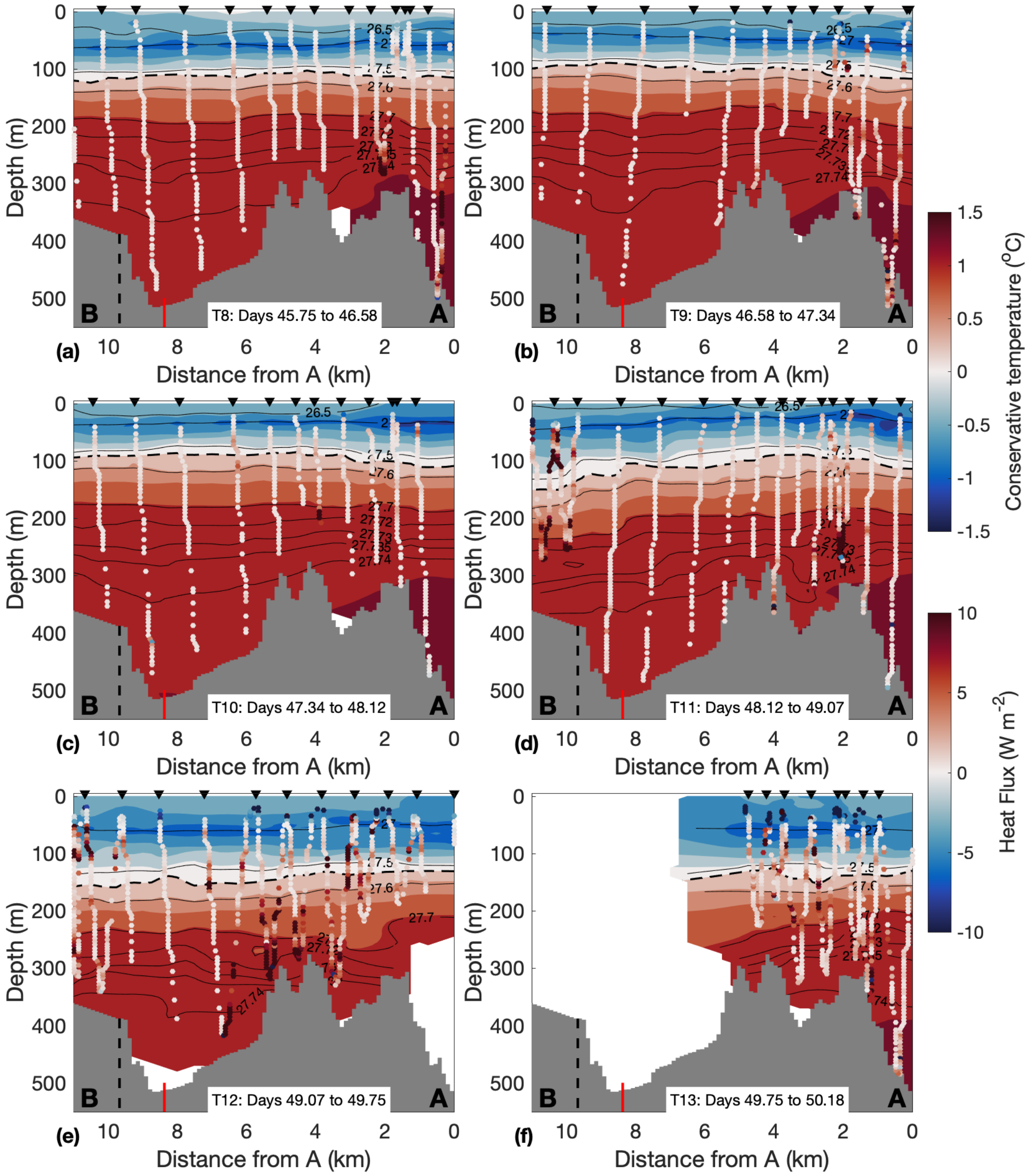

FIGURE 3.19: Vertical sections of conservative temperature for Transects 8 − 13, with individual heat fluxes overlain. Temperature contours are in 0.25 °C increments from −1.25 to 1.5 °C. Heat flux contours are in 0.5 W m^{-2} increments from −10 to 10 W m^{-2}. The black arrows indicate the start of each downcast. Dashed black lines denote the thermocline (defined using the 0.25 °C isotherm). Black contours indicate the 26.5 − 27.74 kg m^{-3} surface-referenced potential density isopycnals. The ADCP mooring location is shown using the vertical red line overlaying the grey bathymetry. Bathymetry is from Fremand (2020) up until ∼ 9.7 km (dashed vertical line), after which, no real data exists. Therefore, the bathymetry is linearly interpolated up to a depth of 350 m at 12 km along the section, in line with the glider data.

13 causes strong heat fluxes, often between $10 - 20$ W m^{-2}, but in places greater than 40 W m^{-2}.

As with dissipation, heat fluxes over the topographic ridges are generally higher than those in the deep basin. Individual heat fluxes in Transects $2 - 5$ commonly exceed 10 W m^{-2} where the isopycnals are pinching and steeply sloping, and can often be greater than $\sim$ 25 W m^{-2}; for example, in Transect 3 at 2.2 km between $210 - 330$ m depth, and in Transect 4 at 3.5, 4.7 and 5.5 km and 240, 300 and 230 m depths. The small region of elevated dissipation where the isopyncals pinch together at 2 km in Transect 6, causes positive upward heat fluxes of $\sim$ 15 W m^{-2}. In Transect 7, heat fluxes greater than 10 W m^{-2} are observed at 2.7 and 3.7 km, with the highest values of $\sim$ 40 W m^{-2} occurring where the isopycnals are most closely pinching together. Transect 8 again is similar to Transect 6, with strong heat fluxes ($\sim$ 15 W m^{-2}) at 2 km. Heat fluxes over the ridge in Transects $9 - 11$ are similar to the heat fluxes in the basin, typically < 0.5 W m^{-2}, though Transect 11 does have > 20 W m^{-2} heat fluxes at 2 and 4 km and 235 and 355 m depth. The weakened heat fluxes at depth within these transects could indicate a hiatus in the dominant mixing mechanism over the ridge. Transect 12 contains the strongest heat fluxes over the ridge, with heat fluxes up to $\sim$ 60 W m^{-2} in the lee of the second ridge crest. Strong heat fluxes of $20 - 50$ W m^{-2} are also observed between $250 - 410$ m up to 6.6 km along the section. Heat fluxes over the ridge in Transect 13 are generally < 1 W m^{-2}, but there are values of $10 - 15$ W m^{-2} at 1.2 km and 304 m depth.

This section has shown that the heat fluxes within Ryder Bay have similar temporal patterns as dissipation. Figure 3.20 provides a useful summary of these temporal patterns, showing median heat fluxes in the different regions mentioned above (note that surface fluxes are defined here as ≤ 50 m to aid analysis in Section 3.5). In the upper $\sim$ 50 m, heat fluxes are predominantly negative and sporadic, with the strongest fluxes of -1 W m^{-2} and -2.5 W m^{-2} occurring in Transects 3 and 12 respectively. However, upper 50 m heat fluxes are positive ($\sim$ 0.6 W m^{-2}) in Transects 10 and 11. Heat fluxes across the base of the thermocline are generally weak ($\sim$ 0.6 W m^{-2}), though strong positive upward heat fluxes double (1.3 W m^{-2}) during the basin-wide dissipation event in Transect 12. Heat fluxes over the ridge are relatively strong and consistently positive in Transects $2 - 5$ ($\sim$ 2 W m^{-2}), then weaken in Transect 6, before increasing again slightly in Transects $7 - 8$. The heat fluxes over the ridge then undergo a weakened period between Transects $9 - 11$ with fluxes similar to those across the thermocline, before dramatically increasing in Transect 12 to $\sim$ 5 W m^{-2}.

3.5 Summary and Discussion

This chapter describes the hydrography, dissipation and associated heat fluxes observed during the 2016 glider deployment, finding significant spatial and temporal

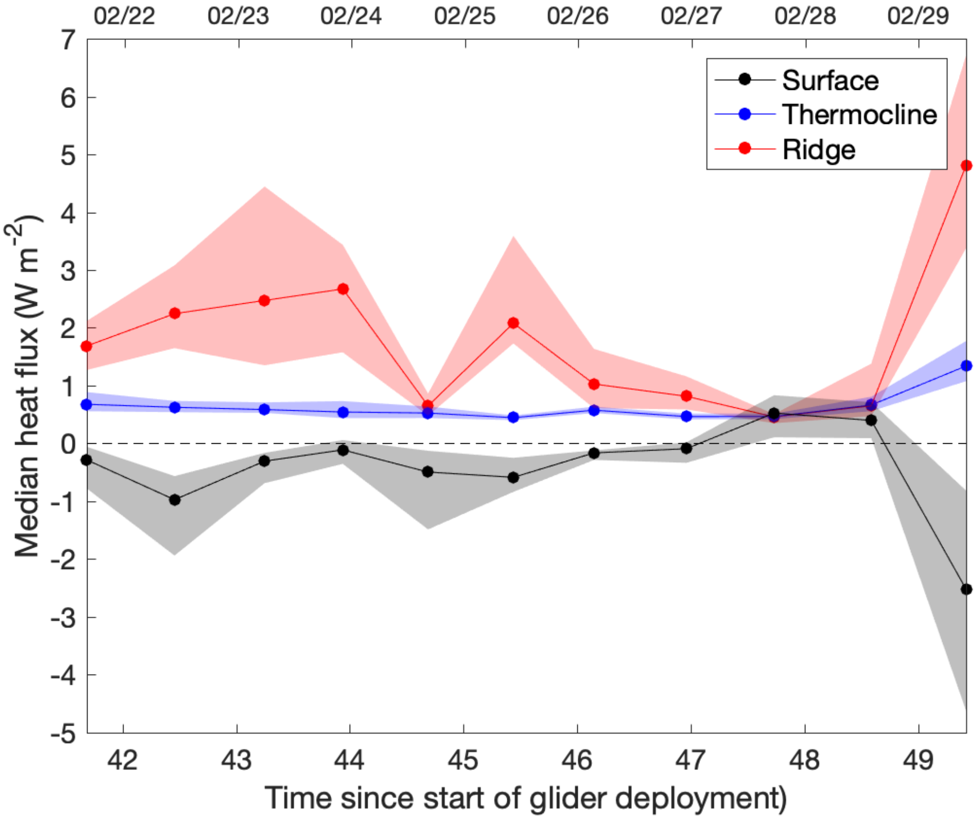

FIGURE 3.20: Comparison of median vertical heat fluxes for Transects $2-12$ (the complete transects). Deep heat fluxes were calculated at $\leq$ 200 m and between $1.3-5.5$ km. Thermocline heat fluxes are calculated over $100-200$ m depth, across the full length of the section. Surface heat fluxes are calculated in the upper 50 m, across the full length of the section. Shaded regions show 90% bootstrapped errors, using 1000 bootstrap datasets. A positive heat flux is upwards.

variability in all of these quantities across Ryder Bay.

Mean vertical sections of temperature and salinity reveal warm saline CDW underlying colder WW and AASW, with the warmest CDW found at depths $>$ 345 m, close to the first ridge crest at the entrance to Ryder Bay. This suggests that there is a reservoir of heat that is available for mixing upwards over the ridge. Indeed, mean dissipation rates and heat fluxes over the ridge are statistically significantly larger than those observed in the basin; $O(1\times10^{-8})$ W kg^{-1} and $\sim$ 2.5 W m^{-2}, versus $O(1\times10^{-10})$ W kg^{-1} and $\sim$ 0.4 W m^{-2}. This is true for up to $\sim$ 140 m above the seafloor, suggesting that the presence of the ridge is a significant control on deep dissipation and mixing within Ryder Bay, and it therefore has a key role in controlling the amount of heat fluxed into overlying waters.

The individual temperature transects show significant temporal variability, with multiple patterns of interest. The first of these is the warming of AASW in the upper $50-100$ m between Transects $2-8$, before cooling in Transects $9-10$, and then subsequently warming again in Transect 11. This period of AASW temperature variability coincides

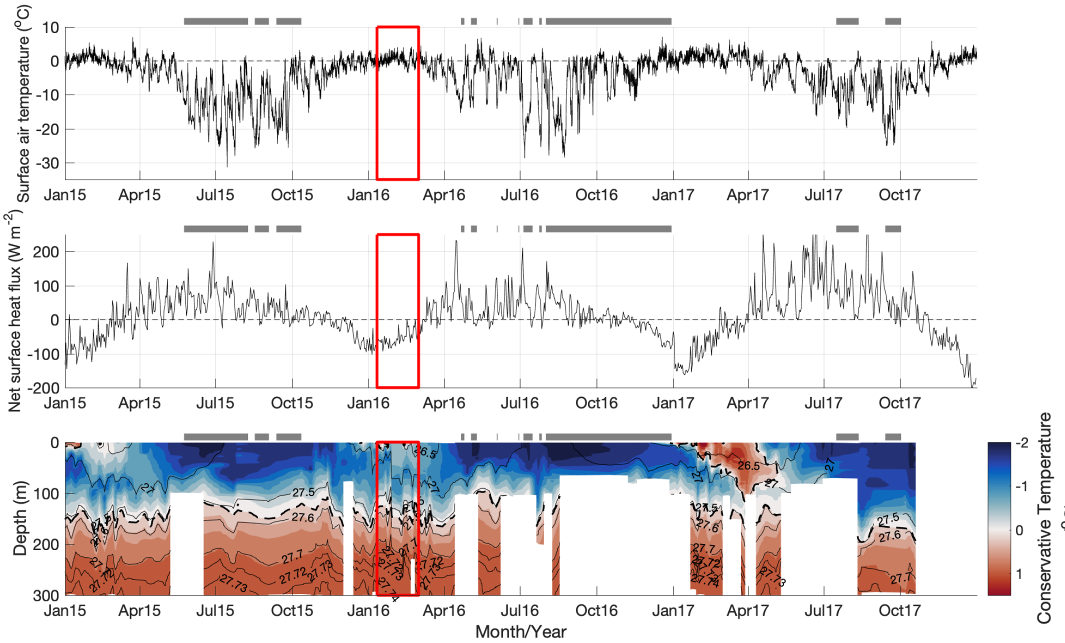

FIGURE 3.21: Comparison of surface temperature and heat fluxes with the upper water column in Ryder Bay between 2015 – 2017. (Top) Surface air temperature from Rothera Meteorological Station. (Middle) Daily net surface heat flux from ERA5 reanalysis data (middle panel, see text for terms included in calculation; Hersbach et al., 2020). Positive heat fluxes here are upward, in order to be consistent with the heat fluxes discussed earlier in the chapter. (Bottom) Upper 300 m conservative temperature from the RaTS. Surface-referenced potential density contours between 26.5 – 27.4 kg m^{-3} are overlain. The thick black dashed line represents the thermocline, defined here as the 0.25 °C isotherm. The red boxes indicate the glider deployment, and the grey bars along the top of the panels represent periods of 100% fast-ice, made by human observation.

with erosion of the underlying WW layer. Surface heat fluxes are possibly a major control on such changes to surface water properties. Since the surface waters are not discussed in detail elsewhere in this thesis, the controls will be explored a little further here.

It is first necessary to put the 2016 glider deployment surface heat fluxes into context. Figure 3.21 shows how the upper 300 m of the water column changed with respect to variations in surface air temperature and the net surface heat flux. The net surface heat flux, Q_{net}, is computed here for Ryder Bay using mean ERA5 reanalysis data (Hersbach et al., 2020) within the region 67.45 – 67.70 °S and 68.00 – 68.25 °W and the following equation:

$$Q_{net} = SW_{net} + LW_{net} + LH + SH \, , \tag{3.3}$$

where SW_{net}, LW_{net}, LH and SH are the surface net solar (shortwave) radiation, the surface net thermal (longwave) radiation, the surface latent heat flux, and the surface sensible heat flux variables respectively (here, positive is defined as upwards). The heat flux direction is determined by the temperature gradient between the ocean surface and the atmosphere. Lower air temperatures cause positive upward heat fluxes (i.e., a release of heat from the ocean to the atmosphere), and higher air temperatures cause negative upward heat fluxes (i.e., an injection of heat from the atmosphere to the ocean). The surface heat fluxes qualitatively correspond with the surface air temperatures. The 2016 glider deployment took place when atmospheric temperatures were moderate (mean of 0.23 °C over the deployment) and there were negative surface heat fluxes (mean of ~ -54 W m^{-2}). However, the mean air temperature over the same time period in 2017 was over a degree higher (1.3 °C), with peak and mean surface heat fluxes of -162 and -86 W m^{-2}. The differences in heat fluxes between 2016 and 2017 are reflected in changes to the surface waters. The shallow seasonal thermocline at the start of the glider deployment ($5 - 10$ m) is likely due to the lower surface fluxes, whilst the record seasonal thermocline depth of ~ 100 m occurs shortly after the peak negative heat flux in January 2017.

Figure 3.22 displays the surface heat fluxes over the final portion of the Ryder Bay deployment, when the glider conducted the 13 transects into and out of the bay. Between Transects $1 - 5$ (days $41 - 44$), winds stresses are small, air temperatures are typically high, and the subsequent surface heat flux is strongly negative, with maximum values of ~ -55 W m^{-2}. These negative heat fluxes inject heat downwards into the surface waters, likely leading to the observed increase in AASW temperatures in the upper ~ 50 m and the thinning of the underlying WW layer moving from transect $5 - 8$ (after some delay, as also observed in summer 2017; Figure 3.21). The strongly negative heat fluxes then weaken as air temperatures fall below 0 °C after Transect 5, reaching $+0.5$ W m^{-2} on Transect 8 (day 46). This brief switch could signify a period when there was a tendency for heat to be transferred from the ocean to the atmosphere. This could potentially account for some of the AASW cooling observed during Transects $9 - 10$. Indeed, the upper 50 m surface fluxes shown in Figure 3.20 also show a similar positive heat flux period, albeit slightly later in Transects $10 - 11$; this delay could reflect the fact that the glider observations are deeper than the surface. However, perhaps a more likely candidate for the cooling of the AASW between Transects 9 and 10 is the erosion of the underlying WW layer. This could have occurred due to wind driven mixing associated with the concurrent strong wind events, and may have been exacerbated by the shoaling of the thermocline. Surface temperatures after Transect 11 remain relatively high, and there is a corresponding increase in AASW temperature. This could reflect the negative upper 50 m surface heat fluxes recorded by the glider in Transects 12 and 13, with heat being injected downwards into the water column. Consequently, whilst it is possible that some of the observed variation in AASW temperature is of spatial origin or due to lateral advection, the surface heat fluxes and wind stress appear to be able to explain much of the surface water temporal variability in Ryder Bay.

Aside from variability in the surface waters, there are three other key features from the

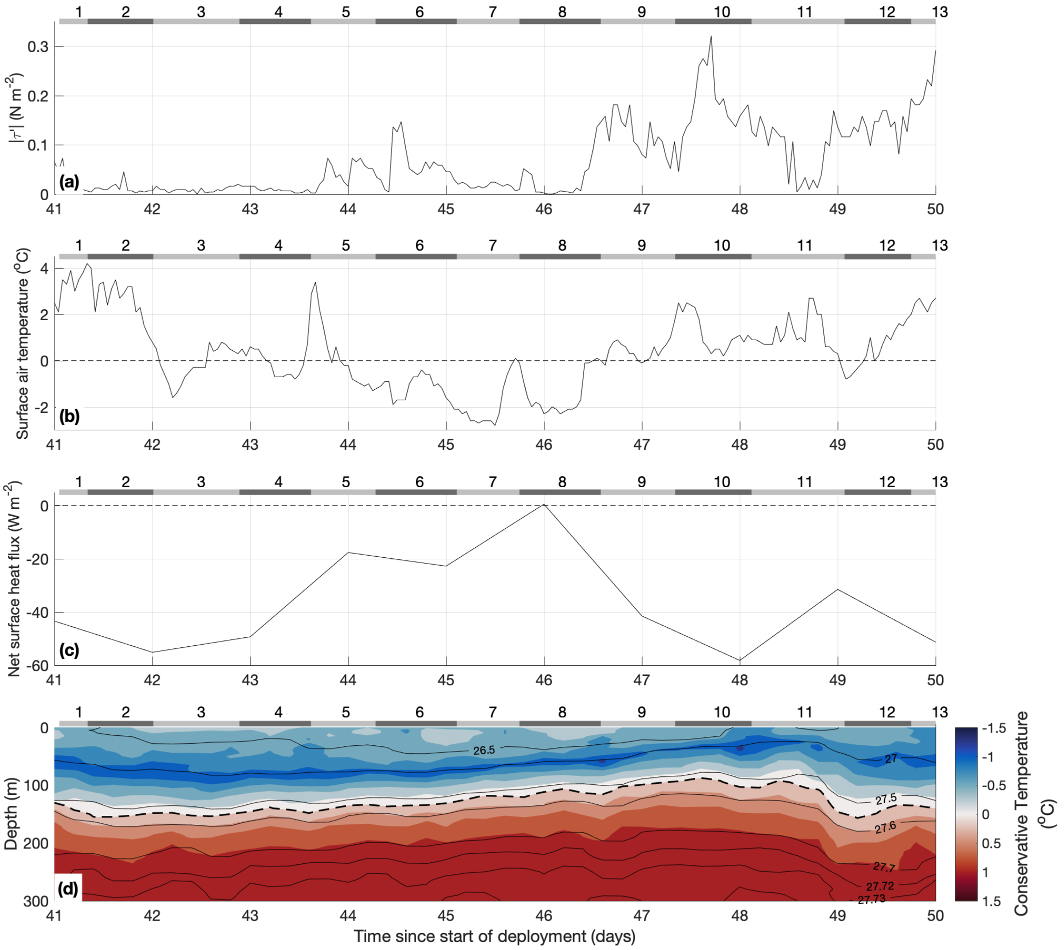

FIGURE 3.22: Analysis of surface forcing over the final portion of glider deployment (days 41 – 50). Hourly wind stress magnitude ($|\tau|$) (a) and surface air temperature (b) from Rothera Meteorological Station. (c) Daily total surface heat flux, where positive is upwards (ocean to atmosphere). (c) Upper 300 m conservative temperature collected from the glider, interpolated onto a 5 m depth and 1/5 day time grid using laplacian-spline interpolation. Surface-referenced potential density contours between 26.5 – 27.4 kg m^{-3} are overlain. The thick black dashed line represents the thermocline, defined here as the 0.25 °C isotherm. Note the different colour scale here compared to in Figure 3.21. The alternating grey bar along the top of each panel indicates the respective individual glider transects.

individual glider transects that are worthy of further investigation. The first of these is the gradual ∼ 60 m shoaling of the thermocline between Transects 3 – 11, followed by a dramatic ∼ 50 m deepening in Transect 12. Such a pattern is characteristic of wind-driven upwelling. The second feature is the basin-wide elevated dissipation and heat fluxes within and across the thermocline in Transect 12. These contrast to values observed in upper water column in the preceding transects, which are sporadic and patchy. A primary candidate for the observed basin-wide distribution of elevated dissipation rates are wind-driven internal waves. The third feature is the elevated dissipation above the topographic ridge, which moves with the location of the pinching and steeply sloping isopyncals. This is suggestive of dissipation that is tidally-driven or controlled hydraulically. The elevated dissipation rates and heat fluxes over the ridge occur in 7/11 (64%) of the complete transects, suggesting that they are a consistent feature that is potentially very important for the WAP heat budget. Chapter 4 will investigate the mechanisms responsible for these observed spatial and temporal patterns within Ryder Bay in more detail.

Chapter 4

Mixing Mechanisms in a Coastal Embayment of the West Antarctic Peninsula

The work in this chapter contributed to the following published paper:
Scott, R. M., J. A. Brearley, A. C. Naveira Garabato, H. J. Venables, and M. P. Meredith, 2021b: Rates and mechanisms of turbulent mixing in a coastal embayment of the west antarctic peninsula. *Journal of Geophysical Research: Oceans*, **126**, e2020JC016 861.

4.1 Introduction

The last chapter described the spatial and temporal variability in hydrographic, dissipation and associated heat flux patterns within Ryder Bay. In this chapter, glider data are used in conjunction with mooring-based current and Rothera meteorological data to investigate the mechanisms responsible for controlling the observed patterns. Section 4.2 introduces the most likely candidate mixing mechanisms for Ryder Bay. Sections 4.3, 4.4 and 4.5 each address one of the three key temporal features described in Chapter 3: (i) variations in the thermocline depth; (ii) basin-wide dissipation at the thermocline; and (iii) deep dissipation over the ridge. Lastly, Section 4.6 is a summary and discussion.

4.2 Potential Mixing Mechanisms

A number of vertical mixing mechanisms are relevant to polar shelf environments, including double-diffusion, wind-driven mixing and breaking internal waves. The first of these, double-diffusion, occurs because salinity has a lower rate of diffusion than temperature (Huppert and Turner, 1981). Double-diffusion has two regimes, salt fingering and double-diffusive convection, and which of these occurs depends on how the water column is stratified. Salt fingering occurs when warm, saline water overlies cold, fresh water (where the ocean is temperature-stratified), so it commonly forms at low latitudes. Double-diffusive convection occurs when cold, fresh water overlies warm, saline water (in salinity-stratified regions; Huppert and Turner, 1981). This forms thermohaline staircases with quasi-homogeneous layers separated by strong density gradients that are identifiable in CTD or microstructure profiles. Double-diffusive convection is generally thought to be important in both the Arctic (Padman and Dillon, 1987) and the Antarctic (Muench et al., 1990; Robertson et al., 1995), where the conditions favourable to its development typically occur. However, on the western side of the WAP, the double-diffusive contribution to vertical mixing appears to be small (Howard et al., 2004; Brearley et al., 2017), despite Turner angles (Ruddick, 1983) being apparently conducive to double-diffusive activity (Turner angles are a tool used to assess the double-diffusion stability regime of a water column - see Section 1.3.2 for more detail). This is because double-diffusion requires background mixing levels to be low, and shear instabilities appear to dominate vertical mixing on the WAP (e.g., Howard et al., 2004; Brearley et al., 2017). Consequently, whilst double-diffusive mixing is plausible in Ryder Bay, it is not the focus of this work.

A second potential mixing mechanism is via wind-driven near-inertial waves, which, upon breaking, produce shear-driven turbulence. Winds impart momentum into the surface layers of the ocean, forcing near-inertial shear into the water column, with Howard et al. (2004) concluding that this mechanism provided most of the observed shear across the pycnocline in Marguerite Bay. Brearley et al. (2017) also suggested that wind-driven baroclinic waves are the dominant source of shear in the summer months in Ryder Bay, when the region is not covered by fast ice. During this period, winds can also influence the WAP heat budget by driving Ekman upwelling / downwelling at the coast: if the orientation of the winds is in the alongshore direction, Ekman transport will drive water towards or away from the coast (Mitchum and Clarke, 1986). This process is thought to be significant within Ryder Bay, where wind-induced oscillations of the water column's hydrographic structure are observed (Wallace et al., 2008), causing vertical migration of the interface between CDW and the overlying cold WW. As summer progresses, the upper layers are heated by insolation (as shown in Section 3.5), and there is an input of fresh meltwater from nearby glacial runoff and sea ice melt. This leads to an increase in stratification and inhibits vertical mixing. In addition, during winter, fast-ice (immobile sea ice that is connected to land) within Ryder Bay hinders the transfer of momentum between the atmosphere and the ocean, thereby reducing the influence of the wind on vertical mixing (Venables and Meredith, 2014). At this time, there is a shift to internal tides as the dominant source of shear (Hyatt et al., 2011;

Brearley et al., 2017), highlighting the central role of sea ice as a controlling influence on the WAP oceanic heat budget.

Beneath the ocean's upper layers, the breaking of internal waves over rough topography can lead to enhanced vertical mixing at depth (e.g., Polzin et al., 1997). Internal tides are a primary source of such vertical mixing, transferring energy from barotropic to baroclinic motions (Stigebrandt, 1999) and thus enhancing shear and mixing (see Whalen et al., 2020, for a comprehensive review on internal wave-driven mixing). Despite barotropic tides being weak along much of the WAP margins (≤ 3 cm s^{-1}), multiple internal tide generation sites are thought to exist close to Ryder Bay (Wallace et al., 2008). Freely propagating waves must have a frequency, ω, higher than the inertial frequency, f, where $f^2 < \omega^2$ (LeBlond and Mysak, 1981). Since Ryder Bay is located poleward of the critical latitude for free propagation of diurnal tides ($f^2 < \omega^2 <$ is not satisfied poleward of $\sim 30°$), these internal waves dissipate and break locally and are therefore potential candidates for generating vertical mixing and upward heat fluxes between CDW and near-surface water masses.

Other types of internal wave that may be important for shear-driven vertical mixing on the WAP are Coastal-Trapped Waves (CTWs; Allen, 1975) and basin-scale wave modes (Arneborg and Liljebladh, 2001). CTWs are low frequency sub-inertial waves that become trapped to topographic slopes due to a combination of the Coriolis effect and vertical stratification, and are a large source of sub-inertial variability at ocean margins (Allen, 1975). Basin-scale wave modes are standing waves that can form within lakes and semi-enclosed embayments, the simplest mode-1 being an internal seiching motion; a standing wave on the thermocline with a one elevation node half way into the embayment. Both CTWs and basin-scale wave modes are typically forced by winds. Storms passing over a slope are a primary candidate for generating CTWs, with wind stress providing a source of potential vorticity on scales needed to drive the rotational waves (Mysak, 1980). Unlike basin-scale wave modes, whose properties are typically set by the vertical stratification and the geometry of the bay, the properties of CTWs are commonly determined by the weather systems that force them, with wavelengths, periods and velocities of $O(10-100)$ km, $O(0.5-10)$ days, and $O(0.5-10)$ m s^{-1}, respectively (Inall et al., 2015). Whilst basin-scale wave modes are naturally restricted to their formation region, the low period and long wavelengths of CTWs enables them to propagate remotely-forced pycnocline perturbations over large distances. These processes are thought to be important in Arctic fjordic systems (e.g., Inall et al., 2015; Fraser et al., 2018), where tides are weak and fjords are typically wide with respect to the internal Rossby radius of deformation (so rotational effects are more easily observed). Similar fjords, such as Ryder Bay, exist along the WAP, so it is possible that CTWs may also be important in driving mixing in Antarctica.

In certain oceanographic contexts, topographic ridges can also lead to enhanced mixing due to the formation of hydraulic structures (e.g., Farmer and Smith, 1980; Farmer and

Denton, 1985; Klymak and Gregg, 2004; Legg and Klymak, 2008; Gregg and Klymak, 2014). A hydraulic structure may form when a stratified fluid flows sufficiently rapidly over topography to arrest the upstream propagation of interfacial waves, resulting in an asymmetric steady-state flow field (Farmer and Denton, 1985), with a transition from sub-critical (slow) flow upstream to super-critical (fast) flow over the topography (Armi, 1986). While classical hydraulic theory suggests that hydraulic structures are formed when sub-inertial flow moves over ridges, tidal flow is also thought to result in hydraulic conditions with vigorous turbulent dissipation at rates exceeding background levels by several orders of magnitude (e.g., $O(10^{-4})$ W kg^{-1} compared to $O(10^{-7}) - (10^{-8})$ W kg^{-1}; Klymak and Gregg, 2004). Such dissipation bursts can arise due to both an increase in flow speed over the ridge, and a sudden decrease in flow speed downstream in a hydraulic jump (Farmer and Denton, 1985). Owing to the large number of ridges present off the WAP (e.g., Venables et al., 2017), and the occurrence of vigorous sub-inertial eddy flows (e.g., Moffat et al., 2009), flow that is controlled hydraulically may also be an important driver of vertical mixing.

4.3 Variability in Thermocline Depth

The first key temporal feature revealed in Chapter 3 was a gradual shoaling of the thermocline between Transects $3 - 11$, followed by a sudden ~ 50 m heaving/deepening in Transect 12. A primary candidate for driving such thermocline depth variation are changes in wind forcing, which have previously been shown to be important within Ryder Bay (Wallace et al., 2008). Plots of ERA5 mean sea level pressure reanalysis data (Hersbach et al., 2020) reveal quasi-permanent high pressure over the continent, with large-scale low pressure systems transit cyclonically around Antarctica, on $\sim 4 - 6$ day time scales (Figure 4.1). The large number of low pressure systems that pass through the South Pacific sector of the Southern Ocean form the semi-permanent Amundsen Sea Low (Raphael et al., 2016), which influences meridional wind variability and is a strong control on temperature, precipitation and sea ice extent (Hosking et al., 2013). Over the deployment period, several of these cyclonic storms pass over the WAP and Ryder Bay, and the Amundsen Sea Low is clearly seen between 23rd $-$ 25th February (Figure 4.1). These storms can largely be accountable for the range of wind strengths and directions that were recorded at Rothera Research Station. Wind roses from three important days in the Rothera time series illustrate the nature of this variability (Figure 4.2a). Strong winds > 25 m s^{-1} are observed in both the south-westward (e.g., days 40 and 47) and north / north-westward (e.g., day 44) directions. These directions are predominantly cross-shore (red), but do have an alongshore (blue) component (dashed lines in Figure 4.2a represent the cross-shore / alongshore reference frame; see also Figure 2.1). Mean wind directions are calculated for each day since the start of the deployment (Figure

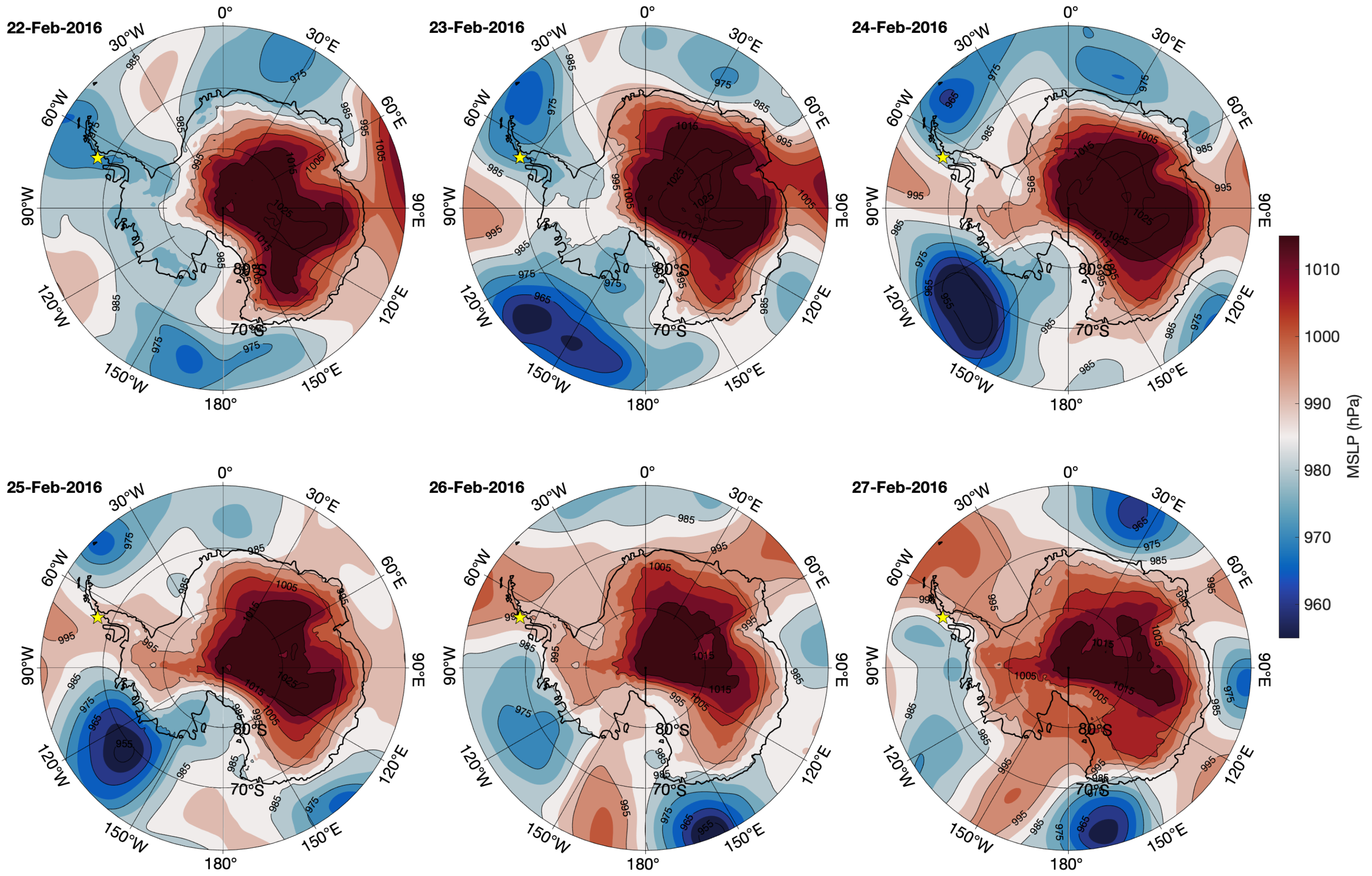

FIGURE 4.1: Mean sea level pressure between 22nd and 27th February 2016 (42 – 47 days since the start of the glider deployment), using ERA5 m reanalysis data (Hersbach et al., 2020). Large-scale, low pressure systems move cyclonically around Antarctica, passing over WAP and Ryder Bay (yellow star).

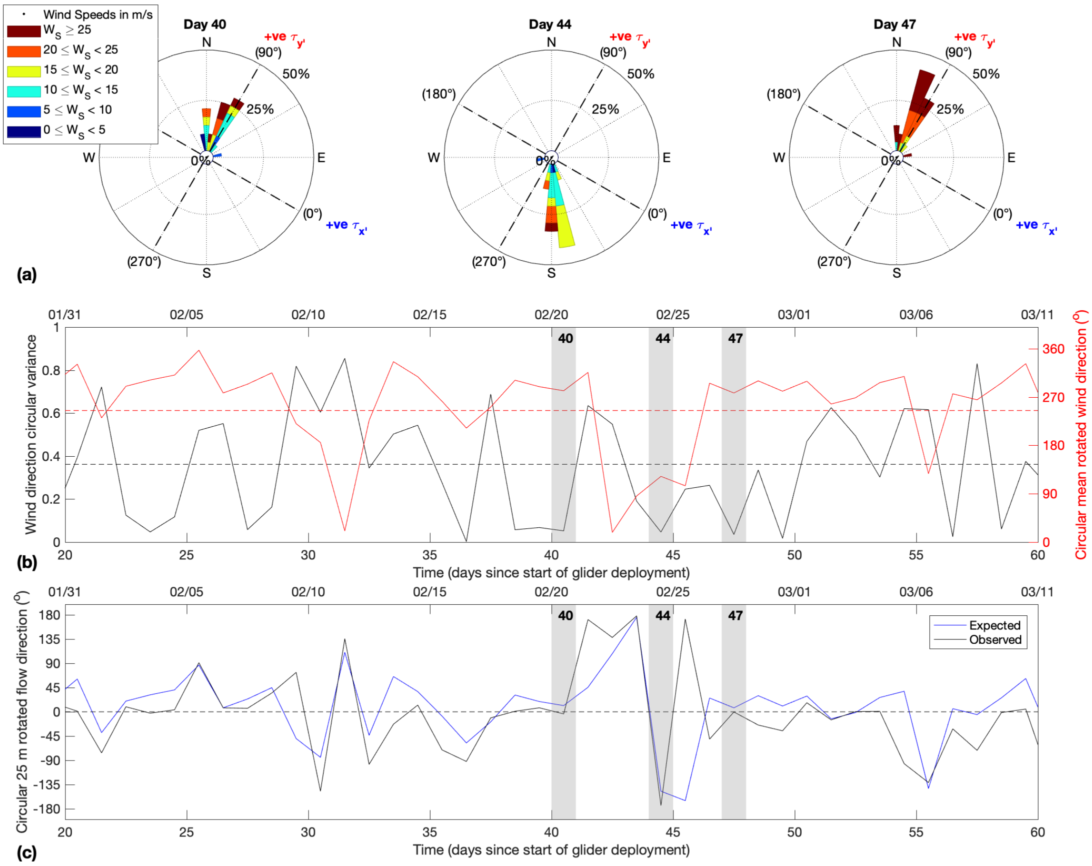

FIGURE 4.2: (a) Rothera wind rose plots for days 40, 44 and 47. The coordinate frame has been rotated by -30 °, so that wind directions of 0 ° and 90 ° are in the positive $\tau_{x'}$ and $\tau_{y'}$ directions, respectively. (Red and blue wind stress labels are for reference when examining Figure 4.5). (b) Circular variance of wind direction (black solid line) and mean coordinate-rotated wind direction (red solid line). Dashed lines represent the corresponding mean for the first 100 days since the start of the glider deployment, when there is no fast-ice. (c) Comparison of the expected and observed flow directions at 25 m depth, using angles between 0° and ±180° (see text for details). Days 40, 44 and 47 are highlighted in grey because they are referred to in the text. Date in 2016 is shown along the top (b,c).

4.2b) using the method of Berens (2009), which transforms the directions into unit vectors and then vector-averages to produce the mean resultant vector $\bar{r}$ (angles calculated using this method are labelled with a T). Days 40, 44 and 47 are characterised by mean rotated directions of 280 °T, 122 °T and 277 °T, respectively. The circular variance of wind direction (S), which is given by $S = 1 - ||\bar{r}||$ (Berens, 2009), is a metric of how variable the wind direction is on any given day (vertical bars indicate the modulus). S changes throughout the deployment (Figure 4.2b): low variances (compared to the 0.36 mean) are observed on days 40 (0.05), 44 (0.05) and 47 (0.04), whereas other days experience much larger variability in wind direction (e.g., day 31 has a variance of 0.85). Days with lower wind speeds typically have higher variances.

The internal Rossby radius of deformation (r_r; see Equation 1.1) provides a characteristic scale over which rotational processes, such as Ekman flow, are likely to be important in a given region. Values used here are $N^2 = 3.4 \times 10^{-4}\ \mathrm{s}^{-2}$, corresponding to the median maximum stratification from the individual glider profiles, H as the characteristic depth of the pycnocline (50 m; the corresponding median depth), and $f = 1.3 \times 10^{-4}$ rad s^{-1} (at 67.58 °S). This gives $r_r = 6.8$ km within Ryder Bay. The width of Ryder Bay is $\sim$ 4 km, the same order of magnitude as the Rossby radius. The velocities recorded by the ADCP are thus likely to be significantly influenced by Ekman dynamics. Ekman transport is expected to be 90 ° to the left of the wind direction in the Southern Hemisphere, so daily-mean wind directions (Figure 4.2b) are used to predict Ekman flow directions. Predicted flow directions are compared with 25 m ADCP-derived values (Figure 4.2c; the shallowest interpolated depth), where that depth is chosen because it is close to the median, glider-derived MLD of 22 m, calculated using a density difference of 0.03 kg m^{-3} compared to the 10 m density. This is thought to be an appropriate comparison, since the Ekman depth is typically similar to the MLD (Thomas and Lee, 2005). Directions ranging from 180 to 360 ° are converted to values between -180 and 0 ° in order to enable ready comparison of angles close to 0 °. The jump between expected and observed angles of -180 and 180 ° on day 45 is misleading because the converted -180 ° is the same angle as 180 °. Expected and observed flow directions have a correlation of 0.63 ($p \ll 0.001$) with a median absolute difference of 22 °. There is no systematic difference in the sign of the offset, with positive and negative values occurring 48% and 40% of the time, respectively. Differences likely depend on the strength of the wind and the precise location of the ADCP within the Ekman layer, with stronger winds likely penetrating deeper into the water column and causing smaller directional differences (e.g, 8 ° on days 40 and 47) than weaker winds (e.g., -27 ° on day 44).

The importance of Ekman processes is assessed in greater depth using the mixed layer slab model first proposed by Pollard and Millard (1970). This simple model uses mixed layer depth (H) and wind stress ($\tau_{x'}, \tau_{y'}$) to predict wind-generated flow (Z). The model equation is expressed using complex notation as in D'Asaro (1985):

$$\frac{dZ}{dt} + \omega Z = \frac{T}{H}\,, \tag{4.1}$$

where

$$Z = u + iv\,, \omega = r_d + if \text{ and } T = \frac{\tau_{x'} + i\tau_{y'}}{\rho}.$$

ω and T are the damping / Coriolis and wind stress body force terms, and ρ is the overall mean density of the mixed layer (1026.53 kg m^{-3} from observations). r_d is an artificial linear Rayleigh damping parameter used as a simple representation of momentum sinks (e.g., including momentum expended in generating internal waves and small-scale turbulence; Mickett et al., 2010). r_d can be used to tune the model and, following Alford (2001), $r = 0.4f$ was chosen here to optimise the correlation between the observed and modelled near-inertial velocities (Figure 4.3). Section 4.4 discusses the near-inertial velocities in detail. The model assumes uniform velocity and density, and

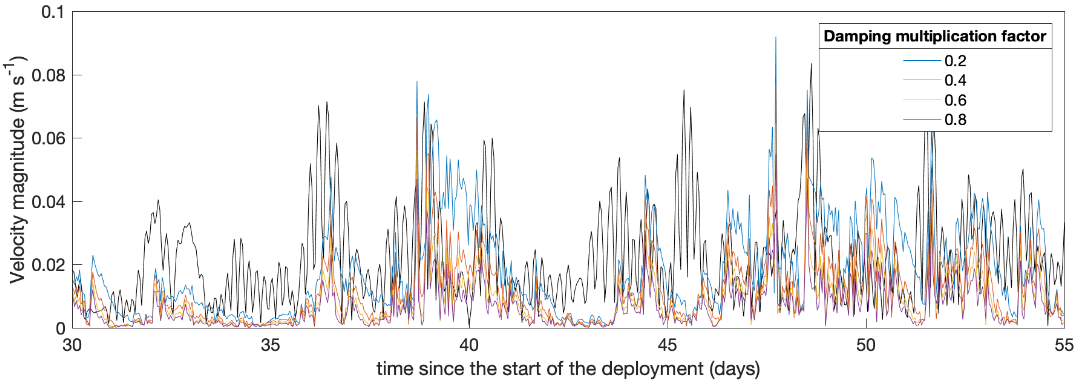

FIGURE 4.3: Near-inertial modelled velocities using different multiplication factors. Following Alford (2001), the factor that provided the best correlation with observed near-inertial velocities (thick black line) was used in the final model run. r_d values of $0.2f, 0.4f, 0.6f$ and $0.8f$ produced correlations of 0.25 ($p = 0.07$), 0.28 ($p = 0.01$), 0.26 ($p = 0.007$) and 0.25 ($p = 0.008$), respectively.

realistic simulations require $r_d^2 << f^2$ (D'Asaro, 1985) and $r_d > 0$ for stability (Alford, 2001).

The mixed layer model decomposes the overall wind-generated flow into Ekman, Z_E, and near-inertial, Z_I, velocity components using:

$$Z = Z_I + Z_E. \tag{4.2}$$

Adopting a constant mixed layer depth of $H = 20$ m (comparable to the shallowest ADCP velocities and the glider-derived mixed layer depth of 22 m) and using observed wind stress magnitudes, the modelled Ekman velocities are given by Equation 4.3, following D'Asaro (1985):

$$Z_E = \frac{T}{\omega H}\ . \tag{4.3}$$

The model sufficiently replicates observed Ekman flows, with a correlation of $R = 0.60$ ($p \ll 0.001$) between modelled and observed values (Figure 4.4), including agreement on days thought to be important for Ekman upwelling / downwelling (as suggested in the analysis of Figure 4.5). Observed Ekman velocities were calculated by subtracting the band-pass filtered near-inertial velocities (using a frequency range of $0.9 - 1.9f$; see Section 4.4.3 for more details) from the total observed velocities, in the same way as in Equation 4.2. The R^2 value between Z and Z_E ($R^2 = 0.80$) is larger than that between Z and Z_I ($R^2 = 0.44$), suggesting that Ekman processes are important within Ryder Bay (both correlations have $p \ll 0.001$).

A time series of bay-rotated wind stress ($\tau_{x'}, \tau_{y'}$) reveals that the cross-shore, south-westward and north / north-westward winds on days 40 and 44 are part of strong $\sim$ 3-day duration wind forcing events (Figure 4.5a) that have alongshore components that blow out of and into the bay, respectively (positive and negative $\tau_{x'}$). The mid

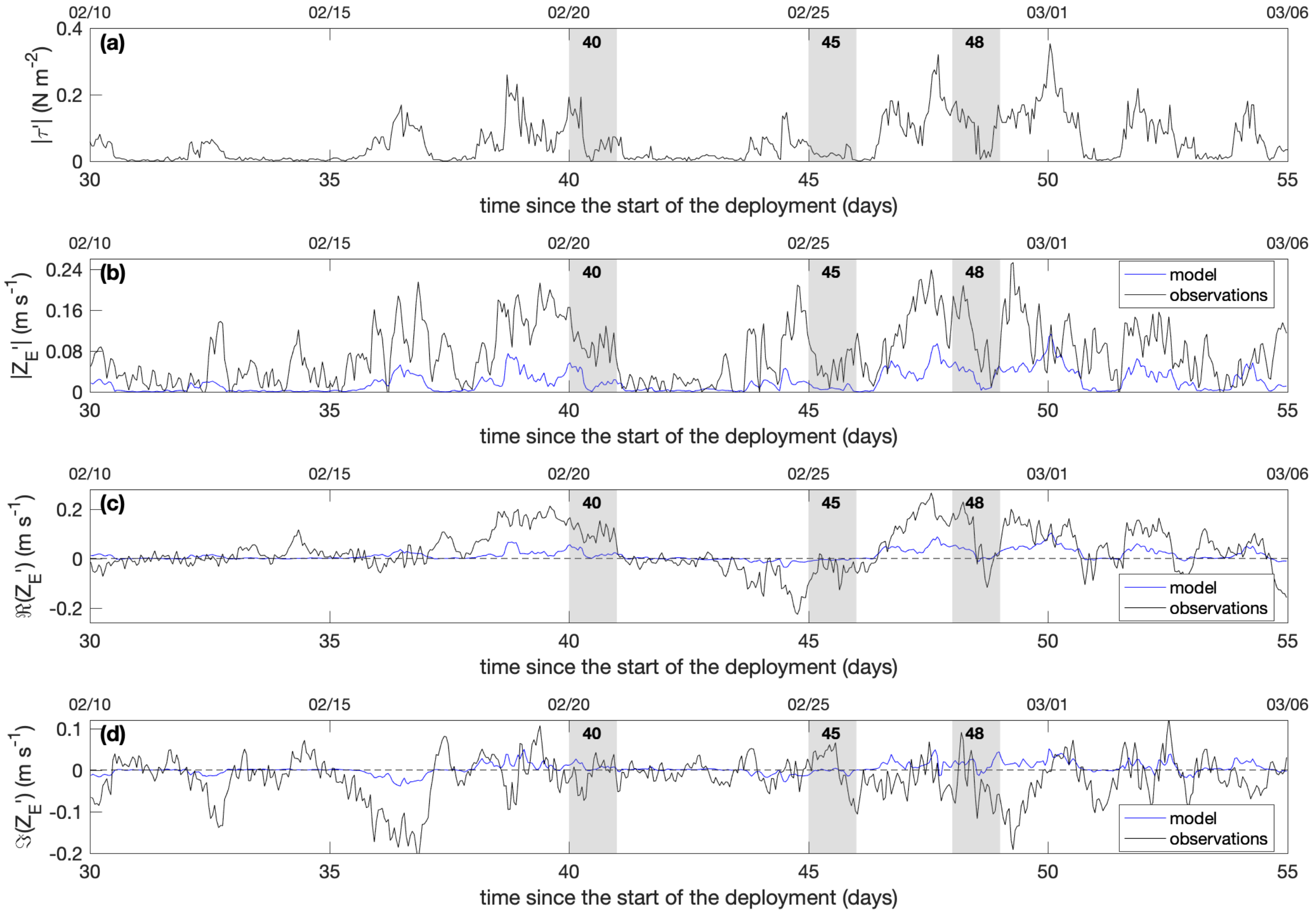

FIGURE 4.4: (a) Wind stress magnitude used in the mixed layer slab model (Pollard and Millard, 1970). (b) Comparison between modelled and observed Ekman velocity magnitudes. The real (c) and imaginary (d) velocity components are positive in the u' and v' directions respectively. Grey columns show the following days of interest: 40, 45 and 48.

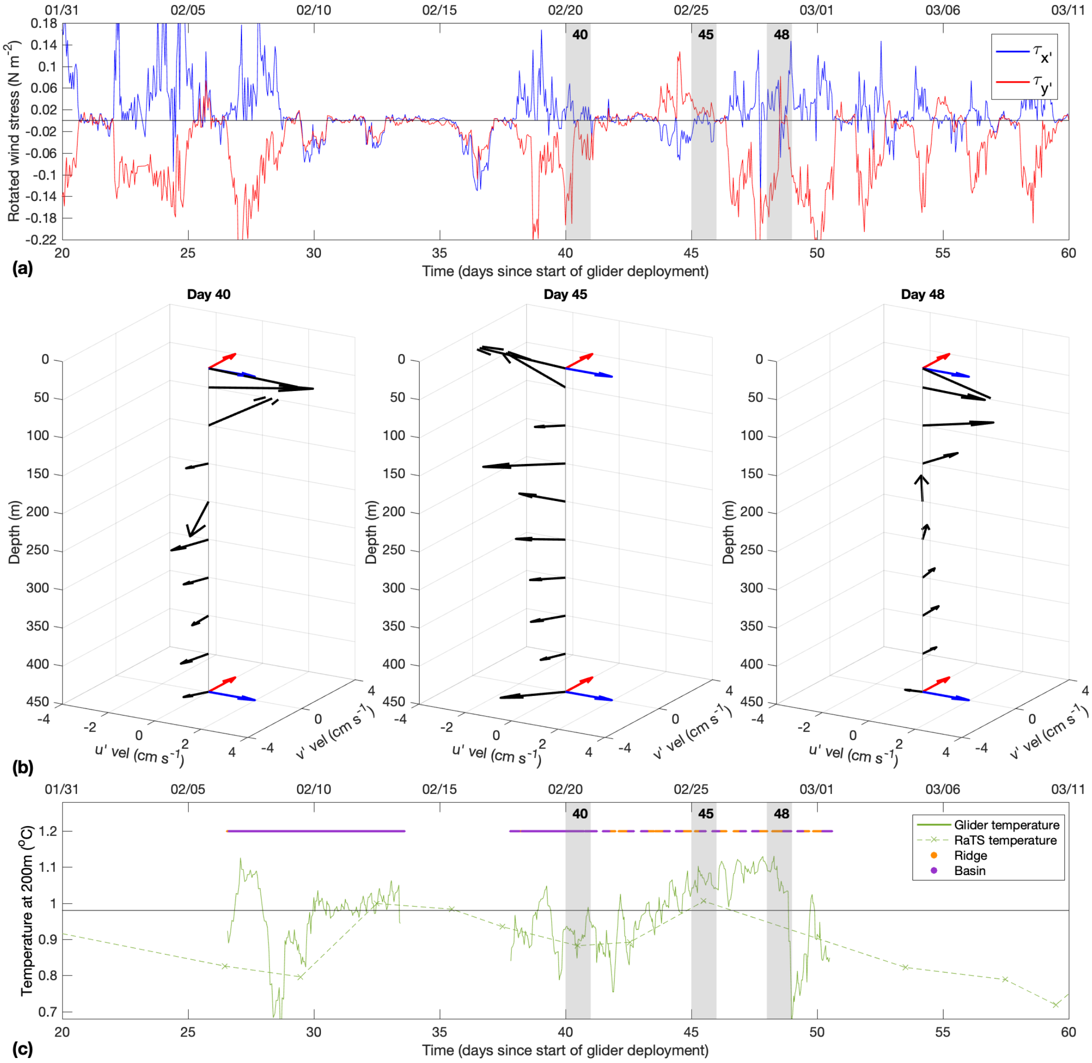

FIGURE 4.5: (a) Time series of rotated $\tau_{x'}$ and $\tau_{y'}$ wind stress. (b) Mean ADCP velocities for days 40, 45 and 48, interpolated onto depths of 25 m and then every 50 m between 50 − 440 m, shown with a three-dimensional perspective. 2 cm s^{-1} in the u' and v' directions are represented by the red and blue scale arrows, respectively. (c) Time series of glider (solid) and interpolated RaTS (dashed; crosses are sample points) temperature at 200 m. The black line at 0.98 °C is the overall mean glider temperature, and is used to determine whether or not the temperature is elevated. The purple and orange lines are used to show when the glider is above the ridge or in the basin, respectively. Grey columns show the following days of interest: 40, 45 and 48.

point of each event lies on day 39 and 44, so these will be referred to hereafter as the Day 39 and Day 44 events. The events are preceded by a long, relatively quiescent period between days 29 and 37, are separated by a 2-day-long quiescent period, and are followed by a prolonged period of strong winds that vary on shorter time scales (< 2 days) from day 46 onward (e.g., note the large west / south-westward and southward wind stress peaks on days 47 and 50, respectively). With Ekman processes likely playing an important role, the potential impact of these wind events on the water column velocities is investigated below.

Mean ADCP velocity profiles for days 40, 45 and 48 (Figure 4.5b) are chosen to illustrate how the structure of the water column changed over the period of glider observations. Velocities on day 40 have a dipole structure with a zero crossing at a depth of ~ 100 m. The uppermost velocity (25 m; close to the MLD) flows out of the bay in the positive alongshore direction (the expected Ekman transport direction; Figure 4.2c). Flow rotates to the left with increasing depth, down to the zero crossing at ~ 100 m, where the flow is quasi-parallel with the positive cross-shore direction (v'). This is qualitatively similar to an Ekman spiral, but it must be noted that an Ekman depth this deep is unlikely given the mean upper 200 m diapycnal diffusivities are $O(10^{-5})$ m^2 s^{-1} (Figure 3.12). Ekman-influenced flow can extend up to two-times the mixed layer depth following strong wind events, as previously observed in the mid-latitude Atlantic Ocean (Chereskin and Roemmich, 1991). This produces a maximum Ekman depth of ~ 44 m. Velocities between the MLD and ~ 44 m have a northward component, consistent with Ekman-induced flow towards the northern boundary of Ryder Bay. In the lower layers (below ~ 150 m), flow is generally uniform, with both negative cross-shore (v') and alongshore (u') components. The orientation of this dipole (with positive cross-shore velocities above the pycnocline and negative below) is consistent with a circulation structure that has upwelling at the southern boundary and downwelling at the northern boundary of Ryder Bay.

The dipole persists for approximately 4 days until the Day 44 wind event, when the surface flow rotates to an inflowing direction (negative alongshore u') in response to the north / north-westward wind, and there is predominantly negative cross-shore flow (south-westward) in the upper layers (day 45; Figure 4.5b). A quasi-barotropic southward velocity structure forms and persists for approximately 3 days, including strong, negative cross-shore velocities in the upper water column on day 47 (not shown). On day 48, the lower-layer velocities switch to a positive cross-shore direction, which is likely a delayed response to the negative cross-shore upper velocities, and reflects a change from wind-induced coastal upwelling to downwelling on Ryder Bay's southern boundary. The positive cross-shore velocities at depth are not sustained in any given direction after day 48, possibly due to the strong variation in wind direction after day 46.

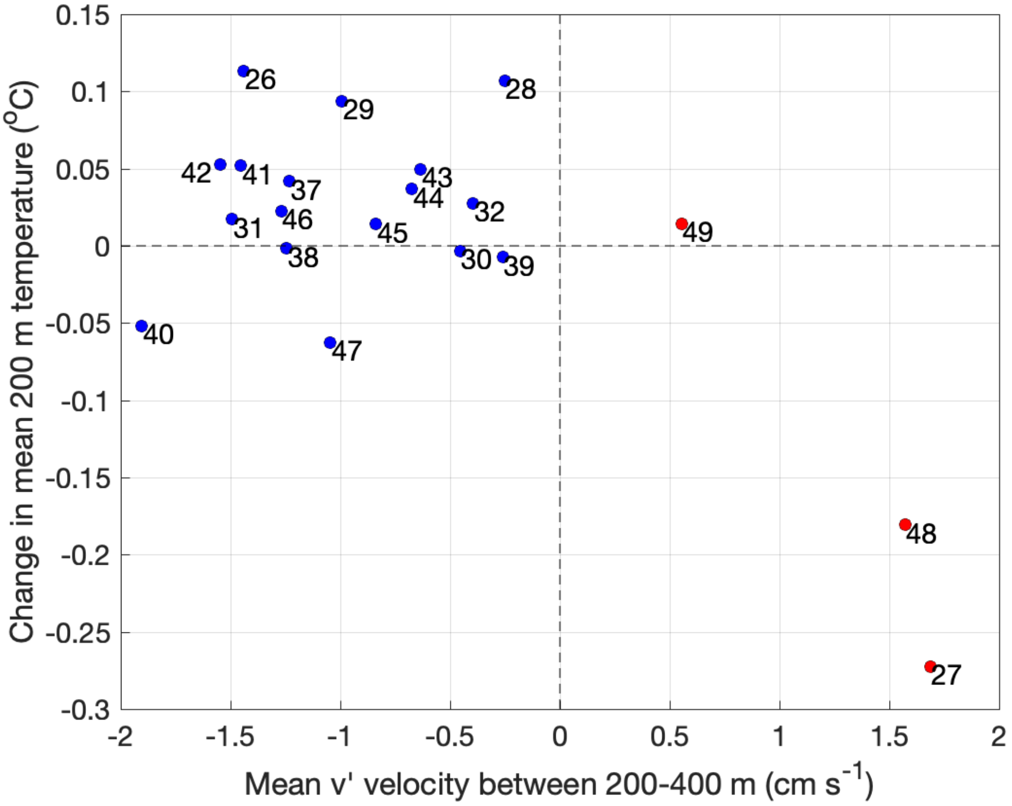

FIGURE 4.6: Change in daily mean 200 m glider temperature for positive and negative v' velocities. Negative (positive) v' velocities are towards the southern (northern) boundary. Although there are fewer days with positive v' flow, negative (positive) v' tends to cause an increase (decrease) in temperature. Using two-sided Wilcoxon rank sum test this result is statistically-significantly at the 5% level ($p = 0.04$).

If, as argued, the observed velocities are associated with wind-induced coastal upwelling / downwelling, one would expect to see corresponding changes in the glider and RaTS mean 200 m temperature (Figure 4.5c). The glider data exhibits the same low-frequency variability as the RaTS data, but the increased resolution reveals higher-frequency variability that is not captured by RaTS's sparser sampling (nominally twice a week in summer). Large decreases in temperature of 0.40 °C and 0.46 °C are observed on days 28 and 48, respectively, which coincide with changes between negative and positive cross-shore flow at depth (e.g., day 48; Figure 4.5b). Both decreases also occur when the glider is in the basin (as opposed to over the ridge), so spatial differences in flow can be ruled out. The mean 200 m glider temperature increases steadily from 0.92 °C to 1.06 °C between days 40 and 46, and reaches 1.13 °C at the start of day 48. This coincides with the period of negative cross-shore flow at depth, and upwelling on the southern side of Ryder Bay.

Figure 4.6 compares the change in daily mean 200 m glider temperature with the corresponding daily mean cross-shore v' velocities. There were 20 days where both glider temperature and ADCP velocity data were recorded, with 17 (3) days of negative (positive) v' velocities. On 70% of the negative velocity days, an increase in mean temperature was observed the following day. Although there are a low number of days with positive v' velocities, a two-sided Wilcoxon rank sum test comparing the change in temperature following days of positive and negative v' velocities indicates that the medians are statistically-significantly different ($p = 0.04$). This dependence of the 200 m temperature on the flow direction at depth confirms our earlier supposition that flow is largely controlled by Ekman coastal upwelling and downwelling.

4.4 Basin-Wide Turbulent Dissipation at the Thermocline

This section is an investigation into the second key feature from Chapter 3: basin-wide dissipation across the base of the thermocline.

4.4.1 Tides

Although tidal magnitudes in Ryder Bay are weak (Wallace et al., 2008; Brearley et al., 2017), because the bay is located poleward of the critical latitude for free propagation of diurnal tides, any internal tides generated locally are also likely to dissipate locally. Multiple generation sites are thought to exist near Ryder Bay (Wallace et al., 2008), suggesting that internal tides could influence the flow within the bay and cause localised vertical mixing and upward heat fluxes between the CDW and near-surface water masses. Consequently, this sub-section explores the role tides may have on controlling the flow and observed dissipation at the thermocline (between $\sim 105 - 205$ m).

Power Spectral Density (PSD) analysis is used to identify the dominant frequencies within a time series. Using the Welch method, with 8 Hamming windows and a 50% overlap, deployment-mean power spectra are created for mean u' and v' ADCP velocities between $\sim 100 - 200$ m (Figure 4.7). A sensitivity analysis revealed that the shape of the spectra were not sensitive to the choice of spectral windowing. The largest peaks are observed at K_1 tidal frequencies in both u' (a) and v' (b) velocities, with a peak also observed at O_1 frequencies in the v' velocities, though the peaks in v' are greater than those in u'. Smaller peaks are also observed within the near-inertial range $(0.9f - 1.9f)$ at M_2 and S_2 frequencies. Additionally, more power is found in the v' direction at low frequencies (particularly between $0.45 - 1$ cpd / $\sim 1 - 2$ days), suggesting that there is increased flow variability over longer periods in the across-shore direction. This low frequency variability could reflect changes in flow direction associated with the upwelling / downwelling discussed above.

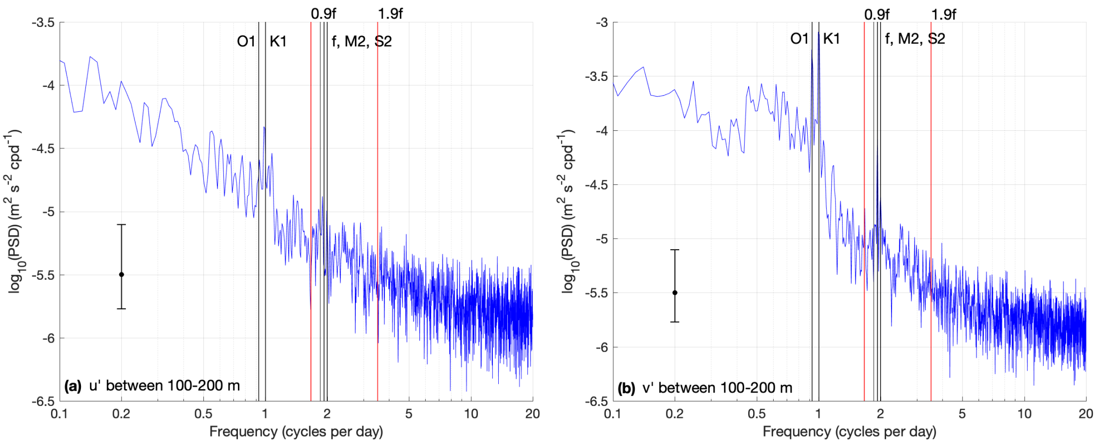

FIGURE 4.7: Mean Power Spectral Density (PSD) spectra (using the Welch method with 8 Hamming windows and a 50% overlap) of u' (a) and v' (b) velocities, for the whole ADCP deployment and taking a mean between $\sim 100 - 200$ m (the base of the thermocline). Vertical lines indicate frequencies of interest. The red lines represent the near-inertial frequency range ($0.9f - 1.9f$) used later in analysis. 95% confidence intervals on the spectral density estimate are shown.

The UTide Matlab package (Codiga, 2011) is used to carry out harmonic analysis of the ADCP mooring data for the whole deployment period, enabling further analysis of the dominant tidal constituents. Barotropic velocities were first used in the harmonic analysis (in a similar way to Brearley et al. (2017), barotropic is simply defined here as the depth-averaged velocity over the available depths), revealing that K_1 and O_1, and M_2 and S_2 are the major diurnal and semi-diurnal constituents respectively, accounting for 32%, 14%, 3% and $\sim$ 1% of the total tidal amplitude (of all constituents). The mean depth structure of the K_1, O_1, M_2 and S_2 tidal amplitudes are shown in Figure 4.8 (again calculated using depth-averaged velocity but conducting the harmonic analysis using just these 4 major constituents). K_1, O_1 and M_2 have respective maximum tidal amplitudes of $\sim$ 1, 0.65 and 0.34 cm s^{-1} between $\sim 100 - 200$ m. K_1 has minimum amplitudes of $\sim$ 0.3 cm s^{-1} close to the surface and at $\sim$ 300 m, but increases up to $\sim$ 0.46 cm s^{-1} between $320 - 390$ m. The O_1 amplitudes decrease with depth down to 0.2 cm s^{-1} at 450 m. M_2 amplitudes above and below the peak described above are relatively constant at $\sim$ 0.15 cm s^{-1}. The S_2 tidal amplitude decreases from 0.25 cm s^{-1} at the surface, down to $\sim$ 0.04 cm s^{-1} at ≥ 180 m. These tidal amplitudes are weak (as previously observed; Wallace et al., 2008; Brearley et al., 2017), however, the dominance of the K_1 and O_1 constituents, and their maximum amplitudes between $\sim 100 - 200$ m, suggests that they could have some role in controlling flow variability and therefore dissipation across the base of the thermocline.

Figure 4.9 shows the mean depth structure of the tidal phases averaged over the whole deployment. Phase shifts of 180° are known as reversals and are indicative of internal tidal activity (Gill, 1982) and water column shear. Using an upwards looking ADCP with a vertical resolution of 4 m, Wallace et al. (2008) found multiple phase reversals in

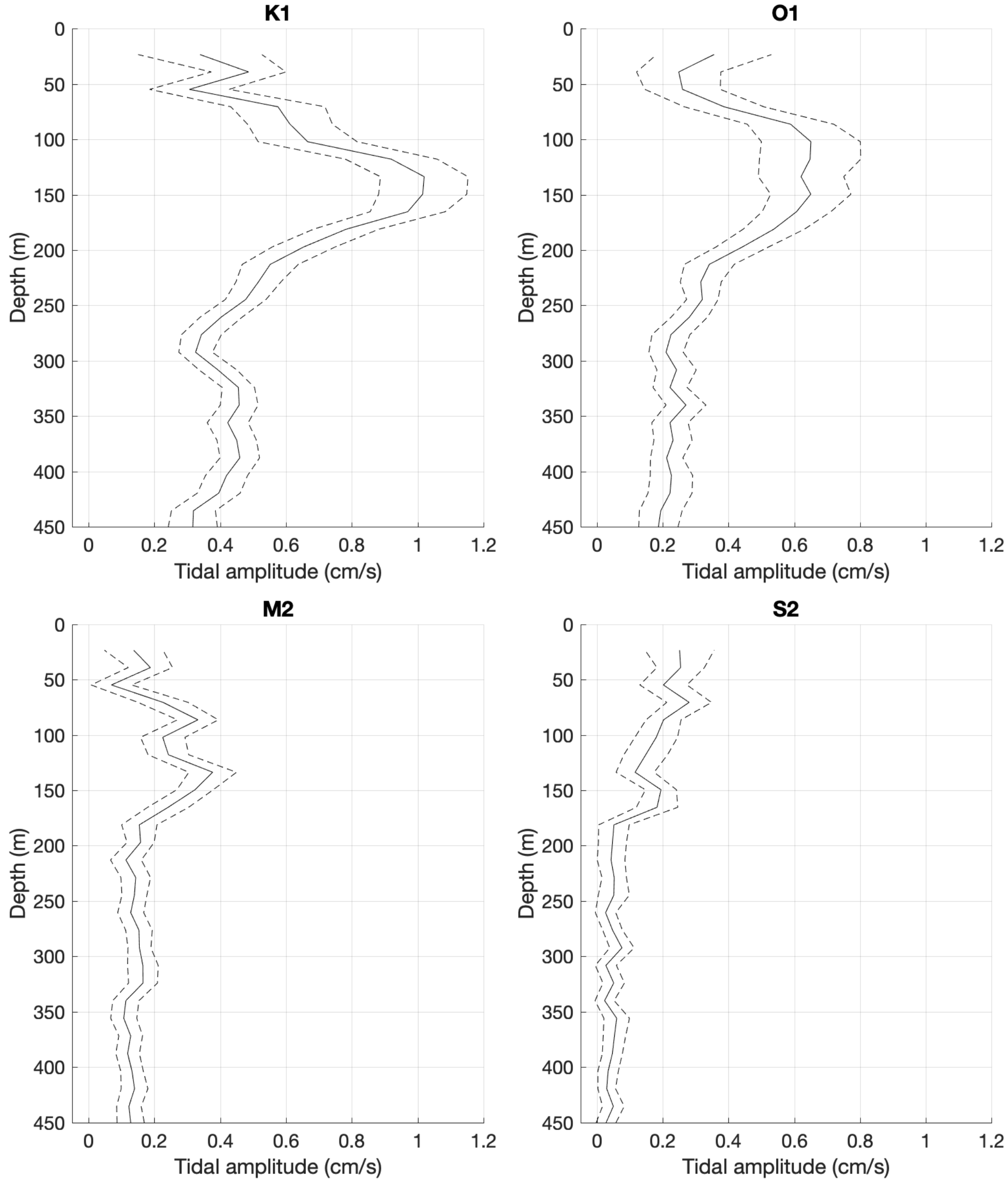

FIGURE 4.8: Depth structure of the K_1, O_1, M_2 and S_2 tidal amplitudes for the whole ADCP mooring deployment. Dashed lines are 95% confidence intervals.

the upper 200 m of Ryder Bay. In this study, few phase reversals appear in the mean phase profiles for the major tidal constituents, though this could (in part) be due to the lower vertical resolution (16 m) of the ADCP used here. Single reversals are observed at $\sim$ 30 and 47 m in the O_1 and M_2 profiles respectively, and two in the S_2 profile at $\sim$ 280 and 420 m. A smaller phase shift of $\sim 130^\circ$ occurs in the upper 50 m of the K_1 profile. Generally, the phase of the tides varies gradually by $\sim 80^\circ$ across the depths of each of the constituents, with the S_2 structure having significantly higher variability. The low number of phase reversals in these mean profiles, particularly around the depth of the thermocline ($\sim 100 - 200$ m), therefore suggests that internal tides are perhaps not

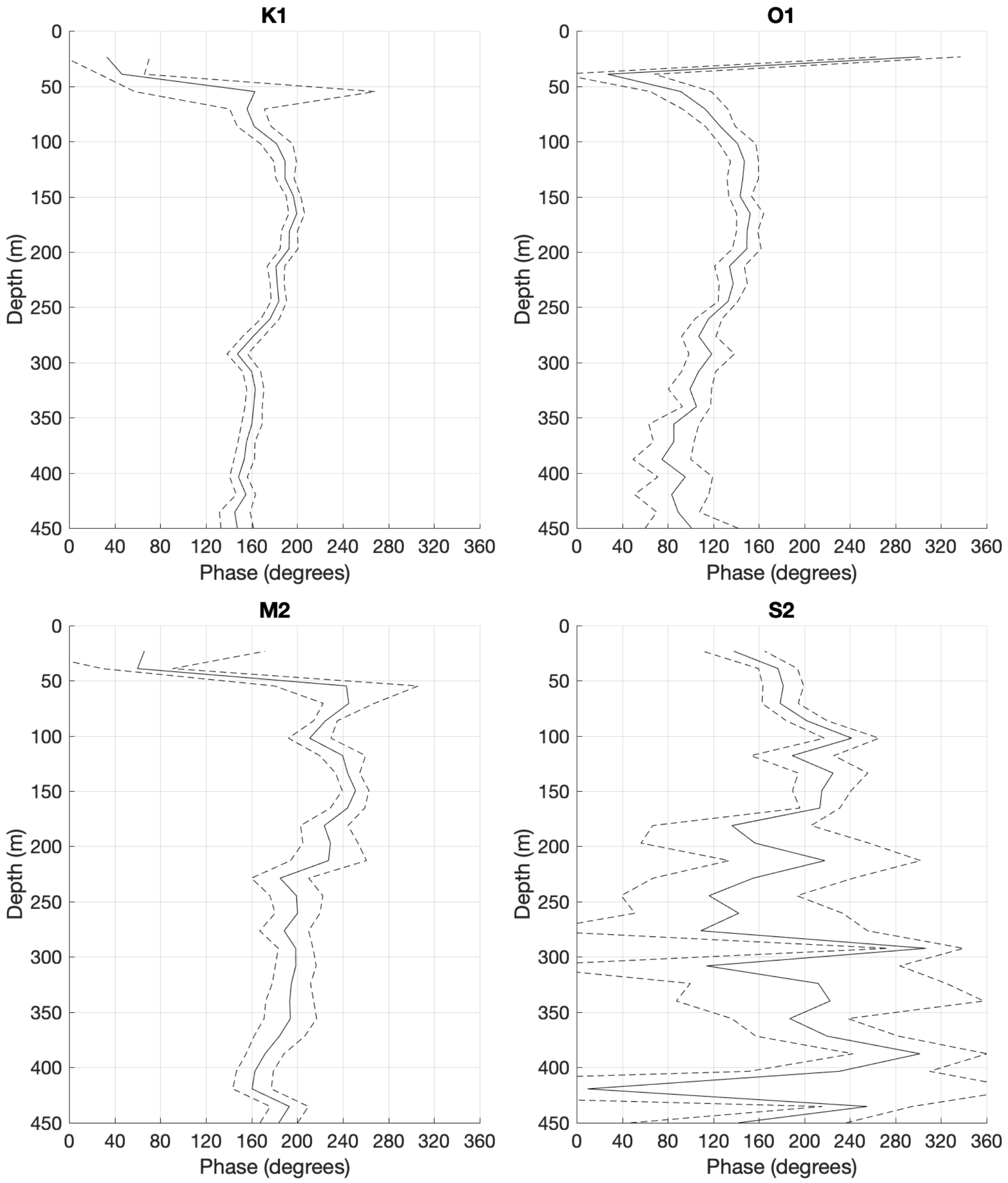

FIGURE 4.9: Depth structure of the K_1, O_1, M_2 and S_2 tidal phases for the whole ADCP mooring deployment. Dashed lines are 95% confidence intervals.

important for thermocline dissipation, at least during the deployment period.

Tidal ellipses are another way to look at the phase, however, they also provide a sense of the orientation and direction of rotation. Tidal ellipses for the K_1 and O_1 tidal constituents at selected depths are shown in Figure 4.10. Both constituents are predominantly cross-shore between $\sim 100 - 200$ m (the long axis is top to bottom of the plot), perhaps reflecting the greater peak in power at the K_1O_1 tidal frequencies in the v' velocities compared with the u' velocities (alongshore; Figure 4.7). The alongshore component has a greater importance in the upper 55 m of the K_1 tide, and at 24 m and below

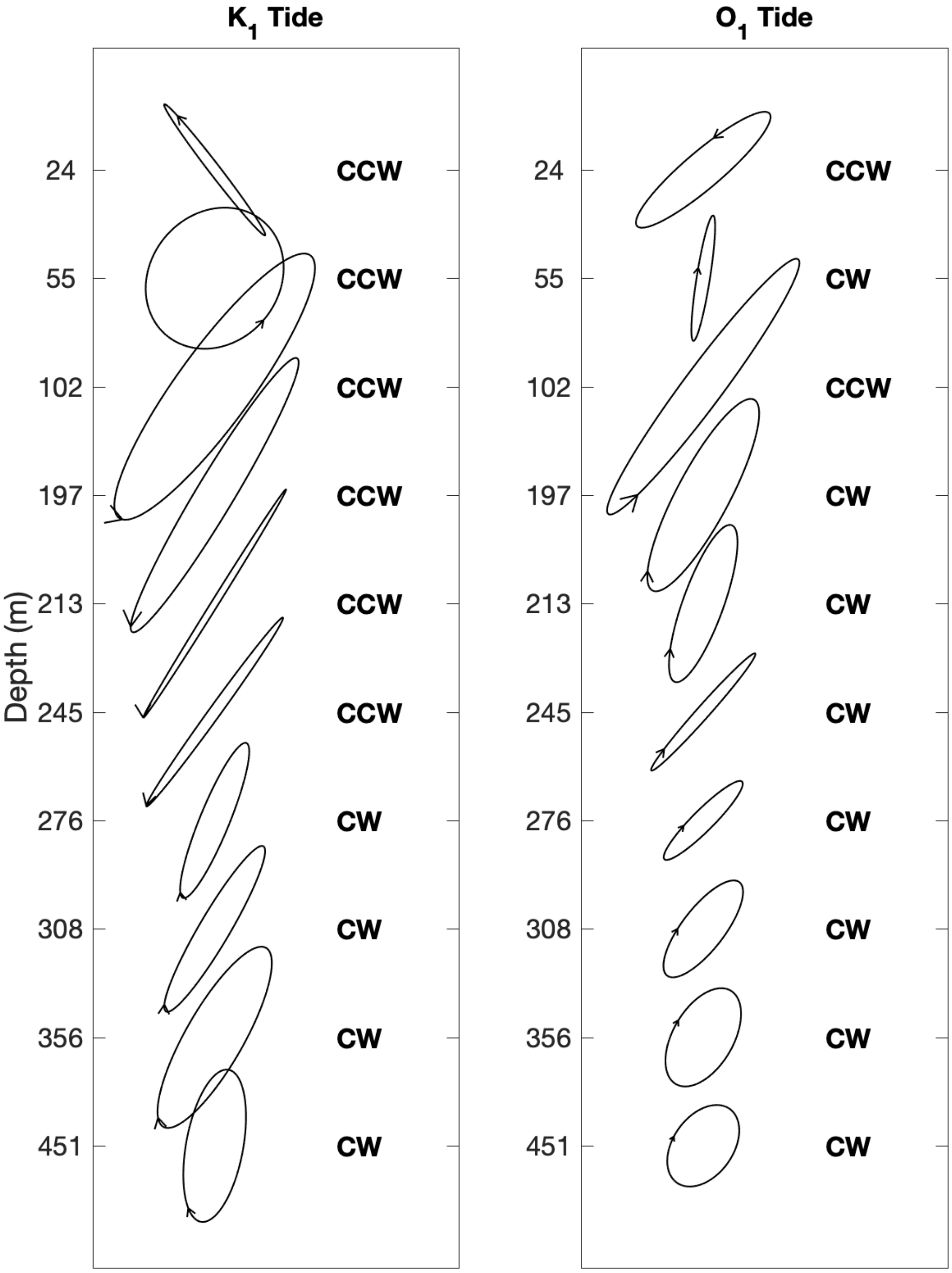

FIGURE 4.10: Tidal ellipses for the K$_1$ and O$_1$ diurnal tides (the dominant constituents) at selected depths. These were created using rotated ADCP velocities across the whole ADCP mooring deployment (i.e., cross-shore direction is top to bottom, alongshore is left to right of plot). The ellipses span the whole water column, though note the non-uniform depth spacing. The arrows show the direction of rotation and their position on the ellipse indicates the phase point.

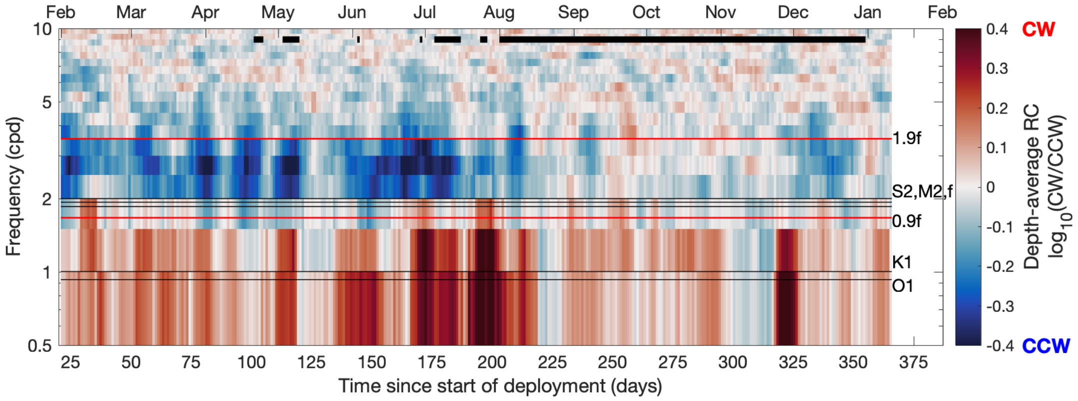

FIGURE 4.11: Full depth-average rotary coefficients (RC), using a 7 day window to provide high enough temporal resolution for resolving the spring neap cycle. Frequencies of interest (horizontal lines) are labeled. Red lines show the $0.9 - 1.9f$ near-inertial (NI) frequency range used in the text, particularly in Section 4.4.3. Black bars along the top indicate periods of fast-ice cover.

308 m in the O_1 tide. As shown in Figure 4.9, the K_1 phase is relatively barotropic, with changes only in the upper 55 m. However, here the K_1 tidal ellipses show a clear change in rotation direction with depth, moving from counter-clockwise (CCW) in the upper 245 m to clockwise (CW) below 276 m. A change in rotation direction at this depth could be indicative of shearing and therefore dissipation, however, this occurs below the thermocline. This contrasts to the O_1 tide, which has barotropic CW rotation and phase, apart from CCW rotation at 24 and 102 m and phase reversals in the upper 55 m. This could be indicative of shearing and therefore dissipation above the thermocline.

The ADCP velocity spectra can be decomposed into clockwise and counter-clockwise rotating components through rotary analysis, providing further diagnostics for understanding the mechanisms controlling flow variability within Ryder Bay. Rotary coefficients, the $\log_{10}$(CW/CCW) ratio, reveal the dominant sense of rotation, with negative (positive) values indicating enhanced CCW (CW) rotation. Figure 4.11 shows how the barotropic rotary coefficients change with time over a range of frequencies. Immediately apparent are the positive and negative rotary coefficients throughout the year at sub-inertial ($< 0.9f$) and near-inertial ($0.9 - 1.9f$) frequencies, respectively. The K_1O_1 tides lie in the range of the strong, positive rotary coefficients, suggesting that the barotropic tides at these frequencies could be a source of CW rotation. In contrast, rotary coefficients at the M_2S_2 tidal frequencies are much weaker, and commonly fluctuate between positive and negative values. The strongest rotary coefficients of $\sim \pm 0.4$ predominantly occur up until the start of August (day 200), after which the magnitudes of both the positive, and particularly the negative, rotary coefficients decrease considerably. This coincides with the extended period of fast-ice cover after the start of August (day 200), suggesting that fast-ice cover reduces the dominance of CCW and to

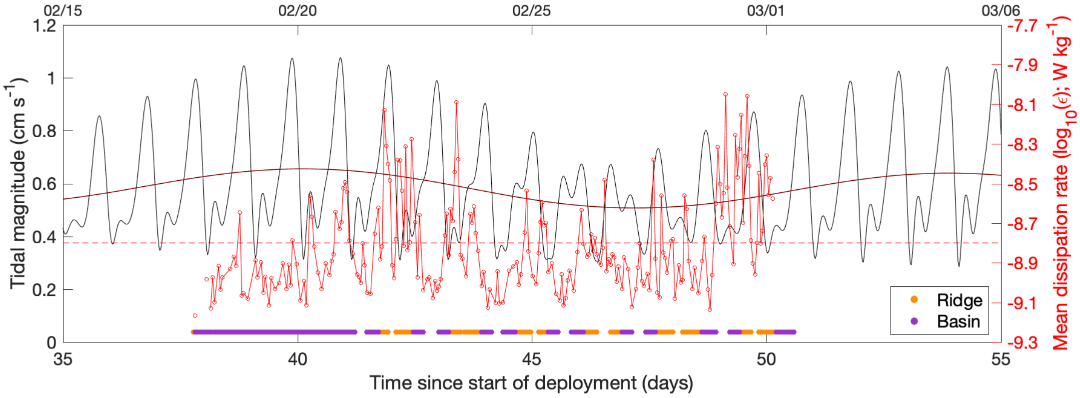

FIGURE 4.12: Comparison of total tidal magnitude (using the K_1, O_1, M_2 and S_2 constituents combined) with the hourly-mean interpolated dissipation rates. Real dissipation estimates (red circles) occur 70% of the time, with 94% of the gaps being 1 hour and a maximum gap of 3 hours. Thick burgundy line shows 2-day low-pass Butterworth filtered total tidal magnitude. Red horizontal dashed line shows the mean dissipation rate between $20 - 100$ days. Thick purple (orange) lines represent periods when the glider was in the basin (ridge) region. Date in 2016 is shown along the top axis.

a smaller degree CW rotation at near- and sub-inertial frequencies respectively. A primary source of near-inertial energy are strong, anticyclonic winds (e.g., D'Asaro, 1985), so this dampening could reflect a decrease in the effect of the winds, as suggested by Hyatt et al. (2011); Venables and Meredith (2014). This is explored further in Section 4.4.3.

Figure 4.12 compares the mean thermocline dissipation with both the unfiltered and 2-day low-pass filtered reconstructed total tidal magnitude (calculated using depth-averaged currents and the K_1, O_1, M_2 and S_2 constituents). Elevated dissipation occurs at all stages of the spring/neap and diurnal tidal cycles, strongly suggesting that tides do not have a control over the thermocline dissipation. This is supported by no statistically-significant correlation between the thermocline dissipation and the total tidal magnitude. Consequently, focus is moved away from the tides and onto other processes.

4.4.2 Basin-Scale Wave Modes and Coastal-Trapped Waves

Basin-scale wave modes and CTWs are important for governing flow in Arctic fjordic systems similar to Ryder Bay (e.g., Fraser et al., 2018; Inall et al., 2015). CTWs typically propagate along slopes in the form of elliptical eddies of opposing signs (see Inall et al., 2015, Figure 1), with the slope to the left (right) of the along-slope phase propagation in the Southern (Northern) Hemisphere, and are often viewed as a hybrid between shelf waves and Kelvin waves. Basin-scale wave modes are standing waves, which result from the collision of a pair of equal but oppositely directed waves (Thorpe, 2005);

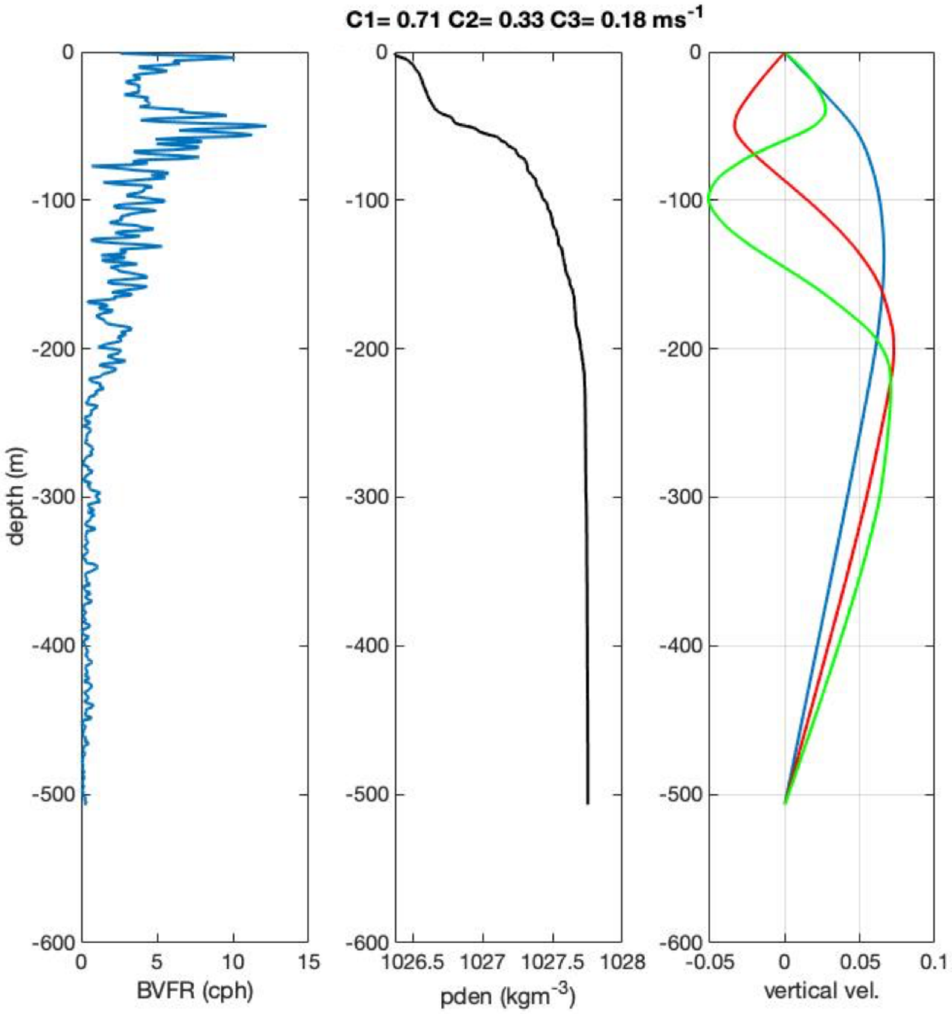

FIGURE 4.13: Basin-scale wave mode analysis (Inall, M. E., personal comms., December, 2020). Brunt-Vaisala frequency squared (left) and potential density (middle) profiles from February 2016 are used to calculate the first three internal long-wave modes (right; units in m s^{-1}). Corresponding phase speeds are shown above.

for example, this can occur when a wave is reflected at the end of a fjord. As mentioned in Section 4.2, both basin-scale wave modes and CTWs are typically forced by winds and can lead to enhanced shear, thereby increasing the likelihood of shear-driven mixing (e.g., Fraser et al., 2018; Arneborg and Liljebladh, 2001). This is particularly expected at lateral boundaries where friction is important, however, internal wave modes can also break through overturning at their velocity nodes (e.g., Thorpe, 2005), which would lead to elevated dissipation and enhanced mixing. Consequently, both CTWs and basin-scale wave modes could be responsible for the basin-wide dissipation event that occurred above and across the thermocline during Transect 12 (Figure 3.17e).

The first three internal wave modal eigenvalue solutions were computed from the Taylor-Goldstein equation with zero vertical background shear using a density profile from February 2016 (Figure 4.13). The mode-1 phase speed is $C1 = 0.71$ m s^{-1}, which can be used to calculate the fundamental 'quarter pipe' resonance period using:

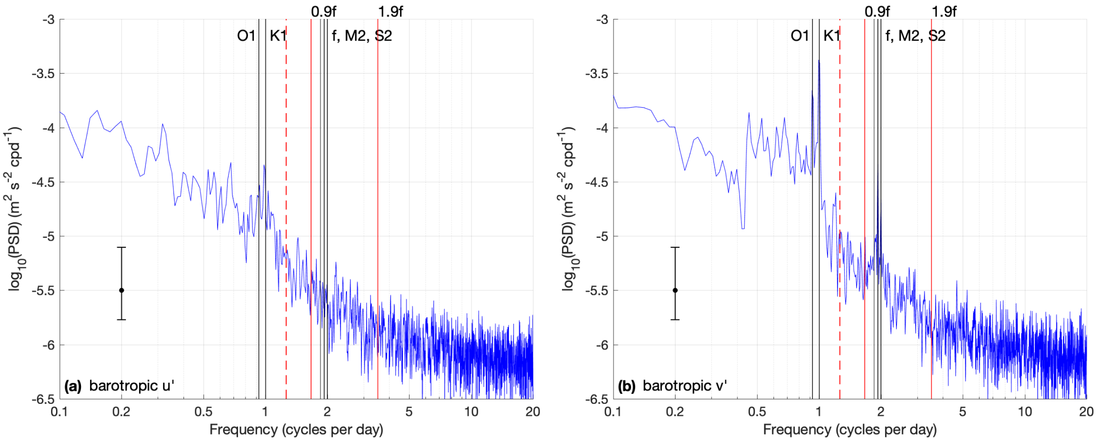

FIGURE 4.14: Mean Power Spectral Density (PSD) spectra (using the Welch method with 8 Hamming windows and a 50% overlap) of u' (a) and v' (b) velocities, for the whole ADCP deployment using barotropic velocities. Vertical lines indicate frequencies of interest. Vertical dashed line shows the fundamental 'quarter pipe' resonant period of 19 hr. The red solid lines represent the near-inertial frequency range $(0.9f - 1.9f)$ used later in analysis. 95% confidence intervals on the spectral density estimate are shown.

$T = 4L/C1$ (following the method of Fraser et al., 2018). The length of Ryder Bay is $L =\sim 12$ km, giving a resonance period of $T =\sim 19$ hr. A PSD of the barotropic alongshore (u') velocities reveals no peak in power at the 'quarter pipe' resonance frequency (red dashed vertical line in Figure 4.14).

The oscillatory nature of basin-scale wave modes and CTWs means one might expect periodic bursts of flow into/within Ryder Bay. This lends itself to the use of wavelet analysis, which can be used to assess how the dominant frequencies within a time series change with time. ADCP data in the upper layers of the water column (above the thermocline) are often too noisy for wavelet analysis (they are dominated by broadband power), so lower layer velocities (below the thermocline) are typically used (e.g., Inall et al., 2015). Using a Morlet wavelet, a wavelet analysis was conducted on mean alongshore (u') ADCP velocities between $200 - 355$ m (Figure 4.15). In addition to the reason above, this depth range was chosen because flow variability at these depths may also be an important control on the deep elevated dissipation over the ridge, discussed in Section 4.5.

Figure 4.15a shows the velocity time series used in the analysis, grey regions indicate periods when fast-ice is present and the blue box indicates the glider deployment. Figure 4.15b is the wavelet power spectrum showing how the power at different periods changes with time. The wavelet analysis reveals times of statistically-significant high power between February and August, spanning a broad range of periods, typically from $\sim 32 - 96$ hr. The times of high power are episodic (as expected for CTWs), however, they are likely too broadband to be of CTW origin (e.g., $40 - 60$ h; Inall et al., 2015). Scattering off of rough bathymetry might be expected to broaden the observed range

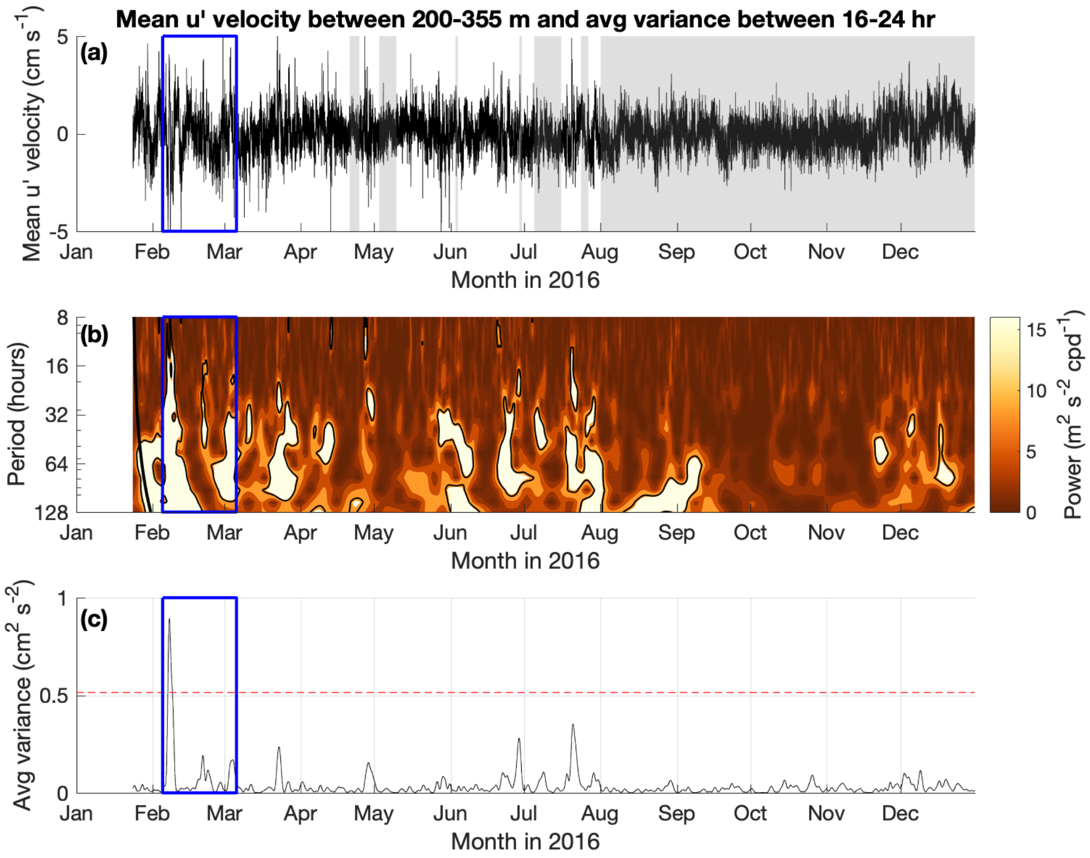

FIGURE 4.15: (a) Mean u' velocity between $200 - 355$ m for 2016. The grey regions are periods of fast-ice coverage. (b) Wavelet analysis of (a). Black contours indicate significant regions at the 90% confidence level. Thick black vertical line at the start of the wavelet is part of the cone of influence, data below is dubious. (c) Average variance over the $16 - 24$ hr period range, with the 90% significance level indicated with a red-dashed line. This range was chosen to incorporate the resonant 'quarter pipe' period. The blue box in each panel shows the period over which the glider was deployed.

of CTW periods, however, to fully characterise any potentially important wave-types, upstream velocity measurements would be required for calculation of the wavelength and velocity. Additionally, it is evident that times of suppressed power in the $32 - 96$ hr period range coincide with those of fast-ice cover within Ryder Bay. The most notable of these is between August and December. This suggests that fast-ice cover is an important control on the observed flow variability between $200 - 355$ m. Sea ice acts as a thermal and mechanical barrier to atmospheric forcing (Hyatt et al., 2011; Venables and Meredith, 2014), so the observed variability could be associated with local wind related processes. This observation is significant because the low period and long wavelengths of CTWs allows them to propagate over large distances, so if CTWs were important for flow variability in Ryder Bay, one might expect the episodic bursts of power to occur year round (as the CTWs could form in ice-free areas).

Figure 4.15c shows the average variance over the $16 - 24$ hr period range; a small range incorporating the $\sim$ 19 hour seiche period. If seiching were important for Ryder Bay, one would expect episodic bursts of power in this frequency range. However, only one large peak in power at the start of the glider deployment exceeds the 90% confidence interval. This suggests that there is no evidence for seiching at the fundamental 'quarter pipe' period in Ryder Bay. While higher mode seiche-like motions are possible, higher modes are invariably less energetic than the fundamental mode (Inall et al., 2014). The lack of evidence of a first mode within Ryder Bay thus leads to the conclusion that higher order modes are likely unimportant. Consequently, the analysis here points to other processes other than CTWs and basin-scale wave modes being responsible for the thermocline dissipation.

4.4.3 Near-Inertial Shear

Winds are a primary source of near-inertial kinetic energy and shear in the upper water column (D'Asaro, 1985; Wunsch and Ferrari, 2004), and are another mechanism that may have generated the basin-wide thermocline dissipation in Transect 3.17e. A time series of wind stress magnitude between $20 - 100$ days (31^{st} January - 20^{th} April 2016) shows multiple strong wind events occurring during the glider deployment (e.g., days 27, 39, 47 and 50; Figure 4.16a). Integrated near-inertial shear squared values, U_z^2, within the $105 - 205$ m layer are calculated using $0.9 - 1.9f$ band-pass Butterworth filtered ADCP velocities (u_{NI}, v_{NI}) on an hourly time grid (Figure 4.16b):

$$U_z^2 = \left(\int_{z=105}^{z=205} \left(\frac{du_{NI}}{dz} \right)^2 + \left(\frac{dv_{NI}}{dz} \right)^2 \right) dz. \tag{4.4}$$

An hourly time grid was used here to match the time grid used for the dissipation and wind data, and the binned ADCP velocities were regridded to provide velocities every 10 m between $25 - 445$ m. The $0.9 - 1.9f$ frequency range was selected as it corresponds to the strongly negative rotary coefficients in Figure 4.11 (red horizontal lines). The $105 - 205$ m depth range was chosen to focus on processes occurring across the main thermocline, a region important for the exchange of heat between the CDW and AASW layers. A depth layer definition was chosen instead of a vertical range centred on the 0.25 °C thermocline isotherm because the former definition does not require hydrographic data and ensures a continuous integrated shear time series. However, a sensitivity test revealed that differences between shear values generated by these two methods were small (Figure 4.17).

Elevated near-inertial shear is observed on days 28, 41, 49 and 50 (at similar times to the wind events highlighted above), yet there is no significant correlation between the $20 - 100$ day unfiltered wind stress magnitude and near-inertial shear squared time series. Applying a 4-day low-pass Butterworth filter to both time series (magenta lines; Figures 4.16a,b) and conducting a cross-correlation analysis reveals that the highest

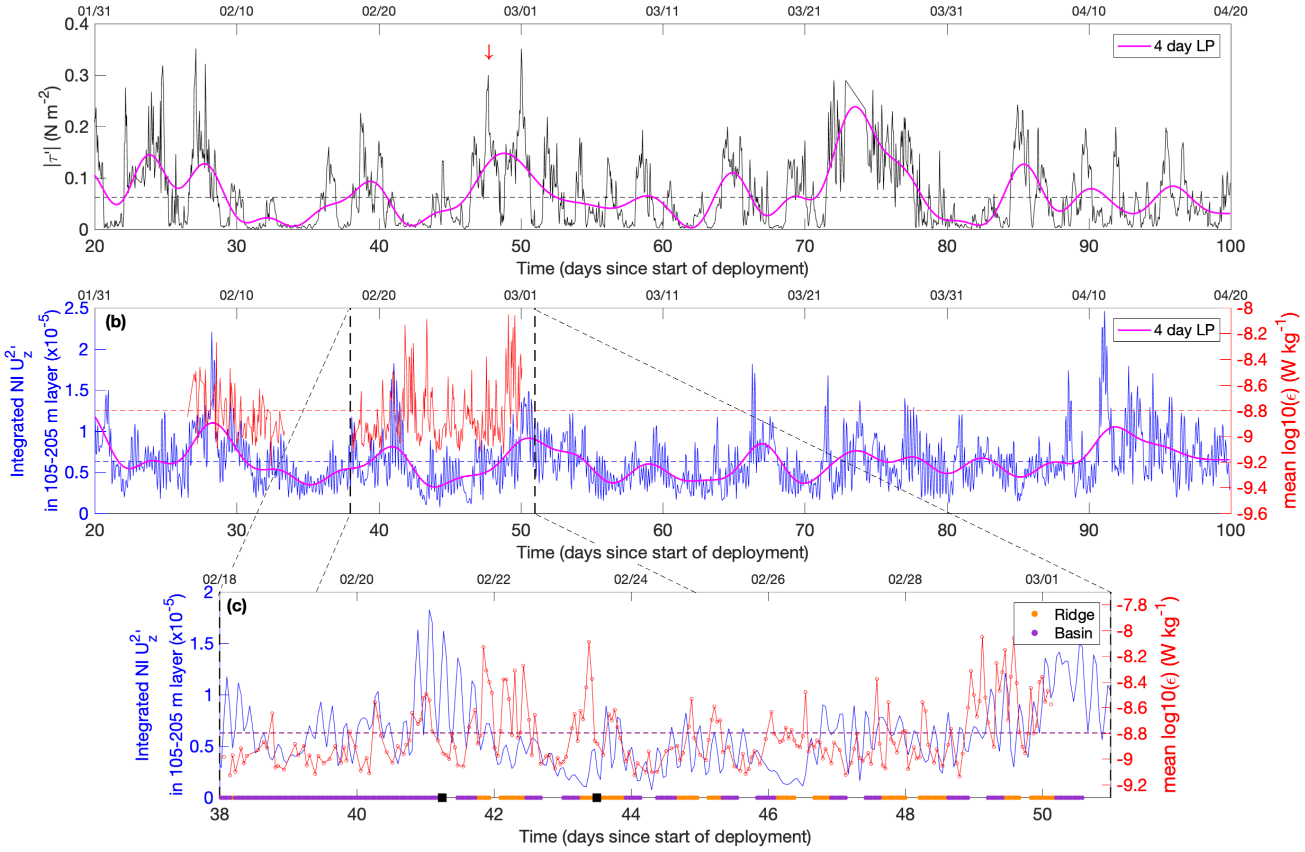

FIGURE 4.16: (a) Time series of hourly wind stress magnitude. The magenta line represents the 4-day low-pass Butterworth filtered signal. The red arrow indicates the wind event that likely caused the elevated dissipation in Transect 12 (Figure 3.17e). (b) Integrated near-inertial ($0.9 - 1.9f$) shear squared within the $105 - 205$ m layer, with magenta line as in (a). Overlain are interpolated hourly-mean dissipation rates. Real dissipation estimates (red circles) occur 70% of the time, with 94% of the gaps being 1 hour and a maximum gap of 3 hours. Vertical dashed lines indicate the period shown in (c). Black squares show periods considered for correlations. All horizontal dashed lines represent the quantity means between $20 - 100$ days; these have been aligned in (c).

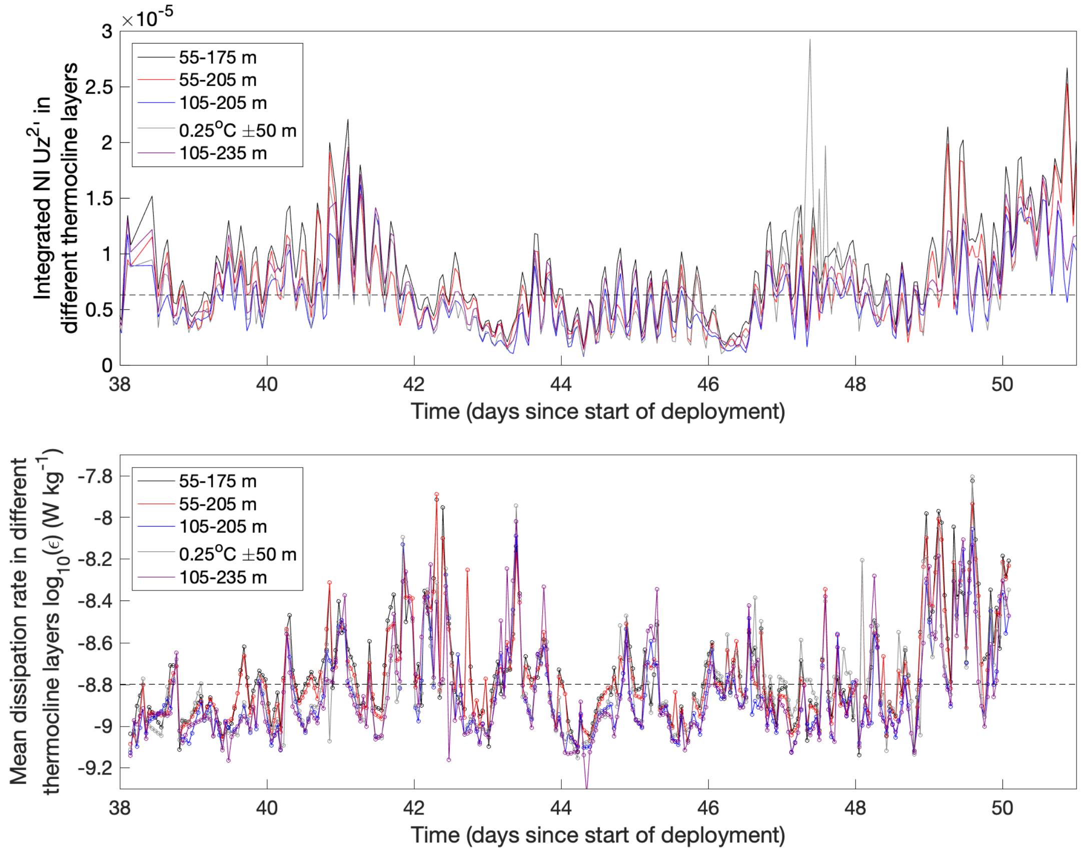

FIGURE 4.17: Sensitivity analysis of different thermocline depth ranges on the near-inertial (NI; top) and dissipation (bottom) time series. The only noticeable difference in the near-inertial shear is on day 47, with a peak in thermocline layer using the ±50 m from the 0.25 °C isotherm definition. Black dashed lines show the deployment mean $105-205$ thermocline NI shear (top), and overall-mean dissipation (bottom).

correlations occur when the near-inertial shear lags behind the wind stress between 0.7 and 1.7 days (Figure 4.18a). Accounting for a 1.7-day lag between the low-passed time series gives a correlation of $R = 0.47$ ($p = 2 \times 10^{-3}$), which increases to $R = 0.92$ ($p \ll 0.001$) using only data between days $30 - 55$ (the mixed layer model period, see below). Figure 4.18b shows that the best correlation occurs when using this larger lag; using a lag of 0.7 days, the correlation between the filtered wind stress magnitude and the near-inertial shear is $R = 0.76$ ($p \ll 0.001$). This suggests that winds are an important controlling influence on the shear within the thermocline during the period of our observations.

Comparison of the near-inertial shear with hourly mean dissipation estimates within the $105 - 205$ m layer shows that periods of elevated dissipation coincide with enhanced shear on days 28, 40 and 48 (Figure 4.16b). Mean dissipation estimates are linearly interpolated where required; over the zoomed-in period when the glider made multiple transects (Figure 4.16c), mean dissipation estimates were calculated $\sim$ 70% of the time (circles), and $\sim$ 90% of the interpolated gaps were only 1 hour long (the

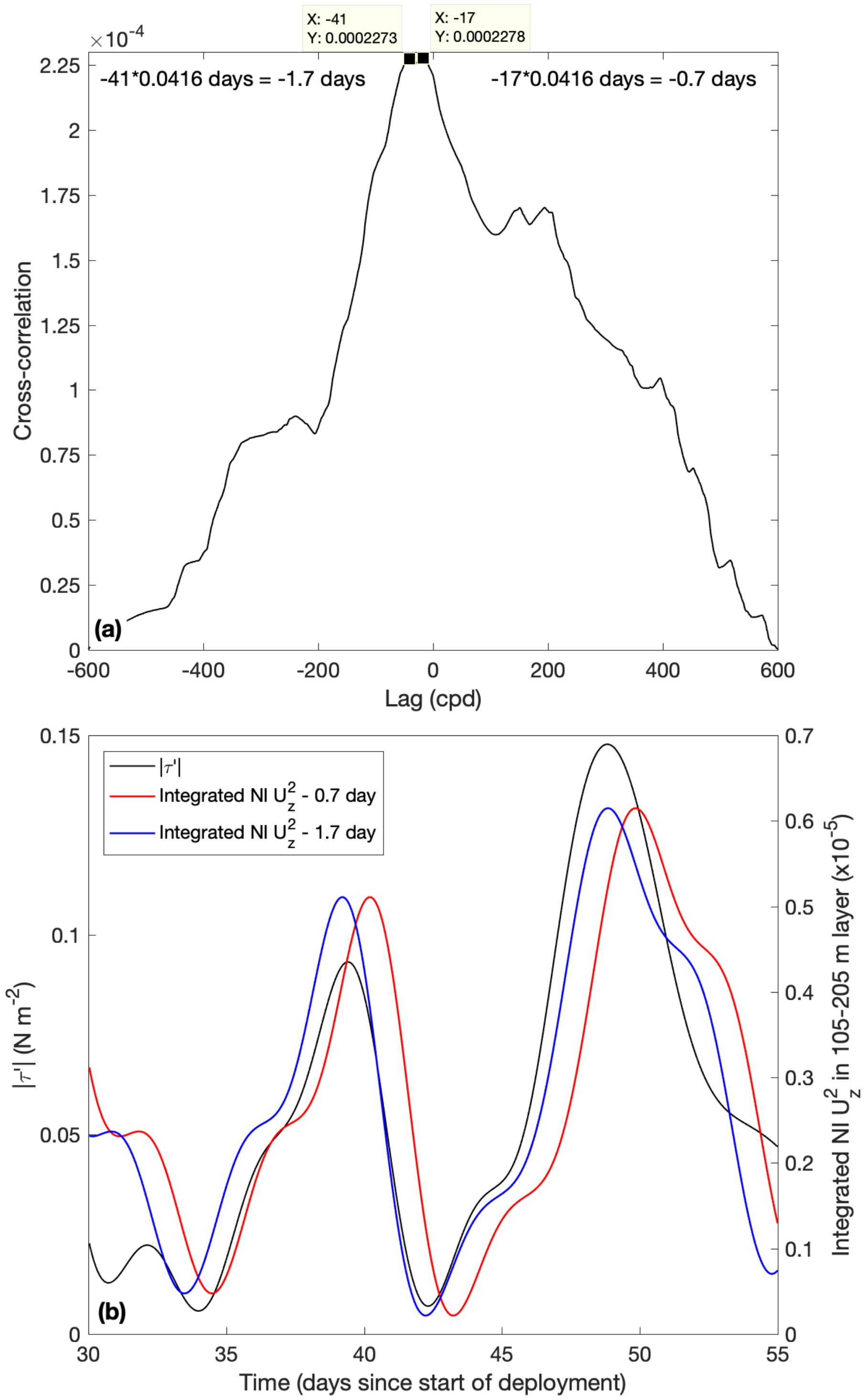

FIGURE 4.18: (a) A cross-correlation between the 4-day low-pass Butterworth filtered wind stress magnitude and near-inertial (NI) thermocline shear ($105 - 205$ m) reveals a lag of -0.7 to -1.7 days. (b) Comparison of filtered wind stress with the lag-adjusted filtered near-inertial shear, using the two lags above. A lag of -1.7 days best matches the peak in wind stress on day 47/48 (Figure 4.16).

maximum interpolated gap length over this period was 3 hours). The dissipation in Figure 4.16b is offset vertically from the near-inertial shear to aid visibility of the latter; however, mean near-inertial shear and dissipation values are aligned in Figure 4.16c (horizontal lines) so that elevated periods are more easily visible. Although periods of low (high) shear appear to coincide with periods of low (high) dissipation, overall there is no statistically-significant relationship between near-inertial shear and dissipation between days $38 - 51$. The large differences found between days $41.25 - 43.50$ are likely responsible. The correlations before and after this period are $R = 0.38$ ($p = 0.01$) and $R = 0.24$ ($p = 0.06$), respectively. The statistically-significant correlation between days $38 - 41.25$ could reflect the glider maintaining close proximity to the ADCP mooring. The second correlation's statistical significance is marginal at the 5% level, which may initially suggest that other processes could be responsible for the thermocline dissipation. However, as stated above, other candidate processes such as basin-scale wave modes and CTWs are not thought to be important within Ryder Bay. Consequently, some of the difference between near-inertial shear and dissipation could, at least in part, be of spatial origin (with higher dissipation always present over the ridge, where other processes could contribute to the observed dissipation in the $105 - 205$ m layer). Indeed, the median thermocline dissipation over the ridge is $\sim 1/3$ greater than that observed over the basin. A two-sided Wilcoxon rank sum test shows that this result is statistically-significant at the 5% level ($p \ll 0.001$). Additionally, some periods of elevated dissipation but only moderate near-inertial shear can be attributed to super-inertial energy, which may have either been directly generated by wind events, or transferred from the near-inertial band to higher frequencies through the breaking of internal waves; for example, the elevated dissipation spike at the start of day 49 (Figure 4.19).

The mixed layer slab model introduced above can be used to investigate wind-driven near-inertial motions (e.g., D'Asaro, 1985; Alford, 2001, 2003; Mickett et al., 2010). The simplicity of the model (only requiring 2 inputs - the MLD and wind stress magnitude) enables its use as an independent method of estimating wind-generated near-inertial velocities that can be compared to observed flows. Assuming changes in the mixed layer depth to be negligible compared to wind stress changes, the equation for Z_I is (D'Asaro, 1985):

$$\frac{dZ_I}{dt} + \omega Z_I = -\frac{1}{\omega H}\frac{dT}{dt}. \tag{4.5}$$

The model was ran between days $30 - 55$ by integrating Equation 4.5 using $H = 20$ m, the observed wind stress magnitudes (Figure 4.20a), and the near-inertial velocity at the start of day 30 as the initial condition. Although impulse wind stresses can force near-inertial velocities, in the Southern (Northern) Hemisphere, near-inertial velocities best respond to anticlockwise- (clockwise-) rotating wind stresses (D'Asaro, 1985). Anticlockwise-rotating wind stress vectors are observed during the strong wind events around days 39, 44, 47, 48 and 50, and these produce correspondingly strong modelled

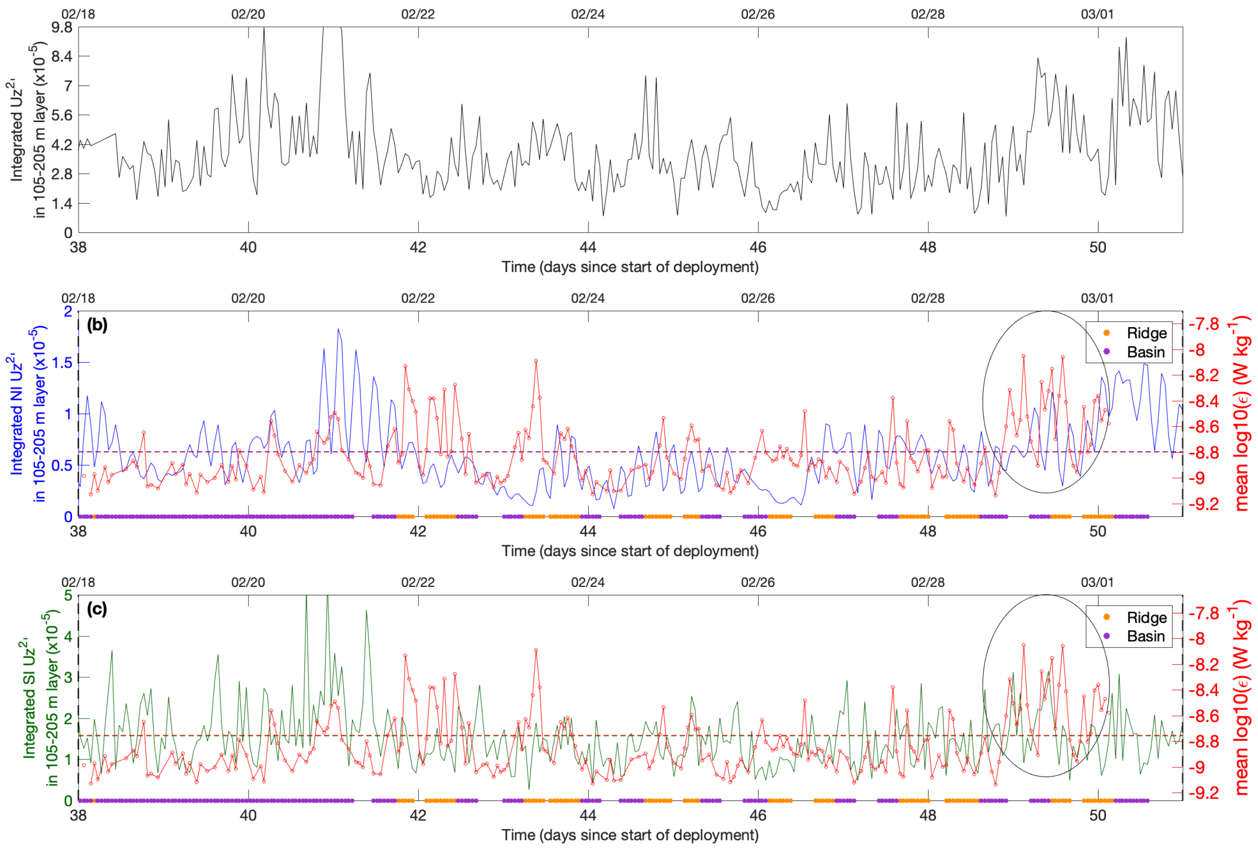

FIGURE 4.19: (a) Integrated unfiltered (a), near-inertial ($0.9 - 1.9f$; b) and super-inertial ($> 1.9f$; c) shear squared within the $105 - 205$ m layer. Overlain are hourly-mean dissipation rates (b,c), linearly interpolated where required. Horizontal dashed lines represent the quantity means between $20 - 100$ days and have been aligned. The circles in (b,c) show an example referred to in the text, where the super-inertial shear likely contributes to the observed dissipation.

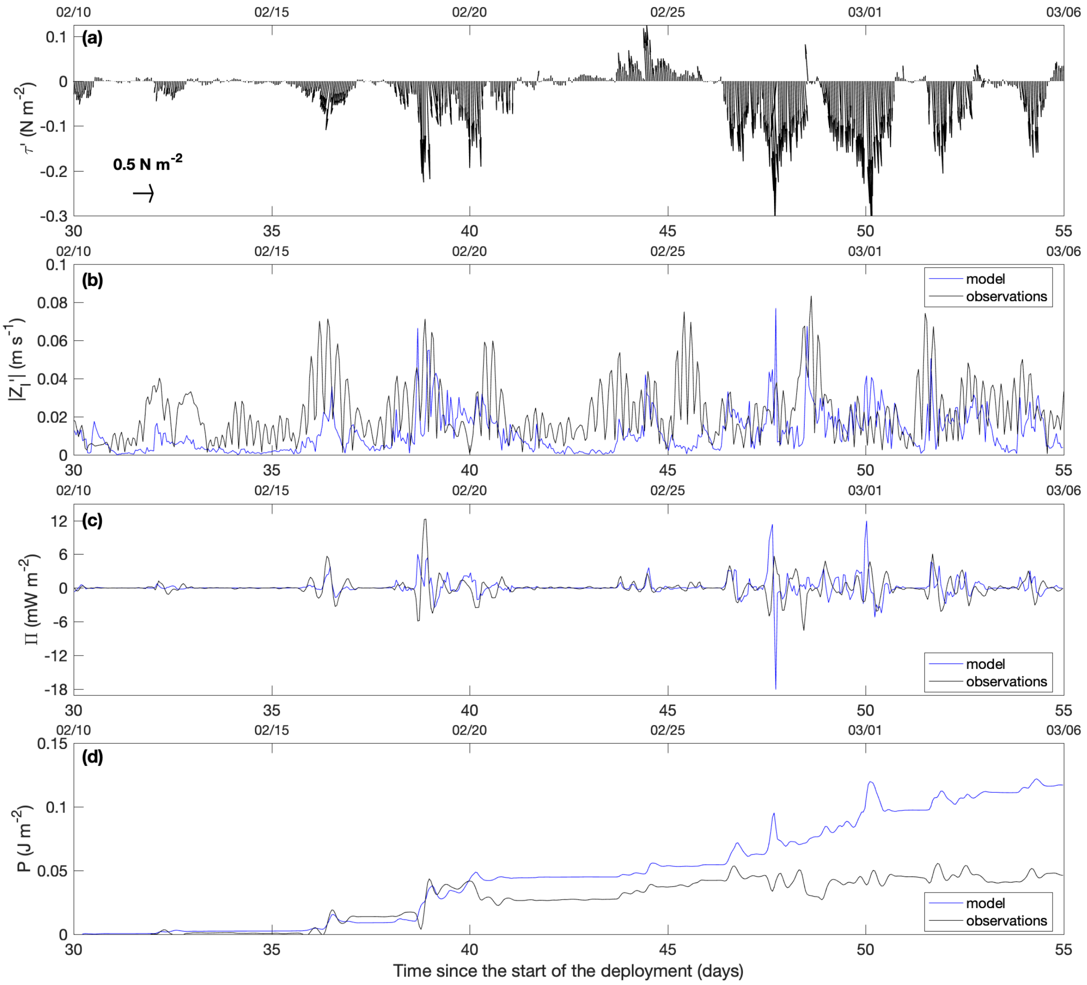

FIGURE 4.20: (a) Wind stress vectors used in the mixed layer slab model (Pollard and Millard, 1970). (b) Comparison between modelled and observed near-inertial velocity magnitudes. (c) Energy flux from the wind to near-inertial velocity. (d) Time integral of the energy flux in (c).

near-inertial velocities with magnitudes of $\sim 0.05 - 0.09$ m s^{-1} (Figure 4.20b). The modelled near-inertial velocity magnitudes exhibit a significant correlation of $R = 0.28$ ($p = 0.01$) with observations. The modelled velocities in response to the strong wind events are generally overestimated after day ~ 40. This could be a consequence of the observed mixed layer deepening (and likely associated near-inertial flow dampening) that is not captured by the model, which relies on a constant mixed layer depth; the mixed layer deepened from ~ 15 m on day 37 to ~ 30 m on day 43. The model's inability to characterise rapid mixed layer deepening has been documented previously, and is thought to cause biases in near-inertial velocities of up to a factor of 4 (Plueddemann and Farrar, 2006).

An approximation of the energy flux into inertial motions from the winds can be given by Alford (2003):

$$\Pi = \Re[\rho Z_I T^*], \tag{4.6}$$

where $\Re$ extracts the real part of the solution and * indicates the complex conjugate. Although this equation neglects a term of order r_d/f (Alford, 2003), it does have utility in estimating the likely energy transfers. The energy flux can be positive or negative, with winds either accelerating or decelerating the inertial velocities, respectively (Figure 4.20c). Negative fluxes occur when the winds do work against the surface currents, causing increased shear and promoting the dissipation of turbulent kinetic energy (D'Asaro, 1985). The modelled energy fluxes typically have the same sign as the observations, but often produce larger velocities during strong wind events. This is seen more clearly in a time integral of the energy flux (Figure 4.20d), which shows a significant divergence between modelled and observed values after the first large wind event on day 39. Although this exemplifies the model caveats mentioned above, Figures 4.20c,d also show large positive and negative fluxes on days 39, 44, 47, and 50. This likely means that those wind events are particularly important for affecting thermocline dissipation.

4.5 Deep Turbulent Dissipation

This section explores the mechanisms likely responsible for the third key feature from Chapter 3: deep, elevated dissipation over the topographic ridge at Ryder Bay's entrance.

4.5.1 Tides

A common mechanism proposed for elevated mixing over topographic ridges similar to that found at the mouth of Ryder Bay is the breaking of internal tides (e.g., Polzin et al., 1997). As mentioned in Section 4.4.1, the dominant barotropic constituents are the K_1 (32% of the total tidal amplitude) and O_1 (14%) tides. These tidal constituents are reconstructed and compared to the measured barotropic u' (Figure 4.21a,c) and v' (Figure 4.21b,d) velocities. Overall, mean absolute velocities of 1 cm s^{-1} were observed in both the u' and v' barotropic signals, with maximum total velocities of $\sim 5-6$ cm s^{-1}. The u' tidal component is comparatively weak throughout the deployment, with maximum amplitudes of 0.4 cm s^{-1}. The v' tidal velocities are larger ($\sim$ 1 cm s^{-1}) and can be of similar amplitude as the overall flow during periods of the spring tidal maximum (e.g., between days $36-44$; Figure 4.21d). Nevertheless, similarly large sub-inertial flows ($\sim 4-5$ cm s^{-1}) occur, both at the spring maximum (e.g., days $25-40$) and neap minimum (e.g, days $44-50$). This implies that other processes are also implicated in setting the dynamics of the flow over the ridge. This is also supported by a substantial reduction in the larger velocities with the presence of fast-ice (Figures 4.21a,b), suggesting a significant influence of surface processes on the deep sub-inertial velocity field.

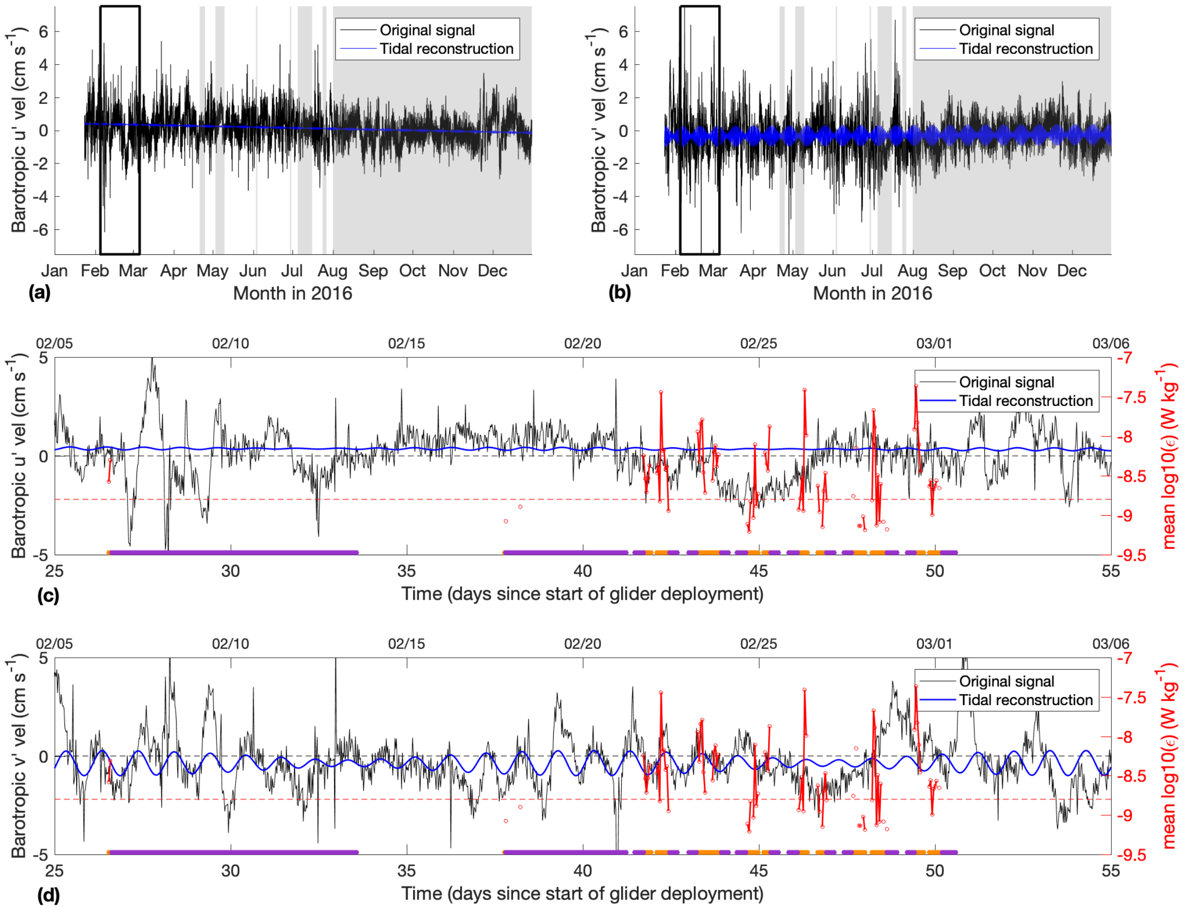

FIGURE 4.21: (a) Comparison of the barotropic u' velocity with corresponding reconstructed K_1O_1 tidal component for 2016. The black outline and grey regions highlight days 25 – 55 and periods with fast-ice present, respectively. (b) As (a), but for v' velocity. (c) u' velocity between days 25 – 55 of the glider deployment. Overlain are hourly mean dissipation rates above the ridge (below 200 m and between 1.3 – 5.5 km along the A-B Transect). Horizontal dashed lines are corresponding overall mean values between days 20 – 100 (the first ice-free period). (d) Same as (c) but for v' velocity.

Hourly mean dissipation rates below 200 m and between 1.3 − 5.5 km along the A-B Transect (i.e. over the ridge) are compared with the observed K_1O_1 tidal barotropic velocities (Figures 4.21c,d). During certain periods, peaks in dissipation rate do appear to coincide with peaks in the reconstructed v' tidal velocities (e.g., on days 42 and 43); however, there are also clearly instances when this is not the case (e.g., on day 49). No statistically-significant correlation is found between the u' and v' barotropic K_1O_1 tidal components and the mean dissipation over the ridge. Therefore, while the tides may play a role in governing the cross-shore flow and could potentially be a source of elevated dissipation over the ridge, other processes are also likely to be at least as significant.

4.5.2 Hydraulic Control

Various features of the hydrographic and dissipation rate data suggest that the flow over the ridge may be subject to hydraulic control, which could be implicated in the enhanced near-bottom dissipation over the ridge. The first piece of evidence for this is the elevated dissipation over the ridge, which typically occurs where the 27.74 kg m^{-3} isopycnal has the steepest slope (e.g., in Transect 4 at $\sim$ 340 m depth; Figure 3.16c). Such an arrangement, including pinching of the 27.73 − 27.74 kg m^{-3} isopycnal structure over the ridge, and deepening in its lee, is strongly reminiscent of flow that is controlled hydraulically (Farmer and Smith, 1980). Consequently, a layered hydraulic control theory is applied to explore whether hydraulic physics may be applicable to the observations in this study (i.e. whether such a control may be a plausible explanation for the observed dissipation over the ridge in Ryder Bay). There are several possible theories that could be used here. For example, Smeed (2000) presents a three-layered hydraulic control theory, where each layer can have different densities and flow directions, whilst Armi (1986) presents a two-layer theory below a free surface. There are large limitations to using either theory in this way, however, since no upstream velocity measurements are available (particularly above the ridge); such data would provide flow direction information over the ridge and help to define the layers used when applying the hydraulic control theory. A sensitivity analysis was therefore conducted using the simplest theory available that also contained stratification. Consequently, the composite Froude number, G^2, for a two-layer flow with a free surface is considered (Armi, 1986):

$$G^2 = F_1^2 + F_2^2 - \frac{\rho_2 - \rho_1}{\rho_2} F_1^2 F_2^2, \tag{4.7}$$

where

$$F_{1,2}^2 = \frac{u_{1,2}^2}{g' y_{1,2}} \text{ and } g' = g\frac{\rho_2 - \rho_1}{\rho_2}.$$

$u_{1,2}$ (m s^{-1}) and $y_{1,2}$ (m) are the upper (1) and lower (2) layer velocities and thicknesses, respectively, and g' is the reduced gravity (Figure 4.22). This theory assumes

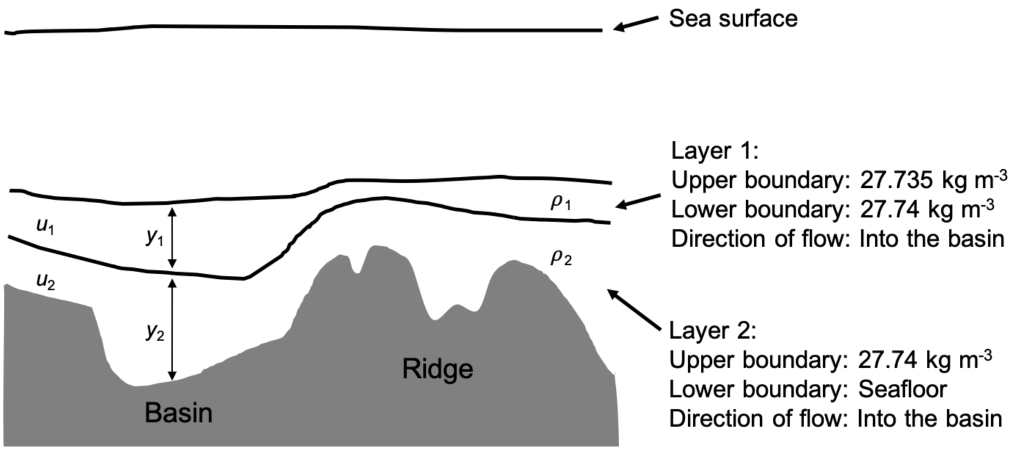

FIGURE 4.22: Schematic showing the conceptual layers used in the hydraulic control sensitivity analysis for Ryder Bay (using Equation 4.7). See text for reasons behind the layer choices. Note that by using Armi (1986)'s two-layer theory, flow above layer 1 does not affect hydraulic control; this is not unreasonable when the isopycnals above have smaller vertical displacements.

frictionless, non-rotational, incompressible and hydrostatic flow with layers of uniform density and velocity (Armi, 1986). Additionally, time-dependent, mixing and stable stratification effects are ignored (Hogg and Killworth, 2004).

In a system that is controlled hydraulically, flow transitions from low velocities in a sub-critical regime ($G^2 < 1$) upstream of a topographic ridge, to fast velocities in a super-critical ($G^2 > 1$) regime above and in the lee of the ridge, before transitioning back to sub-critical flow further downstream (Armi, 1986). The point of criticality ($G^2 = 1$) marks the transition between sub- to super-critical flow, and can move with respect to the ridge due to changes in flow speed, where a faster flow tends to move the point of criticality upstream (Farmer and Denton, 1985). In a super-critical flow over a ridge, dissipation rates can reach several orders of magnitude higher than background values, due to increased ridge-flow interactions (Gregg and Klymak, 2014). At the transition between super- to sub-critical flow, the decrease in flow speed can cause the formation of a hydraulic jump and the release of a large amount of energy through elevated dissipation (Farmer and Denton, 1985).

The downstream ADCP mooring within Ryder Bay provides a range of likely velocities that can be used in the composite Froude number sensitivity analysis (Figure 4.23). Over 95% of the observed $|u'|$ values between $\sim 250 - 300$ m fall between 0 and 6 cm s^{-1}, with mean, 25th and 75th percentile velocities of 1.8, 0.7 and 2.6 cm s^{-1}, respectively (exact ADCP depth bins are quoted in the caption; also shown as horizontal lines in Figures 4.24, 4.25). This depth range spans the region over the ridge where the $27.73 - 27.74$ kg m^{-3} isopycnals commonly pinch together (e.g., Transect 4; Figure 3.16c). Only velocities between days $20 - 100$ are considered, as this is the ice-free period over which the same processes are thought to occur. Consequently, the sensitivity analysis applies

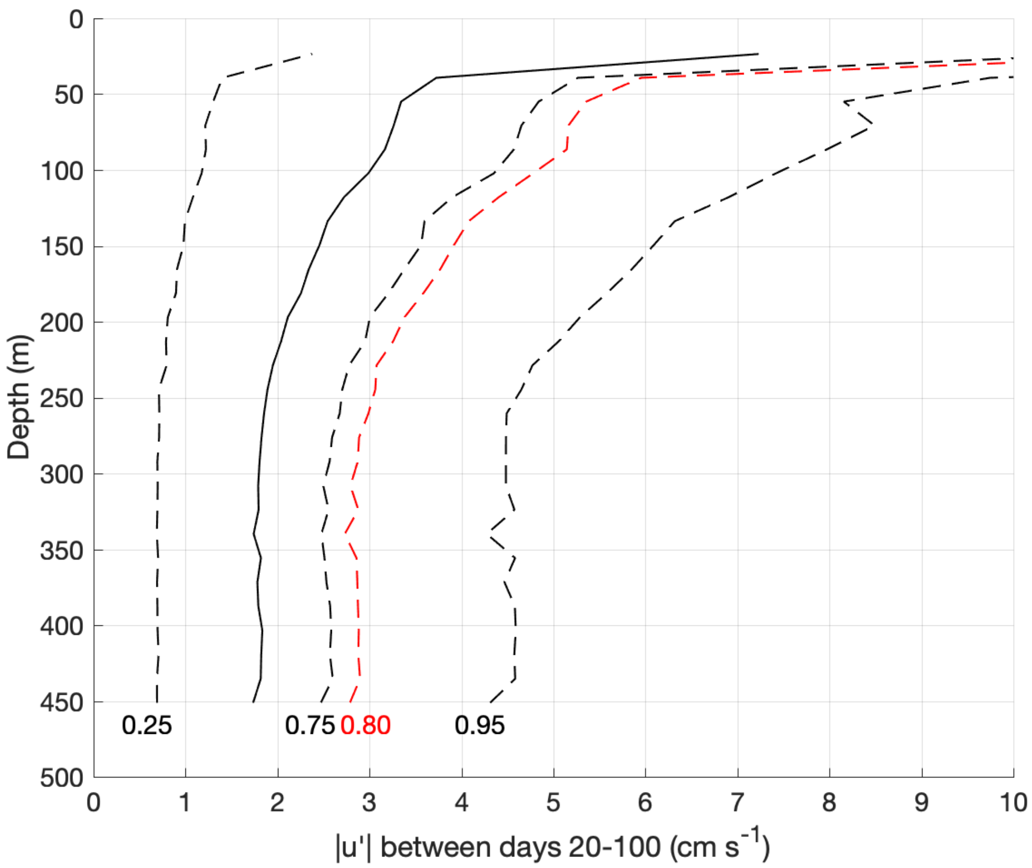

FIGURE 4.23: Mean absolute velocity depth profile between days 20 – 100. Absolute velocities between 245 – 308 m (corresponding to the ADCP depth bins) are relatively constant at 1.8 cm s^{-2}. The 25, 75, 80 and 95th percentiles are also shown.

constant velocities between 0 and 6 cm s^{-1} across the length of the transect. ADCP velocities below 250 m depth are relatively constant, so here $u_1 = u_2$; note that setting $u_2 > u_1$, as may be expected over the ridge, only acts to increase the composite Froude numbers (not shown).

The composite Froude number analysis requires assignment of a constant density to each of the two layers within the equation. Since the data is continuous, there is no rigorous way to choose these layers, so the isopycnals selected are those most reminiscent of hydraulic control, pinching over the ridge and steeply sloping in its lee, and that still have significant layer thicknesses at the mooring location (e.g., > 50 m in Transect 4; Figure 3.16c). Consequently, the 27.735 and 27.74 kg m^{-3} isopycnals are selected as the upper bounds for each of the two layers, and the layer thicknesses are calculated from the density field of each glider transect (Figure 4.22). The layer thicknesses are then used, in conjunction with the velocities mentioned above, to generate G^2 values along the A-B Transect for each glider transect (Figures 4.24, 4.25). In Transects 2 – 9, composite Froude numbers greater than 1 are generated at the mean velocity and between

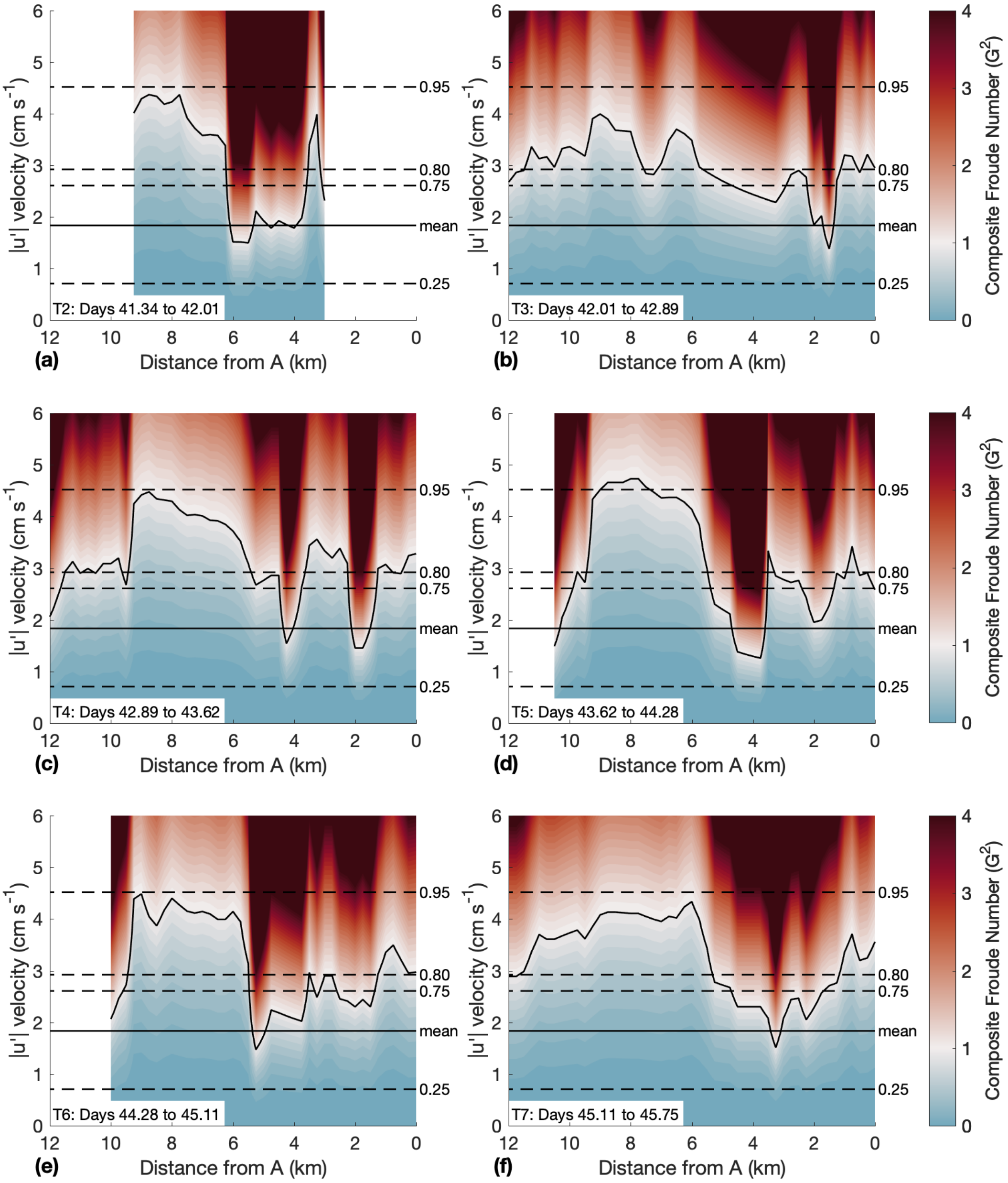

FIGURE 4.24: Composite Froude number sensitivity analysis, using layer thicknesses from Transects 2 – 7. The black contour depicts 1, the critical Froude number. The mean absolute velocity between 245 – 308 m (corresponding to the ADCP depth bins) and days 20 – 100 is overlain, along with the 25, 75, 80 and 95th percentiles. Contours are in 0.1 increments from 0 to 4.

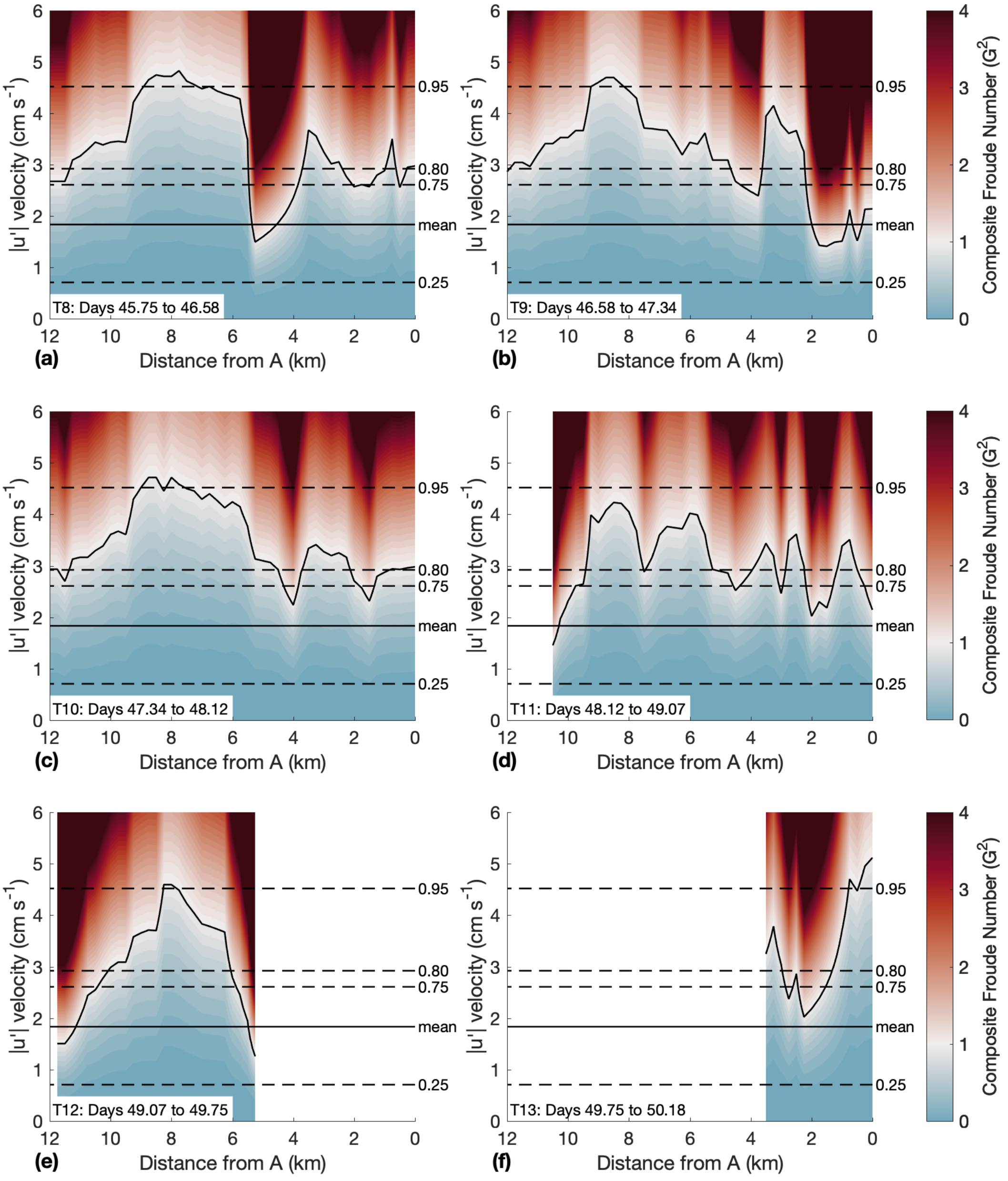

FIGURE 4.25: Composite Froude number sensitivity analysis, using layer thicknesses from Transects 8 – 13. The black contour depicts 1, the critical Froude number. The mean absolute velocity between 245 – 308 m (corresponding to the ADCP depth bins) and days 20 – 100 is overlain, along with the 25, 75, 80 and 95th percentiles. Contours are in 0.1 increments from 0 to 4.

$\sim 1-6$ km along the section. For example, in Transect 4 G^2 values of ~ 1.5 and ~ 4 were produced at 1.75 and 4.25 km along the section. With downstream Froude numbers in the basin (e.g., between $\sim 5.75-9.25$ km) being below 1 at mean velocities and for all transects, this indicates a transition from super- to sub-critical flow, and suggests that the flow over the ridge into Ryder Bay could indeed be controlled hydraulically. Transects 10 and 11 do not have Froude numbers greater than 1 at the mean velocity, suggesting that a hydraulic control is perhaps unlikely to form. A combination of a lack of data (e.g., Transects 2 and 13) and no observed water of ≥ 27.74 kg m^{-3} density, which are required for the calculation of the composite Froude numbers (e.g., Transects 2 and 12), prevented the generation of G^2 values for portions of some transects. Despite this, at the mean velocity Froude numbers greater than 1 occur at 5.25 km in Transect 12, suggesting that flow could be controlled hydraulically over the ridge. In Transect 13, Froude numbers greater than 1 are not observed at the mean velocity, suggesting that flow over the ridge is less likely to be controlled hydraulically.

It must be reiterated that this analysis is limited, however, the lack of upstream velocities means that the simplest layered theory is the best available option. To assess the sensitivity of this analysis to layer choices, G^2 was recalculated while keeping all inputs the same, but using the 27.72 and 27.74 kg m^{-3} isopycnals, thereby increasing the density difference between the two layers (over the ridge in Transect 4, this is equivalent to a ~ 40 m increase in vertical distance between the two isopycnals). The 27.72 kg m^{-3} isopycnal was selected because it is close to the lightest density thought to be influenced by the hydraulic control (judging by the decrease in depth at ~ 6.5 km in Transect 4; Figure 3.16c). Composite Froude numbers are greatly reduced across the A-B Transect, and larger velocities are required to reach criticality (Figure 4.26). That said, G^2 values > 1 are still found over the ridge (at 1.75 and 4.25 km) and are sub-critical downstream, at velocities marginally greater than the 80th percentile velocity of 2.9 cm s^{-1}. Under hydraulic conditions, velocities increase where the density layers thin and pinch together. Consequently, velocities greater than the mean from the downstream mooring are perhaps actually expected. If velocities are enhanced over the ridge in this way, the likelihood a hydraulic control scenario increases; for example, in Transect 7 (Figure 4.24f), the region of super-critical flow widens from a point at ~ 3.25 km at the mean velocity, to between $1.25-5.25$ km at the 80th percentile velocity.

Although the composite Froude numbers are a way of seeing whether hydraulic control is plausible, they are just one criteria used here to suggest the presence of hydraulically-controlled flow over the ridge. The three criteria are: (i) elevated dissipation; (ii) $G^2 > 1$ at the mean absolute velocity; and (iii) pinching and steeply sloping $27.73-27.74$ kg m^{-3} isopycnals. The temperature transects with dissipation overlain (Figures 3.16 and 3.17 in Chapter 3) show that whilst Transects $9-11$ and 13 do not have elevated dissipation over the ridge, Transects 6 and 8 have small regions of elevated dissipation, and Transects $2-5$, 7 and 12 have larger regions of elevated dissipation over the ridge.

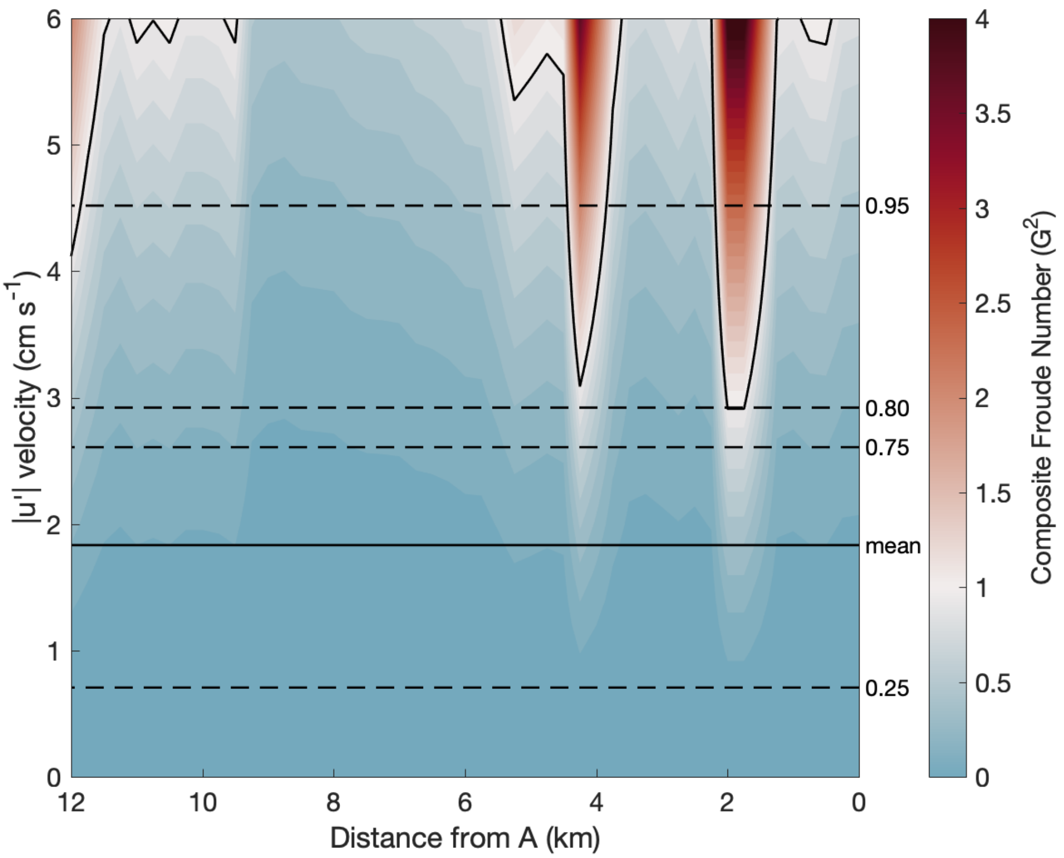

FIGURE 4.26: Composite Froude number sensitivity analysis for Transect 4, using the 27.72 kg m^{-3} and 27.74 kg m^{-3} isopycnals to calculate layer thicknesses. The black contour depicts 1, the critical Froude number. The mean absolute velocity between 245 − 308 m (corresponding to the ADCP depth bins) and days 20 − 100 is overlain, along with the 25, 75, 80 and 95th percentiles. Contours are in 0.1 increments from 0 to 4.

The relationship between the maximum slope of the 27.74 kg m^{-3} isopycnal and the mean dissipation rate in the vicinity of the ridge (defined here as between 2 − 6 km along the section and 245 − 308 m depth - corresponding to the ADCP depth bins) is analysed in Figure 4.27. Transect 12 is excluded from the analysis due to a lack of any water as dense as 27.74 kg m^{-3} recorded at distances $<$ 5.3 km along the A-B section, however, large slopes do occur in lighter isopycnals (e.g., the 27.72 and 27.73 kg m^{-3} isopycnals), so a hydraulic control is still thought to be possible in this transect. If flow was controlled hydraulically, a large isopycnal slope is expected to coincide with high dissipation estimates above the ridge. In contrast, when the flow is not controlled hydraulically, isopycnals above the ridge are expected to be flat, with lower dissipation estimates. The MATLAB fit function is used to fit a 1st order polynomial to the maximum slopes in Figure 4.27, using the linear least-squares method and equal weighting (i.e., it is assumed that there are no outliers). There are 10 transects in the calculation and 2 polynomial coefficients, giving 8 degrees of freedom in the error. Adjusting for

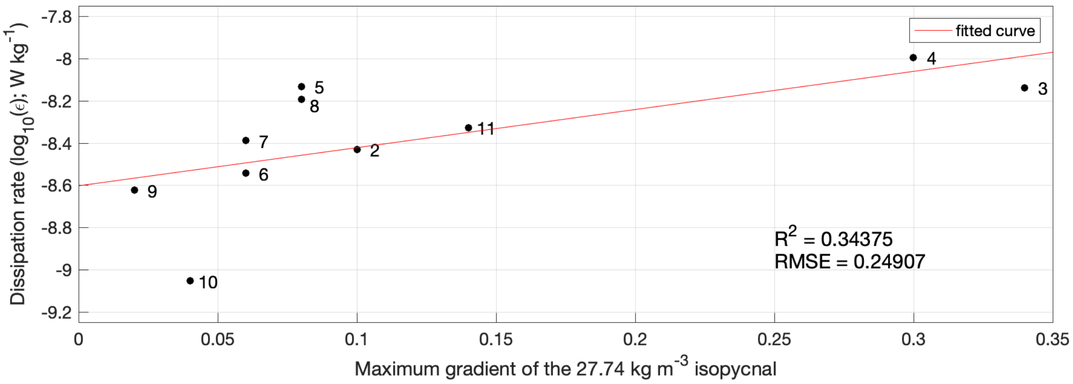

FIGURE 4.27: Correlation between the maximum slope of the 27.74 kg m^{-3} isopycnal in the vicinity of the ridge (between $2-6$ km) and the mean dissipation rate in this region at depths between $245-308$ m (corresponding to the ADCP depth bins), using Transects $2-11$ (labels). Red line shows the fitted linear polynomial curve, solved using the linear least-squares method.

the degrees of freedom gives $R^2 = 0.34$, with an $RMSE = 0.25$ (where the RMSE is an estimate of the standard deviation of the random component in the data; closer to 0 suggests the fit useful for prediction). This loosely supports the suggestion that there is a relationship between isopycnal slope and dissipation, though a greater number of estimates are required to make this statistically-significant. It is worth noting, however, that the Froude number analysis for Transects 9 and 10 suggests that flow is not controlled hydraulically, and these transects also had the lowest maximum slopes (0.02 and 0.04) and dissipation estimates (2.4×10^{-9} W kg^{-1} and 8.8×10^{-10} W kg^{-1}). Meanwhile, Transects 3 and 4 (during which flow is expected to be controlled hydraulically) had the highest maximum slopes (0.34 and 0.30) and dissipation estimates (7.3×10^{-9} W kg^{-1} and 1.0×10^{-8} W kg^{-1}). Additionally, although the slope and dissipation rate for Transect 11 appear to agree with the trend, the maximum slope occurs at $\sim$ 3 km, and is part of a structure that is clearly not reminiscent of a hydraulic control, highlighting the need to look at the overall density structure.

Synthesising the analyses of dissipation, isopycnal slope and the Froude number sensitivity using the 27.735 and 27.74 kg m^{-3} isopycnals, reveals that dissipation in seven of the eleven complete transects is likely controlled hydraulically (64%). This demonstrates that the deep elevated dissipation is a consistent feature. The location of the pinching and steeply sloping isopycnals varies between these transects, and the location of the elevated dissipation changes accordingly. This likely represents a shift in the position of flow criticality (due to variable flow speeds), moving the region of supercritical flow and elevated dissipation rates accordingly. To analyse this in more detail, the relationship between the location of the maximum 27.74 kg m^{-3} slope along the A-B Transect and the alongshore (u') velocities was assessed (not shown). Variation in the location along the transect was observed, however, no discernible relationship with

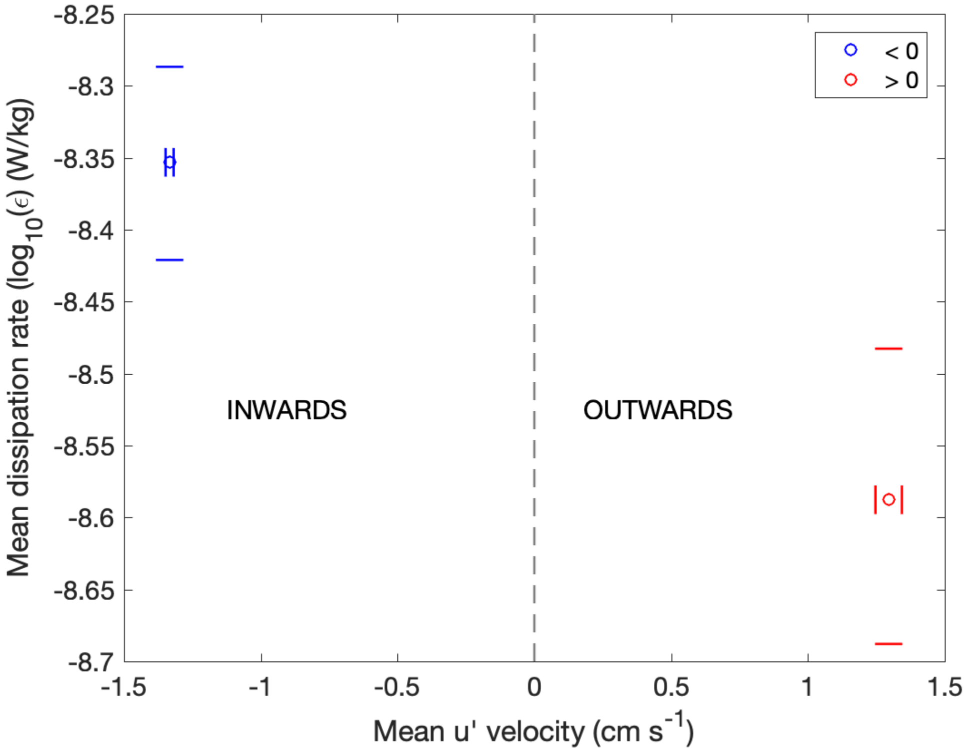

FIGURE 4.28: Comparison of the mean dissipation rates over the ridge when the u' velocity is positive and negative. The area used in the calculation is between $245 - 308$ m (corresponding to the ADCP depth bins) and $1.3 - 5.4$ km along the section (for the dissipation). 90% bootstrapped error bars are shown, calculated using 1000 bootstrap datasets.

velocity was found. This is perhaps due to velocity measurements being downstream in the basin - upstream velocity data are needed for an accurate analysis. Taken alongside the scant evidence for internal tidal control of dissipation at this ridge, the analysis here suggests that hydraulic control is likely to be a key mechanism in determining the observed deep dissipation within Ryder Bay. The implications of this result for the vertical heat fluxes in Ryder Bay is discussed in greater detail in Section 4.6.2.

Further analysis supports the suggestion that dissipation over the ridge at Ryder Bay's entrance is controlled hydraulically. Figure 4.28 compares the mean dissipation rates between $245 - 308$ m depth and $1.3 - 5.4$ km along the section, during periods of positive and negative mean u' velocity (using the same depth range). Under a hydraulic control scenario, flow over the ridge is expected to be into the bay (in the negative u' direction). The mean inflow velocity is 1.3 cm s^{-1}, and the corresponding mean dissipation estimate is 4.4×10^{-9} W kg^{-1}. This is statistically different than mean dissipation for periods when flow is out of the bay and a hydraulic control is not expected (the error bars do not overlap). The mean outflow velocity of these periods is 1.3 cm s^{-1} and the dissipation is 2.6×10^{-9} W kg^{-1}. Therefore mean dissipation estimates are ~ 1.7 times larger when the flow immediately above the ridge is into the bay.

4.6 Summary and Discussion

This chapter has explored the mechanisms behind the three key temporal features found in Chapter 3: (i) variations in the thermocline depth; (ii) basin-wide dissipation at the thermocline; and (iii) deep dissipation over the ridge. Synthesising the analysis above, the proposed mechanisms for this observed temporal variability are discussed next (Figure 4.29), and their likely contribution to Ryder Bay's heat budget is assessed.

4.6.1 Proposed Mechanisms Regulating Hydrography and Dissipation

4.6.1.1 Thermocline Depth - Wind-Induced Coastal Upwelling / Downwelling

The observed shoaling followed by sudden deepening of the thermocline between Transects 10 and 12 (days 47 and 49, respectively; Figures 3.17c,e) is interpreted here as coastal upwelling (Figure 4.29a) followed by downwelling (Figure 4.29b) on Ryder Bay's southern boundary. This occurred in response to south-westward and north / north-westward wind events centered around days 39 and 44. This interpretation is supported by the mixed layer slab model, which predicts upper layer velocities that are conducive to Ekman upwelling and downwelling in response to the Day 39 and 44 wind events (Figure 4.4).

Wind stress magnitude and direction are seemingly important for the spin up of this bay-scale circulation, with both events coinciding with strong winds of > 25 m s^{-1} over a period of ~ 3 days, and low wind direction variance (Figure 4.2b). The Day 39 and 44 wind events were therefore able to drive sustained surface Ekman layer flow towards Ryder Bay's northern and southern boundaries, respectively, and acted over a sufficiently long time to initiate a deep opposing flow at depth (through mass conservation). This lower-layer response occurred ~ 3 days after the start and end of the respective wind events, in line with previous estimates of wind-induced upwelling time scales of $2 - 7$ days within Ryder Bay (Wallace et al., 2008). The longer lower-layer response to the Day 44 wind event (i.e from the end of the event rather than the start) could be associated with the stalling and reversal of upwelling on the bay's southern boundary. This is reflected in the mean 200 m temperature data; the temperature steadily increases, stabilises, and then rapidly decreases on day 48 (Figure 4.5c). The rate of downwelling on day 48 may have been invigorated by the south-westward winds on day 47 (Figure 4.2a) which, due to their strength and low variance, must have induced large upper-layer flow with a similar alignment to the winds to penetrate deeper into the water column (not shown). Although strong south-westward winds similar to those of the Day 39 wind event are observed after day 46 (Figure 4.5a), the lack of an upwelling signal (Figure 4.5c) may relate to the large variability in flow direction, with most days possessing elevated circular variance from day 50 onward (Figure 4.2b).

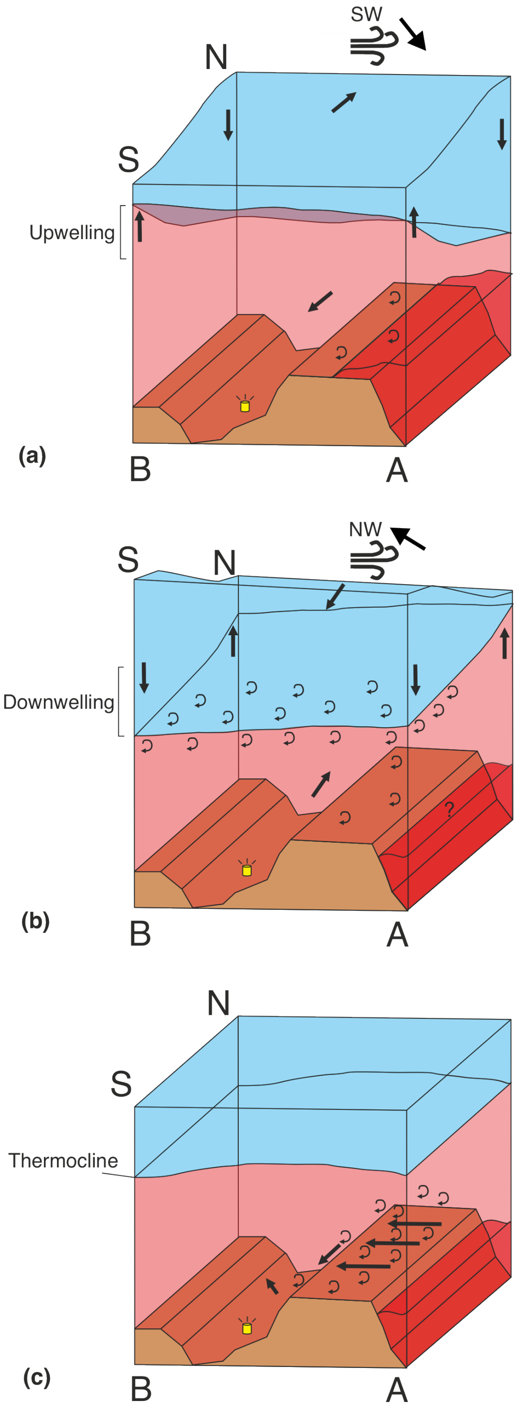

FIGURE 4.29: Three-stage schematic showing the processes proposed to explain the observed dissipation patterns within Ryder Bay. Mechanisms are in the order discussed in the text. Straight arrows show flow direction; curly arrows represent enhanced dissipation; yellow symbol shows the ADCP mooring. (a) South-westward winds drive flow towards the bay's northern boundary above the pycnocline, and towards the southern boundary at depth, leading to upwelling on the southern side of Ryder Bay, as recorded by the ADCP mooring. (b) North / north-westward winds have the opposite effect, driving southward flow above the pycnocline and northward flow at depth, leading to downwelling on the southern side of Ryder Bay. Following downwelling, winds rotate anticlockwise and generate near-inertial shear and dissipation at the base of the thermocline. (c) Hydraulic control causes faster flow over the ridge leading to enhanced dissipation.

4.6.1.2 Thermocline Dissipation - Wind-Generated Near-Inertial Shear

Dissipation rates within the thermocline ($105 - 205$ m) are believed to be to be significantly controlled by wind-induced near-inertial shear (Figures 4.16 and 4.29b). In particular, the basin-wide dissipation event on day 49 (Transect 12; Figure 3.17e) is ascribed to strong wind stress on day 47 (red arrow; Figure 4.16a). This interpretation is supported by the statistically-significant correlations between the 4-day low-pass filtered wind stress and near-inertial thermocline shear ($R = 0.92$, $p \ll 0.001$; after a 1.7-day lag-adjustment), and between the thermocline shear and dissipation before day 41.25 ($R = 0.38, p = 0.01$). Although the correlation after day 43.5 is only significant to the 10% level ($R = 0.24, p = 0.06$), wind-driven near-inertial shear is believed to be the primary control for thermocline dissipation, since other possible mechanisms, such as CTWs and basin-scale wave modes, do not appear to be important within Ryder Bay (as shown in Section 4.4.2). Additionally, the 1.7-day lag is similar to that documented by Forryan et al. (2015), and supports their proposition that undocumented frontal-scale processes must efficiently inject near-inertial shear into the ocean interior. The interpretation is also supported by the mixed layer slab model, which predicted high near-inertial velocities and negative energy fluxes (promoting shear and dissipation) in response to strong wind forcing (D'Asaro, 1985).

Differences between near-inertial shear and dissipation at the thermocline may be due to both spatial variability and the presence of super-inertial shear. Even within the $105 - 205$ m layer, there is still a spatial pattern in the dissipation, with elevated dissipation over the ridge compared to above the basin. Differentiating between this spatial pattern and the temporal control associated with wind-induced shear is not possible with the data available in this study. This could explain the high dissipation between days $41.25 - 43.50$, and the marginal statistical insignificance (at the 5% level) for the correlation after day 43.5. Additionally, storms can also generate super-inertial shear and dissipation, both via the wind working to directly excite super-inertial waves, and via the nonlinear cascade of energy from near- to super-inertial frequencies (Jing et al., 2015). Super-inertial energy could therefore be responsible for other periods of elevated dissipation concurrent with low near-inertial shear away from the ridge; for example, the elevated dissipation spike at the start of day 49 (Figure 4.19). This would suggest that different frequency bands may be important for causing enhanced dissipation at different times.

4.6.1.3 Deep Dissipation - Hydraulic Structure

The elevated dissipation observed above the ridge at depths ≥ 200 m is interpreted here as being, at least in part, controlled hydraulically (Figure 4.29c). This is primarily due to the elevated dissipation consistently occurring at the location of the steepest isopycnals, despite their position relative to the ridge varying with time. This is characteristic of a hydraulic structure translated spatially by changing flow speeds. Although this study lacks upstream velocity measurements, and therefore the calculation can only be indicative, the presence of a hydraulic control is supported by a composite Froude number sensitivity analysis, which exhibits the required transition from super- to sub-critical flow moving over the ridge into the basin in multiple transects (Figures 4.24 and 4.25). This occurs over a range of possible velocities, including those similar to the overall mean (1.8 cm s^{-1}), the day 45 mean barotropic u' velocity ($\sim$ 2 cm s^{-1}), and the 80th percentile (2.9 cm s^{-1}). A transition from super- to sub-critical flow is still generated when using larger density differences in the calculation, although higher velocities are required to reach criticality (Figure 4.26).

While internal tides commonly form hydraulic structure and cause elevated dissipation over topography (e.g., Klymak and Gregg, 2004; Gregg and Klymak, 2014), reconstructed K_1O_1 tidal velocities into and out of the bay are negligible (alongshore, u'; Figure 4.21c), in line with previous observations of weak tides in Ryder Bay (e.g., Wallace et al., 2008; Brearley et al., 2017). This suggests that internal tides are not responsible for the formation of a hydraulic structure over the ridge. Cross-shore K_1O_1 velocities are larger and could have a role in controlling dissipation, particularly during the spring / neap maximum when they can dominate barotropic flow (Figure 4.21c). However, the orientation of these tides (down the length of the ridge) is not conducive to a hydraulic control scenario, and elevated dissipation is observed throughout the deployment, at different stages of the spring / neap tidal cycle. This suggests that other processes are likely at play. For example, the role of wind-driven Ekman upwelling / downwelling in driving the deep dissipation is unknown, but could cause elevated dissipation through increased ridge-flow interaction during times of enhanced deep inflow into the bay. Additionally, the deep flow towards Ryder Bay's southern boundary could induce bottom Ekman flow into the bay, potentially leading to a hydraulic structure and elevated dissipation. Indeed, the lower-frequency variability in the barotropic velocities decreases with the presence of sea ice, suggesting that atmospheric forcing is (at least in part) important. The low-frequency variability could be related to wind-driven changes on the continental slope, either linked to local winds (Dotto et al., 2019), or large-scale wind forcing (Naveira Garabato et al., 2019). Increases in north-eastward wind stress at the shelf break can cause greater along-shelf current velocities (e.g., Graham et al., 2016), and could lead to the formation of more eddies through ACC-topographic interactions (e.g., St-Laurent et al., 2013). Such sub-inertial eddy flows have been observed on the WAP, and in particular in Marguerite Trough (e.g., Moffat et al., 2009), and could be responsible for the low-frequency velocity variation observed at depth in Ryder Bay.

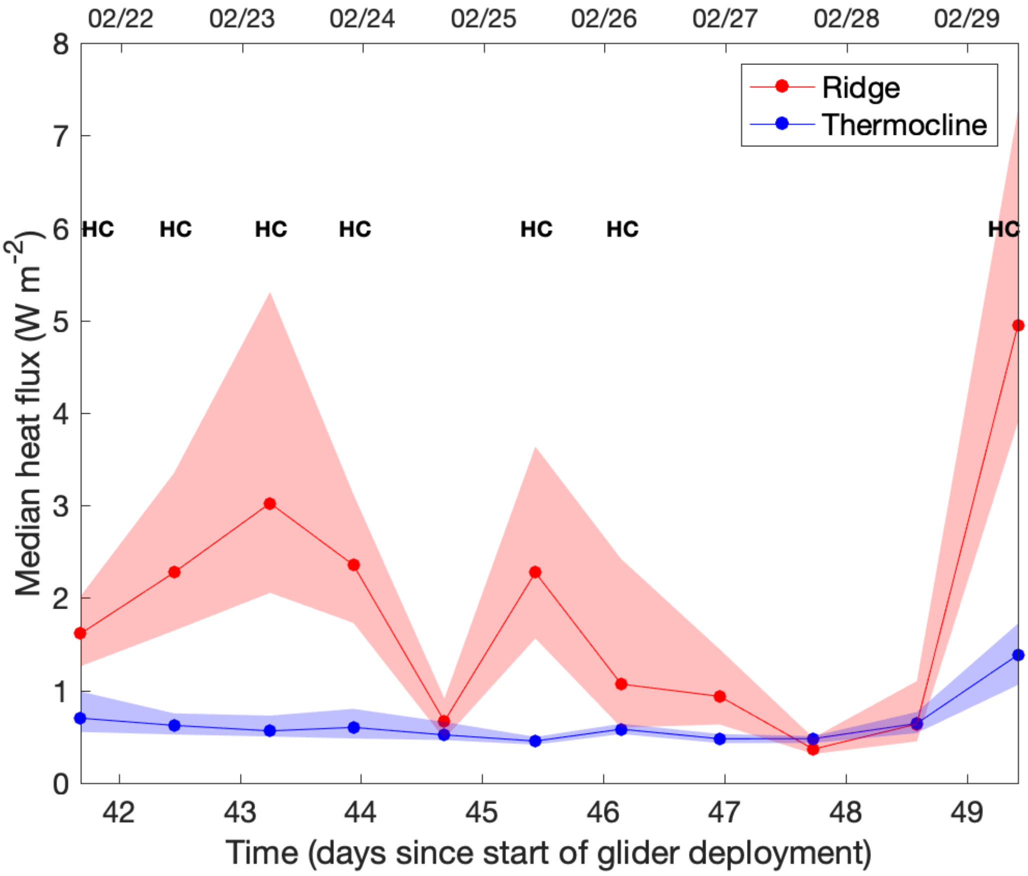

FIGURE 4.30: Comparison of median vertical heat fluxes for Transects 2 – 12 (the complete transects). Deep heat fluxes were calculated at ≤ 200 m and between 1.3 – 5.5 km. Thermocline heat fluxes are calculated over 105 – 205 m depth, across the full length of the section. Shaded regions show 90% bootstrapped errors, calculated using 1000 bootstrap datasets. Transects that meet the three criteria resembling a hydraulic control (HC) scenario, are indicated.

4.6.2 Two-Stage Upward Heat Flux

The contributions of the proposed mechanisms to the heat budget are explored by calculating the upward heat flux, (Q), associated with the deep and thermocline dissipation in each of the complete transects (2 – 12; Figure 4.30), using Equation 3.2. As in Chapter 3, positive Q is upwards, ρ_0 is the reference density (1.025×10^3 kg m^{-3}), and C_p is the specific heat capacity at constant pressure (4000 J kg^{-1} °C^{-1}). Overall, median heat fluxes over the ridge are $\sim$ 3 times greater than in the thermocline. Sloping isopycnals and elevated dissipation reminiscent of a hydraulic control scenario are observed in 7 out of 11 transects (64%); in these cases, the mean median ridge heat flux is 2.4 W m^{-2}, $\sim$ 4 times greater than thermocline fluxes and transects without such features ($\sim$ 0.6 W m^{-2}). These heat fluxes are of a similar magnitude to previous estimates on the WAP shelf (Howard et al., 2004; Brearley et al., 2017).

The disparity between the ridge and thermocline heat flux magnitudes suggests either an accumulation of heat at the base of the thermocline above the ridge, or perhaps more likely, that the heat spreads laterally at this depth, with spatially homogeneous mixing across the thermocline's base at a lower rate but over a larger area. Given the available data, these lateral heat fluxes could not be quantified, so here a crude, one-dimensional order-of-magnitude calculation is conducted. If the ridge heat fluxes associated with a hydraulic structure occur in $\sim$ 60% of the transects (which take approximately a day to complete), over the 6-month spring / summer period (when the proposed mechanisms might be expected) there would be a $\sim$ 22 MJ m^{-2} upward heat flux to the base of the thermocline. Over an unknown area, this heat would then mix across the thermocline into the overlying waters at a slower rate of 0.6 W m^{-2} per day ($\sim$ 9 MJ m^{-2} over 6 months).

Basin-wide thermocline dissipation events, generated by wind-induced near-inertial shear, support periods of intensified mixing. Figure 4.30 shows that the median thermocline heat flux on day 49, the day of the basin-wide thermocline dissipation (Figure 3.17e), is twice as large (1.3 W m^{-2}) as typical values ($\sim$ 0.6 W m^{-2}). This suggests that strong winds events like that observed on day 47 (red arrow; Figure 4.16a) can cause a widespread release of heat across the thermocline and into the overlying cooler waters. Day 49, ridge heat fluxes are especially elevated, however, given the available data it is not possible to attribute this to a single mechanism. Additionally, the Ekman coastal upwelling / downwelling processes discussed here are important because, by altering the depth of the thermocline, they can alter the amount of heat readily available for wind- and ridge-induced vertical mixing.

Chapter 5

Three-dimensional Structure of a Cold-Core Arctic Eddy Interacting with the Chukchi Slope Current

The work in this chapter contributed to the following published paper:
Scott, R. M., R. S. Pickart, P. Lin, A. Münchow, M. Li, D. A. Stockwell, and J. A. Brearley, 2019: Three-dimensional structure of a cold-core arctic eddy interacting with the chukchi slope current. *Journal of Geophysical Research: Oceans*, **124 (11)**, 8375–8391.

5.1 Introduction

Whilst chapters 3 and 4 focus on vertical mixing estimates on the WAP shelf, this chapter switches focus to the Arctic Ocean. This chapter studies a major feature thought to be important for shelf-ocean exchange in the polar regions: eddies.

Eddies are found throughout the Arctic Ocean's water column (e.g., Carpenter and Timmermans, 2012; Zhao et al., 2014; Zhao and Timmermans, 2015). As outlined in Chapter 1, halocline eddies are particularly important because they can influence the stratification at the depth of the cold halocline. Halocline stratification must be maintained in order to prevent warm Atlantic water from mixing upwards towards the surface, where it can readily melt sea ice (Carmack et al., 2015). Halocline eddies are ubiquitous in the Canada Basin, the majority of which are cold-core anticyclones with lateral scales on the order of the Rossby deformation radius (between $10 - 15$ km, see Equation 1.1; Zhao et al., 2014). Consequently, such halocline eddies are thought to be an important source of the dense winter water required for ventilating the cold halocline.

Zhao et al. (2014) use ITPs to characterise eddies in the Canada Basin into four groups dependent on their water type: Canadian versus Eurasian, and their core-depth, shallow ($<$ 80 m) versus deep ($>$ 80 m). Eddies in the northern Canada Basin are typically shallow, and are thought to form through baroclinic instability of the hydrographic front between the two water types (Timmermans et al., 2008). Eddies to the south are deep, denser and more saline, and could emanate from one of the two canyons on the Chukchi shelf, or from one of the region's boundary currents (see Figure 1.18). In the canyons, anticyclonic eddies could be produced through side-wall friction (D'Asaro, 1988), flow-topography interactions (Cenedese and Whitehead, 2000; Chao and Shaw, 2003) or baroclinic instability (Pickart et al., 2005). Along the shelf in the Chukchi and Beaufort Seas, the shelfbreak jet is baroclinically unstable and is believed to readily form anticyclonic eddies with the same characteristics as observed in the Canada Basin (Spall et al., 2008).

While anticyclonic cold-core eddies have been observed extensively in the Canada Basin, most notably using the ITP database, to date there have been no surveys revealing the full three-dimensional structure of one of these features. In addition, at the time of the study, no other work had investigated the role of the Chukchi Slope Current in either generating or influencing the eddies (more recently, Boury et al. (2020) investigate the influence of eddies on the Chukchi Slope Current). This Chapter presents a high-resolution shipboard survey of a cold-core anticyclonic Pacific water eddy that was collected in September 2004. The feature was situated on the Chukchi continental slope to the northwest of Barrow Canyon (see Figures 2.33, 2.34 and 2.35), adjacent to the seaward edge of the Chukchi Slope Current. The eddy, and its surrounding waters, was mapped using a combination of expendable probes, lowered instrumentation, and underway sensors (a description of the data is found in the Data and Methodology chapter, Section 2.2). The uniform horizontal grid spacing in both longitude and latitude (0.02° and 0.01°, respectively) provided an unprecedented three-dimensional view of the feature. Sections 5.2 and 5.3 analyse the eddy's water mass, and kinematic and dynamical structure, respectively. Section 5.4 is a summary and discussion about the interaction between the Chukchi Slope Current and the observed eddy.

5.2 Eddy Hydrographic Characteristics

Cross-slope vertical sections of temperature (Figure 5.1) and salinity (Figure 5.2) from the XCTD grid (Figure 2.35) show a clear progression through the eddy. The survey reveals that the feature was a cold-core eddy centred vertically near 150 m depth, embedded within the halocline, roughly confined to the density layer $26.4 - 27.2$ kg m^{-3}. Moving towards the eddy centre, the temperature and layer thickness decreases and increases, respectively. On the western side (Transect 6, Figure 5.1) there is only a slight widening of this density layer, corresponding to a lens of cold water < -1.6 °C, approximately 45 m thick and centred laterally near a meridional distance of 20 km. Near the eddy centre (Transect 2, Figure 5.1), core temperatures reach -1.77 °C, and the layer thickness doubles to $\sim$ 90 m. On the eastern side of the feature (Transect 3, Figure 5.1) the cold layer is only $\sim$ 30 m thick and there is little to no widening of the density layer. At these cold temperatures, the density is dictated by salinity and only transects close to the eddy centre show a noticeable signature of the isohalines (transects 4, 2 and 1; Figure 5.2), which spread apart from the core absolute salinity of 33.3 g kg^{-1}. This core value corresponds to the upper portion of the cold halocline in the southern Canada Basin (Melling, 1998; Pickart, 2004).

The cold water within the eddy corresponds to NVWW, which is formed via convection in the Bering Sea (e.g., Muench et al., 1988) and Chukchi Sea (e.g., Pickart et al., 2016), and is colder than -1.6 °C and saltier than 31.5 (e.g., Pisareva et al., 2015; Corlett and Pickart, 2017). NVWW flows through the Bering Strait approximately between January to April (Woodgate et al., 2005). The other type of winter water is RWW, which is NVWW that has warmed either by mixing or via solar heating to temperatures between -1.6 to -1 °C (Gong and Pickart, 2016). It should be noted that most of the NVWW is typically flushed off of the Chukchi shelf by late summer (Shroyer and Pickart, 2019; Pickart et al., 2019).

The CTD section through the centre of the cold-core eddy (Figure 2.35, magenta squares) provides additional information about the feature (Figure 5.3). Transmissivity within the eddy is lower than the surrounding water (Figure 5.3a). Some of this is likely due to suspended sediments since the dense NVWW flows along the bottom of the Chukchi shelf as it progresses northward (prior to eddy formation near the shelf edge). However, the elevated values of fluorescence (Figure 5.3b) and dissolved oxygen (Figure 5.3c) indicate recent biological activity. It is well documented that primary production on the Chukchi shelf is strongly tied to the presence of winter water (e.g., Lowry et al., 2015, 2018). This is because winter waters are generally high in nutrients. In fact, the NVWW has the highest levels of nitrate on the Chukchi shelf during early summer (Pickart et al., 2016). The eddy also contained elevated levels of nitrate sufficient to spur primary production (Figure 5.3d). However, the depth of the core was well beneath the euphotic zone (typically < 25 m at this time of year), implying that photosynthesis completely ceased once the eddy left the edge of the shelf and descended to its equilibrium depth.

The lack of photosynthesis is consistent with the low levels of chlorophyll within the eddy (not shown), while there was an enhanced phaeopigment signal (Figure 5.3e). This implies that the chlorophyll cells in the feature were either dead and or in the process of dying, which is expected when nutrients are drawn down, or, in this case, the access to sunlight is cut off. It should be noted, however, that phaeopigments do fluoresce, which would account for the signal in Figure 5.3b. Using radium isotope data,

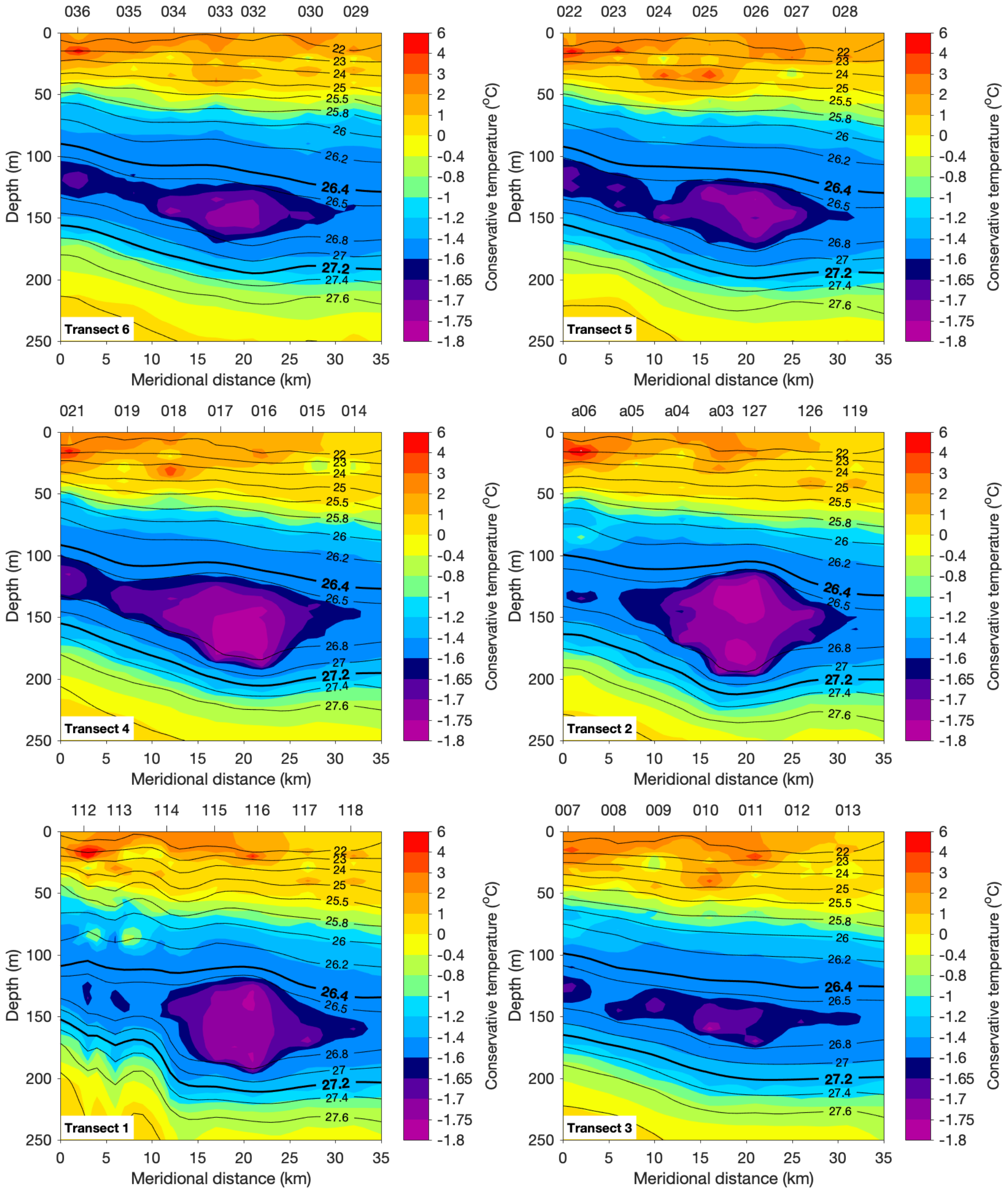

FIGURE 5.1: Vertical XCTD sections of conservative temperature through the eddy, overlain by potential density (contours referenced to the surface, kg m^{-3}). See Figure 2.35 for the locations of the transects. The viewer is looking to the west. Station numbers are marked along the top (Station 119 and transect 1 are CTD stations). The highlighted density contours correspond to the layer averages in Figures 5.8 and 5.12.

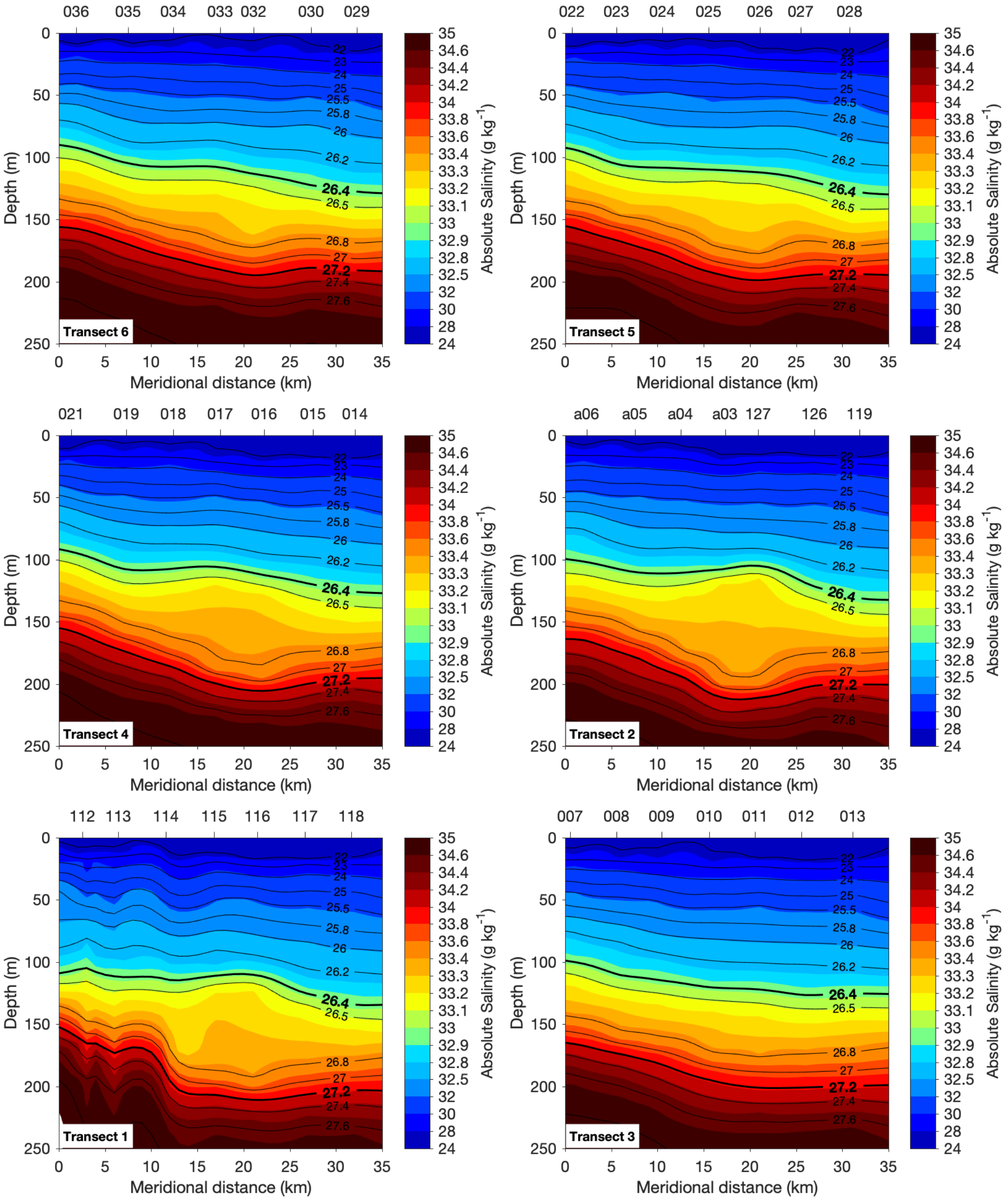

FIGURE 5.2: Vertical XCTD sections of absolute salinity through the eddy, overlain by potential density (contours referenced to the surface, kg m^{-3}). See Figure 2.35 for the locations of the three transects. The viewer is looking to the west. Station numbers are marked along the top (Station 119 and transect 1 are CTD stations). The highlighted density contours correspond to the layer averages in Figures 5.8 and 5.12.

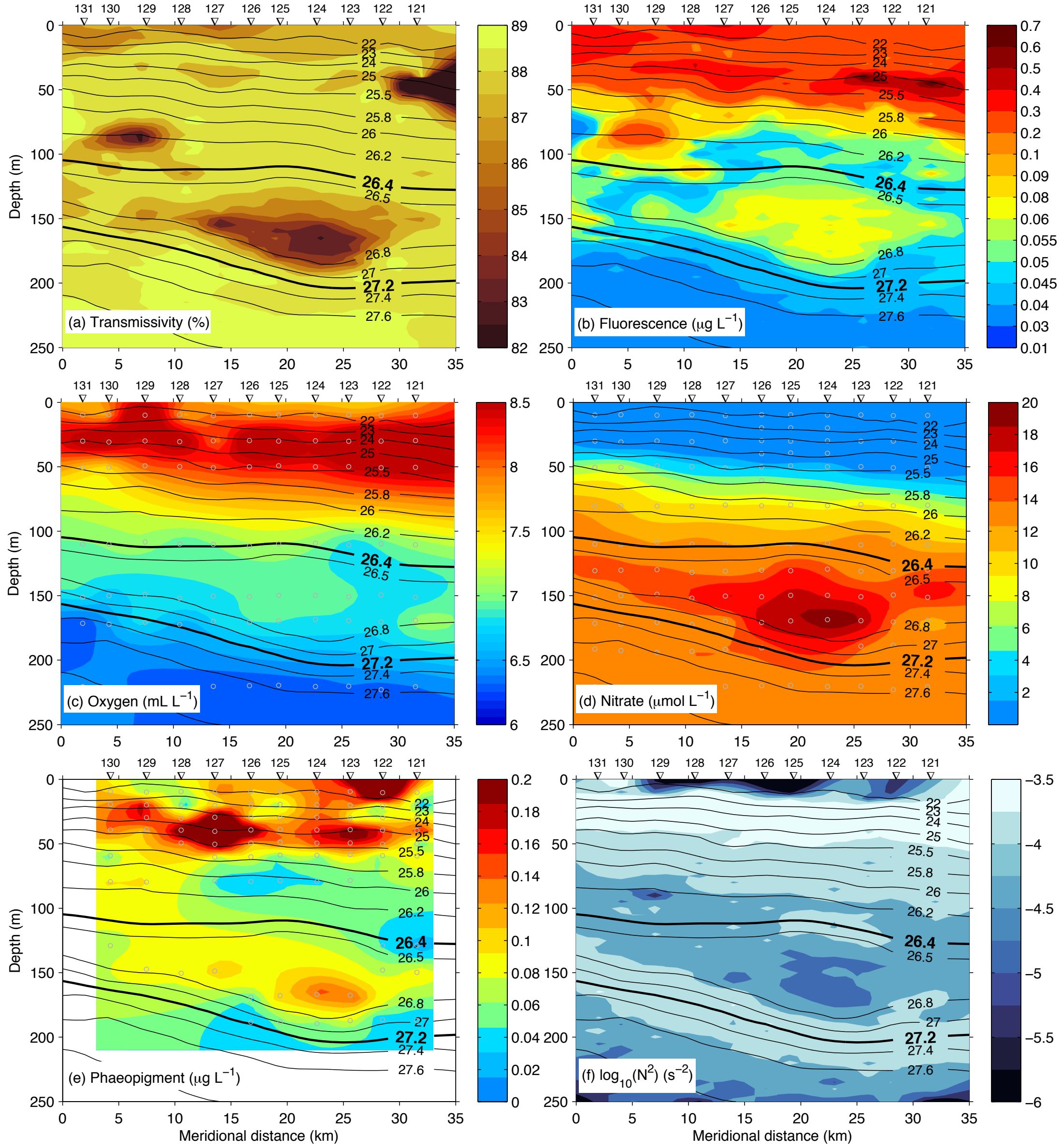

FIGURE 5.3: Vertical sections through the centre of the eddy using data from the CTD and Niskin bottles (see Figure 2.35, magenta squares, for the location of the section). The viewer is looking to the west. Station numbers are marked along the top. In each panel the contours are potential density (kg m^{-3}). The highlighted density contours correspond to the layer averages in Figures 5.8 and 5.12 (a) Transmissivity. (b) Fluorescence. (c) oxygen, where the bottle data points are indicated by the open grey circles. (d) Nitrate. (e) Phaeopigments. (f) Log of the buoyancy frequency squared.

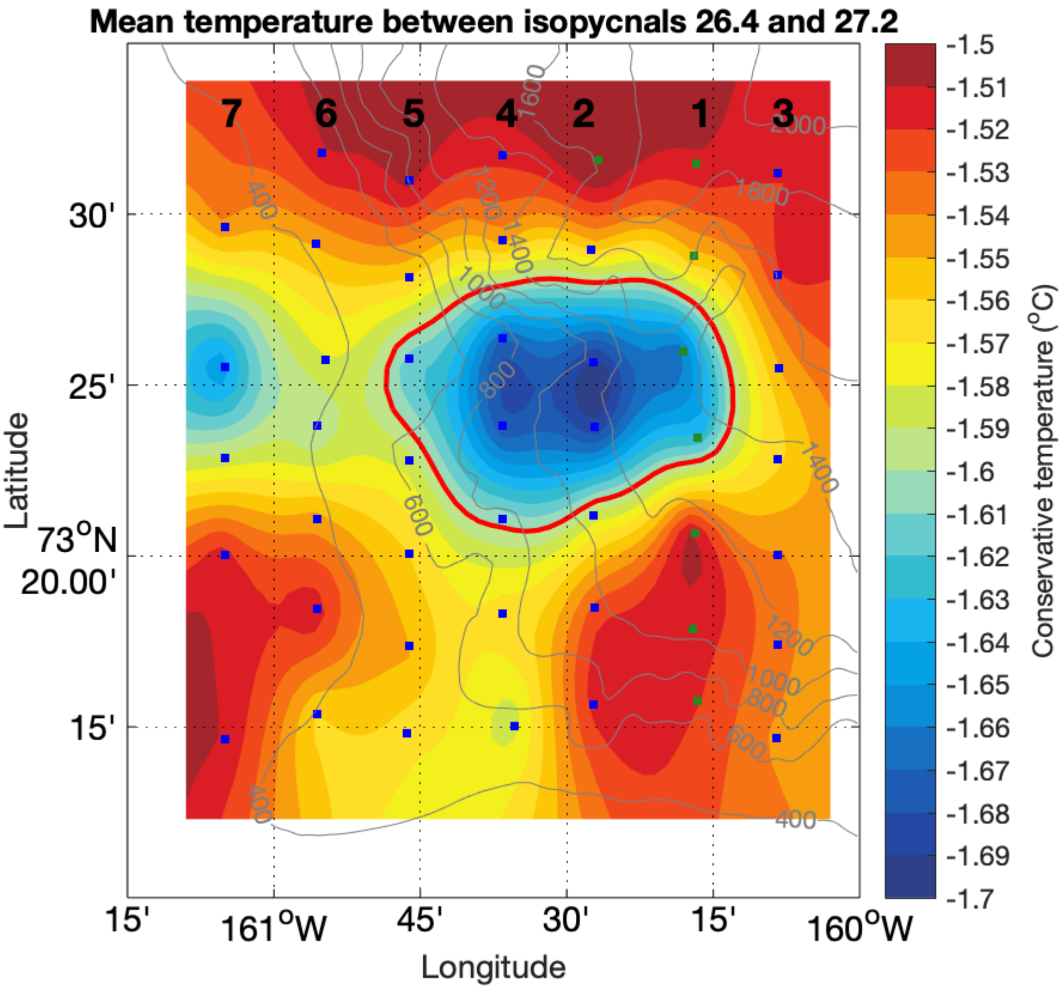

FIGURE 5.4: Conservative temperature averaged within the density layer 26.4 – 27.2 kg m^{-3} (see Figure 5.1 for the location of the layer in the vertical plane). The −1.6 °C contour, taken to delimit the core of the eddy, is highlighted red. The XCTD stations are marked by the blue squares, and the CTD stations are marked by the green squares. The transect numbers are labeled along the top. The bathymetry is from the ship's multi-beam system.

Kadko et al. (2008) estimated the age of the eddy in this study to be on the order of months (i.e. the time since it left the shelf). The chlorophyll to phaeopigment differential observed here is consistent with this timeframe (i.e. significantly shorter than a year; Stockwell, D. A., personal comms., July, 2019). In addition, the weak stratification of the eddy core (Figure 5.3f), and the fact that it contains NVWW, suggests that the water in the feature was ventilated earlier in the year during the winter months, as opposed to the previous winter. This is because NVWW is modified fairly quickly into RWW (Gong and Pickart, 2016). This supports the radium age estimate as well.

A lateral map of the mean temperature within the density layer bounding the eddy (26.4 – 27.2 kg m^{-3}, shown in the vertical sections of Figures 5.1, 5.2 and 5.3) indicates that the XCTD survey completely encompassed the feature (Figure 5.4). The eddy's core, defined here as within the −1.6 °C isotherm, has a quasi-circular shape, with a

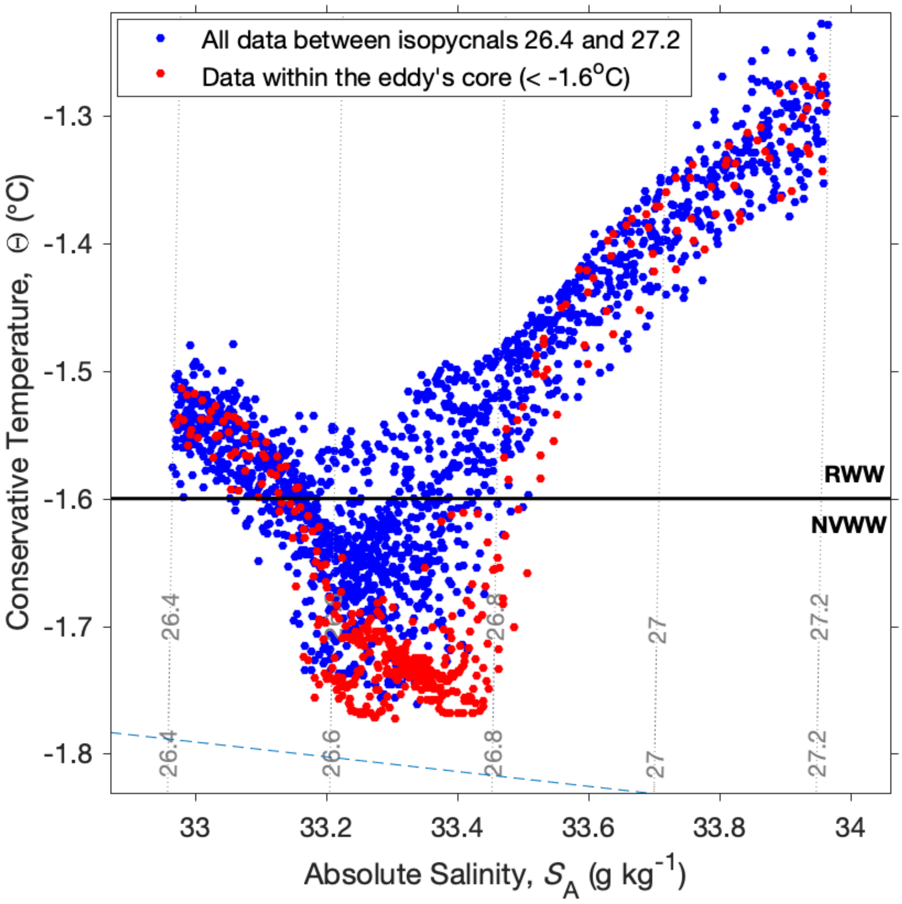

FIGURE 5.5: Conservative temperature-absolute salinity plot for the XCTD/CTD data points within the density layer 26.4 – 27.2 kg m^{-3} (see Figure 5.1 for the location of the layer in the vertical plane). Data are taken from all stations shown in Figure 5.4. The data points within the core of the eddy are highlighted red (see Figure 5.4 for where the core of the eddy is situated). The thin grey lines are contours of potential density (kg m^{-3}). The thick black line shows the division between the newly ventilated winter water (NVWW) and remnant winter water (RWW); see text for details. The freezing point is marked by the dashed blue line.

zonal diameter of ∼ 19 km and a meridional diameter of ∼ 14 km. It is located over the deep continental slope, centred on the 1000 m isobath, roughly 50 km seaward of the shelfbreak. The water surrounding the eddy displays some patchiness in temperature, particularly to the west and south, which could be a reflection of mixing processes as the eddy spins down. For example, the NVWW to the west (blue region) may have originated in the eddy but been subsequently exchanged with ambient waters (see Section 5.4).

A conservative temperature-absolute salinity diagram characterizes the water in the survey region between the bounding isopycnals of the eddy (Figure 5.5). As noted above, the water in the core of the eddy is NVWW. The coldest water in the eddy is predominantly confined to the density layer 26.6 – 26.8 kg m^{-3}, and at the centre of the

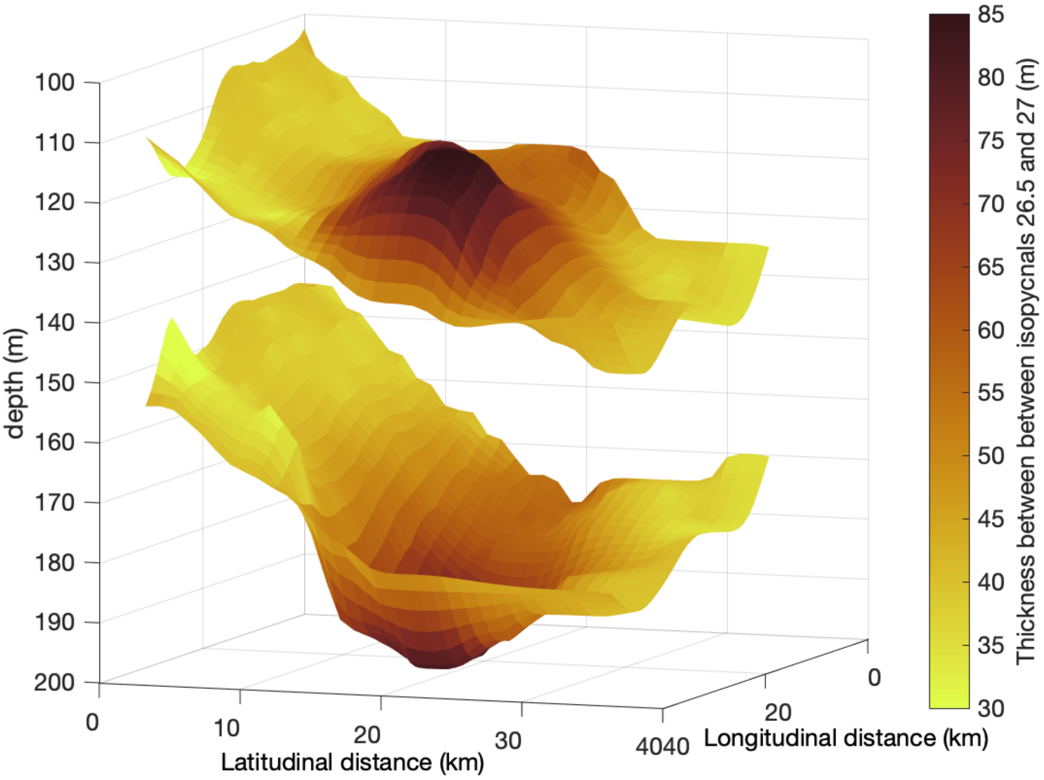

FIGURE 5.6: Three-dimensional view of two isopycnal surfaces, 26.5 and 27 kg m^{-3}, near the top and bottom of the eddy, respectively. The colour corresponds to the thickness of the layer bounded by the two isopycnals.

feature, the temperature is near the local freezing point (−1.8 °C at this salinity). Even outside of the eddy some of the water is NVWW, although most of the surrounding water is slightly warmer RWW, which is the dominant water mass of the cold halocline in the Canada Basin. As the eddy eventually spins down, the anomalously cold NVWW in its core will moderate to RWW.

The rapid, high-resolution XCTD grid enables the presentation of the first three-dimensional view of an Arctic cold-core anticyclone. Figure 5.6 shows the topography of the bounding density layers 26.5 and 27 kg m^{-3} (these surfaces are slightly more restrictive than those used above in order to highlight the deflection of the isopycnals), where the viewer is looking to the southwest. The maximum layer thickness is 85 m, compared to a thickness of 37 m outside of the eddy. Note that the entire feature is slanted in the vertical; i.e. the density surfaces are shallower on the onshore side of the eddy versus the offshore side. This background density tilt is also evident in the vertical sections of Figure 5.1. This gradient is due to the presence of the Chukchi Slope Current, as explained below.

5.3 Eddy Kinematics and Dynamics

Vertical sections of zonal VMADCP velocity (Figure 5.7) capture the eddy's three-dimensional velocity structure and the surrounding flow (see Figures 2.34 and 2.35 for the lateral coverage of the VMADCP data). Unlike Figures 5.1 and 5.2, Transect 5 is excluded here due to very little VMADCP data and instead Transect 7 is shown. Vertical coverage typically extends to between $225 - 250$ m depth, however, coverage in transects 1 and 3 does not extend so deep (indicated using the grey regions; likely due to a lack of scattering particles). In the southern half of each of the sections ($0 - 20$ km), strong westward (negative) flow is observed across the full depth of the sections, with maximum velocities up to 40 cm s^{-1} at depths of approximately 70 m. Given that VMADCP data is commonly noisy, measuring many different types of velocities from near-inertial to Ekman flow (tides have been removed; see Section 2.2.2), it is perhaps surprising how clearly the anticyclonic eddy signature is observed in transects $4, 2$ and 1. Eastward (positive) velocities between $10 - 15$ cm s^{-1} are found north of the eddy centre, at depths of $125 - 225$ m, within and below the $26.4 - 27.2$ kg m^{-3} density range (the same density layer as in Figure 5.4). Similar flow is not observed north of the eddy centre (> 20 km) in transects $7, 6$ and 3, where flow is predominantly westward. Note that VMADCP velocities shallower and deeper than the $\sim 50 - 200$ m depth range are approaching the limits of the survey where the data are noisy and cannot be fully trusted. However, this is acceptable because these regions are not the focus of this study.

Figure 5.8 shows the vertically averaged velocity within the $26.4 - 27.2$ kg m^{-3} density range in relation to the thickness of the layer. The azimuthal anticyclonic flow of the eddy is evident. However, also clear is the asymmetric circulation of the feature, with enhanced flow on the southern side of the eddy versus the northern side. In addition, there is strong flow in both the western (sections 7 and 6) and eastern (section 3) parts of the domain. These aspects of the circulation are due to the fact that the eddy is embedded in the offshore part of the Chukchi Slope Current.

To demonstrate this more clearly, and to be more certain about the physics controlling the observed velocity patterns, Figure 5.9 shows vertical sections of absolute geostrophic velocity (referenced to the surface; see Section 2.2.2, Equations 2.8, 2.9). The azimuthal flow of the eddy is clearly evident in Transect 2 through the centre of the feature (compare to the equivalent temperature section, Figure 5.1, Transect 2). Similar anticyclonic flow is observed to the west (Transect 4) and east (Transect 1) of the central section, with eastward flow also occurring slightly above and below the $26.4 - 27.2$ kg m^{-3} density layer on the western side of the eddy. However, in all of the transects in Figure 5.9, the strongest westward flow is above 50 m in the southern portion of the section; this is the signature of the Chukchi Slope Current. At this time of year the slope current is surface-intensified and extends to $150 - 200$ m depth (Corlett and Pickart, 2017; Li et al., 2019). Based on data from a year-long mooring array across the Chukchi Slope,

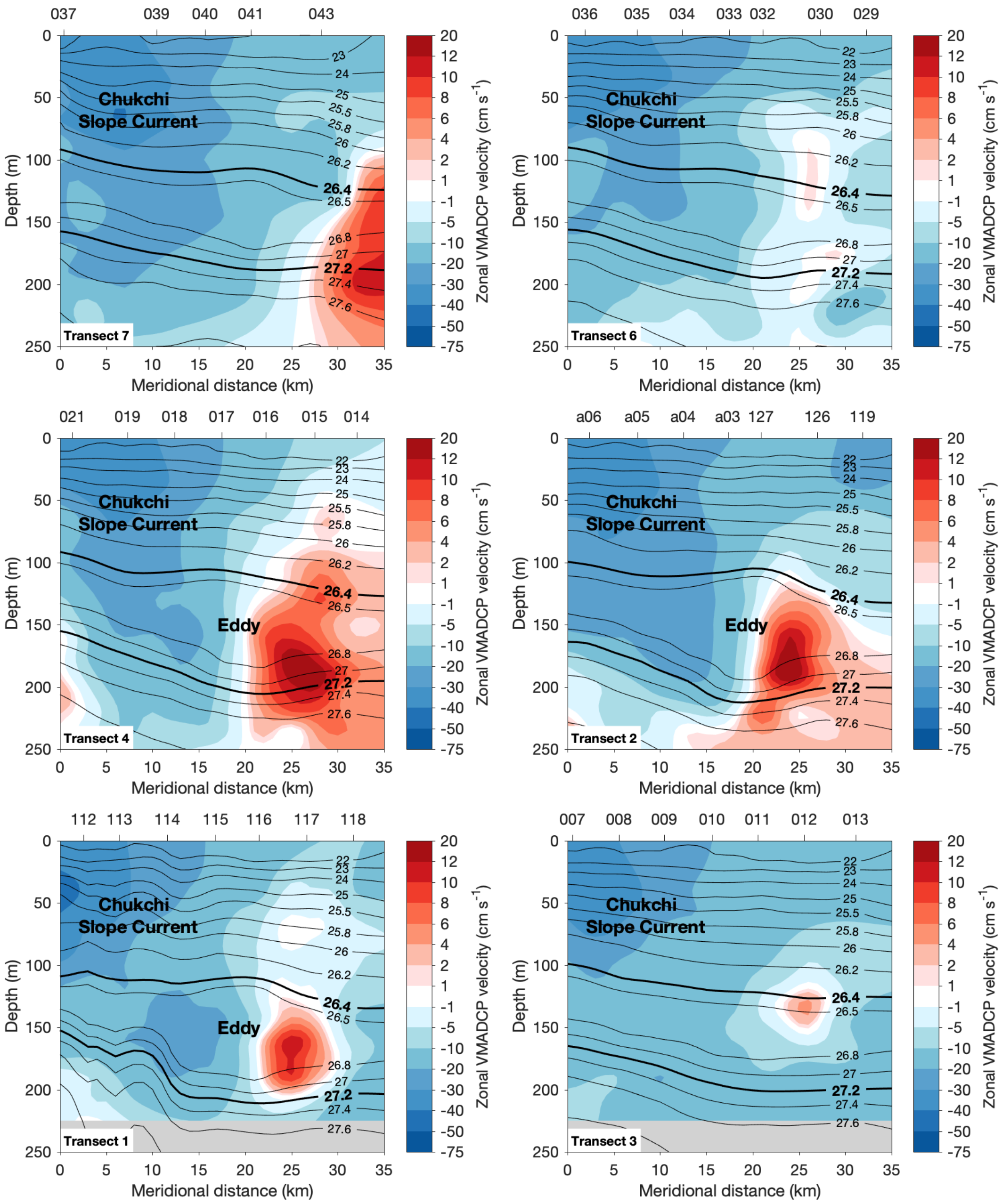

FIGURE 5.7: Vertical sections of zonal VMADCP velocity through the eddy, corresponding to the XCTD sections in Figures 5.1,5.2. Overlain are potential density contours (kg m^{-3}). See Figure 2.35 for the locations of the transects. The viewer is looking to the west. Positive flow is to the east. Station numbers are marked along the top (Station 119 and transect 1 are CTD stations). The highlighted density contours correspond to the layer averages in Figures 5.8 and 5.12. The Chukchi Slope Current is labeled as is the centre of the eddy. Grey regions indicate deep areas without VMADCP data.

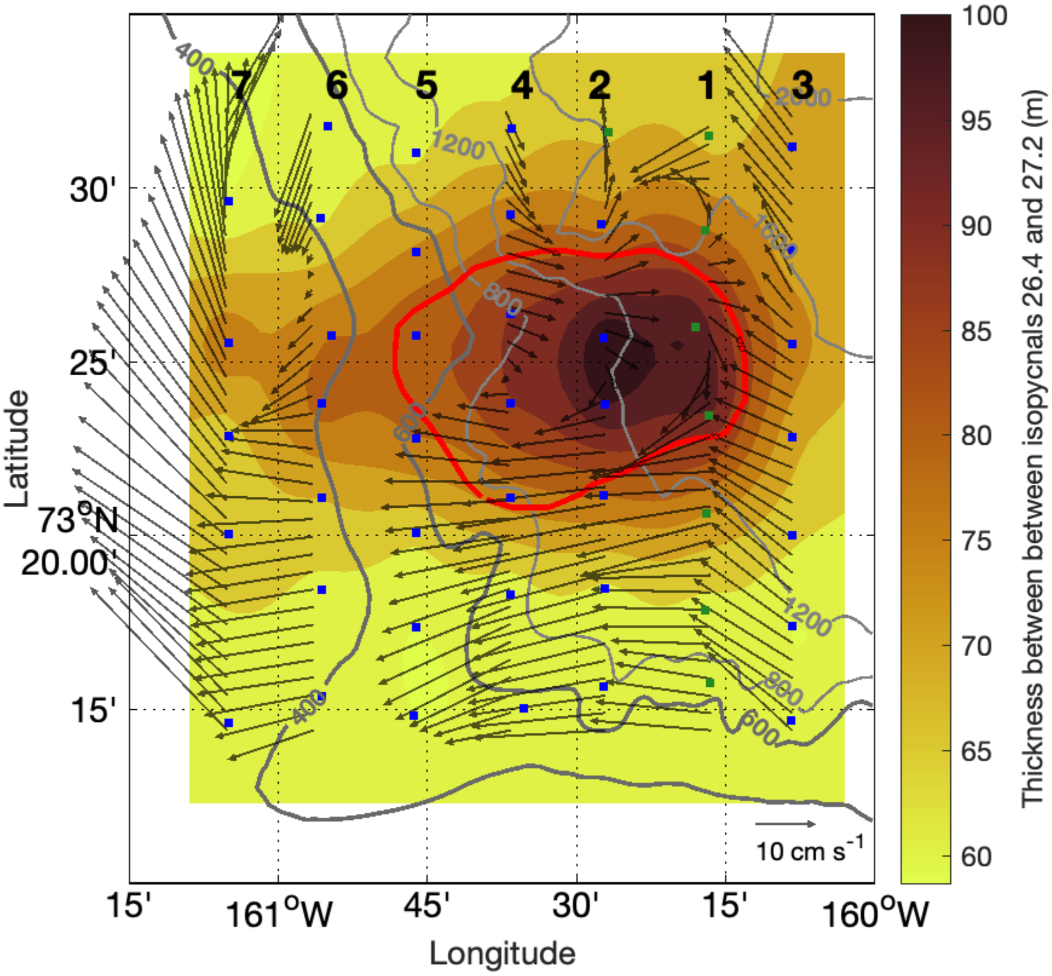

FIGURE 5.8: VMADCP velocity averaged within the density layer 26.4 – 27.2 kg m^{-3} (black vectors; the key is located in the lower right). Velocities from Transect 5 are excluded due to a lack of data in the density layer. The colour represents the thickness of the density layer, and the red line denotes the core of the eddy (see Figure 5.4). The XCTD stations are marked by the blue squares, and the CTD stations are marked by the green squares. The transect numbers are labeled along the top. The bathymetry is from the ship's multi-beam system. The 400 and 600 m bathymetry contours are thicker, highlighting the sharp bend in bathymetry.

the mean transport of the current in early fall is 1.0 ± 0.48 Sv. This compares well to the September survey data presented here; the transport of the slope current in transects 6 and 3 (away from the eddy core) were both 0.83 Sv, where transports were calculated over the domain 0 – 21 km in distance and 0 – 185 m in depth (the approximate boundaries of the slope current in Figure 5.9).

As discussed above, the vertical sections of hydrographic properties for transects 6 and 3, through the western and eastern sides of the eddy, respectively, show relatively little signature in the density field but a clear signal of cold NVWW (Figures 5.1 and 5.2). The

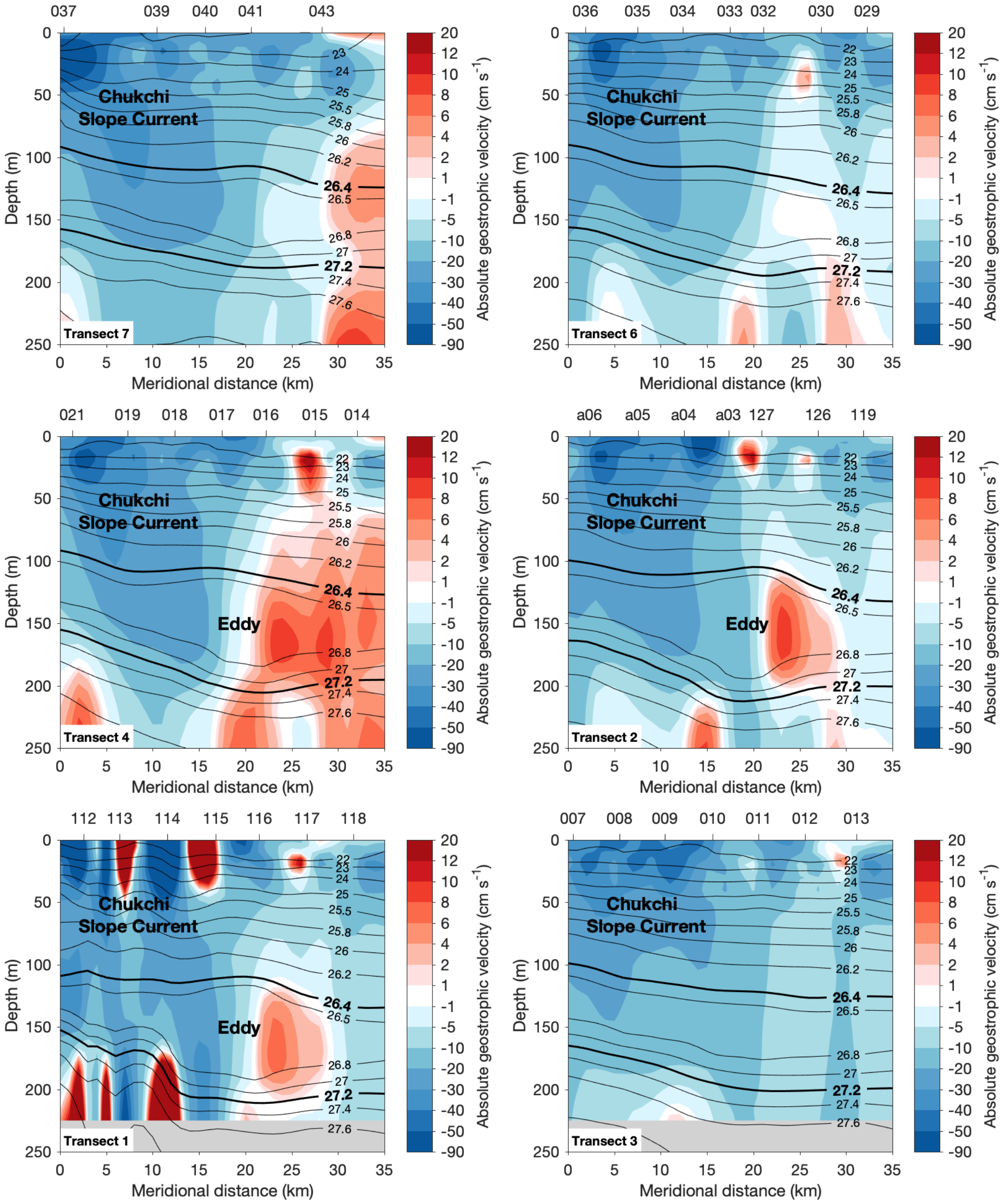

FIGURE 5.9: Vertical sections of absolute geostrophic velocity (colour) overlain by potential density (contours, kg m^{-3}). See Figure 2.35 for the locations of the transects. The viewer is looking to the west. Positive flow is to the east. Station numbers are marked along the top (Station 119 and transect 1 are CTD stations). The highlighted density contours correspond to the layer averages in Figures 5.8 and 5.12. The Chukchi Slope Current is labeled as is the centre of the eddy. Grey regions indicate deep areas without VMADCP data.

absolute geostrophic velocity sections on the two sides of the eddy show a much more muted signal than the central transect (Figure 5.9). On the western side (Figure 5.9, transects 6 and 7) there is just a hint of positive flow on the northern side of the eddy, while on the southern side there is no extremum of negative flow; the flow of the slope current masks any signature of this half of the eddy. On the eastern side (Figure 5.9, Transect 3), one would not notice that there is an eddy signature at all. These sections clearly demonstrate that the eddy is caught in the seaward side of the Chukchi Slope Current. Figure 5.8 indicates that the strong westward flow of the slope current in the southern portion of the domain (transects $1-4$) bends to the northwest on the western side of the domain (transects 6 and 7). This deflection of the slope current is likely in response to the northward diversion of the isobaths due to Hanna Canyon (see Figure 5.8 but also Figure 2.33 for a clearer view of the isobaths).

In order to isolate the velocity signature of the eddy, an attempt was made to remove the signature of the slope current from the VMADCP data. The layer-averaged velocity vectors on Transect 4 (Figure 5.8) display the signature of a Rankine vortex for the northern half of the feature. This structure of intrahalocline Arctic eddies has been noted previously (Zhao et al., 2014). In particular, the eastward velocity increases from the eddy centre until a maximum at the edge of the eddy (indicated by the red line in Figure 5.8). Consequently, the northern half of the eddy for Transect 4 is therefore assumed not to be significantly influenced by the slope current; the slope current only needs to be removed from the southern half of the section (Figure 5.10, top panel). The eddy signature is thus multiplied by -1 and mirrored about its centre (Figure 5.10, middle panel), before being subtracted from the the southern half of Transect 4. This leaves values of 0 cm s^{-1} north of the eddy's centre (greyed out to focus on the slope current) and an undisturbed signature of the slope current in the southern half of the section (Figure 5.10, bottom panel). Following this, the undisturbed slope current signal is subtracted from the southern halves of Transects $1, 2$ and 4, which encompass the strongest part of the eddy. The slope current cannot be objectively removed to the east of the eddy (Transect 3), or to the west (transects 6 and 7). This is due to the slope current extending into the northern half of the sections (potentially masking the eddy's eastward flow north of the eddy centre), particularly after the current bends with the bathymetry to the northwest.

Figure 5.11 shows the vertical VMADCP sections with the slope current removed. The first thing to note is that this simple method of removing the slope current does not work for depths outside the influence of the eddy. This is particularly evident at depths shallower than 100 m, where a strong eastward (positive) flow is generated; this is caused by the calculated slope current being too large in this region. This is a result of the eastward flow that is produced in the upper water column when mirroring and multiplying the northern half of Transect 4 by -1 (to complete the anticyclonic circulation of the eddy). Consequently, only velocities in the vicinity of the $26.4-27.2$ kg m^{-3}

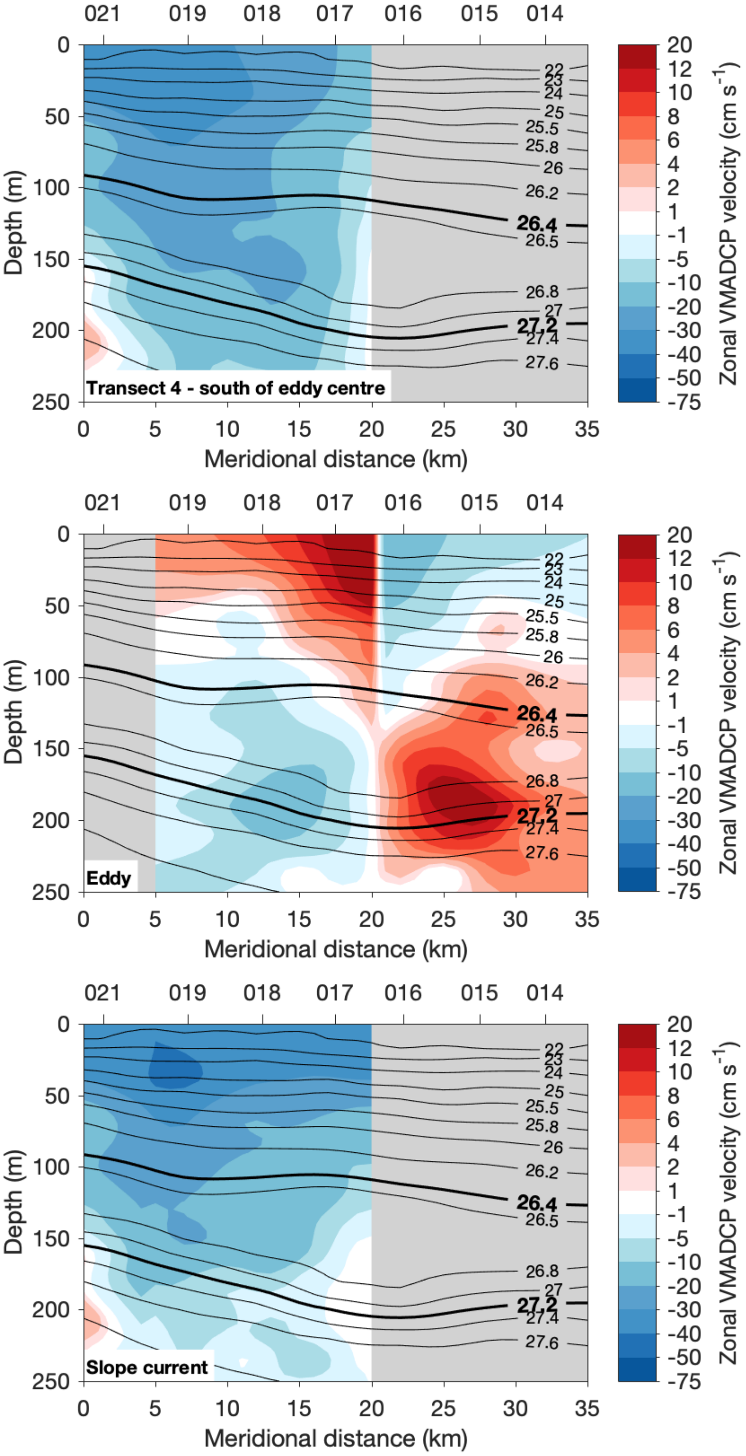

FIGURE 5.10: Slope current calculation. (Top) Transect 4 zonal VMADCP velocities south of the eddy centre. (Middle) Transect 4 zonal VMADCP velocities north of the eddy centre, and mirrored and reversed to the south. (Bottom) The slope current signal, calculated by subtracting (middle) from (top). The viewer is looking to the west. Positive flow is to the east. Station numbers are marked along the top. The highlighted density contours correspond to the layer averages in Figures 5.8 and 5.12. Grey regions are used here to highlight the portions of the section that are not used in the calculation.

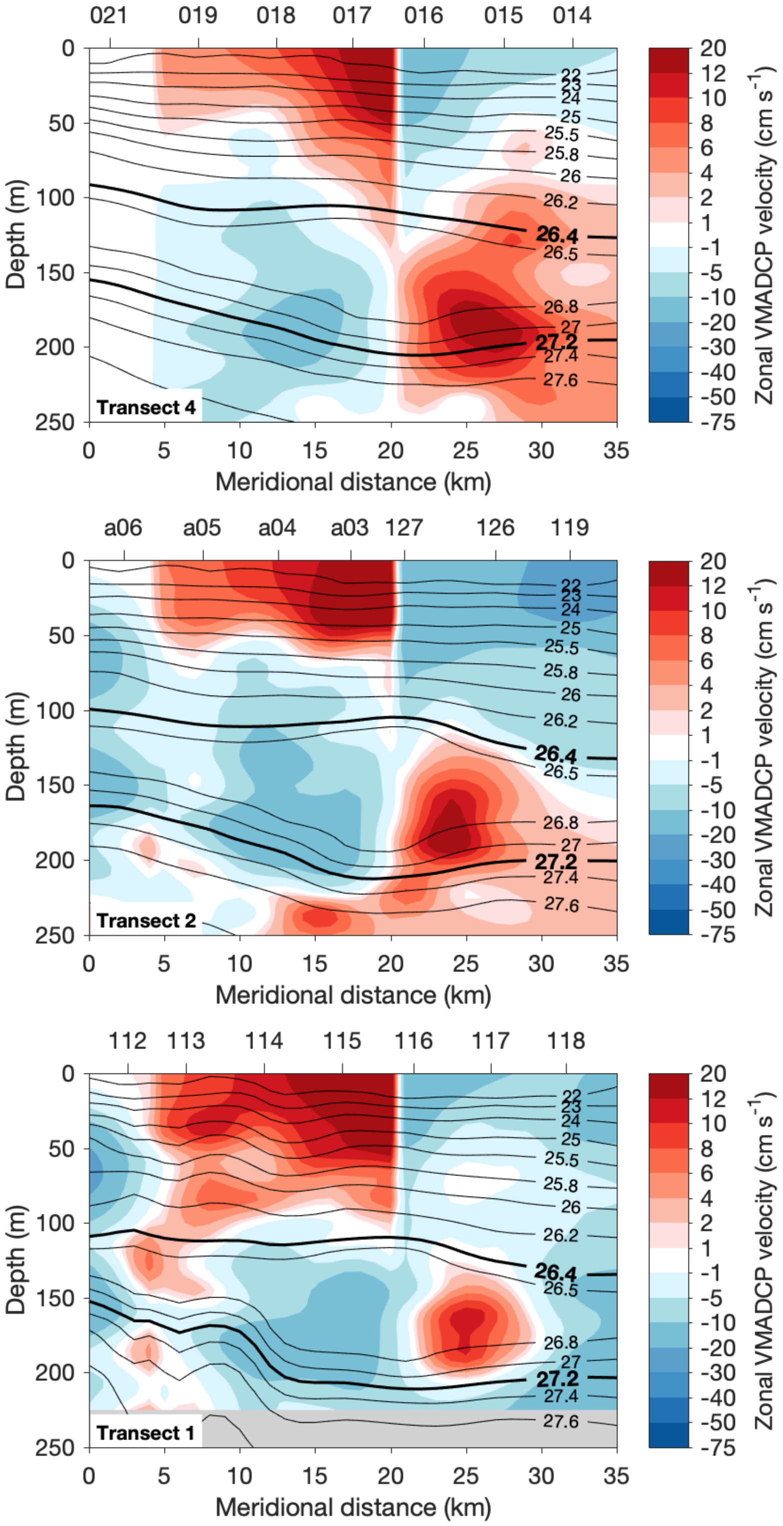

FIGURE 5.11: Vertical sections of zonal VMADCP velocity through the eddy, with the slope current removed. Overlain are potential density contours (kg m^{-3}). See Figure 2.35 for the locations of the transects. The viewer is looking to the west. Positive flow is to the east. Station numbers are marked along the top (Station 119 and transect 1 are CTD stations). The highlighted density contours correspond to the layer averages in Figures 5.8 and 5.12. The centre of the eddy is labelled. Grey regions indicate deep areas without VMADCP data.

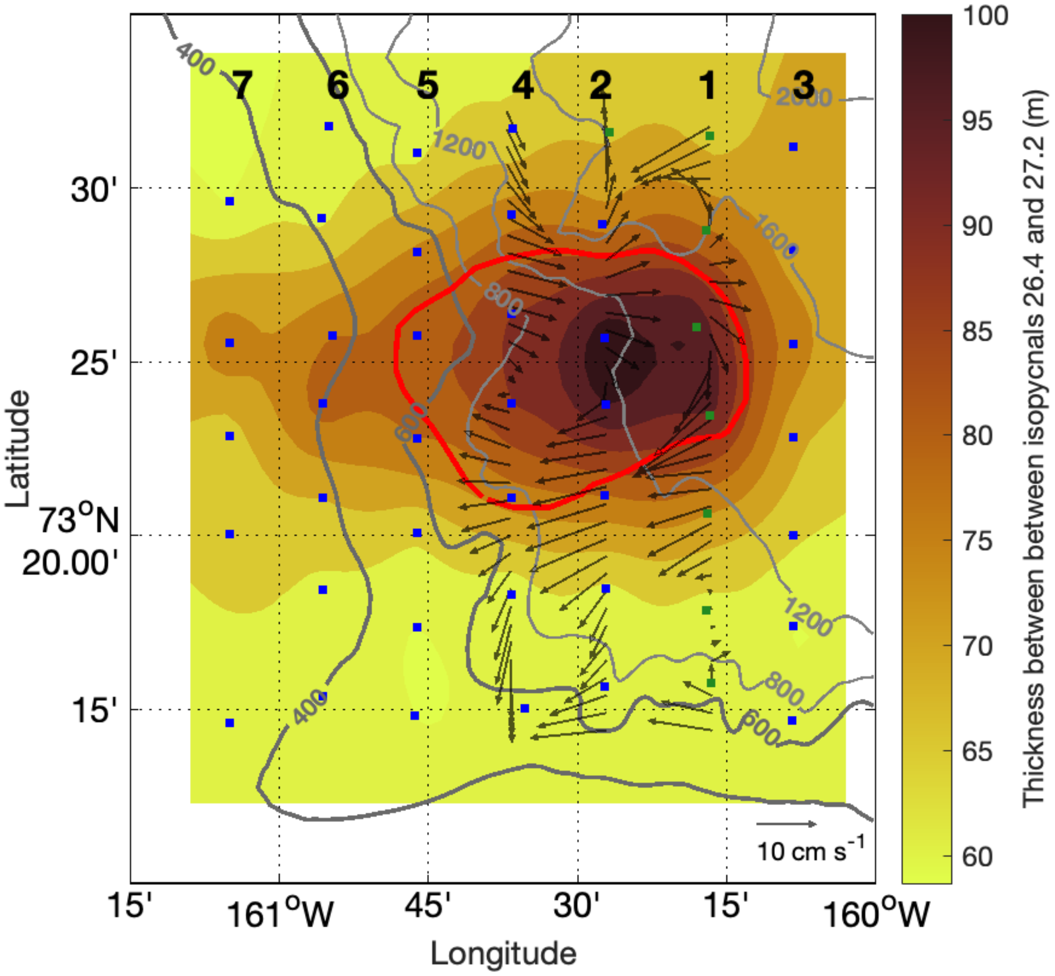

FIGURE 5.12: Same as Figure 5.8 except that the slope current signature has been removed. Transect 5 did not have enough data to be included, and transects 3, 6 and 7 are excluded because the slope current could not objectively be removed (see text for details).

density layer, approximately bounding the eddy, should be considered. Additionally, by definition the velocities in Transect 4 have to be symmetrical about the eddy centre. Values of zero are observed between $0 - 5$ km in Transect 4 because the recorded velocities were untouched in the slope current calculation (Figure 5.10). Despite these calculation artefacts, the anticyclonic circulation of the eddy is clearly captured in each of the transects.

Figure 5.12 shows the depth-averaged velocities within the $26.4 - 27.2$ kg m^{-3} density layer, following the subtraction of the slope current. In comparison with the original velocities (Figure 5.8), a more symmetrical eddy signature with peak azimuthal speeds of 8 cm s^{-1} appears. A three-dimensional view displaying both the eddy velocity field and the temperature field is shown in Figure 5.13. At the top-most surface (100 m; just above the 26.4 kg m^{-3} isopycnal) there is little indication of the eddy: no NVWW is present and there is no consistent azimuthal signature. As one progresses downward through the feature (125 m, 150 m, 175 m) the cold core becomes evident, as does the anticyclonic azimuthal flow. At the bottom of the feature (200 m) the azimuthal speed remains strong. This is consistent with the modeling results of Spall et al. (2008) that show that the velocity signal of cold-core Arctic eddies often extends deeper into the water column than the property signature (see also the bottom of the transects in Figure 5.11).

Previous studies have observed intrahalocline eddies in cyclostrophic balance with large Rossby numbers (near 1), and also eddies in approximate geostrophic balance with small Rossby numbers (Zhao et al., 2014; Fine et al., 2018). To assess the dynamical balance in the eddy sampled here, the following cyclogeostrophic equation is evaluated (Lin, P., personal comms., July, 2019):

$$\frac{v^2}{r} - fv - \frac{1}{\rho}\frac{\partial p}{\partial r} = 0, \tag{5.1}$$

where v is the eddy azimuthal velocity, r is distance from the eddy core, f is the Coriolis parameter (1.4×10^{-4} s^{-1} at a latitude of 73 °N). In Equation 5.1 the first term on the left is the centrifugal acceleration, the second term is the Coriolis acceleration, and the third term is the pressure gradient force. The three terms were computed for Transect 2 (the XCTD line that passes through the eddy's centre), averaged between the isopycnals $26.4 - 27.2$ kg m^{-3} (the same density layer as in Figure 5.4). Figure 5.14a shows that the cyclogeostrophic velocity (the full solution to Equation 5.1) is dominated by the geostrophic component (the balance of the two right-hand terms in Equation 5.1, where both velocity terms are referenced to 250 m). This is not surprising in light of the relatively weak azimuthal speeds of the feature (Figure 5.12); Zhao et al. (2014) found mean azimuthal speeds of 14 cm s^{-1}. The Rossby number can be calculated as $R_o = \frac{\gamma}{f}$, where in cylindrical coordinates the relative vorticity $\gamma = \frac{\partial(rv)}{r\partial(r)}$. Figure 5.14b shows how R_o varies across Transect 2. The maximum value on the two sides of the feature is ~ 0.4, suggesting a geostrophic balance. This is consistent with the warm-core eddy sampled by Fine et al. (2018) which had a similarly small Rossby number and in which the geostrophic term accounted for most of the cyclogeostrophic velocity.

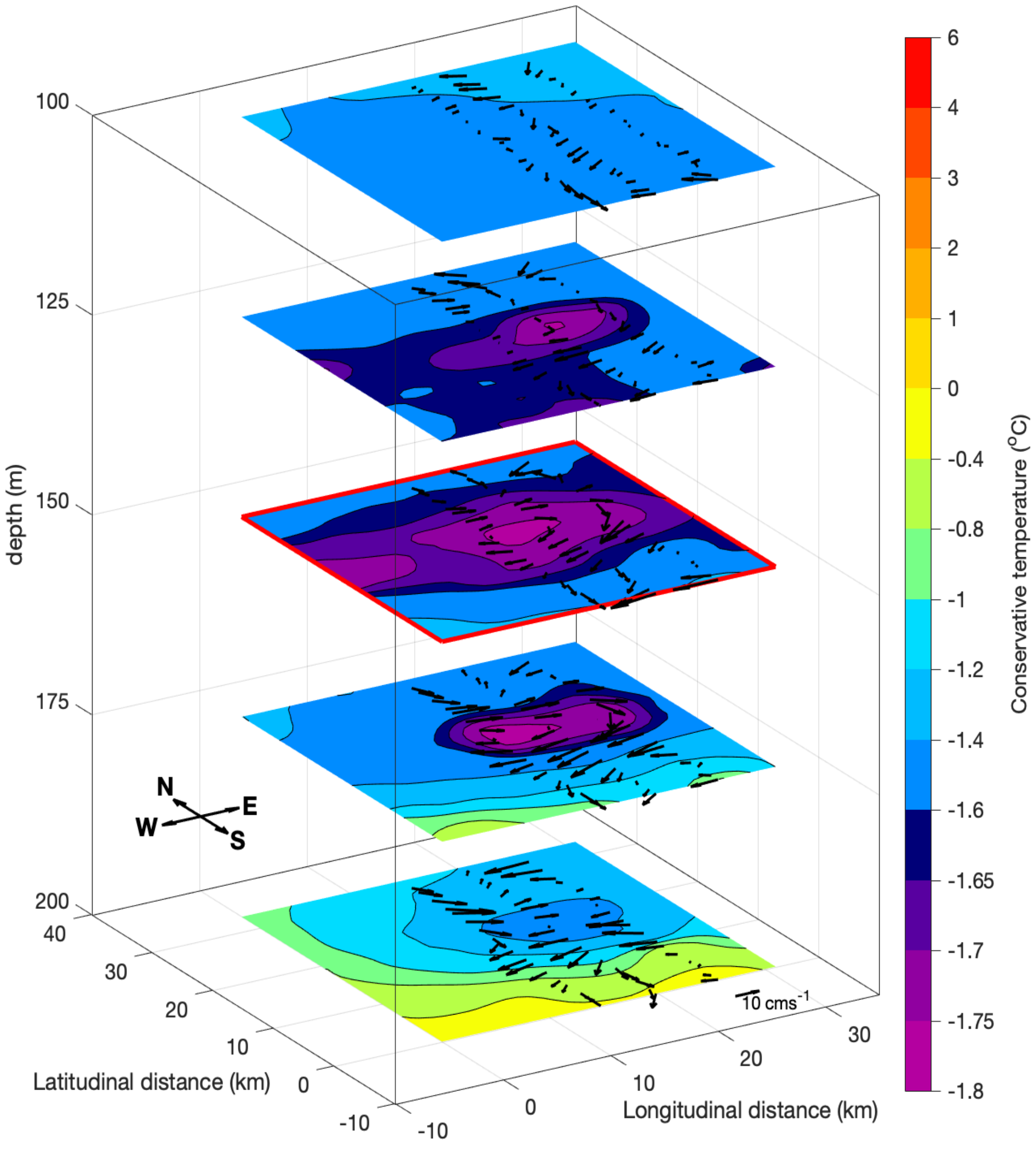

FIGURE 5.13: Lateral sections through the eddy at different depths showing the temperature (colour) and velocity vectors after the slope current signature has been removed (see text for details).

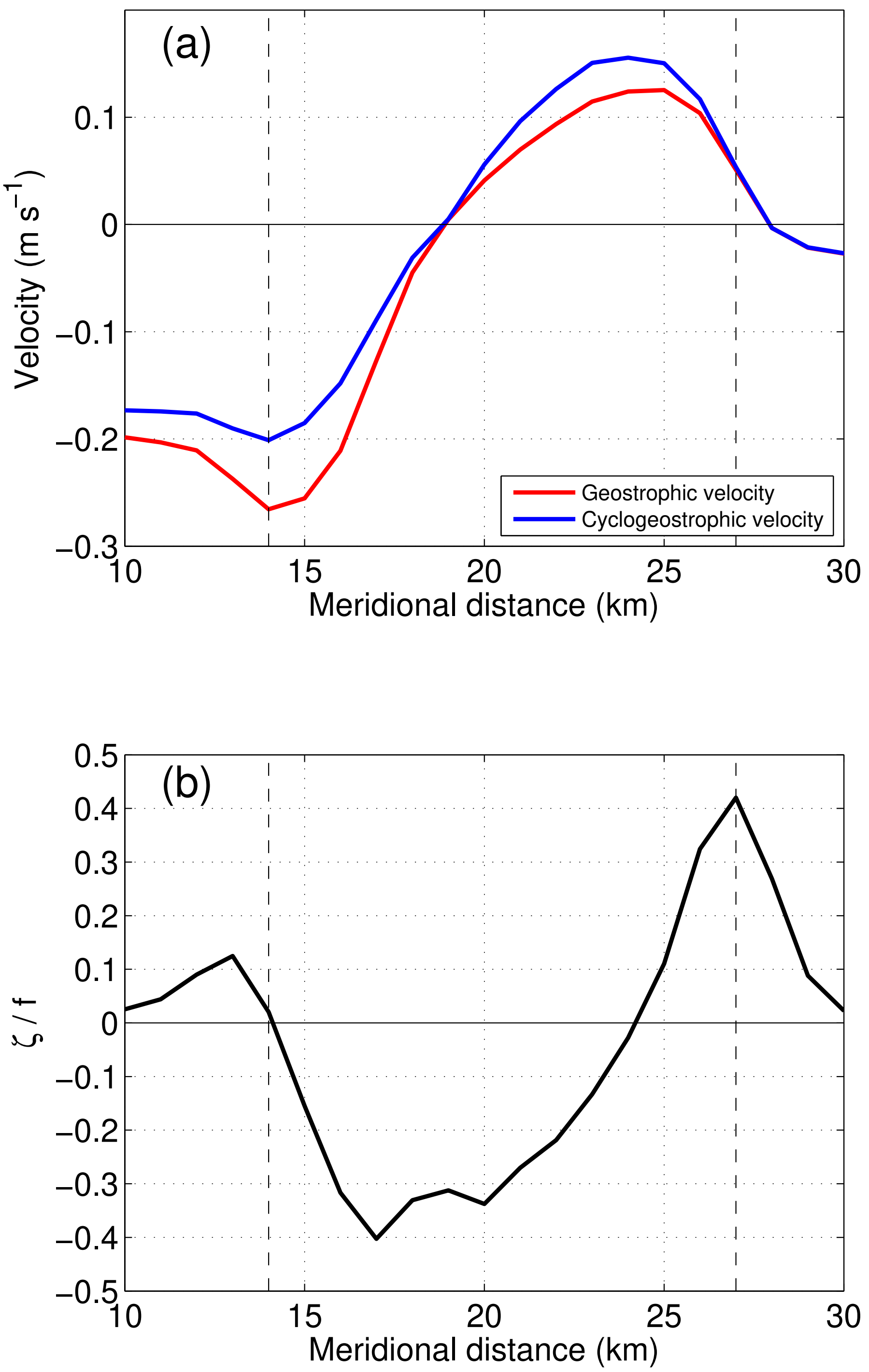

FIGURE 5.14: (a) Relative geostrophic velocity (red curve) and cyclogeostrophic velocity (blue curve) for transect 2 (Lin, P., personal comms., July, 2019), averaged between the isopycnals $26.4 - 27.2$ kg m^{-3} (see Figure 5.12). Both velocity terms are referenced to 250 m. (b) Rossby number along the same transect averaged within the same density layer. The vertical dashed lines are the edges of the eddy, which are visually obtained from Figure 5.9.

5.4 Summary and Discussion

This work has presented a unique three-dimensional view of an Arctic cold-core eddy located roughly 50 km seaward of the Chukchi Sea shelfbreak over the 1000 m isobath. It had a zonal diameter of $\sim$ 19 km and a meridional diameter of $\sim$ 14 km, with cold NVWW in its core centred at 150 m depth. Elevated levels of nutrients, fluorescence and dissolved oxygen indicated biological activity within the eddy. However, the fluorescence was due to phaeopigments instead of healthy chlorophyll, indicating that photosynthesis was no longer active. This is to be expected since the eddy descended to a depth well below the euphotic depth after leaving the shelf. The chlorophyll to phaeopigment differential is consistent with the eddy age being on the order of months, which was previously deduced using radium dating (Kadko et al., 2008).

The shipboard velocity data indicated that the eddy was embedded in the offshore edge of the westward-flowing Chukchi Slope Current, which was surface-intensified with a volume transport roughly 0.8 Sv - similar to previous autumn measurements of the current. Subtracting out the slope current signal, produced an eddy velocity field that was symmetrical with a peak azimuthal speed of order 10 cm s^{-1}. Its Rossby number was small ($\sim$ 0.4), consistent with the fact that the measured cyclogeostrophic velocity was dominated by the geostrophic component. The azimuthal speed extended below the depth of the property core of the eddy, in line with previous modeling results (Spall et al., 2008).

Using the surface velocity field derived from the satellite absolute dynamic topography during the period of observation (see section 2.2.4), the path of the Chukchi Slope Current in relation to the location of the eddy can be mapped out (Figure 5.15). The eddy is situated precisely where the slope current is diverted to the north (see also Figure 5.8). As such, one might be tempted to think that anticyclonic eddy is altering the path of the current (causing the slope current to partially wrap around the eddy). It is more likely, however, that the slope current is bending northward in response to the local bathymetry of Hanna Canyon, which causes the isobaths to bend to the north (Boury et al., 2020).

The measurements here are not the only ones revealing an intrahalocline eddy embedded in the seaward side of the Chukchi Slope Current. Kawaguchi et al. (2012) reported on a large, warm-core anticyclone similarly situated (the authors referred to the strong westward flow as a southern branch of the Beaufort Gyre). How do such eddies end up here? As noted in Chapter 1, the Chukchi shelfbreak jet is highly unstable and readily spawns anticyclonic eddies (Pickart et al., 2005; Spall et al., 2008). However, the relative locations of the Chukchi Slope Current and shelfbreak jet suggest that eddies formed by this process would end up getting entrained into the onshore side of the slope current, not its offshore side; i.e., as the eddies progress northward they encounter the southern side of the slope current. It should be remembered, however, that the slope current is

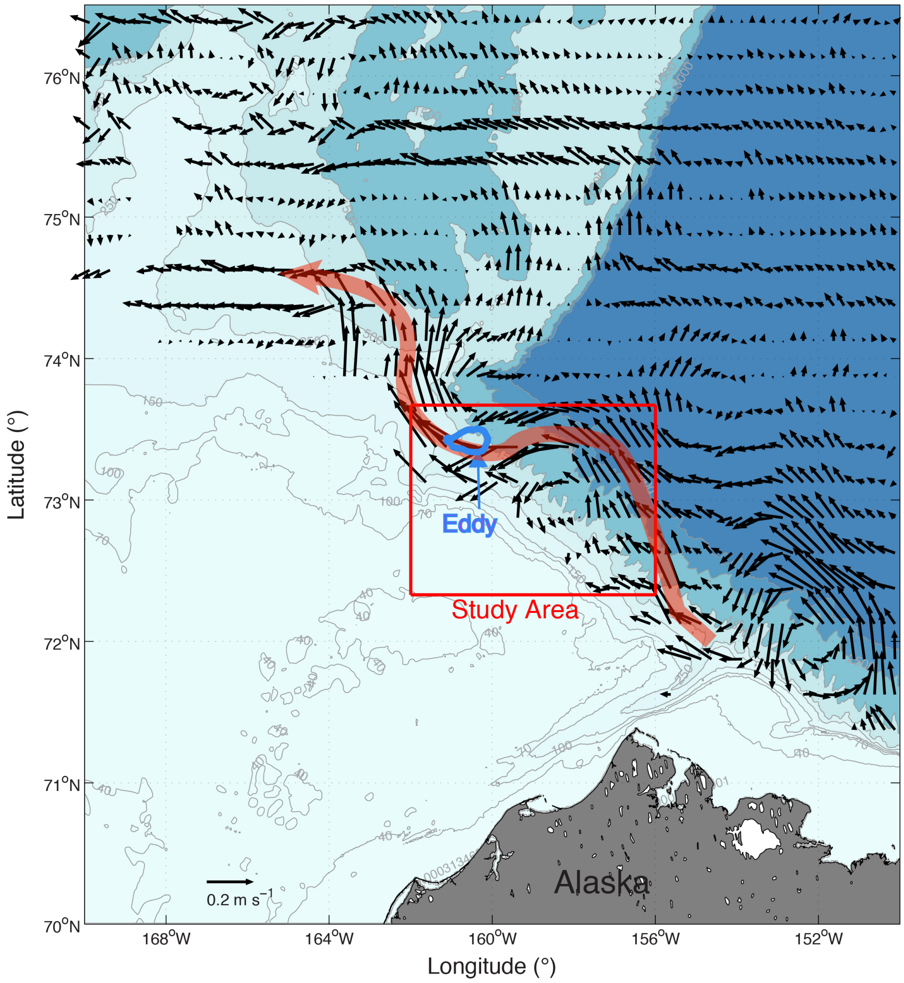

FIGURE 5.15: Surface velocity vectors derived from the absolute dynamic topography for the day of the eddy survey (Pickart, R. S., personal comms., July, 2019). The red line denotes the approximate path of the Chukchi Slope Current. The blue contour denotes the edge of the eddy (the −1.6 °C contour from Figure 5.4). The bathymetry is from IBCAO v3 (Jakobsson et al., 2012). The study area outlined in red is shown in Figure 2.34.

strongly influenced by wind. In particular, Li et al. (2019) demonstrated that the current is enhanced when the wind stress curl is positive on the Chukchi shelf. This is due to the decrease in sea surface height (SSH) on the shelf relative to the slope, which results in a stronger northward SSH gradient and hence stronger westward flow. By contrast, when the wind stress curl is negative on the Chukchi shelf, the slope current is retarded or absent due to the increase in SSH on the shelf versus the slope, which weakens or flattens the northward SSH gradient. Thus, eddies emanating from the Chukchi shelfbreak jet after a negative wind stress curl event might be able to progress offshore before the slope current re-establishes itself.

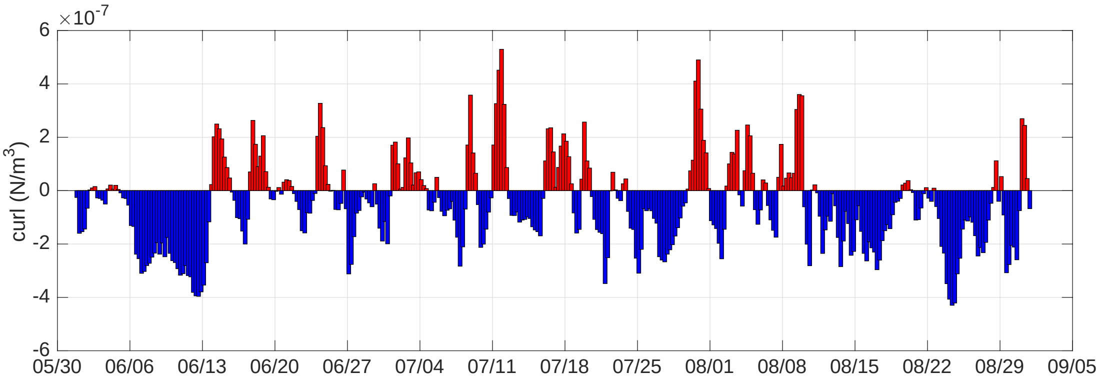

FIGURE 5.16: Time series of wind stress curl (every 6 hours) averaged over the region marked in Figure 2.33 on the northeast Chukchi shelf (Li, M., personal comms., July, 2019). The period shown (June-August 2004) is the three months before the eddy survey in this study was conducted.

To investigate this, a time series of wind stress curl over the same region of the Chukchi shelf considered by Li et al. (2019) was computed for the time period of June to August 2004 - the hypothesis being that the eddy was formed some months before it was measured (see Figure 2.33 for the region). Figure 5.16 shows that there were plenty of periods over this three-month time span when the slope current might have been disrupted, allowing the eddy to move well offshore. As discussed by Spall et al. (2008), the shelfbreak eddies are originally formed as dipole pairs that self-propagate seaward. Fairly soon after formation the cyclone partner spins down, which is why the Canada Basin is dominated by anticyclones.

It is perhaps more likely that the eddy embedded on the seaward side of the Chukchi Slope Current emanated from Barrow Canyon (where it would have had a straightforward path to its observed location). As discussed in Chapter 1, different mechanisms are believed to result in eddy formation from the canyon outflow, and eddies have been observed seaward of the canyon mouth. Hence, as the slope current forms from the westward-turning flow leaving the canyon, it could influence a previously formed eddy residing farther offshore. Velocities in the calculated slope current are between $0 - 20$ cm s^{-1} close to the eddy's core (i.e., using VMADCP data in Figure 5.10, lower panel), or are between $5 - 10$ cm s^{-1} using velocities at the offshore edge of the current in Transect 3 (i.e., using absolute geostrophic velocities, Figure 5.9). Whichever slope current velocities are used in the calculation, in this scenario the eddy would have been advected to the survey site in this study within $1 - 2$ months. This is consistent with the estimated age of the eddy.

If this were a regular occurrence it would mean that some fraction of the turbulent outflow from Barrow Canyon is also transported to the west, in addition to the Pacific water directly forming the slope current. Furthermore, any eddies stemming from the Chukchi shelfbreak jet under positive (or weak) wind stress curl conditions would likely follow a similar pathway via the inshore side of the slope current. One implication is that the primary geographical region of halocline ventilation in the Canada Basin - via cold-core eddies plus the Chukchi Slope Current - is to the west of Barrow Canyon. However, it is unknown how many eddies emanating from the canyon are entrained by the slope current, and, as noted in Chapter 1, cold-core eddies are also spawned to the east by the Beaufort shelfbreak jet - although the transport of the Beaufort shelfbreak jet is roughly five times smaller than that of the Chukchi Slope Current. Further investigation is necessary to elucidate precisely where the halocline ventilation occurs as well as the degree to which the ventilation is accomplished via mesoscale eddies versus the advective source of the Chukchi Slope Current. Assessing this will be challenging in part because how often eddies are formed during the winter months is unknown.

Previous papers have addressed the spin down of eddies in the Canada Basin. Ou and Gordon (1986) considered the effect of pack ice in retarding the eddy flow due to ocean-ice stress, and estimated a decay timescale of $1-10$ years. Using this methodology, Zhao et al. (2014) estimated the lifetime of their observed small, cold-core anticyclones to be from 0.9 years to 5 years. However, here the velocity signature of the eddy is typically absent at depths shallower than 100 m, with only the north western side of the eddy reaching depths of 90 m (Figure 5.11, Transect 4), so it is unlikely that ice friction will impact its ultimate decay. Padman et al. (1990) considered the effect of background dissipation on the spin-down of a small cyclone located in the cold halocline layer, and deduced a decay timescale on the order of 10 years. The impact of such small-scale mixing cannot be assessed here using the available data, but there is no reason to suspect that the conclusion would be different than that reached by Padman et al. (1990).

Another mechanism for spinning down a cold-core anticyclone is due to convergence / divergence of the radial flow which can lead to vertical and horizontal exchanges of water masses. This in turn would flatten the displaced isopycnals of the eddy. Zhao et al. (2014) assessed this process for a representative eddy in their data set and deduced a much shorter decay time of roughly 7 months. Following the same methodology for the radial velocities along Transect 2 through the centre of the eddy in this study, a spin-down time on the order of half a year is estimated, which is comparable to Zhao et al. (2014)'s result. As noted above, there is NVWW outside of the eddy (i.e. the patch of cold water to the west of the eddy in the lateral map of Figure 5.4), which could be a reflection of this process.

A final thing to consider is, does the interaction of an eddy with the Chukchi Slope Current impact the eddy's decay process and spin-down time? For the cold-core eddy observed here, the onshore side of the feature was in contact with the slope current while the offshore side of the eddy was not (or was less impacted). This would suggest that the eddy will become sheared at some point; recall that the zonal diameter of the eddy was longer than its meridional diameter. This in turn implies that it would spin down more rapidly as the lateral gradients are enhanced. Further work is necessary to address this and other ramifications of eddy-slope current interactions for ventilation of the cold Arctic halocline.

Chapter 6

Summary and Implications

Earth's polar regions have undergone extraordinary change over recent decades. In the Arctic, air temperatures are increasing at more than twice the global average rate (e.g., Serreze et al., 2009), ocean temperatures are increasing (e.g., Carmack et al., 2015; Timmermans et al., 2018), sea ice is rapidly declining (e.g., Perovich et al., 2019), the freshwater distribution has been changing (e.g., Carmack et al., 2016; Proshutinsky et al., 2020), and large-scale wind patterns are becoming more variable (e.g., Moore et al., 2018). Although there is greater regional variability, significant changes have also been observed in Antarctica. This is particularly the case in West Antarctica: the deep waters have been warming and shoaling (e.g., Schmidtko et al., 2014), there is greater inter-annual variability in sea ice extent, with a dramatic decrease in extent in 2016 (e.g., Reid et al., 2020), there is an increased freshwater flux away from the continent (e.g., Jacobs et al., 2002; Haumann et al., 2016), and westerly winds are shifting further south (e.g., Fogt and Marshall, 2020).

The changes at both poles will impact the shelf-ocean exchange and small-scale mixing mechanisms that are critical to the ventilation of the cold halocline in the Arctic (e.g., Aagaard et al., 1981), and the flux of warm CDW towards the coast in the Antarctic (e.g., Martinson and McKee, 2012). The major shelf-ocean exchange mechanisms are wind-driven upwelling (e.g., Martinson et al., 2008; Pickart et al., 2009) and downwelling (e.g., Foukal et al., 2019), advection through canyons (e.g., Arneborg et al., 2012; Spall et al., 2018), and eddies (e.g., Spall et al., 2008; Moffat et al., 2009; Martinson and McKee, 2012). Changes to these processes have further implications on both local and global scales. These include but are not limited to: the melting of ice shelves (e.g., Pritchard et al., 2012) and marine-terminating glaciers (e.g., Cook et al., 2016), changes to ecosystem dynamics (e.g., Montes-Hugo et al., 2009; Wassmann et al., 2011) and the increase of global sea levels (e.g., Bamber et al., 2009). Motivated by these implications, this thesis has focused on furthering our understanding of various shelf-ocean exchange and mixing mechanisms. This chapter summarises the main findings from this thesis, before exploring how the mechanisms studied may change under predicted conditions and what the associated implications may be for future polar regions.

6.1 Summary

6.1.1 Automated Processing of Glider Microstructure Data

The aim of the NEXUSS Centre for Doctoral Training is to answer scientific questions through the development and application of novel autonomous vehicles. Consequently, a primary outcome of this thesis is the adaptation of the existing RSI ODAS software to enable automatic processing of glider microstructure data. A 2016 Ryder Bay dataset provided some of the first direct dissipation measurements from a glider off West Antarctica. Traditionally, microstructure data were collected in single profiles using VMPs and processing was conducted manually. However, the large quantity of data produced by a microstructure-equipped glider meant it was necessary to automate the processing. A major element of this automation was the creation of the QAA. This first searched for and removed, if necessary, a $1-3$ Hz peak that was found in shear spectra from both upcasts and downcasts throughout the deployment. The algorithm then compared each individual shear spectrum to its corresponding Nasmyth spectrum by fitting second order polynomials and assessing the coefficients against 8 conditions. Using these somewhat conservative criteria, 26% of the microstructure data were accepted for analysis. The high percentage of rejected spectra stems from Ryder Bay being typically a low-dissipation environment, with dissipation rates close to the noise floor of the instrument, leading to flat spectra that did not clearly agree with the Nasmyth spectra. Additionally, the presence of the $1-3$ Hz peak was investigated. The peak is believed to be related to the glider's flight quality, which in turn is related to the ballasting of the glider; this is made more difficult with the use of a microstructure probe guard.

6.1.2 Two-Stage Mechanism for Upward Heat Flux on West Antarctic Peninsula

The semi-enclosed nature of Ryder Bay and its close proximity to multiple marine-terminating glaciers means that it can be considered an end point for CDW, which intrudes southwards through Marguerite Trough and towards the coast (Klinck et al., 2004). Couto et al. (2017) suggest that two thirds of the heat advected across the shelf-break is fluxed vertically upwards across the pycnocline, and Venables et al. (2017) found evidence of enhanced vertical mixing over multiple topographic ridges within the trough and the adjacent Laubeuf Fjord. With a topographic ridge also found at the entrance to Ryder Bay, the region was ideal for studying the role such ridges might have in generating vertical mixing and an associated upward heat flux. The glider deployed in 2016 was programmed to conduct multiple transects over the ridge and into Ryder Bay. Chapter 3 described significant spatio-temporal variability in the hydrography, dissipation, and heat fluxes. Chapter 4 then explored the different mechanisms that could be responsible for controlling the observed patterns.

Elevated dissipation estimates were consistently observed over the topographic ridge at Ryder Bay's entrance, with mean dissipation estimates $O(1 \times 10^{-8})$ W kg^{-1} compared with estimates $O(1 \times 10^{-(9-10)})$ W kg^{-1} in the basin. Although elevated dissipation over topographic ridges is commonly associated with tides (e.g., Klymak and Gregg, 2004), tidally-driven dissipation was shown to be small in Ryder Bay, owing largely to the very weak magnitude of the barotropic and internal tides. The elevated dissipation estimates were co-located and moved with the location of pinching and steeply sloping isopycnals. This is reminiscent of flow that is controlled hydraulically (Figure 4.29c), and a Froude number sensitivity analysis revealed that a hydraulic control scenario was likely in 64% of the transects (at mean alongshore velocities). The corresponding mean heat flux over the ridge in these transects was ~ 2.4 W m^{-2}.

Heat fluxes over the ridge were $3-4$ times larger than those typically observed across the base of the thermocline ($\sim$ 0.6 W m^{-2}). However, towards the end of the deployment, a basin-wide elevated dissipation event occurred within and across the base of the thermocline. This was attributed to wind-driven near-inertial shear at the thermocline (Figure 4.29b). A statistically-significant correlation of $R = 0.92$ ($p \ll 0.001$) was observed between the 4-day low pass filtered wind stress magnitude and near-inertial thermocline shear (over a 25 day period, after a $\sim$ 1.7-day lag adjustment). Basin-scale seiching motions and CTWs were also considered as possible controls on the dissipation, however, these processes were not found to be significant in Ryder Bay. The basin-wide dissipation event approximately doubled the mean heat flux across the thermocline to $\sim$ 1.3 W m^{-2}. This suggests a two-stage mechanism for fluxing heat vertically upwards in the water column: the ridge is a consistent source of heat to the base of the thermocline, where it can spread laterally; this heat can then be episodically released across the thermocline through strong wind events that cause near-inertial thermocline shear and dissipation. Additionally, concurrent with the basin-wide dissipation event was a sudden $\sim$ 50 m deepening of the thermocline, preceded by a period of gradual shoaling. This shoaling and deepening of the thermocline was attributed to wind-driven coastal upwelling and downwelling on Ryder Bay's southern boundary (Figure 4.29a). Winds therefore also have a role in controlling the amount of heat available for fluxing upwards within Ryder Bay.

6.1.3 Cold-Core Arctic Eddy Embedded in Seaward Side of Chukchi Slope Current

Chapter 5 switched focus to a larger-scale shelf-ocean exchange feature in the Arctic. In particular, it presents the first survey that captures the full three-dimensional structure of a mesoscale cold-core anticyclonic eddy in the Chukchi Sea, Arctic Ocean. The eddy had zonal and meridional diameters of $\sim$ 19 and $\sim$ 14 km, with a NVWW core centered at 150 m. Such eddies are ubiquitous in the Canada Basin (Zhao et al., 2014) and are likely important for ventilating the cold Arctic halocline and preventing the warm AW from mixing upwards and melting the pack ice (Carmack et al., 2015). Data from a VMADCP revealed that the eddy was embedded in the northern edge of the Chukchi Slope Current. Consequently, the slope current's signature was removed, leaving a symmetrical eddy field with azimuthal velocities $O(10)$ cm s^{-1}. The eddy's Rossby number was small ($\sim$ 0.4), consistent with the geostrophic component dominating the cyclo-geostrophic velocity.

There are several possible formation locations of the eddy. Multiple periods of negative wind stress curl occurred in the months preceding the survey, caused by anticyclonic winds that are associated with high sea level pressure in the Canada Basin and low over the Chukchi shelf (Li et al., 2019). Consequently, the eddy could have formed through baroclinic instability in an enhanced Chukchi shelfbreak jet (e.g., Pickart et al., 2005), entering the Canada Basin when the slope current was in its weakened state (state 2 in Li et al., 2019). Perhaps it is more likely the eddy originated in Barrow Canyon and was advected westward in the Chukchi Slope Current (where it would have had a straightforward path to its observed location). With slope current velocities of $\sim$ 10 cm s^{-1} at its offshore edge, the eddy would have been advected to its observed location within $1-2$ months. This is consistent with an estimated eddy age on the order of $1-2$ months, calculated from the phaeopigment/chlorophyll differential and by Kadko et al. (2008) using radium isotope data. Lastly, an eddy spin-down time on the order of half a year was estimated, however, increased shear from the slope current may have caused the eddy to spin down more rapidly.

6.2 Implications for Future Polar Regions

Condensing the summary above, the work in this thesis relates to the shelf-ocean exchange of warm, saline CDW in the Southern Ocean, and of cold, saline NVWW in the Arctic Ocean. It particular, Chapter 4 documents a two-stage upward heat flux within Ryder Bay, WAP. There is a persistent flux of CDW heat towards the themocline above a topographic ridge, believed to be associated with a hydraulic control, and heat fluxes across the thermocline are periodically enhanced by wind-driven near inertial shear events. Ekman upwelling and downwelling within the bay also acts to

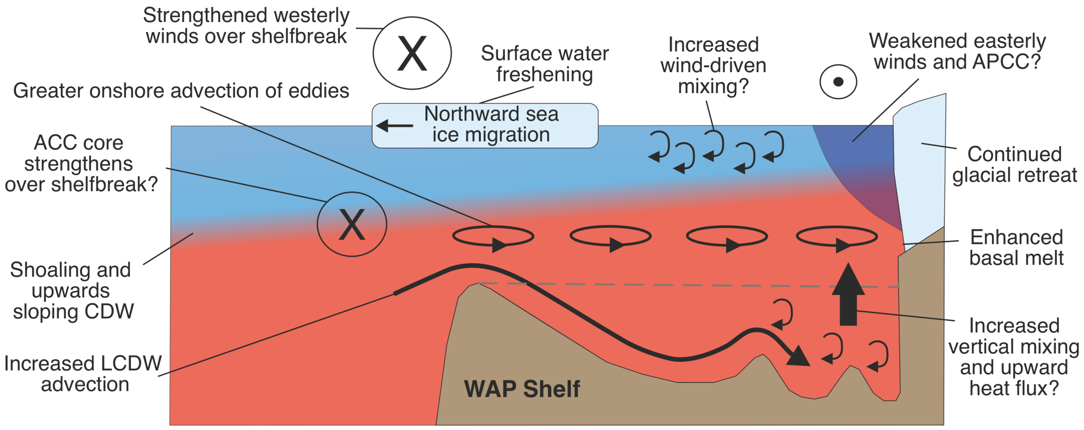

FIGURE 6.1: Schematic showing how shelf-ocean exchange on the West Antarctic Peninsula (WAP) Shelf could change in the future. This is an adapted version of Moffat and Meredith (2018)'s WAP heat budget schematic (shown in Chapter 1, Figure 1.14). Please see the text for a detailed discussion on each of the changes shown. Please note that this simple schematic does not represent all of the processes or possible changes that might occur on the WAP in the future.

alter the amount of heat available for vertical mixing. Chapter 5 analysed a cold-core eddy situated on the seaward edge of the Chukchi Slope Current, features thought to be important for ventilating the cold Arctic halocline. As highlighted above, such eddies can form through flow-interaction with the canyons on the Chukchi shelf or through baroclinic instability of the boundary currents. This section explores how changes to the polar regions may impact these processes.

6.2.1 Changes to Heat Content

6.2.1.1 Antarctic

The heat content of the polar oceans has changed significantly over recent years. In the Southern Ocean trends are regional, with cooling of near-bottom shelf waters in the Weddell Sea at rates of -0.05 ± 0.04 °C decade^{-1} since the 1970s, but significant warming occurring along the central WAP and through the Bellinghausen and Amundsen Seas (Schmidtko et al., 2014). In these regions, shelf bottom waters have warmed at rates of $0.1 - 0.3$ °C decade^{-1} since the 1990s, and this is associated with warming and shoaling of CDW within the ACC (Figure 6.1), at rates of 0.1 °C decade^{-1} and -30 m decade^{-1}, respectively (Schmidtko et al., 2014). The LTER research program on the WAP's continental margin (Martinson et al., 2008) and a study north of 60 °S (Gille, 2008) have found similar CDW warming trends.

Variability in shelf-ocean exchange processes will strongly affect the WAP's heat content and in particular, the availability of CDW. A primary candidate for fluxing heat onto the WAP shelf is advection through topographic troughs, such as Marguerite

Trough (e.g., Dinniman and Klinck, 2004; Dinniman et al., 2011). Dinniman et al. (2011) showed that by forcing interaction of the ACC with bends in the shelfbreak, variations in large-scale along-shelf wind forcing can lead to greater flux of CDW into Marguerite Trough through momentum advection. Consequently, a poleward shift in westerly winds, associated with a positive SAM (Fogt and Marshall, 2020), could lead to a strengthening of the ACC over the shelfbreak and therefore an increase in the amount of LCDW advected through such troughs (Figure 6.1).

Eddies are perhaps the most prominent mechanism for fluxing CDW onto the WAP shelf (e.g., Moffat et al., 2009; Martinson and McKee, 2012; Graham et al., 2016; Couto et al., 2017). The dominant eddy formation mechanisms are yet to be determined, however, Brearley et al. (2019) find baroclinic and barotropic instabilities in the open ocean near the mouth of Marguerite Trough, suggesting an active, instability-driven eddy field. Brearley et al. (2019) also observe multiple cold-core eddies that propagate along the slope and supply a quasi-stationary eddy at the mouth of Marguerite Trough; this can detach from the boundary current and propagate into the ACC, thereby facilitating shelf-ocean exchange. Additionally, eddies can form through interaction of the boundary current with the topography (St-Laurent et al., 2013), and Rossby waves can propagate along the shelfbreak and interact with topographic features such as bends and entrances to canyons, generating eddies similar to those observed in Marguerite Trough (Zhang et al., 2011; St-Laurent et al., 2013). The formation of Rossby waves, flow-topographic interactions and baroclinic/barotropic instabilities could be influenced by a poleward shift in westerly winds in response to large-scale wind patterns (Fogt and Marshall, 2020). For example, stronger winds in an eddy saturated ACC could increase isopycnal tilt and lead to the formation of more eddies through baroclinic instability (Hogg et al., 2008), or an ACC shift over the shelfbreak may lead to greater velocities, increased shear and more topographic instabilities. Exactly how these processes may change is uncertain, however, if more eddies are generated, one could perhaps expect increased onshore advection of CDW within eddies (Figure 6.1).

If the trends in CDW warming continue and a greater volume is fluxed onto the continental shelf, there could be significant implications for the Ryder Bay mechanisms studied in this thesis. An increase in CDW temperature within Ryder Bay may cause larger temperature variations due to wind driven upwelling of the warm waters, and could also lead to enhanced heat fluxes over the ridge at the bay's entrance. For example, increasing the core CDW temperature in the 2016 glider transects by 0.1 °C (the rate observed over the last decade; Schmidtko et al., 2014) leads to an overall increase in the mean bulk heat flux over the ridge by $\sim$ 80% (calculated between $150 - 350$ m). For transects where a hydraulic control scenario is likely, the mean heat flux over the ridge increased to $\sim$ 4.1 W m^{-2}. This back of the envelope estimation has several caveats; it assumes that salinity does not change, that other processes remain unaltered, and that all of the increase in temperature would be observed in Ryder Bay (an end point for CDW), without being mixed elsewhere further upstream. Additionally, although the exact process forcing a hydraulic control over the ridge at Ryder Bay's entrance is unknown, greater advection of CDW through an increased number of eddies (generated by the mechanisms mentioned above) may lead to increased current velocities and more frequent enhanced vertical heat fluxes over such ridges (Figure 6.1). Ultimately, these changes may lead to more heat being fluxed to the base of the thermocline, where it can be mixed with overlying waters and cause basal melting (changes to the thermocline mixing are explored in Section 6.2.4).

6.2.1.2 Arctic

In the Arctic, warming has been much faster and more widespread. An overall warming trend of 0.03 ± 0.01 °C yr^{-1} is observed for August SSTs north of 67 °N between $1982 - 2019$ (Timmermans et al., 2020). Atlantification (the penetration of AW further into the Arctic Ocean) is an important driver of warming in the Eurasian Basin and adjacent seas; for example, by causing annual-mean SST warming of the Barents Sea, thereby preventing the formation of sea ice (Barton et al., 2018). Climate models show continued Atlantification (Årthun et al., 2019), suggesting this process may become increasingly important in the future. However, currently the greatest August SST warming trends of up to 1 °C decade^{-1} occur in the Beaufort, Chukchi, and Laptev Seas (Timmermans et al., 2020). These are regions that were covered by the $1982 - 2010$ median sea ice extent but are now uncovered (see Figure 1.3), with SST anomalies of $1 - 7$ °C compared to the earlier period (Timmermans et al., 2020). Consequently, the significant warming of Arctic Ocean surface waters in these regions has largely been attributed to increased absorption of incoming solar radiation, a result of decreasing sea ice extent and therefore surface albedo (Timmermans et al., 2018, 2020). The warming triggers an ice-albedo feedback mechanism, delays the onset of freezing in winter and results in a thinner winter sea ice layer (Timmermans and Marshall, 2020). The Chukchi Sea in particular has experienced the fastest summer sea ice decline in the Arctic Ocean (e.g., Serreze et al., 2016; Timmermans and Marshall, 2020), with above-average SST warming trends of 0.07 ± 0.03 °C yr^{-1} (Timmermans et al., 2020). This is also associated with increased heat advection through the Bering Strait (Woodgate et al., 2010) from the Bering Sea, where SST warming trends are similar to those in the Chukchi Sea (0.05 ± 0.02 °C yr^{-1}; Timmermans et al., 2020). Heat transport increased by 60% between $2001 - 2014$, attributed to increases in both temperature and volume flux associated with increased far-field pressure head forcing (Woodgate et al., 2015; Woodgate, 2018).

Warming in the Chukchi Sea region has significant implications for the interior basin. The northern Chukchi Sea is believed to be a major ventilation region for the Arctic Ocean's halocline (e.g., Aagaard et al., 1981; Anderson et al., 2013). Timmermans et al.

(2018) show that a near doubling of the warm halocline's heat content in the Beaufort Gyre's interior between 1987 − 2017 (relative to the local freezing temperature and integrated between 31 − 33 PSU) can be associated with a fivefold increase in heat fluxed into the Chukchi Sea surface waters. Timmermans et al. (2014, 2017, 2018) attribute this to Ekman-driven subduction and lateral induction of warmed Pacific waters where halocline isopycnals outcrop in the northern Chukchi Sea. While this mechanism could contribute the ventilation of the halocline, it does not account for the complex boundary current system at the shelfbreak, and Corlett and Pickart (2017) note that any volume flux off the shelf would likely get entrained in either the Chukchi shelfbreak jet or the Chukchi Slope Current. Spall et al. (2018) also argue that the majority of the Pacific water exiting the Chukchi Shelf leaves through Barrow Canyon in the Chukchi Slope Current. Consequently, these boundary currents are likely to have a significant role for halocline ventilation.

As previously mentioned, in addition to Pacific water that is directly exported off the shelf in the Chukchi Slope Current, the formation of eddies from the canyons and boundary current system in the northern Chukchi Sea are a primary candidate for halocline ventilation. Assuming the eddy generation mechanisms stay the same, the observed warming in the Bering and Chukchi Seas could be reflected in the properties of future eddies. For example, the NVWW found at the core of eddies similar to the one studied in Chapter 5 is formed in these regions (e.g., Pacini et al., 2019), so the eddies may become warmer and potentially more buoyant (see Figure 6.2 below). In these salinity stratified regions a temperature increase alone may have little effect on ventilation, however, as warming continues, these regions could transition into 'alpha' oceans (temperature dominated, as opposed to 'beta' oceans, which are salinity dominated) where such temperature changes would be important for the stability of the cold halocline (Timmermans and Marshall, 2020). Additionally, as the heat content of the surface waters in the Bering and Chukchi Sea continues to rise, the NVWW formation regions may shift further north. Reduced sea ice formation could also lead to a smaller volume of NVWW being produced and exported from the shelf into the interior basin (see Figure 6.2 below). This is supported by Pacini et al. (2019) who demonstrate that sea ice leads on the Chukchi Shelf provide an important contribution to NVWW formation. Consequently, if Arctic warming trends continue, a significant weakening of the Arctic halocline may increase the likelihood of releasing the AW heat into the overlying waters, thereby amplifying the ice-albedo feedback mechanism (as observed in the Eurasian Basin; Polyakov et al., 2020b).

6.2.2 Changes to Freshwater Content

6.2.2.1 Antarctic

The Southern Ocean is generally experiencing long-term freshening trends, with circumpolar freshening rates of $1.1 \times 10^{-3} \pm 4 \times 10^{-4}$ PSU yr^{-1} occurring since the 1960s in the upper 100 m south of the ACC (De Lavergne et al., 2014). However, despite the observed overall freshening there are strong regional differences. Freshening typically strengthens towards the coast, particularly in the Weddell and Ross Seas, with values increasing up to 0.01 PSU yr^{-1} on most continental shelves (Schmidtko et al., 2014). This might initially suggest the freshening is due to increased glacial melt, however, the freshwater controls are still not fully understood (e.g., Skliris et al., 2014), and anthropogenic-induced surface fluxes (changes in precipitation and evaporation) and northward sea ice transport are believed to dominate (Swart et al., 2018; Haumann et al., 2016). Additionally, at mid-depths, the salinity of CDW in the ACC is increasing (Swart et al., 2018) and this change is being reflected in the salinity of shelf bottom waters on the WAP, and in the Bellingshausen and Amundsen Seas; rates of $0.01 - 0.04$ g kg^{-1} decade^{-1} have occurred since the 1990s (Schmidtko et al., 2014). Schmidtko et al. (2014) attribute the observed salinification to increases in the volume of CDW being delivered onto the shelf, in response to weak easterly / westerly winds that cause upward sloping isopycnals and a shoaling of the CDW layer. This tilt could also increase the number of instability-generated eddies mentioned in Section 6.2.1, however, it is possible that an increase in salinity may suppress the formation of instabilities.

The observed salinification of CDW in the ACC (Swart et al., 2018) and in WAP shelf bottom waters (Schmidtko et al., 2014) will directly impact the vertical mixing processes over the ridge discussed in Chapter 4. The waters on the WAP are salinity-stratified, so this increase in salinity could act to inhibit vertical mixing. For example, when conducting the same bulk heat flux calculation as in Section 6.2.1, but rather than changing temperature, increasing the core CDW salinity by 0.01 and 0.04 g kg^{-1} (the range observed by Schmidtko et al., 2014), leads to decreases in the upward heat flux over the ridge by 16% and 42% respectively (again assuming that no other processes change). However, when combining these salinity changes with the 0.1 $^{\circ}C$ increase in CDW temperature, the mean bulk upward heat flux over the ridge is altered by +45% and −10% respectively. This suggests that salinification could act against the observed increases in CDW temperature. Consequently, a better understanding of the regional salinity trends in Antarctica will be crucial for determining future marine-terminating glacier and ice shelf basal melt rates.

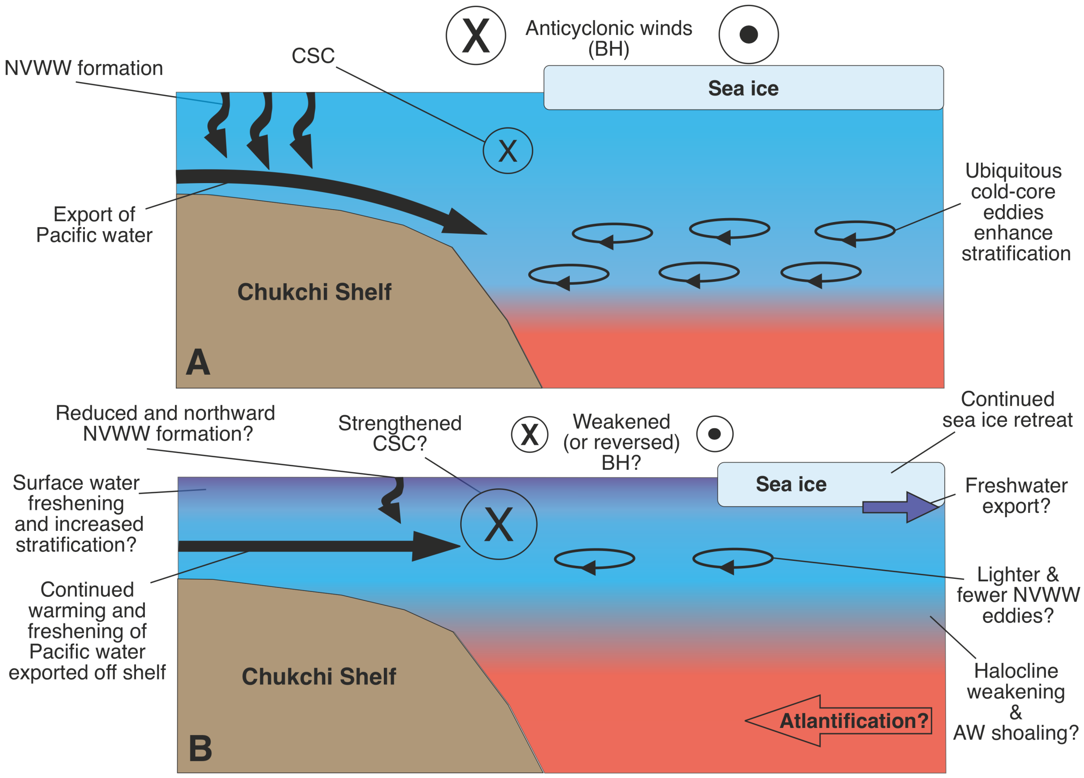

FIGURE 6.2: Schematic showing how shelf-ocean exchange on the Chukchi Shelf could change in the future. (A) Approximation of present processes. (B) Potential processes in the future. Please see the text for a detailed discussion on each of the changes shown. Please note that this simple schematic does not represent all of the processes or possible changes that might occur on the Chukchi Shelf in the future.

6.2.2.2 Arctic

The Arctic Ocean has experienced widespread freshening in recent years. The total freshwater content (relative to a salinity 34.8 PSU; approximately the top of the AW layer) has increased at a rate of 600 ± 300 km^3 year^{-1} between 1992 – 2012, with a third being attributed to a thickening of the freshwater layer and two thirds due to salinity decreases (Rabe et al., 2014; Haine et al., 2015; Carmack et al., 2016). This is largely observed in the western Arctic Ocean, in particular the Beaufort Gyre, where a 40% increase in the total freshwater content has occurred since the 1970s (Proshutinsky et al., 2020). This freshwater increase is associated with a strengthening of the Beaufort Gyre in response to anticyclonic winds in the Canada Basin and increased freshwater availability: from sea ice melt (10 – 20%), freshwater flux through the Bering Strait (5 – 50%), and from the Mackenzie River (5 – 50%; Krishfield et al., 2014; Proshutinsky et al., 2015; Woodgate, 2018; Proshutinsky et al., 2019).

The observed freshening in the Arctic is likely to impact both the warm and cold halocline ventilation mechanisms. Continued freshening of surface waters on the northern

Chukchi Shelf and Canada Basin margins will weaken the surface front and potentially inhibit the wind-driven halocline ventilation mechanism suggested by Timmermans et al. (2014, 2017). However, despite freshwater changes potentially influencing the wind-driven ventilation of the Arctic halocline, the water subducted through this mechanism is typically too fresh to ventilate the densest halocline regions.

The ability of cold-core anticyclonic eddies, such as the one focused on in Chapter 5, to ventilate the cold Arctic halocline could also change in response to freshwater changes. For example, freshening of surface waters in the Chukchi Sea region could increase surface stratification and potentially hinder NVWW formation, leading to lighter / fewer eddies with NVWW at their cores (Figure 6.2). Changes in salinity are perhaps more likely to affect the formation of eddies than changes in temperature given that the Arctic Ocean is salinity-stratified, though exactly how is not clear and would depend on which mechanism dominates eddy formation. As previously mentioned, baroclinic instability of boundary currents is perhaps the most likely eddy formation mechanism, with both the Chukchi and Beaufort shelfbreak jets and the Chukchi Slope Current all showing signs of baroclinic instability (e.g., Pickart et al., 2005; Spall et al., 2008; Corlett and Pickart, 2017). In order for baroclinic instability to occur, a necessary condition is that there must be a vertical change of sign in the cross-stream potential vorticity gradient within the current. Consequently, the stability of the boundary currents are sensitive to their potential vorticity structures (Spall et al., 2008). The potential vorticity of the boundary current waters in the free shelfbreak jet (in zero wind conditions) is primarily controlled by the stratification on the shelf where the waters originate; the weak stratification on the Chukchi shelf giving the water potential vorticity close to zero (Spall et al., 2008). Consequently, changes to the stratification on the shelf could affect the stability of these currents. An increase in stratification due to increased meltwater would increase the potential vorticity of the NVWW, potentially weakening potential vorticity gradients (depending on how the stratification in the basin changes), leading to a stabilisation of the current and resulting in the formation of fewer eddies through baroclinic instability.

6.2.3 Large-Scale Atmospheric Modes

6.2.3.1 Antarctic

Section 6.2.1 highlighted how changes to the SAM may alter heat content on the WAP, however, together with ENSO, such large-scale atmospheric climate modes are also thought to strongly control the Southern Ocean's freshwater distribution. The climatic modes control the WAP's atmospheric temperature, precipitation and winds, and therefore the sea ice and meteoric freshwater distribution. A $10-20\%$ increase in wind-driven northward transport of sea ice was observed between $1982-2008$, and is associated with a freshening of $2\times10^{-3}\pm1\times10^{-3}$ yr $^{-1}$ in surface and intermediate waters (Haumann et al., 2016). With westerly winds shifting further south (Fogt and Marshall, 2020), this northward transport of sea ice (and therefore freshwater) could increase (Figure 6.1. Additionally, van Wessem et al. (2017) find that when periods with positive SAM coincide with La Niña events, there are strong westerly winds and high snowfall over the WAP mountains, Marguerite Bay and the Bellingshausen Sea. However, when positive SAM periods coincide with El Niño events, northerly winds, warmer air and increased rainfall occurs over the ocean, whilst orographic snowfall over the WAP mountains increases (van Wessem et al., 2017). The APCC is a strong narrow current, forced by freshwater discharge, melting sea ice and downwelling-favourable winds in the spring / summer months (Moffat et al., 2008), and is therefore likely to change in response to changes in these large-scale wind patterns. A weakening of the APCC and its associated front may lead to easier access of CDW to marine-terminating glaciers in these regions (Figure 6.1), which otherwise can block dense CDW intrusion events (Moffat et al., 2009). However, with air temperatures continuing to rise, it is also possible that more freshwater will be discharged from glacier on the WAP and the APCC could strengthen. This could potentially further inhibit CDW intrusions and partially insulate the glaciers for basal melting. However, the exact extent of the APCC in Marguerite Bay is yet to be determined, and a better understanding of its along-shelf variability is required to understand how such changes may effect the vertical mixing processes studied in this work.

6.2.3.2 Arctic

Large-scale atmospheric climate modes also appear to be a dominant control on the Arctic freshwater distribution. Anticyclonic winds involved in the accumulation of freshwater in the centre of the Beaufort Gyre are associated with the Beaufort High (e.g., Timmermans and Marshall, 2020). The Beaufort High is coupled with the Icelandic Low, and their dominance shifts on timescales of $5-7$ years (Proshutinsky and Johnson, 1997), although the controlling mechanism is unclear (Proshutinsky et al., 2015). A strengthening of the Icelandic Low would cause a shift to a cyclonic wind regime and therefore weaken the anticyclonic winds associated with the Beaufort High that drive the Beaufort Gyre. Such a shift could lead to a release of the freshwater from the Beaufort Gyre's interior into the North Atlantic (Figure 6.2), which is thought could cause warming of the AW layer and increased penetration into the Arctic Ocean (Zhang et al., 1998). Such changes in AW have been observed (e.g., Morison et al., 1998) and would cause a weakening of the halocline. This has significant implications for its ventilation, as denser water would need to be fluxed from the shelf into the interior basin to prevent the upward mixing of heat towards the sea ice. Additionally, atmospheric warming and sea ice loss could lead to a weakened Beaufort High. A reversal of the anticyclonic winds in the Beaufort Gyre region was observed in winter 2017 (Moore et al., 2018). This was associated with high autumn air temperatures and reduced sea ice cover in October-December 2016, leading to an intensified low in the Barents Sea and increased propagation of low pressure (cyclonic) systems in the Beaufort Sea (Moore et al., 2018). Consequently, a future with higher air temperatures and less sea ice may result in less freshwater accumulation and a decrease in halocline ventilation in the Beaufort Gyre.

Changes to the large-scale wind patterns mentioned above will also affect circulation at the Chukchi shelfbreak and are therefore likely to influence the generation of cold-core eddies such as the one studied in Chapter 5. Li et al. (2019) show that circulation in the region is dependent on the wind stress curl on the Chukchi shelf; positive wind stress curl (associated with cyclonic winds) causes an enhanced westward slope current and reversed shelfbreak jet, whilst negative wind stress curl causes a strong eastward shelfbreak jet and weak slope current. Consequently, a weakening of the Beaufort High could increase the tendency for cyclonic winds and positive wind stress curl on the shelf, thereby strengthening the Chukchi Slope Current and reducing the number of eddies that could be generated by the Chukchi shelfbreak jet and exported into the Canada Basin interior (Figure 6.2). However, by altering the strength of the current, changes to prevailing winds may also shift the state of these boundary currents, potentially altering the likelihood for baroclinic instability. The winds may therefore change the boundary currents' ability to generate cold-core eddies and ventilate the cold halocline. Additionally, Boury et al. (2020) highlight the importance of considering both wind forcing and eddy-slope current interactions in the fate of the Chukchi Slope Current. They show that eddies have the ability to temporarily slow down the slope current, and expel water away from main flow, which otherwise likely ends up becoming entrained into the Beaufort Gyre. Consequently, eddies such as the one studied in Chapter 5 may be of greater importance for determining the region of cold halocline ventilation.

6.2.4 Sea Ice and Mixing Rates

6.2.4.1 Antarctic

Chapter 4 documents a two-stage upward heat flux within Ryder Bay: a persistent flux over the ridge, likely associated with a hydraulic control scenario; and an intermittent, usually weaker cross-thermocline flux linked to strong wind forcing events that releases heat into the overlying winter mixed layer. Waters in this layer can come into direct contact with the atmosphere (during winter, when the mixed layer is deeper), ice shelves at similar depths, and marine-terminating glaciers (Sheldon Glacier's grounding line is thought to be $\sim$ 200 m). This result, in conjunction with the comparable magnitude of the observed heat fluxes and those commonly associated with the ice shelf melting (8 W m^{-2}; Jenkins and Jacobs, 2008), highlights the potential importance of a two-stage upwards heat flux triggered by ridge-flow interaction and wind forcing for the WAP heat budget. However, there are other factors that can influence vertical mixing rates which must also be considered.

Variations in sea ice extent have the potential to significantly impact the vertical mixing mechanisms mentioned above. Sea ice inhibits momentum transfer between the atmosphere and the ocean, and can therefore reduce wind-driven vertical mixing (Venables and Meredith, 2014). Trends in Antarctic sea ice extent are uncertain, with a significant positive trend being observed between 1979 − 2015 (Comiso et al., 2017) and a drop to below average coverage occurring and persisting since 2016 (e.g., Turner et al., 2017), however, the WAP's sea ice season is getting shorter (Stammerjohn et al., 2008). Decreases in sea ice extent leave the surface of the ocean exposed to storm events for longer periods, so there is a greater potential for wind-driven near-inertial shear to cause vertical mixing (Venables and Meredith, 2014; Brearley et al., 2017) and an upward flux of heat across the thermocline towards ice (Figure 6.1). Additionally, given the shift to a greater positive SAM index (Lefebvre et al., 2004), an increase in storm activity on the WAP could lead to a greater number of intense storms than penetrate deeper into the water column. Indeed, greater mixed layer depths are observed during SAM and ENSO extremes (Moffat and Meredith, 2018). This could enhance the wind-driven near-inertial shear and lead to greater upward heat fluxes across the thermocline.

Reduced sea ice coverage may expose the water column to increased wind-driven vertical mixing, however, there is a balance between this process and the increased stratification associated with the low-density freshwater that accumulates at the surface as sea ice melts. Section 6.2.2 suggests that the freshwater distribution is strongly controlled by northward wind-driven transport of sea ice (Haumann et al., 2016). Recent studies have highlighted the importance of considering such freshwater fluxes on vertical mixing (Haumann et al., 2020; Schultz et al., 2020). Schultz et al. (2020) show that capturing sea ice volume and redistribution is critical for successfully reproducing the MLD in ocean models, and Moffat and Meredith (2018) suggest that the MLD is necessary for understanding observed meteoric water concentrations. Additionally, Haumann et al. (2020) find that the increased stratification associated with sea ice melt can act as an insulator, preventing vertical mixing of the colder overlying surface water, leading to warming of the subsurface waters. Haumann et al. (2020) suggest that this process is particularly prevalent on the WAP. The increased stratification from sea ice melt could therefore explain the 0.6 W m^{-2} yr^{-1} decreasing trend in ocean to atmosphere heat flux observed on the WAP between 1993 − 2004 (Martinson et al., 2008), and is thought to account for 8 ± 2% of the observed global ocean warming between 1982 − 2011 (Haumann et al., 2020). CDW enters Ryder Bay having first been advected through Marguerite Trough and Laubeuf Fjord, both of which contain many ridges where vertical mixing could occur (Venables et al., 2017). Consequently, these ridges are likely to be hotspots for bringing heat to the base of the thermocline in a similar way as outlined above. However, the increased stratification, due to the northward drift and then subsequent melting of sea ice, may prevent the second stage of the upward heat flux mechanism occurring (suggested in Chapter 4, the thermocline dissipation caused by wind-driven near-inertial shear). This could result in less heat getting released across the thermocline on the outer shelf, thereby delivering more heat to the base of the marine-terminating glaciers and ice shelves.

6.2.4.2 Arctic

Unlike the Southern Ocean, the Arctic Ocean has experienced sustained sea ice loss across all seasons since 1979 (Stroeve and Notz, 2018, and Figure 1.3). The ice loss has similar implications for vertical mixing and the balance between increased wind-driven momentum and increased stratification, and has the potential for altering the strength of the cold halocline. The interior Arctic Ocean, particularly the Canada Basin (Peralta-Ferriz and Woodgate, 2015; Timmermans and Marshall, 2020), is strongly stratified and is typified by low vertical mixing (e.g., Padman, 1995), and heat fluxes between the underlying AW in the Pacific water are dominated by double-diffusive convection (e.g., Timmermans et al., 2008). This low mixing state could be altered as the Arctic Ocean moves towards a future with ice-free summers (e.g., Rainville et al., 2011). Indeed, record low sea ice coverage and strong cyclonic storms in the summer of 2012 led to an enhancement of internal waves (Lincoln et al., 2016). However, due to the stratification being too great, this did not translate into elevated mixing rates away from topography, and thermohaline staircases were still observed (Lincoln et al., 2016). Peralta-Ferriz and Woodgate (2015) highlight the importance of freshwater changes over wind variations in determining Arctic mixed layer depths, and suggest that the observed surface freshening has lead to a shoaling of the Arctic mixed layer at a rate of $0.5 - 1$ m yr^{-1} between $1979 - 2012$. However, Rainville et al. (2011) point out that thinner mixed layers could lead to more effective momentum transfer and injection of near-inertial energy into the Arctic water column.

Similar inhibition of vertical mixing does not appear to be the case in the Eurasian Basin, where the stratification is weaker than in the Canada Basin (Peralta-Ferriz and Woodgate, 2015; Timmermans and Marshall, 2020). Polyakov et al. (2020a) observe enhanced current velocities and increased vertical shear in the upper 50 m of the ocean, particularly at the near-inertial frequencies, that are associated with with increased coupling of wind, ice and the upper ocean between $2004 - 2018$. This strengthening of the upper ocean currents and shear coincides, for the first time, with a weakening of stratification (Polyakov et al., 2020a). These changes concurrently occurred with a weakening of the cold halocline, associated with increased winter convection through brine rejection and upwelling of the AW layer (Atlantification; Polyakov et al., 2020b). This enhanced winter vertical mixing and increased upward heat fluxes between the AW and the cold halocline from $3-4$ W m^{-2}, to >10 W m^{-2} between $2007-2008$ and $2016-2018$, respectively (Polyakov et al., 2020b). Despite similar observations not yet being observed in the Canada Basin, if sea ice, wind trends and AW shoaling continue, a weakening of the cold halocline in the region may be observed, potentially releasing AW heat and leading to further rapid melting of Arctic sea ice. As outlined in Section 1.2, this would have major implications both for local ecosystems (e.g., by altering the predator-prey distributions; Hamilton et al., 2017) and for global climate.

6.3 Future Research

The automated processing algorithm developed in this thesis has only been used with the Ryder Bay dataset, the focus of this thesis, and the small Oban test dataset. Consequently, the processing algorithm, and in particular the QAA, could likely be improved by using it to process additional datasets. For example, the thresholds used to compare the shear spectra with the empirically derived Nasmyth spectra (Nasmyth, 1970) could be automatically adjusted depending on the expected background dissipation levels. The speed and error handling of the automated algorithm could also possibly be improved. The methodology could also be further developed into a machine learning algorithm, which could be trained to accept, reject, and process the greater volumes of shear spectra that can be expected in the future.

The Ryder Bay work in this thesis highlights the importance of considering topographic ridges in the WAP oceanic heat budget. Multiple similar ridges exist across the WAP continental shelf (Venables et al., 2017), so it is likely there are many hotspots for bringing CDW heat to the base of the thermocline. Quantifying the dissipation, vertical mixing rates and corresponding heat flux over these additional ridges will enable assessment of how representative the Ryder Bay data are for reliably scaling up the results. Microstructure equipped gliders are likely the best way to obtain these observations in the future, with their ability to travel long distances and ship time becoming more limited. For example, it might be that as the CDW is modified by vertical mixing over upstream ridges, less heat is available to be fluxed upwards over downstream ridges towards the coast. This could lead to reduced heat fluxes close the end point for CDW (i.e., near Ryder Bay), and larger heat fluxes closer to the shelfbreak and source of CDW. Once we have established how representative the observations over the ridge at Ryder Bay's entrance are, parameterisations of mixing in both small-scale process and large-scale climate models can be improved. Future work could also focus on how (if at all) the heat fluxes over the ridges are changing as the CDW warms, has a higher salinity, and becomes more readily available on the WAP.

Another big question is how representative are the wind-driven upwelling / downwelling and near-inertial shear processes within Ryder Bay compared to similar embayments along the WAP? Observations from additional bays on the WAP, such as Börgen Bay (Anvers Island) and Potter Cove (Kind George Island), would help to answer this question, and could be used in conjunction with the Ryder Bay datasets to assess how well regional models capture the observed processes. Satellite data could be used to identify bays that have reduced sea ice coverage in summer, and therefore areas where similar wind-driven processes may be occurring. Additionally, as under ice navigation for gliders is further developed, future work could better quantify how the mechanisms discussed here vary between seasons, in particular during wintertime when there are very limited observations. For example, would longer ice free periods and increased influence of winter storms lead to more intense vertical mixing, or would increased surface freshwater, both from sea ice melt and glacial discharge, increase stratification and inhibit vertical mixing?

The work focusing on the cold-core Arctic eddy in the Chukchi Sea provides a useful insight into the three-dimensional structure of such eddies. However, several questions still remain. The eddy being located on the seaward side of the Chukchi Slope Current perhaps suggests that it most likely originated from Barrow Canyon, though as previously suggested, multiple formation mechanisms and locations are possible. For example, eddies could also form to the west and east in the Chukchi and Beaufort shelfbreak jets, respectively. More work is therefore necessary to determine which of the eddy formation mechanisms dominate; i.e. how often do they form the cold-core eddies? This would require year-round identification of eddies and therefore wintertime measurements (this could be a possible application for gliders in the future). Understanding the dominant eddy formation mechanisms would help uncover the relative importance of the eddies compared to other ventilation mechanisms, such as advection from the Chukchi Slope Current. It would also be valuable to determine the likelihood of eddy-slope current interactions similar to that observed in Chapter 5, and the role they may have on both an eddy’s lifespan and the fate of the Chukchi Slope Current. Answering these questions will provide us with a better understanding of the primary region for halocline ventilation in the Arctic Ocean.

Bibliography

Aagaard, K., L. K. Coachman, and E. Carmack, 1981: On the halocline of the arctic ocean. *Deep Sea Research Part A. Oceanographic Research Papers*, **28 (6)**, 529–545.

Aksenov, Y., V. V. Ivanov, A. J. G. Nurser, S. Bacon, I. V. Polyakov, A. C. Coward, A. C. Naveira Garabato, and A. Beszczynska-Moeller, 2011: The arctic circumpolar boundary current. *Journal of Geophysical Research: Oceans*, **116 (C9)**.

Alford, M. H., 2001: Internal swell generation: The spatial distribution of energy flux from the wind to mixed layer near-inertial motions. *Journal of Physical Oceanography*, **31 (8)**, 2359–2368.

Alford, M. H., 2003: Improved global maps and 54-year history of wind-work on ocean inertial motions. *Geophysical Research Letters*, **30 (8)**.

Allen, J. S., 1975: Coastal trapped waves in a stratified ocean. *Journal of Physical Oceanography*, **5 (2)**, 300–325.

Anderson, L. G., P. S. Andersson, G. Björk, E. P. Jones, S. Jutterström, and I. Wåhlström, 2013: Source and formation of the upper halocline of the arctic ocean. *Journal of Geophysical Research: Oceans*, **118 (1)**, 410–421.

Armi, L., 1986: The hydraulics of two flowing layers with different densities. *Journal of Fluid Mechanics*, **163**, 27–58.

Armitage, T. W. K., S. Bacon, A. L. Ridout, A. A. Petty, S. Wolbach, and M. Tsamados, 2017: Arctic ocean surface geostrophic circulation 2003–2014. *The Cryosphere*, **11 (4)**, 1767–1780.

Armitage, T. W. K., R. Kwok, A. F. Thompson, and G. Cunningham, 2018: Dynamic topography and sea level anomalies of the southern ocean: Variability and teleconnections. *Journal of Geophysical Research: Oceans*, **123 (1)**, 613–630.

Arneborg, L. and B. Liljebladh, 2001: The internal seiches in gullmar fjord. part ii: Contribution to basin water mixing. *Journal of Physical Oceanography*, **31 (9)**, 2567 – 2574.

Arneborg, L., A. K. Wåhlin, G. Björk, B. Liljebladh, and A. H. Orsi, 2012: Persistent inflow of warm water onto the central amundsen shelf. *Nature Geoscience*, **5 (12)**, 876.

Arrigo, K. R., M. M. Mills, G. L. van Dijken, K. E. Lowry, R. S. Pickart, and R. Schlitzer, 2017: Late spring nitrate distributions beneath the ice-covered northeastern chukchi shelf. *Journal of Geophysical Research: Biogeosciences*, **122 (9)**, 2409–2417.

Årthun, M., T. Eldevik, and L. H. Smedsrud, 2019: The role of atlantic heat transport in future arctic winter sea ice loss. *Journal of Climate*, **32 (11)**, 3327–3341.

Årthun, M., T. Eldevik, L. H. Smedsrud, Ø. Skagseth, and R. B. Ingvaldsen, 2012: Quantifying the influence of atlantic heat on barents sea ice variability and retreat. *Journal of Climate*, **25 (13)**, 4736–4743.

Bamber, J. L., R. E. M. Riva, B. L. A. Vermeersen, and A. M. LeBrocq, 2009: Reassessment of the potential sea-level rise from a collapse of the west antarctic ice sheet. *Science*, **324 (5929)**, 901–903.

Bamber, J. L., R. M. Westaway, B. Marzeion, and B. Wouters, 2018: The land ice contribution to sea level during the satellite era. *Environmental Research Letters*, **13 (6)**, 063 008.

Barton, B. I., Y.-D. Lenn, and C. Lique, 2018: Observed atlantification of the barents sea causes the polar front to limit the expansion of winter sea ice. *Journal of Physical Oceanography*, **48 (8)**, 1849–1866.

Bebieva, Y. and K. Speer, 2019: The regulation of sea ice thickness by double-diffusive processes in the ross gyre. *Journal of Geophysical Research: Oceans*, **124 (10)**, 7068–7081.

Bénard, F., J.-P. Callot, R. Vially, J. Schmitz, W. Roest, M. Patriat, and B. Loubrieu, 2010: The kerguelen plateau: Records from a long-living/composite microcontinent. *Marine and Petroleum Geology*, **27 (3)**, 633 – 649.

Berens, P., 2009: Circstat: a matlab toolbox for circular statistics. *J Stat Softw*, **31 (10)**, 1–21.

Berrisford, P., D. Dee, K. Fielding, M. Fuentes, P. Kallberg, S. Kobayashi, and S. Uppala, 2009: The era-interim archive. Technical report, ECMWF, 1-16 pp., Shinfield Park, Reading.

Bohoyo, F., et al., 2019: Morphological and geological features of drake passage, antarctica, from a new digital bathymetric model. *Journal of Maps*, **15 (2)**, 49–59.

Bourassa, M. A., et al., 2013: High-latitude ocean and sea ice surface fluxes: Challenges for climate research. *Bulletin of the American Meteorological Society*, **94 (3)**, 403–423.

Boury, S., et al., 2020: Whither the chukchi slope current? *Journal of Physical Oceanography*, **50 (6)**, 1717–1732.

Brandt, A., et al., 2011: Maud rise - a snapshot through the water column. *Deep Sea Research Part II: Topical Studies in Oceanography*, **58 (19-20)**, 1962–1982.

Brearley, J. A., M. P. Meredith, A. C. N. Garabato, H. J. Venables, and M. E. Inall, 2017: Controls on turbulent mixing on the west antarctic peninsula shelf. *Deep Sea Research Part II: Topical Studies in Oceanography*, **139**, 18–30.

Brearley, J. A., C. Moffat, H. J. Venables, M. P. Meredith, and M. S. Dinniman, 2019: The role of eddies and topography in the export of shelf waters from the west antarctic peninsula shelf. *Journal of Geophysical Research: Oceans*, **124 (11)**, 7718–7742.

Brugler, E. T., R. S. Pickart, G. W. K. Moore, S. Roberts, T. J. Weingartner, and H. Statscewich, 2014: Seasonal to interannual variability of the pacific water boundary current in the beaufort sea. *Progress in Oceanography*, **127**, 1–20.

Carmack, E., et al., 2015: Toward quantifying the increasing role of oceanic heat in sea ice loss in the new arctic. *Bulletin of the American Meteorological Society*, **96 (12)**, 2079–2105.

Carmack, E. C., et al., 2016: Freshwater and its role in the arctic marine system: Sources, disposition, storage, export, and physical and biogeochemical consequences in the arctic and global oceans. *Journal of Geophysical Research: Biogeosciences*, **121 (3)**, 2169–8953.

Carpenter, J. R. and M.-L. Timmermans, 2012: Deep mesoscale eddies in the canada basin, arctic ocean. *Geophysical Research Letters*, **39 (20)**.

Cenedese, C. and J. A. Whitehead, 2000: Eddy shedding from a boundary current around a cape over a sloping bottom. *Journal of Physical Oceanography*, **30 (7)**, 1514–1531.

Chao, S. Y. and P. T. Shaw, 2003: A numerical study of dense water outflows and halocline anticyclones in an arctic baroclinic slope current. *Journal of Geophysical Research: Oceans*, **108 (C7)**.

Chereskin, T. K. and D. Roemmich, 1991: A comparison of measured and wind-derived ekman transport at 11 n in the atlantic ocean. *Journal of Physical Oceanography*, **21 (6)**, 869–878.

Cochran, J. R., M. H. Edwards, and B. J. Coakley, 2006: Morphology and structure of the lomonosov ridge, arctic ocean. *Geochemistry, Geophysics, Geosystems*, **7 (5)**.

Cochran, P., O. H. Huntington, C. Pungowiyi, S. Tom, F. S. Chapin, H. P. Huntington, N. G. Maynard, and S. F. Trainor, 2013: Indigenous frameworks for observing and responding to climate change in alaska. *Climate Change and Indigenous Peoples in the United States*, Springer, 49–59.

Codiga, D. L., 2011: *Unified tidal analysis and prediction using the UTide Matlab functions*. Graduate School of Oceanography, University of Rhode Island Narragansett, RI.

Codispoti, L. A., C. Flagg, V. Kelly, and J. H. Swift, 2005: Hydrographic conditions during the 2002 sbi process experiments. *Deep Sea Research Part II: Topical Studies in Oceanography*, **52 (24)**, 3199 – 3226.

Comiso, J. C., R. A. Gersten, L. V. Stock, J. Turner, G. J. Perez, and K. Cho, 2017: Positive trend in the antarctic sea ice cover and associated changes in surface temperature. *Journal of Climate*, **30 (6)**, 2251–2267.

Cook, A. J., A. J. Fox, D. G. Vaughan, and J. G. Ferrigno, 2005: Retreating glacier fronts on the antarctic peninsula over the past half-century. *Science*, **308 (5721)**, 541–544.

Cook, A. J., P. R. Holland, M. P. Meredith, T. Murray, A. Luckman, and D. G. Vaughan, 2016: Ocean forcing of glacier retreat in the western antarctic peninsula. *Science*, **353 (6296)**, 283–286.

Cooper, L. W., T. E. Whitledge, J. M. Grebmeier, and T. Weingartner, 1997: The nutrient, salinity, and stable oxygen isotope composition of bering and chukchi seas waters in and near the bering strait. *Journal of Geophysical Research: Oceans*, **102 (C6)**, 12 563–12 573.

Corlett, W. B. and R. S. Pickart, 2017: The chukchi slope current. *Progress in Oceanography*, **153**, 50–65.

Couto, N., D. G. Martinson, J. Kohut, and O. Schofield, 2017: Distribution of upper circumpolar deep water on the warming continental shelf of the west antarctic peninsula. *Journal of Geophysical Research: Oceans*, **122 (7)**, 5306–5315.

Cushman-Roisin, B. and J.-M. Beckers, 2011: *Introduction to geophysical fluid dynamics: physical and numerical aspects*. Academic press, Oxford, UK.

D'Asaro, E. A., 1985: The energy flux from the wind to near-inertial motions in the surface mixed layer. *Journal of Physical Oceanography*, **15 (8)**, 1043–1059.

D'Asaro, E. A., 1988: Observations of small eddies in the beaufort sea. *Journal of Geophysical Research: Oceans*, **93 (C6)**, 6669–6684.

de Boer, B., P. Stocchi, P. L. Whitehouse, and R. S. W. van de Wal, 2017: Current state and future perspectives on coupled ice-sheet–sea-level modelling. *Quaternary Science Reviews*, **169**, 13–28.

De Lavergne, C., J. B. Palter, E. D. Galbraith, R. Bernardello, and I. Marinov, 2014: Cessation of deep convection in the open southern ocean under anthropogenic climate change. *Nature Climate Change*, **4 (4)**, 278–282.

Depoorter, M. A., J. L. Bamber, J. A. Griggs, J. T. M. Lenaerts, S. R. M. Ligtenberg, M. R. Van den Broeke, and G. Moholdt, 2013: Calving fluxes and basal melt rates of antarctic ice shelves. *Nature*, **502 (7469)**, 89.

Deser, C., R. A. Tomas, and L. Sun, 2015: The role of ocean–atmosphere coupling in the zonal-mean atmospheric response to arctic sea ice loss. *Journal of Climate*, **28 (6)**, 2168–2186.

Dinniman, M. S. and J. M. Klinck, 2004: A model study of circulation and cross-shelf exchange on the west antarctic peninsula continental shelf. *Deep Sea Research Part II: Topical Studies in Oceanography*, **51 (17-19)**, 2003–2022.

Dinniman, M. S., J. M. Klinck, and W. O. Smith, 2011: A model study of circumpolar deep water on the west antarctic peninsula and ross sea continental shelves. *Deep Sea Research Part II: Topical Studies in Oceanography*, **58 (13)**, 1508–1523.

Dmitrenko, I. A., et al., 2016: Shelfbreak current over the canadian beaufort sea continental slope: Wind-driven events in january 2005. *Journal of Geophysical Research: Oceans*, **121 (4)**, 2447–2468.

Donohue, K. A., K. L. Tracey, D. R. Watts, M. P. Chidichimo, and T. K. Chereskin, 2016: Mean antarctic circumpolar current transport measured in drake passage. *Geophysical Research Letters*, **43 (22)**, 11,760–11,767.

Dotto, T. S., et al., 2018: Variability of the ross gyre, southern ocean: Drivers and responses revealed by satellite altimetry. *Geophysical Research Letters*, **45 (12)**, 6195–6204.

Dotto, T. S., et al., 2019: Wind-driven processes controlling oceanic heat delivery to the amundsen sea, antarctica. *Journal of Physical Oceanography*, **49 (11)**, 2829–2849.

Dupont, T. K. and R. B. Alley, 2005: Assessment of the importance of ice-shelf buttressing to ice-sheet flow. *Geophysical Research Letters*, **32 (4)**.

Ekman, V. W., 1905: On the influence of the earth's rotation on ocean-currents. *Arch. Mach. Astron. Phys.*, **2 (11)**, 1–53.

Emery, W. J. and R. E. Thomson, 2004: *Data analysis methods in physical oceanography*. Elsevier, Amsterdam.

Evans, C. A., J. E. O'Reilly, and J. P. Thomas, 1987: *Part 1, A Handbook for the measurement of chlorophyll a in netplankton and nannoplankton*, BIOMASS Scientific Series, Vol. 8. College Station, TX (USA) Texas A&M Univ., 3-46 pp.

Farinotti, D., M. Huss, J. J. Fürst, J. Landmann, H. Machguth, F. Maussion, and A. Pandit, 2019: A consensus estimate for the ice thickness distribution of all glaciers on earth. *Nature Geoscience*, **12 (3)**, 168–173.

Farmer, D. M. and R. A. Denton, 1985: Hydraulic control of flow over the sill in observatory inlet. *Journal of Geophysical Research: Oceans*, **90 (C5)**, 9051–9068.

Farmer, D. M. and J. D. Smith, 1980: Tidal interaction of stratified flow with a sill in knight inlet. *Deep Sea Research Part A. Oceanographic Research Papers*, **27 (3)**, 239 – 254.

Feldmann, J. and A. Levermann, 2015: Collapse of the west antarctic ice sheet after local destabilization of the amundsen basin. *Proceedings of the National Academy of Sciences*, **112 (46)**, 14 191–14 196.

Fer, I., A. K. Peterson, and J. E. Ullgren, 2014: Microstructure measurements from an underwater glider in the turbulent faroe bank channel overflow. *Journal of Atmospheric and Oceanic Technology*, **31 (5)**, 1128–1150.

Fer, I., G. Voet, K. S. Seim, B. Rudels, and K. Latarius, 2010: Intense mixing of the faroe bank channel overflow. *Geophysical Research Letters*, **37 (2)**.

Ferrari, R., M. F. Jansen, J. F. Adkins, A. Burke, A. L. Stewart, and A. F. Thompson, 2014: Antarctic sea ice control on ocean circulation in present and glacial climates. *Proceedings of the National Academy of Sciences*, **111 (24)**, 8753–8758.

Ferrari, R. and C. Wunsch, 2009: Ocean circulation kinetic energy: Reservoirs, sources, and sinks. *Annual Review of Fluid Mechanics*, **41 (1)**, 253–282.

Fiedler, P. C., 2010: Comparison of objective descriptions of the thermocline. *Limnology and Oceanography: Methods*, **8 (6)**, 313–325.

Fine, E. C., J. A. MacKinnon, M. H. Alford, and J. B. Mickett, 2018: Microstructure observations of turbulent heat fluxes in a warm-core canada basin eddy. *Journal of Physical Oceanography*, **48 (10)**, 2397–2418.

Fogt, R. L. and G. J. Marshall, 2020: The southern annular mode: Variability, trends, and climate impacts across the southern hemisphere. *WIREs Climate Change*, **11 (4)**, e652.

Forryan, A., A. C. Naveira Garabato, K. L. Polzin, and S. Waterman, 2015: Rapid injection of near-inertial shear into the stratified upper ocean at an antarctic circumpolar current front. *Geophysical Research Letters*, **42 (9)**, 3431–3441.

Foukal, N. P., R. S. Pickart, G. W. K. Moore, and P. Lin, 2019: Shelfbreak downwelling in the alaskan beaufort sea. *Journal of Geophysical Research: Oceans*, **124 (10)**, 7201–7225.

Fraser, N. J., M. E. Inall, M. G. Magaldi, T. W. N. Haine, and S. C. Jones, 2018: Wintertime fjord-shelf interaction and ice sheet melting in southeast greenland. *Journal of Geophysical Research: Oceans*, **123 (12)**, 9156–9177.

Fremand, A., 2020: Gridded bathymetric compilation of ryder bay from raw and processed multibeam echosounder data collected by the rrs james clark ross (2001 - 2016) [data set]. UK Polar Data Centre.

Fretwell, P., et al., 2013: Bedmap2: improved ice bed, surface and thickness datasets for antarctica. *The Cryosphere*, **7 (1)**, 375–393.

Frölicher, T. L., J. L. Sarmiento, D. J. Paynter, J. P. Dunne, J. P. Krasting, and M. Winton, 2015: Dominance of the southern ocean in anthropogenic carbon and heat uptake in cmip5 models. *Journal of Climate*, **28 (2)**, 862–886.

Garau, B., S. Ruiz, W. G. Zhang, A. Pascual, E. Heslop, J. Kerfoot, and J. Tintoré, 2011: Thermal lag correction on slocum ctd glider data. *Journal of Atmospheric and Oceanic Technology*, **28 (9)**, 1065–1071.

Gill, A. E., 1982: *Atmosphere—ocean dynamics*. Academic Press Inc, London.

Gille, S. T., 2008: Decadal-scale temperature trends in the southern hemisphere ocean. *Journal of Climate*, **21 (18)**, 4749–4765.

Gong, D. and R. S. Pickart, 2016: Early summer water mass transformation in the eastern chukchi sea. *Deep Sea Research Part II: Topical Studies in Oceanography*, **130**, 43–55.

Goodman, L., E. R. Levine, and R. G. Lueck, 2006: On measuring the terms of the turbulent kinetic energy budget from an auv. *Journal of Atmospheric and Oceanic Technology*, **23 (7)**, 977–990.

Gordon, A. L., 1971: *Oceanography of Antarctic waters*. Wiley Online Library.

Graham, J. A., M. S. Dinniman, and J. M. Klinck, 2016: Impact of model resolution for on-shelf heat transport along the west antarctic peninsula. *Journal of Geophysical Research: Oceans*, **121 (10)**, 7880–7897.

Gregg, M. C. and J. M. Klymak, 2014: Mode-2 hydraulic control of flow over a small ridge on a continental shelf. *Journal of Geophysical Research: Oceans*, **119 (11)**, 8093–8108.

Gregg, M. C., T. B. Sanford, and D. P. Winkel, 2003: Reduced mixing from the breaking of internal waves in equatorial waters. *Nature*, **422 (6931)**, 513–515.

Haine, T. W. N., et al., 2015: Arctic freshwater export: Status, mechanisms, and prospects. *Global and Planetary Change*, **125**, 13 – 35.

Hamilton, C. D., K. M. Kovacs, R. A. Ims, J. Aars, and C. Lydersen, 2017: An arctic predator–prey system in flux: climate change impacts on coastal space use by polar bears and ringed seals. *Journal of Animal Ecology*, **86 (5)**, 1054–1064.

Haumann, F. A., N. Gruber, and M. Münnich, 2020: Sea-ice induced southern ocean subsurface warming and surface cooling in a warming climate. *AGU Advances*, **1 (2)**, e2019AV000 132.

Haumann, F. A., N. Gruber, M. Münnich, I. Frenger, and S. Kern, 2016: Sea-ice transport driving southern ocean salinity and its recent trends. *Nature*, **537 (7618)**, 89–92.

Hersbach, H., et al., 2020: The era5 global reanalysis. *Quarterly Journal of the Royal Meteorological Society*, **146 (730)**, 1999–2049.

Hogg, A. M. and P. D. Killworth, 2004: Continuously stratified exchange flow through a contraction in a channel. *Journal of Fluid Mechanics*, **499**, 257–276.

Hogg, A. M., M. P. Meredith, D. P. Chambers, E. P. Abrahamsen, C. W. Hughes, and A. K. Morrison, 2015: Recent trends in the southern ocean eddy field. *Journal of Geophysical Research: Oceans*, **120 (1)**, 257–267.

Hogg, A. M. C., M. P. Meredith, J. R. Blundell, and C. Wilson, 2008: Eddy heat flux in the southern ocean: Response to variable wind forcing. *Journal of Climate*, **21 (4)**, 608–620.

Holm-Hansen, O., C. J. Lorenzen, R. W. Holmes, and J. D. H. Strickland, 1965: Fluorometric determination of chlorophyll. *ICES Journal of Marine Science*, **30 (1)**, 3–15.

Hosking, J. S., A. Orr, G. J. Marshall, J. Turner, and T. Phillips, 2013: The influence of the amundsen–bellingshausen seas low on the climate of west antarctica and its representation in coupled climate model simulations. *Journal of Climate*, **26 (17)**, 6633–6648.

Howard, S. L., J. Hyatt, and L. Padman, 2004: Mixing in the pycnocline over the western antarctic peninsula shelf during southern ocean globec. *Deep Sea Research Part II: Topical Studies in Oceanography*, **51 (17-19)**, 1965–1979.

Huppert, H. E. and J. S. Turner, 1981: Double-diffusive convection. *Journal of Fluid Mechanics*, **106**, 299–329.

Huss, M. and D. Farinotti, 2012: Distributed ice thickness and volume of all glaciers around the globe. *Journal of Geophysical Research: Earth Surface*, **117 (F4)**.

Huss, M. and D. Farinotti, 2014: A high-resolution bedrock map for the antarctic peninsula. *The Cryosphere*, **8 (4)**, 1261–1273.

Hyatt, J., R. C. Beardsley, and W. B. Owens, 2011: Characterization of sea ice cover, motion and dynamics in marguerite bay, antarctic peninsula. *Deep Sea Research Part II: Topical Studies in Oceanography*, **58 (13-16)**, 1553–1568.

Inall, M. E., T. Murray, F. R. Cottier, K. Scharrer, T. J. Boyd, K. J. Heywood, and S. L. Bevan, 2014: Oceanic heat delivery via kangerdlugssuaq fjord to the south-east greenland ice sheet. *Journal of Geophysical Research: Oceans*, **119 (2)**, 631–645.

Inall, M. E., F. Nilsen, F. R. Cottier, and R. Daae, 2015: Shelf/fjord exchange driven by coastal-trapped waves in the arctic. *Journal of Geophysical Research: Oceans*, **120 (12)**, 8283–8303.

Jacobs, S. S., 1991: On the nature and significance of the antarctic slope front. *Marine Chemistry*, **35 (1-4)**, 9–24.

Jacobs, S. S., C. F. Giulivi, and P. A. Mele, 2002: Freshening of the ross sea during the late 20th century. *Science*, **297 (5580)**, 386–389.

Jacobs, S. S., A. Jenkins, C. F. Giulivi, and P. Dutrieux, 2011: Stronger ocean circulation and increased melting under pine island glacier ice shelf. *Nature Geoscience*, **4 (8)**, 519.

Jakobsson, M., A. Grantz, A. Y. Kristoersen, and R. Macnab, 2004: *Bathymetry and physiography of the arctic ocean and its constituent seas*. Springer, Heidelberg, 1-6 pp.

Jakobsson, M., L. Mayer, B. Coakley, J. A. Dowdeswell, S. Forbes, B. Fridman, and et al., 2012: The international bathymetric chart of the arctic ocean (ibcao) version 3.0. *Geophysical Research Letters*, **39 (12)**.

Jenkins, A. and S. Jacobs, 2008: Circulation and melting beneath george vi ice shelf, antarctica. *Journal of Geophysical Research: Oceans*, **113 (C04013)**.

Jing, Z., P. Chang, S. F. DiMarco, and L. Wu, 2015: Role of near-inertial internal waves in subthermocline diapycnal mixing in the northern gulf of mexico. *Journal of Physical Oceanography*, **45 (12)**, 3137–3154.

Jones, E. P. and L. G. Anderson, 1986: On the origin of the chemical properties of the arctic ocean halocline. *Journal of Geophysical Research: Oceans*, **91 (C9)**, 10 759–10 767.

Joughin, I., B. E. Smith, and B. Medley, 2014: Marine ice sheet collapse potentially under way for the thwaites glacier basin, west antarctica. *Science*, **344 (6185)**, 735–738.

Jullion, L., S. C. Jones, A. C. Naveira Garabato, and M. P. Meredith, 2010: Wind-controlled export of antarctic bottom water from the weddell sea. *Geophysical Research Letters*, **37 (9)**.

Kadko, D., R. S. Pickart, and J. T. Mathis, 2008: Age characteristics of a shelf-break eddy in the western arctic and implications for shelf-basin exchange. *Journal of Geophysical Research: Oceans*, **113 (C2)**.

Kawaguchi, Y., M. Itoh, and S. Nishino, 2012: Detailed survey of a large baroclinic eddy with extremely high temperatures in the western canada basin. *Deep Sea Research Part I: Oceanographic Research Papers*, **66**, 90–102.

Kelly, S. M., P. F. J. Lermusiaux, T. F. Duda, and P. J. Haley Jr, 2016: A coupled-mode shallow-water model for tidal analysis: Internal tide reflection and refraction by the gulf stream. *Journal of Physical Oceanography*, **46 (12)**, 3661–3679.

Klinck, J. M. and M. S. Dinniman, 2010: Exchange across the shelf break at high southern latitudes. *Ocean Science*, **6 (2)**.

Klinck, J. M., E. E. Hofmann, R. C. Beardsley, B. Salihoglu, and S. Howard, 2004: Water-mass properties and circulation on the west antarctic peninsula continental shelf in austral fall and winter 2001. *Deep Sea Research Part II: Topical Studies in Oceanography*, **51 (17-19)**, 1925–1946.

Klymak, J. M. and M. C. Gregg, 2004: Tidally generated turbulence over the knight inlet sill. *Journal of Physical Oceanography*, **34 (5)**, 1135–1151.

Krishfield, R. A., A. Proshutinsky, K. Tateyama, W. J. Williams, E. C. Carmack, F. A. McLaughlin, and M.-L. Timmermans, 2014: Deterioration of perennial sea ice in the beaufort gyre from 2003 to 2012 and its impact on the oceanic freshwater cycle. *Journal of Geophysical Research: Oceans*, **119 (2)**, 1271–1305.

Kunze, E., E. Firing, J. M. Hummon, T. K. Chereskin, and A. M. Thurnherr, 2006: Global abyssal mixing inferred from lowered adcp shear and ctd strain profiles. *Journal of Physical Oceanography*, **36 (8)**, 1553–1576.

Kwok, R., G. Spreen, and S. Pang, 2013: Arctic sea ice circulation and drift speed: Decadal trends and ocean currents. *Journal of Geophysical Research: Oceans*, **118 (5)**, 2408–2425.

Langlais, C. E., S. R. Rintoul, and J. D. Zika, 2015: Sensitivity of antarctic circumpolar current transport and eddy activity to wind patterns in the southern ocean. *Journal of Physical Oceanography*, **45 (4)**, 1051–1067.

Larour, E., E. R. Ivins, and S. Adhikari, 2017: Should coastal planners have concern over where land ice is melting? *Science Advances*, **3 (11)**.

LeBlond, P. H. and L. A. Mysak, 1981: *Waves in the Ocean*. Elsevier, Amsterdam.

Ledwell, J. R., A. J. Watson, and C. S. Law, 1993: Evidence for slow mixing across the pycnocline from an open-ocean tracer-release experiment. *Nature*, **364**, 701.

Lefebvre, W., H. Goosse, R. Timmermann, and T. Fichefet, 2004: Influence of the southern annular mode on the sea ice–ocean system. *Journal of Geophysical Research: Oceans*, **109 (C9)**.

Legg, S. and A. Adcroft, 2003: Internal wave breaking at concave and convex continental slopes. *Journal of Physical Oceanography*, **33 (11)**, 2224–2246.

Legg, S. and J. Klymak, 2008: Internal hydraulic jumps and overturning generated by tidal flow over a tall steep ridge. *Journal of Physical Oceanography*, **38**, 1949–1964.

Li, M., R. S. Pickart, M. A. Spall, T. J. Weingartner, P. Lin, G. W. K. Moore, and Y. Qi, 2019: Circulation of the chukchi sea shelfbreak and slope from moored timeseries. *Progress in oceanography*, **172**, 14–33.

Lin, P., R. S. Pickart, K. M. Stafford, G. W. K. Moore, D. J. Torres, F. Bahr, and J. Hu, 2016: Seasonal variation of the beaufort shelfbreak jet and its relationship to arctic cetacean occurrence. *Journal of Geophysical Research: Oceans*, **121 (12)**, 8434–8454.

Lin, P., et al., 2020: Circulation in the vicinity of mackenzie canyon from a year-long mooring array. *Progress in Oceanography*, **187**, 102 396.

Lincoln, B. J., T. P. Rippeth, Y.-D. Lenn, M.-L. Timmermans, W. J. Williams, and S. Bacon, 2016: Wind-driven mixing at intermediate depths in an ice-free arctic ocean. *Geophysical Research Letters*, **43 (18)**, 9749–9756.

Linders, J., R. S. Pickart, G. Björk, and G. W. K. Moore, 2017: On the nature and origin of water masses in herald canyon, chukchi sea: Synoptic surveys in summer 2004, 2008, and 2009. *Progress in oceanography*, **159**, 99–114.

Livingstone, S. J., C. Ó. Cofaigh, C. R. Stokes, C.-D. Hillenbrand, A. Vieli, and S. S. R. Jamieson, 2012: Antarctic palaeo-ice streams. *Earth-Science Reviews*, **111 (1-2)**, 90–128.

Livingstone, S. J., C. Ó. Cofaigh, C. R. Stokes, C. D. Hillenbrand, A. Vieli, and S. S. R. Jamieson, 2013: Glacial geomorphology of marguerite bay palaeo-ice stream, western antarctic peninsula. *Journal of Maps*, **9 (4)**, 558–572.

Llinás, L., R. S. Pickart, J. T. Mathis, and S. L. Smith, 2009: Zooplankton inside an arctic ocean cold-core eddy: Probable origin and fate. *Deep Sea Research Part II: Topical Studies in Oceanography*, **56 (17)**, 1290 – 1304.

Lowry, K. E., R. S. Pickart, M. M. Mills, Z. W. Brown, G. L. van Dijken, N. R. Bates, and K. R. Arrigo, 2015: The influence of winter water on phytoplankton blooms in the chukchi sea. *Deep Sea Research Part II: Topical Studies in Oceanography*, **118**, 53–72.

Lowry, K. E., et al., 2018: Under-ice phytoplankton blooms inhibited by spring convective mixing in refreezing leads. *Journal of Geophysical Research: Oceans*, **123 (1)**, 90–109.

Lueck, R., 2013: *TN 028: Calculating the rate of dissipation of turbulent kinetic energy*. Tech. Note, Rockland Scientific International Inc, Victoria, BC, 18 pp.

Lueck, R., 2016: *TN 005: Converting shear-probe, thermistor and micro-conductivity signals into physical units*. Tech. Note, Rockland Scientific International Inc, Victoria, BC, 24 pp.

Lueck, R. G. and J. J. Picklo, 1990: Thermal inertia of conductivity cells: Observations with a sea-bird cell. *Journal of Atmospheric and Oceanic Technology*, **7 (5)**, 756–768.

Lueck, R. G., F. Wolk, and H. Yamazaki, 2002: Oceanic velocity microstructure measurements in the 20th century. *Journal of Oceanography*, **58 (1)**, 153–174.

Mackay, N., J. R. Ledwell, M. Messias, A. C. Naveira Garabato, J. A. Brearley, A. J. S. Meijers, D. C. Jones, and A. J. Watson, 2018: Diapycnal mixing in the southern ocean diagnosed using the dimes tracer and realistic velocity fields. *Journal of Geophysical Research: Oceans*.

Manley, T. O. and K. Hunkins, 1985: Mesoscale eddies of the arctic ocean. *Journal of Geophysical Research: Oceans*, **90 (C3)**, 4911–4930.

Marshall, J. and K. Speer, 2012: Closure of the meridional overturning circulation through southern ocean upwelling. *Nature Geoscience*, **5 (3)**, 171–180.

Martinson, D. G. and D. C. McKee, 2012: Transport of warm upper circumpolar deep water onto the western antarctic peninsula continental shelf. *Ocean Science*, **8 (4)**, 433.

Martinson, D. G., S. E. Stammerjohn, R. A. Iannuzzi, R. C. Smith, and M. Vernet, 2008: Western antarctic peninsula physical oceanography and spatio–temporal variability. *Deep Sea Research Part II: Topical Studies in Oceanography*, **55 (18-19)**, 1964–1987.

Massom, R. A., T. A. Scambos, L. G. Bennetts, P. Reid, V. A. Squire, and S. E. Stammerjohn, 2018: Antarctic ice shelf disintegration triggered by sea ice loss and ocean swell. *Nature*, **558 (7710)**, 383–389.

Mathis, J. T., R. S. Pickart, D. A. Hansell, D. Kadko, and N. R. Bates, 2007: Eddy transport of organic carbon and nutrients from the chukchi shelf: Impact on the upper halocline of the western arctic ocean. *Journal of Geophysical Research: Oceans*, **112 (C5)**.

McDougall, T. J. and P. M. Barker, 2011: Getting started with teos-10 and the gibbs seawater (gsw) oceanographic toolbox. *SCOR/IAPSO WG*, **127**, 1–28.

Melling, H., 1993: The formation of a haline shelf front in wintertime in an ice-covered arctic sea. *Continental Shelf Research*, **13 (10)**, 1123–1147.

Melling, H., 1998: Hydrographic changes in the canada basin of the arctic ocean, 1979–1996. *Journal of Geophysical Research: Oceans*, **103 (C4)**, 7637–7645.

Merckelbach, L., A. Berger, G. Krahmann, M. Dengler, and J. R. Carpenter, 2019: A dynamic flight model for slocum gliders and implications for turbulence microstructure measurements. *Journal of Atmospheric and Oceanic Technology*, **36 (2)**, 281–296.

Merckelbach, L., D. Smeed, and G. Griffiths, 2010: Vertical water velocities from underwater gliders. *Journal of Atmospheric and Oceanic Technology*, **27 (3)**, 547–563.

Meredith, M., et al., 2019: Chapter 3: Polar regions. *IPCC special report on the ocean and cryosphere in a changing climate*.

Mickett, J. B., Y. L. Serra, M. F. Cronin, and M. H. Alford, 2010: Resonant forcing of mixed layer inertial motions by atmospheric easterly waves in the northeast tropical pacific. *Journal of physical oceanography*, **40 (2)**, 401–416.

Mitchum, G. T. and A. J. Clarke, 1986: The frictional nearshore response to forcing by synoptic scale winds. *Journal of Physical Oceanography*, **16 (5)**, 934–946.

Moffat, C., R. C. Beardsley, B. Owens, and N. Van Lipzig, 2008: A first description of the antarctic peninsula coastal current. *Deep Sea Research Part II: Topical Studies in Oceanography*, **55 (3-4)**, 277–293.

Moffat, C. and M. Meredith, 2018: Shelf-ocean exchange and hydrography west of the antarctic peninsula: a review. *Philosophical Transactions of the Royal Society A: Mathematical, Physical and Engineering Sciences*, **376 (2122)**.

Moffat, C., B. Owens, and R. C. Beardsley, 2009: On the characteristics of circumpolar deep water intrusions to the west antarctic peninsula continental shelf. *Journal of Geophysical Research: Oceans*, **114 (C5)**.

Montes-Hugo, M., S. C. Doney, H. W. Ducklow, W. Fraser, D. Martinson, S. Stammerjohn, and O. Schofield, 2009: Recent changes in phytoplankton communities associated with rapid regional climate change along the western antarctic peninsula. *Science*, **323 (5920)**, 1470–1473.

Moore, G. W. K., A. Schweiger, J. Zhang, and M. Steele, 2018: Collapse of the 2017 winter beaufort high: A response to thinning sea ice? *Geophysical Research Letters*, **45 (6)**, 2860–2869.

Morison, J., M. Steele, and R. Andersen, 1998: Hydrography of the upper arctic ocean measured from the nuclear submarine uss pargo. *Deep Sea Research Part I: Oceanographic Research Papers*, **45 (1)**, 15–38.

Morlighem, M., et al., 2017: Bedmachine v3: Complete bed topography and ocean bathymetry mapping of greenland from multibeam echo sounding combined with mass conservation. *Geophysical research letters*, **44 (21)**, 11–051.

Muench, R. D., H. J. S. Fernando, and G. R. Stegen, 1990: Temperature and salinity staircases in the northwestern weddell sea. *Journal of Physical Oceanography*, **20 (2)**, 295–306.

Muench, R. D., J. T. Gunn, T. E. Whitledge, P. Schlosser, and W. Smethie, 2000: An arctic ocean cold core eddy. *Journal of Geophysical Research: Oceans*, **105 (C10)**, 23 997–24 006.

Muench, R. D., J. D. Schumacher, and S. A. Salo, 1988: Winter currents and hydrographic conditions on the northern central bering sea shelf. *Journal of Geophysical Research: Oceans*, **93 (C1)**, 516–526.

Münchow, A., K. K. Falkner, and H. Melling, 2015: Baffin island and west greenland current systems in northern baffin bay. *Progress in Oceanography*, **132**, 305–317.

Münchow, A., H. Melling, and K. K. Falkner, 2006: An observational estimate of volume and freshwater flux leaving the arctic ocean through nares strait. *Journal of Physical Oceanography*, **36 (11)**, 2025–2041.

Murowinski, E. and R. Lueck, 2012: *A guide to data processing*. Tech. Note, Rockland Scientific International Inc, Victoria, BC, 50 pp.

Mysak, L. A., 1980: Topographically trapped waves. *Annual Review of Fluid Mechanics*, **12 (1)**, 45–76.

Nasmyth, P. W., 1970: Oceanic turbulence. Ph.D. thesis, University of British Columbia.

Naveira Garabato, A. C., K. L. Polzin, B. A. King, K. J. Heywood, and M. Visbeck, 2004: Widespread intense turbulent mixing in the southern ocean. *Science*, **303 (5655)**, 210–213.

Naveira Garabato, A. C., D. P. Stevens, A. J. Watson, and W. Roether, 2007: Short-circuiting of the overturning circulation in the antarctic circumpolar current. *Nature*, **447 (7141)**, 194–197.

Naveira Garabato, A. C., et al., 2019: Phased response of the subpolar southern ocean to changes in circumpolar winds. *Geophysical Research Letters*, **46 (11)**, 6024–6033.

Nicholls, K. W., S. Østerhus, K. Makinson, T. Gammelsrød, and E. Fahrbach, 2009: Ice-ocean processes over the continental shelf of the southern weddell sea, antarctica: A review. *Reviews of Geophysics*, **47 (3)**.

Nikolopoulos, A., R. S. Pickart, P. S. Fratantoni, K. Shimada, D. J. Torres, and E. P. Jones, 2009: The western arctic boundary current at 152 w: Structure, variability, and transport. *Deep Sea Research Part II: Topical Studies in Oceanography*, **56 (17)**, 1164–1181.

Nikurashin, M. and R. Ferrari, 2013: Overturning circulation driven by breaking internal waves in the deep ocean. *Geophysical Research Letters*, **40 (12)**, 3133–3137.

Nowlin Jr., W. D. and J. M. Klinck, 1986: The physics of the antarctic circumpolar current. *Reviews of Geophysics*, **24 (3)**, 469–491.

Oakey, N. S., 1982: Determination of the rate of dissipation of turbulent energy from simultaneous temperature and velocity shear microstructure measurements. *Journal of Physical Oceanography*, **12 (3)**, 256–271.

Oakey, N. S., 1985: Statistics of mixing parameters in the upper ocean during jasin phase 2. *Journal of Physical Oceanography*, **15 (12)**, 1662–1675.

Olbers, D. J., 1976: Nonlinear energy transfer and the energy balance of the internal wave field in the deep ocean. *Journal of Fluid mechanics*, **74 (2)**, 375–399.

Oppenheimer, M., et al., 2019: Chapter 4: Sea level rise and implications for low-lying islands, coasts and communities. *IPCC special report on the ocean and cryosphere in a changing climate*.

Orsi, A. H., W. M. Smethie Jr., and J. L. Bullister, 2002: On the total input of antarctic waters to the deep ocean: A preliminary estimate from chlorofluorocarbon measurements. *Journal of Geophysical Research: Oceans*, **107 (C8)**, 31–1–31–14.

Orsi, A. H., T. Whitworth, and W. D. Nowlin, 1995: On the meridional extent and fronts of the antarctic circumpolar current. *Deep Sea Research Part I: Oceanographic Research Papers*, **42 (5)**, 641–673.

Osborn, T. R., 1974: Vertical profiling of velocity microstructure. *Journal of Physical Oceanography*, **4 (1)**, 109–115.

Osborn, T. R., 1980: Estimates of the local rate of vertical diffusion from dissipation measurements. *Journal of Physical Oceanography*, **10 (1)**, 83–89.

Ou, H. W. and A. L. Gordon, 1986: Spin-down of baroclinic eddies under sea ice. *Journal of Geophysical Research: Oceans*, **91 (C6)**, 7623–7630.

Pacini, A., G. W. K. Moore, R. S. Pickart, C. Nobre, F. Bahr, K. Våge, and K. R. Arrigo, 2019: Characteristics and transformation of pacific winter water on the chukchi sea shelf in late spring. *Journal of Geophysical Research: Oceans*, **124 (10)**, 7153–7177.

Padman, L., 1995: Small-scale physical processes in the arctic ocean. *Coastal and Estuarine Studies*, 97–97.

Padman, L. and T. M. Dillon, 1987: Vertical heat fluxes through the beaufort sea thermohaline staircase. *Journal of Geophysical Research: Oceans*, **92 (C10)**, 10 799–10 806.

Padman, L. and S. Erofeeva, 2004: A barotropic inverse tidal model for the arctic ocean. *Geophysical Research Letters*, **31 (2)**.

Padman, L., M. Levine, T. Dillon, J. Morison, and R. Pinkel, 1990: Hydrography and microstructure of an arctic cyclonic eddy. *Journal of Geophysical Research: Oceans*, **95 (C6)**, 9411–9420.

Palmer, M. R., G. R. Stephenson, M. E. Inall, C. Balfour, A. Düsterhus, and J. A. M. Green, 2015: Turbulence and mixing by internal waves in the celtic sea determined from ocean glider microstructure measurements. *Journal of Marine Systems*, **144**, 57–69.

Peralta-Ferriz, C. and R. A. Woodgate, 2015: Seasonal and interannual variability of pan-arctic surface mixed layer properties from 1979 to 2012 from hydrographic data, and the dominance of stratification for multiyear mixed layer depth shoaling. *Progress in Oceanography*, **134**, 19–53.

Perovich, D., W. Meier, M. Tschudi, S. Farrell, S. Hendricks, S. Gerland, and et al., 2019: [the arctic] sea ice cover [in “state of the climate in 2018”]. *Bulletin of the American Meteorological Society*, **100 (9)**, S146–S150.

Perovich, D., et al., 2020: [the arctic] sea ice [in “state of the climate in 2019”]. *Bulletin of the American Meteorological Society*, **101 (8)**, S251–S253.

Peterson, A. K. and I. Fer, 2014: Dissipation measurements using temperature microstructure from an underwater glider. *Methods in Oceanography*, **10**, 44–69.

Pickart, R. S., 2004: Shelfbreak circulation in the alaskan beaufort sea: Mean structure and variability. *Journal of Geophysical Research: Oceans*, **109 (C4)**.

Pickart, R. S., G. W. K. Moore, C. Mao, F. Bahr, C. Nobre, and T. J. Weingartner, 2016: Circulation of winter water on the chukchi shelf in early summer. *Deep Sea Research Part II: Topical Studies in Oceanography*, **130**, 56–75.

Pickart, R. S., G. W. K. Moore, D. J. Torres, P. S. Fratantoni, R. A. Goldsmith, and J. Yang, 2009: Upwelling on the continental slope of the alaskan beaufort sea: Storms, ice, and oceanographic response. *Journal of Geophysical Research: Oceans*, **114 (C1)**.

Pickart, R. S., L. M. Schulze, G. W. K. Moore, M. A. Charette, K. R. Arrigo, G. van Dijken, and S. L. Danielson, 2013: Long-term trends of upwelling and impacts on primary productivity in the alaskan beaufort sea. *Deep Sea Research Part I: Oceanographic Research Papers*, **79**, 106–121.

Pickart, R. S., M. A. Spall, G. W. K. Moore, T. J. Weingartner, R. A. Woodgate, K. Aagaard, and K. Shimada, 2011: Upwelling in the alaskan beaufort sea: Atmospheric forcing and local versus non-local response. *Progress in Oceanography*, **88 (1-4)**, 78–100.

Pickart, R. S. and G. Stossmeister, 2008: Outflow of pacific water from the chukchi sea to the arctic ocean. *Chinese Journal of Polar Oceanography*, **19 (2)**, 135–148.

Pickart, R. S., T. J. Weingartner, L. J. Pratt, S. Zimmermann, and D. J. Torres, 2005: Flow of winter-transformed pacific water into the western arctic. *Deep Sea Research Part II: Topical Studies in Oceanography*, **52 (24-26)**, 3175–3198.

Pickart, R. S., et al., 2010: Evolution and dynamics of the flow through herald canyon in the western chukchi sea. *Deep Sea Research Part II: Topical Studies in Oceanography*, **57 (1-2)**, 5–26.

Pickart, R. S., et al., 2019: Seasonal to mesoscale variability of water masses and atmospheric conditions in barrow canyon, chukchi sea. *Deep Sea Research Part II: Topical Studies in Oceanography*, **162**, 32–49.

Pisareva, M. N., R. S. Pickart, M. A. Spall, C. Nobre, D. J. Torres, G. W. K. Moore, and T. E. Whitledge, 2015: Flow of pacific water in the western chukchi sea: Results from the 2009 rusalca expedition. *Deep Sea Research Part I: Oceanographic Research Papers*, **105**, 53–73.

Plueddemann, A., R. Krishfield, and C. Edwards, 1999: Eddies in the beaufort gyre. paper presented at the ocean-atmosphere-ice interactions (oaii) all hands meeting, virginia beach, va.

Plueddemann, A. J. and J. T. Farrar, 2006: Observations and models of the energy flux from the wind to mixed-layer inertial currents. *Deep Sea Research Part II: Topical Studies in Oceanography*, **53 (1)**, 5 – 30.

Pollard, R. T. and R. C. Millard, 1970: Comparison between observed and simulated wind-generated inertial oscillations. *Deep Sea Research and Oceanographic Abstracts*, **17 (4)**, 813 – 821.

Polyakov, I. V., et al., 2017: Greater role for atlantic inflows on sea-ice loss in the eurasian basin of the arctic ocean. *Science*, **356 (6335)**, 285–291.

Polyakov, I. V., et al., 2020a: Intensification of near-surface currents and shear in the eastern arctic ocean. *Geophysical Research Letters*, **47 (16)**, e2020GL089 469.

Polyakov, I. V., et al., 2020b: Weakening of cold halocline layer exposes sea ice to oceanic heat in the eastern arctic ocean. *Journal of Climate*, **33 (18)**, 8107 – 8123.

Polzin, K. L., 2010: Mesoscale eddy-internal wave coupling. part ii: Energetics and results from polymode. *Journal of physical oceanography*, **40 (4)**, 789–801.

Polzin, K. L., J. M. Toole, J. R. Ledwell, and R. W. Schmitt, 1997: Spatial variability of turbulent mixing in the abyssal ocean. *Science*, **276 (5309)**, 93–96.

Pritchard, H. D., S. R. Ligtenberg, H. A. Fricker, D. G. Vaughan, M. R. van den Broeke, and L. Padman, 2012: Antarctic ice-sheet loss driven by basal melting of ice shelves. *Nature*, **484 (7395)**, 502–5.

Proshutinsky, A., D. Dukhovskoy, M.-L. Timmermans, R. Krishfield, and J. L. Bamber, 2015: Arctic circulation regimes. *Philosophical Transactions of the Royal Society A: Mathematical, Physical and Engineering Sciences*, **373 (2052)**, 20140 160.

Proshutinsky, A., R. Krishfield, and M.-L. Timmermans, 2020: Introduction to special collection on arctic ocean modeling and observational synthesis (famos) 2: Beaufort gyre phenomenon. *Journal of Geophysical Research: Oceans*, **125 (2)**, e2019JC015 400.

Proshutinsky, A., et al., 2009: Beaufort gyre freshwater reservoir: State and variability from observations. *Journal of Geophysical Research: Oceans*, **114 (C1)**.

Proshutinsky, A., et al., 2019: Analysis of the beaufort gyre freshwater content in 2003–2018. *Journal of Geophysical Research: Oceans*, **124 (12)**, 9658–9689.

Proshutinsky, A. Y. and M. A. Johnson, 1997: Two circulation regimes of the wind-driven arctic ocean. *Journal of Geophysical Research: Oceans*, **102 (C6)**, 12 493–12 514.

Rabe, B., et al., 2014: Arctic ocean basin liquid freshwater storage trend 1992–2012. *Geophysical Research Letters*, **41 (3)**, 961–968.

Rainville, L., C. M. Lee, and R. A. Woodgate, 2011: Impact of wind-driven mixing in the arctic ocean. *Oceanography*, **24 (3)**, 136–145.

Raphael, M. N., et al., 2016: The amundsen sea low: Variability, change, and impact on antarctic climate. *Bulletin of the American Meteorological Society*, **97 (1)**, 111–121.

Reid, P., S. Stammerjohn, R. A. Massom, S. Barreira, T. Scambos, and J. L. Lieser, 2020: [antarctica and the southern ocean] sea ice extent, concentration, and seasonality [in "state of the climate in 2019"]. *Bulletin of the American Meteorological Society*, **101 (8)**, S304–S306.

Reszka, M. K. and G. E. Swaters, 1999: Eddy formation and interaction in a baroclinic frontal geostrophic model. *Journal of physical oceanography*, **29 (12)**, 3025–3042.

Rignot, E., S. Jacobs, J. Mouginot, and B. Scheuchl, 2013: Ice-shelf melting around antarctica. *Science Volume pp*, 266–270.

Rignot, E. and S. S. Jacobs, 2002: Rapid bottom melting widespread near antarctic ice sheet grounding lines. *Science*, **296 (5575)**, 2020–2023.

Roach, A. T., K. Aagaard, C. H. Pease, S. A. Salo, T. Weingartner, V. Pavlov, and M. Kulakov, 1995: Direct measurements of transport and water properties through the bering strait. *Journal of Geophysical Research: Oceans*, **100 (C9)**, 18 443–18 457.

Robertson, R., L. Padman, and M. D. Levine, 1995: Fine structure, microstructure, and vertical mixing processes in the upper ocean in the western weddell sea. *Journal of Geophysical Research: Oceans*, **100 (C9)**, 18 517–18 535.

Rott, H., W. Rack, P. Skvarca, and H. De Angelis, 2002: Northern larsen ice shelf, antarctica: further retreat after collapse. *Annals of Glaciology*, **34**, 277–282.

Ruddick, B., 1983: A practical indicator of the stability of the water column to double-diffusive activity. *Deep Sea Research Part A. Oceanographic Research Papers*, **30 (10)**, 1105–1107.

Rudels, B., 2015: Arctic ocean circulation, processes and water masses: A description of observations and ideas with focus on the period prior to the international polar year 2007–2009. *Progress in Oceanography*, **132**, 22 – 67, oceanography of the Arctic and North Atlantic Basins.

Santoso, A., M. H. England, and A. C. Hirst, 2006: Circumpolar deep water circulation and variability in a coupled climate model. *Journal of physical oceanography*, **36 (8)**, 1523–1552.

Sasse, T. P., B. I. McNeil, R. J. Matear, and A. Lenton, 2015: Quantifying the influence of co 2 seasonality on future ocean acidification. *Biogeosciences Discussions*, **12 (8)**.

Schaffer, J., R. Timmermann, J. E. Arndt, S. S. Kristensen, C. Mayer, M. Morlighem, and D. Steinhage, 2016: A global, high-resolution data set of ice sheet topography, cavity geometry, and ocean bathymetry. *Earth System Science Data*, **8 (2)**, 543–557.

Schmidtko, S., K. J. Heywood, A. F. Thompson, and S. Aoki, 2014: Multidecadal warming of antarctic waters. *Science*, **346 (6214)**, 1227–1231.

Schofield, O., M. Brown, J. Kohut, S. Nardelli, G. Saba, N. Waite, and H. Ducklow, 2018: Changes in the upper ocean mixed layer and phytoplankton productivity along the west antarctic peninsula. *Philosophical Transactions of the Royal Society A: Mathematical, Physical and Engineering Sciences*, **376 (2122)**, 20170 173.

Schultz, C., S. C. Doney, W. G. Zhang, H. Regan, P. Holland, M. P. Meredith, and S. Stammerjohn, 2020: Modeling of the influence of sea ice cycle and langmuir circulation on the upper ocean mixed layer depth and freshwater distribution at the west antarctic peninsula. *Journal of Geophysical Research: Oceans*, **125 (8)**, e2020JC016 109.

Schultze, L. K. P., L. M. Merckelbach, and J. R. Carpenter, 2017: Turbulence and mixing in a shallow shelf sea from underwater gliders. *Journal of Geophysical Research: Oceans*, **122 (11)**, 9092–9109.

Schulze, L. M. and R. S. Pickart, 2012: Seasonal variation of upwelling in the alaskan beaufort sea: Impact of sea ice cover. *Journal of Geophysical Research: Oceans*, **117 (C6)**.

Scott, R. M., J. A. Brearley, A. C. Naveira Garabato, H. J. Venables, and M. P. Meredith, 2021a: Glider hydrographic and dissipation data collected during 2016 in ryder bay, west antarctic peninsula [data set]. British Oceanographic Data Centre.

Scott, R. M., J. A. Brearley, A. C. Naveira Garabato, H. J. Venables, and M. P. Meredith, 2021b: Rates and mechanisms of turbulent mixing in a coastal embayment of the west antarctic peninsula. *Journal of Geophysical Research: Oceans*, **126**, e2020JC016 861.

Scott, R. M., R. S. Pickart, P. Lin, A. Münchow, M. Li, D. A. Stockwell, and J. A. Brearley, 2019: Three-dimensional structure of a cold-core arctic eddy interacting with the chukchi slope current. *Journal of Geophysical Research: Oceans*, **124 (11)**, 8375–8391.

Serreze, M. C., A. P. Barrett, J. C. Stroeve, D. N. Kindig, and M. M. Holland, 2009: The emergence of surface-based arctic amplification. *The Cryosphere*, **3 (1)**, 11–19.

Serreze, M. C., A. D. Crawford, J. C. Stroeve, A. P. Barrett, and R. A. Woodgate, 2016: Variability, trends, and predictability of seasonal sea ice retreat and advance in the chukchi sea. *Journal of Geophysical Research: Oceans*, **121 (10)**, 7308–7325.

Sheen, K. L., et al., 2013: Rates and mechanisms of turbulent dissipation and mixing in the southern ocean: Results from the diapycnal and isopycnal mixing experiment in the southern ocean (dimes). *Journal of Geophysical Research: Oceans*, **118 (6)**, 2774–2792.

Shroyer, E. L. and R. S. Pickart, 2019: Pathways, timing, and evolution of pacific winter water through barrow canyon. *Deep Sea Research Part II: Topical Studies in Oceanography*, **162**, 50–62.

Skliris, N., R. Marsh, S. A. Josey, S. A. Good, C. Liu, and R. P. Allan, 2014: Salinity changes in the world ocean since 1950 in relation to changing surface freshwater fluxes. *Climate dynamics*, **43 (3-4)**, 709–736.

Smedsrud, L. H., M. H. Halvorsen, J. C. Stroeve, R. Zhang, and K. Kloster, 2017: Fram strait sea ice export variability and september arctic sea ice extent over the last 80 years. *The Cryosphere*, **11 (1)**, 65–79.

Smeed, D. A., 2000: Hydraulic control of three-layer exchange flows: application to the bab al mandab. *Journal of Physical Oceanography*, **30 (10)**, 2574–2588.

Smyth, W. D. and J. N. Moum, 2012: Ocean mixing by kelvin-helmholtz instability. *Oceanography*, **25 (2)**, 140–149.

Spall, M. A., R. S. Pickart, P. S. Fratantoni, and A. J. Plueddemann, 2008: Western arctic shelfbreak eddies: Formation and transport. *Journal of Physical Oceanography*, **38 (8)**, 1644–1668.

Spall, M. A., R. S. Pickart, M. Li, M. Itoh, P. Lin, T. Kikuchi, and Y. Qi, 2018: Transport of pacific water into the canada basin and the formation of the chukchi slope current. *Journal of Geophysical Research: Oceans*, **123 (10)**, 7453–7471.

Spence, P., S. M. Griffies, M. H. England, A. M. C. Hogg, O. A. Saenko, and N. C. Jourdain, 2014: Rapid subsurface warming and circulation changes of antarctic coastal waters by poleward shifting winds. *Geophysical Research Letters*, **41 (13)**, 4601–4610.

St-Laurent, P., J. M. Klinck, and M. S. Dinniman, 2013: On the role of coastal troughs in the circulation of warm circumpolar deep water on antarctic shelves. *Journal of Physical Oceanography*, **43 (1)**, 51–64.

Stammerjohn, S. E., D. G. Martinson, R. C. Smith, and R. A. Iannuzzi, 2008: Sea ice in the western antarctic peninsula region: Spatio-temporal variability from ecological and climate change perspectives. *Deep Sea Research Part II: Topical Studies in Oceanography*, **55 (18-19)**, 2041–2058.

Steele, M., J. Morison, W. Ermold, I. Rigor, M. Ortmeyer, and K. Shimada, 2004: Circulation of summer pacific halocline water in the arctic ocean. *Journal of Geophysical Research: Oceans*, **109 (C2)**.

Steig, E. J., Q. Ding, D. S. Battisti, and A. Jenkins, 2012: Tropical forcing of circumpolar deep water inflow and outlet glacier thinning in the amundsen sea embayment, west antarctica. *Annals of Glaciology*, **53 (60)**, 19–28.

Stewart, A. L. and A. F. Thompson, 2015: Eddy-mediated transport of warm circumpolar deep water across the antarctic shelf break. *Geophysical Research Letters*, **42 (2)**, 432–440.

Stigebrandt, A., 1999: Resistance to barotropic tidal flow in straits by baroclinic wave drag. *Journal of Physical Oceanography*, **29 (2)**, 191–197.

Stroeve, J. and D. Notz, 2018: Changing state of arctic sea ice across all seasons. *Environmental Research Letters*, **13 (10)**, 103 001.

Swart, N. C., S. T. Gille, J. C. Fyfe, and N. P. Gillett, 2018: Recent southern ocean warming and freshening driven by greenhouse gas emissions and ozone depletion. *Nature Geoscience*, **11 (11)**, 836–841.

Thoma, M., A. Jenkins, D. Holland, and S. Jacobs, 2008: Modelling circumpolar deep water intrusions on the amundsen sea continental shelf, antarctica. *Geophysical Research Letters*, **35 (18)**.

Thomas, L. N. and C. M. Lee, 2005: Intensification of ocean fronts by down-front winds. *Journal of Physical Oceanography*, **35 (6)**, 1086–1102.

Thomas, R. H., 1979: The dynamics of marine ice sheets. *Journal of Glaciology*, **24 (90)**, 167–177.

Thompson, A. F., A. L. Stewart, P. Spence, and K. J. Heywood, 2018: The antarctic slope current in a changing climate. *Reviews of Geophysics*, **56 (4)**, 741–770.

Thorpe, S. A., 2005: *The turbulent ocean*. Cambridge University Press, Cambridge, UK.

Thorpe, S. A., 2018: Models of energy loss from internal waves breaking in the ocean. *Journal of Fluid Mechanics*, **836**, 72.

Timmermans, M.-L., Z. Labe, and C. Ladd, 2020: [the arctic] sea surface temperature [in "state of the climate in 2019"]. *Bulletin of the American Meteorological Society*, **101 (8)**, S249–S251.

Timmermans, M.-L. and J. Marshall, 2020: Understanding arctic ocean circulation: A review of ocean dynamics in a changing climate. *Journal of Geophysical Research: Oceans*, **125 (4)**.

Timmermans, M.-L., J. Marshall, A. Proshutinsky, and J. Scott, 2017: Seasonally derived components of the canada basin halocline. *Geophysical Research Letters*, **44 (10)**, 5008–5015.

Timmermans, M.-L., J. Toole, and R. Krishfield, 2018: Warming of the interior arctic ocean linked to sea ice losses at the basin margins. *Science Advances*, **4 (8)**.

Timmermans, M.-L., J. Toole, R. Krishfield, and P. Winsor, 2008: Ice-tethered profiler observations of the double-diffusive staircase in the canada basin thermocline. *Journal of Geophysical Research: Oceans*, **113 (C1)**.

Timmermans, M.-L., et al., 2014: Mechanisms of pacific summer water variability in the arctic's central canada basin. *Journal of Geophysical Research: Oceans*, **119 (11)**, 7523–7548.

Trenberth, K. E., W. G. Large, and J. G. Olson, 1990: The mean annual cycle in global ocean wind stress. *Journal of Physical Oceanography*, **20 (11)**, 1742–1760.

Troupin, C., J. P. Beltran, E. Heslop, M. Torner, B. Garau, J. Allen, S. Ruiz, and J. TintorÃ©, 2015: A toolbox for glider data processing and management. *Methods in Oceanography*, **13-14**, 13 – 23.

Turner, J., T. Maksym, T. Phillips, G. J. Marshall, and M. P. Meredith, 2013: The impact of changes in sea ice advance on the large winter warming on the western antarctic peninsula. *International Journal of Climatology*, **33 (4)**, 852–861.

Turner, J., T. Phillips, G. J. Marshall, J. S. Hosking, J. O. Pope, T. J. Bracegirdle, and P. Deb, 2017: Unprecedented springtime retreat of antarctic sea ice in 2016. *Geophysical Research Letters*, **44 (13)**, 6868–6875.

Turner, J., et al., 2005: Antarctic climate change during the last 50 years. *International journal of Climatology*, **25 (3)**, 279–294.

van Wessem, J. M., M. P. Meredith, C. H. Reijmer, M. R. van den Broeke, and A. J. Cook, 2017: Characteristics of the modelled meteoric freshwater budget of the western antarctic peninsula. *Deep Sea Research Part II: Topical Studies in Oceanography*, **139**, 31 – 39.

Venables, H. J., A. Clarke, and M. P. Meredith, 2013: Wintertime controls on summer stratification and productivity at the western antarctic peninsula. *Limnology and Oceanography*, **58 (3)**, 1035–1047.

Venables, H. J. and M. P. Meredith, 2014: Feedbacks between ice cover, ocean stratification, and heat content in ryder bay, western antarctic peninsula. *Journal of Geophysical Research: Oceans*, **119 (8)**, 5323–5336.

Venables, H. J., M. P. Meredith, and J. A. Brearley, 2017: Modification of deep waters in marguerite bay, western antarctic peninsula, caused by topographic overflows. *Deep Sea Research Part II: Topical Studies in Oceanography*, **139**, 9–17.

Vernet, M., et al., 2019: The weddell gyre, southern ocean: present knowledge and future challenges. *Reviews of Geophysics*, **57 (3)**, 623–708.

von Appen, W.-J. and R. S. Pickart, 2012: Two configurations of the western arctic shelfbreak current in summer. *Journal of Physical Oceanography*, **42 (3)**, 329–351.

Wåhlin, A. K., X. Yuan, G. Björk, and C. Nohr, 2010: Inflow of warm circumpolar deep water in the central amundsen shelf. *Journal of Physical Oceanography*, **40 (6)**, 1427–1434.

Wåhlin, A. K., et al., 2013: Variability of warm deep water inflow in a submarine trough on the amundsen sea shelf. *Journal of Physical Oceanography*, **43 (10)**, 2054–2070.

Wallace, M. I., M. P. Meredith, M. A. Brandon, T. J. Sherwin, A. Dale, and A. Clarke, 2008: On the characteristics of internal tides and coastal upwelling behaviour in marguerite bay, west antarctic peninsula. *Deep Sea Research Part II: Topical Studies in Oceanography*, **55 (18-19)**, 2023–2040.

Wassmann, P., C. M. Duarte, S. Agustí, and M. K. Sejr, 2011: Footprints of climate change in the arctic marine ecosystem. *Global Change Biology*, **17 (2)**, 1235–1249.

Weertman, J., 1974: Stability of the junction of an ice sheet and an ice shelf. *Journal of Glaciology*, **13 (67)**, 3–11.

Weingartner, T., et al., 2017: The summer hydrographic structure of the hanna shoal region on the northeastern chukchi sea shelf: 2011–2013. *Deep Sea Research Part II: Topical Studies in Oceanography*, **144**, 6–20.

Weingartner, T. J., D. J. Cavalieri, K. Aagaard, and Y. Sasaki, 1998: Circulation, dense water formation, and outflow on the northeast chukchi shelf. *Journal of Geophysical Research: Oceans*, **103 (C4)**, 7647–7661.

Whalen, C. B., C. de Lavergne, A. C. N. Garabato, J. M. Klymak, J. A. MacKinnon, and K. L. Sheen, 2020: Internal wave-driven mixing: governing processes and consequences for climate. *Nature Reviews Earth & Environment*, 1–16.

Whitworth III, T. and R. G. Peterson, 1985: Volume transport of the antarctic circumpolar current from bottom pressure measurements. *Journal of Physical Oceanography*, **15 (6)**, 810–816.

Wolk, F., R. G. Lueck, and L. St. Laurent, 2009: Turbulence measurements from a glider. *OCEANS 2009*, 1–6.

Wolk, F., H. Yamazaki, L. Seuront, and R. G. Lueck, 2002: A new free-fall profiler for measuring biophysical microstructure. *Journal of Atmospheric and Oceanic Technology*, **19 (5)**, 780–793.

Woodgate, R. A., 2018: Increases in the pacific inflow to the arctic from 1990 to 2015, and insights into seasonal trends and driving mechanisms from year-round bering strait mooring data. *Progress in Oceanography*, **160**, 124–154.

Woodgate, R. A., K. Aagaard, and T. J. Weingartner, 2005: A year in the physical oceanography of the chukchi sea: Moored measurements from autumn 1990–1991. *Deep Sea Research Part II: Topical Studies in Oceanography*, **52 (24-26)**, 3116–3149.

Woodgate, R. A., K. M. Stafford, and F. G. Prahl, 2015: A synthesis of year-round interdisciplinary mooring measurements in the bering strait (1990-2014) and the rusalca years (2004-2011). *Oceanography*, **28 (3)**, 46–67.

Woodgate, R. A., T. Weingartner, and R. Lindsay, 2010: The 2007 bering strait oceanic heat flux and anomalous arctic sea-ice retreat. *Geophysical Research Letters*, **37 (1)**.

Wunsch, C. and R. Ferrari, 2004: Vertical mixing, energy, and the general circulation of the oceans. *Annual Review of Fluid Mechanics*, **36 (1)**, 281–314.

Zhang, J., D. A. Rothrock, and M. Steele, 1998: Warming of the arctic ocean by a strengthened atlantic inflow: Model results. *Geophysical Research Letters*, **25 (10)**, 1745–1748.

Zhang, Y., J. Pedlosky, and G. R. Flierl, 2011: Cross-shelf and out-of-bay transport driven by an open-ocean current. *Journal of physical oceanography*, **41 (11)**, 2168–2186.

Zhao, M. and M.-L. Timmermans, 2015: Vertical scales and dynamics of eddies in the arctic ocean's canada basin. *Journal of Geophysical Research: Oceans*, **120 (12)**, 8195–8209.

Zhao, M., M.-L. Timmermans, S. Cole, R. Krishfield, A. Proshutinsky, and J. Toole, 2014: Characterizing the eddy field in the arctic ocean halocline. *Journal of Geophysical Research: Oceans*, **119 (12)**, 8800–8817.

Zhao, M., M.-L. Timmermans, S. Cole, R. Krishfield, and J. Toole, 2016: Evolution of the eddy field in the arctic ocean's canada basin, 2005-2015. *Geophysical Research Letters*, **43 (15)**, 8106–8114.